REPORT DOCUMENTATION PAGE

AFRL-SR-AR-TR-06-0082

Public reporting burden for this collection of information is estimated to average 1 hour per response, includir gathering and maintaining the data needed, and completing and reviewing the collection of information. Sen collection of information, including suggestions for reducing this burden, to Washington Headquarters Service Davis Highway, Suite 1204, Arlington, VA 22202-4302, and to the Office of Management and Budget, Paper

1. AGENCY USE ONLY *(Leave blank)*	2. REPORT DATE	3. REPORT TYPE AND DATES COVERED
		15 Oct 2002 - 14 Oct 2005 FINAL

4. TITLE AND SUBTITLE
AN OPTOELECTRONICS RESEARCH CENTER

5. FUNDING NUMBERS
61102F
2301/AX

6. AUTHOR(S)
DR BRUECK

7. PERFORMING ORGANIZATION NAME(S) AND ADDRESS(ES)
UNIVERSITY OF NEW MEXICO
SCHOLES HALL ROOM 102
ALBUQUERQUE NM 87131-6003

8. PERFORMING ORGANIZATION REPORT NUMBER

9. SPONSORING/MONITORING AGENCY NAME(S) AND ADDRESS(ES)
AFOSR/NE
4015 WILSON BLVD
SUITE 713
ARLINGTON VA 22203
Dr. Howard Schlossberg

10. SPONSORING/MONITORING AGENCY REPORT NUMBER
F49620-03-1-0013

11. SUPPLEMENTARY NOTES

12a. DISTRIBUTION AVAILABILITY STATEMENT
DISTRIBUTION STATEMENT A: Unlimited

12b. DISTRIBUTION CODE

13. ABSTRACT *(Maximum 200 words)*

The research description contains 5 tasks divided into two general areas The first area is the area of nanomatenals and nanophotonics Two tasks are described there, the first being to understand and develop applications for a new class of nanostructured thin films, the second exploring circumstances in which metal films can transmit a high fraction of an incident electromagnetic wave.

The second area of research is in new optoelectronic materials, devices and systems The first task here is the development of a full-duplex free space, solar blind communications system that could be of significant use in satellite to satellite communications The second task involves research on nanoheteroepitaxial (NHE) GaN films on SiC substrates We will target an emission wavelength of 280 nm, which is appropriate for many of the biological species of interest Finally a new compound semiconductor alloy, InNAs, will be investigated in the last task for its role in far-IR sources and detectors of interest to the Air Force.

14. SUBJECT TERMS	15. NUMBER OF PAGES
	16. PRICE CODE

17. SECURITY CLASSIFICATION OF REPORT	18. SECURITY CLASSIFICATION OF THIS PAGE	19. SECURITY CLASSIFICATION OF ABSTRACT	20. LIMITATION OF ABSTRACT
Unclassified	Unclassified	Unclassified	UL

AFOSR FINAL REPORT
Optoelectronics Research Center

PRINCIPAL INVESTIGATOR:
Dr S.R.J. Brueck
Center for High Technology Materials
University of New Mexico
1313 Goddard, SE
Albuquerque, NM 87106
OFFICE: (505) 272-7800
e-mail address: brueck@chtm.unm.edu

GRANT NUMBER: F49620-03-1-0013

REPORT PERIOD Annual: 11/15/2002 – 9/30/2005

AFOSR PROGRAM MANAGER:
Dr Howard Schlossberg,.
AFOSR/NE
Arlington, Virginia, 22203
(703) 696 7549
howard.schlossberg@afosr.af.mil@afosr.af.mil

SUBMITTED BY:

S. R. J. Brueck 3/8/06

NAME: S.R.J. Brueck DATE: 3.8.06
TITLE: Professor, EEC

AN OPTOELECTRONICS RESEARCH CENTER

The University of New Mexico's Optoelectronics Research Center (ORC) focuses on nanophotonics and new optical materials, devices, and systems. These areas exemplify the opportunities presented by the combination of nanotechnology with optoelectronics. The Center's comprehensive research plan addresses the challenges inherent in these topics.

The research description contains 5 tasks divided into two general areas. The first area is the area of nanomaterials and nanophotonics. Two tasks are described there, the first being to understand and develop applications for a new class of nanostructured thin films, the second exploring circumstances in which metal films can transmit a high fraction of an incident electromagnetic wave.

The second area of research is in new optoelectronic materials, devices and systems. The first task here is the development of a full-duplex free space, solar blind communications system that could be of significant use in satellite to satellite communications. The second task involves research on nanoheteroepitaxial (NHE) GaN films on SiC substrates. We will target an emission wavelength of 280 nm, which is appropriate for many of the biological species of interest. Finally a new compound semiconductor alloy, InNAs, will be investigated in the last task for its role in far-IR sources and detectors of interest to the Air Force.

Research Area 1 – Nanomaterials and Nanophotonics

1.1 Title: Development of Artificial Dielectrics for Optical and Electrical Applications

Investigator: Thomas W. Sigmon
Graduate Research Assistant: Kai Yang

Summary

Film fabrication

Artificial dielectric films are prepared by spin-coating precursor solutions onto silicon wafers of selected resistivity and carrier type. By changing the weight percentage of gold, different gold loading factors can be obtained for the prepared samples of gold/silica nanocrystal arrays. The films are coated using spin speeds of 300-500 rpm in air with 10-20% relative humidity at 25C. Following formation and spinning onto the substrate the films are cured in vacuum at 50 °C for 12 hours. Typical film thicknesses are approximately 100 to 130nm.

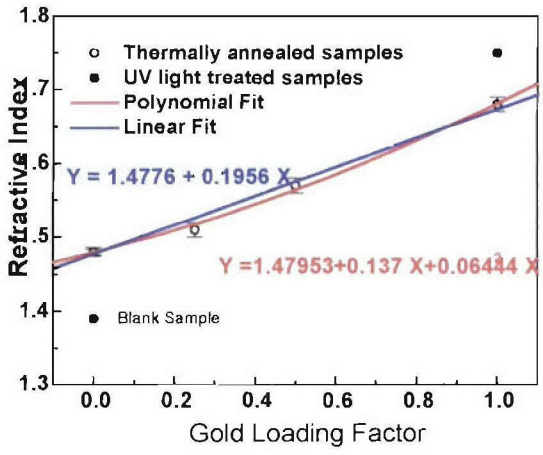


Fig.1 optical refractive index data

Optical refractive index

A set of samples with different gold loading factors (0, 0.25, 0.5, and 1.0) prepared in the previously described manner were anncaled at 180°C for 5 hours. Ellipsometer measurements determined that the film thicknesses of these artificial dielectric films ranged from 110 to 170nm. Figure 1 shows the optical refractive index of the gold/silica thin films The empirical formula for the optical refractive index

of these films was obtained by fitting the experimental data with both a linear and polynomial fit. As shown in Fig.1, for the linear fit, Y = 1.4776 + 0.1956 X, where Y is refractive index, and X is gold loading factor. By adding a bowing factor, we get $Y = 1.4795+0.137X+0.0644X^2$.

Nonlinear optical measurement

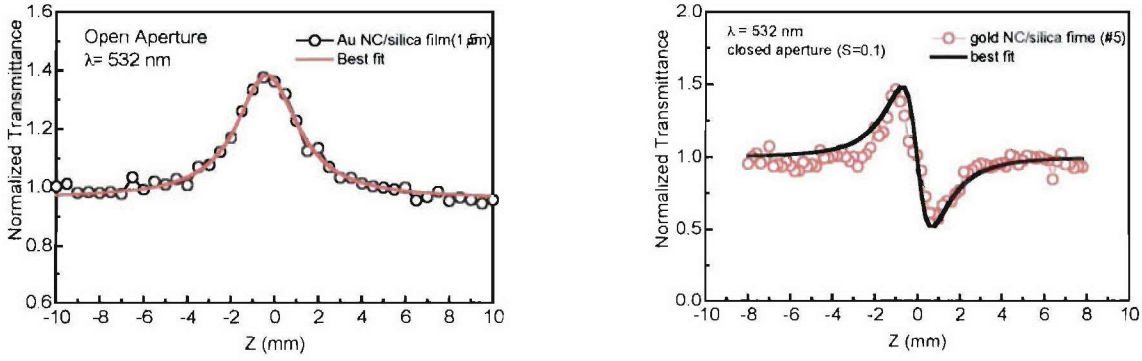


FIG. 2 z-scan normalized transmittance with an open aperture(A) and closed aperture (S = 10%) (B) for gold NC/silica films (~1.5μm) illuminated using nanosecond pulses of peak intensity I_{00} = ~0.19GW/cm^2 at 532 nm.

Third-order nonlinear optical properties of gold nanocrystal(NC)/silica thin films were investigated both on and off the surface plasmon resonance (SPR) wavelength using the *z*-scan method with short pulsed lasers. These films were prepared by self-assembly of water-soluble gold NC micelles and silica using sol-gel processing. The gold NC mean size is ~3 nm and the gold volume fraction is ~5.6 % in these films. The SPR absorption peak of these films occurs at ~520 nm. At a wavelength of 532 nm, the values of the nonlinear absorption coefficient β and nonlinear refractive index coefficient γ were determined to be $\beta = -2.3 \times 10^{-6}$ m/W, and $\gamma = -4.5 \times 10^{-14}$ m^2/W, corresponding to an absolute value of $\chi^{(3)} \sim 1.1 \times 10^{-7}$ esu.

Accomplishments:

- Demonstration of thin films of self-assembled ordered metal nanocrystal arrays
- Fabrication of thin film structures of such arrays
- Engineering the optical refractive index of the metal nanocrystal arrays by changing the gold loading factor
- Third-order nonlinear optical properties of Au NC/silica thin films were studied both on and off the surface plasmon resonance wavelength using Z-scan measurements with short pulsed lasers.
- For the 532 nm measurement, values of the nonlinear absorption coefficient β and nonlinear refractive index coefficient γ were obtained using open- and closed-aperture z-scan measurements with values of $\beta = -2.3 \times 10^{-6}$ m/W and $\gamma = -4.5 \times 10^{-14}$ m^2/W being determined. The large enhancement found for the third-order optical nonlinearities is qualitatively explained by the local field enhancement at the gold NCs occurring at the surface plasmon resonance.

Publications:

1. Kai Yang, Hongyou Fan, Michael J. O'Brien, Kevin J. Malloy, Thomas W. Sigmon, Gabriel P. Lopez, Jeffrey C. Brinker, Mansoor Sheik-Bahae, "Surface plasmon

excitations in 3-D, ordered, gold nanocrystal arrays using a prism coupler", accepted by MRS 05 fall meeting, Boston, 2005

2. Kai Yang, Hongyou Fan, Li Wang, Olivier J. Chalus, Weiliang Chen, Ravi Jain, Kevin J. Malloy, C. Jeffrey Brinker, Jean-Claude Diels, and Thomas W. Sigmon, "Z-scan studies of the third-order optical nonlinearity of sol-gel derived gold nanocrystal/silica films", accepted by MRS 05 fall meeting, Boston, 2005

3. Kai Yang, Hongyou Fan, Kevin J. Malloy, C. Jeffrey Brinker, and Thomas W. Sigmon, "*Optical and electrical properties of self-assembled, ordered gold nanocrystal/silica thin films prepared by sol-gel processing*", Thin Solid Films, 491, 38 2005.

4. Hongyou Fan, Kai Yang, Daniel M. Boye, Thomas W. Sigmon, Kevin J. Malloy, Huifang Xu, Gabriel P. Lopez, and C. Jeffrey Brinker, "*Self-Assembly and Integration of Ordered, Robust, Three-Dimensional Gold Nanocrystal/Silica Array*", Science, 304, 567, 2004

5. Kai Yang, Hongyou Fan, Kevin J. Malloy, C. Jeffrey Brinker, and Thomas W. Sigmon, "*Electrical and optical properties of self-assembled, ordered gold nanocrystal/silica thin films prepared by sol-gel processing*", Mater. Res.Soc. Symp.Proc., Vol 872, pp. J7.5.1-6, 2005

6. Kai Yang, Hongyou Fan, Michael J. O'Brien, Kevin J. Malloy, Thomas W. Sigmon, Gabriel P. Lopez, Jeffrey C. Brinker, Mansoor Sheik-Bahae, "Self-Assembled, Ordered Gold Nanocrystal/Silica Thin Films for Prism-based Surface Plasmon Resonance Sensors", Conference on lasers and Electro-Optics (CLEO/QELS 2005), Technique Digest. TOPS, JTuC102, 2005

Conference Presentations:

1. Kai Yang, Hongyou Fan, Michael J. O'Brien, Kevin J. Malloy, Thomas W. Sigmon, Gabriel P. Lopez, Jeffrey C. Brinker, Mansoor Sheik-Bahae, "Self-Assembled, Ordered Gold Nanocrystal/Silica Thin Films for Prism-based Surface Plasmon Resonance Sensors", CLEO/QELS 2005, in Baltimore, Maryland, May 22-27, 2005.

2. Kai Yang, Hongyou Fan, Kevin J. Malloy, C. Jeffrey Brinker, and Thomas W. Sigmon, "*Electrical and optical properties of self-assembled, ordered gold nanocrystal/silica thin films prepared by sol-gel processing*", MRS 2005 Spring meeting, Symposium J, San Francisco, California, March 28-April 1, 2005

3. Hongyou Fan, Kai Yang, Kevin Malloy, Thomas Sigmon and Jeff Brinker, "*Self-Assembly and Integration of Ordered, Robust, Three-Dimensional Gold Nanocrystal/Silica Arrays*", MRS '04 Spring meeting, Symposium M5.34, San Francisco, California, April 12 - 16, 2004

4. Hongyou Fan, Kai Yang, Kevin Malloy, Thomas Sigmon and Jeff Brinker, "*Surfactant-Assisted self-assembly of water-soluble nanocrystal, ordered arrays, and their integration*", MRS '04 Spring meeting, Symposium O1.7/W1.7, San Francisco, California, April 12 - 16, 2004

1.2 Development of Long Wave Infrared Quantum Dot Detectors

PI: Sanjay Krishna

Prof. Sanjay Krishna, Center for High Technology Materials, University of New Mexico has been involved in developing mid-wave (3-5 mm) and long wave (8-12 mm) sensors based on intersuband transitions in nanoscale quantum dots. This is an active collaboration with constant feedback since the sensors are designed, grown and fabricated in Prof. Krishna' s group and are then characterized by research scientists working closely with the DOD labs (AFRL/ARL). Recently Prof. Krishna's group has been involved in fabricating focal plane arrays based on self assembled quantum dots and strain layer superlattices. One of the processing schemes is shown in Figure 1.

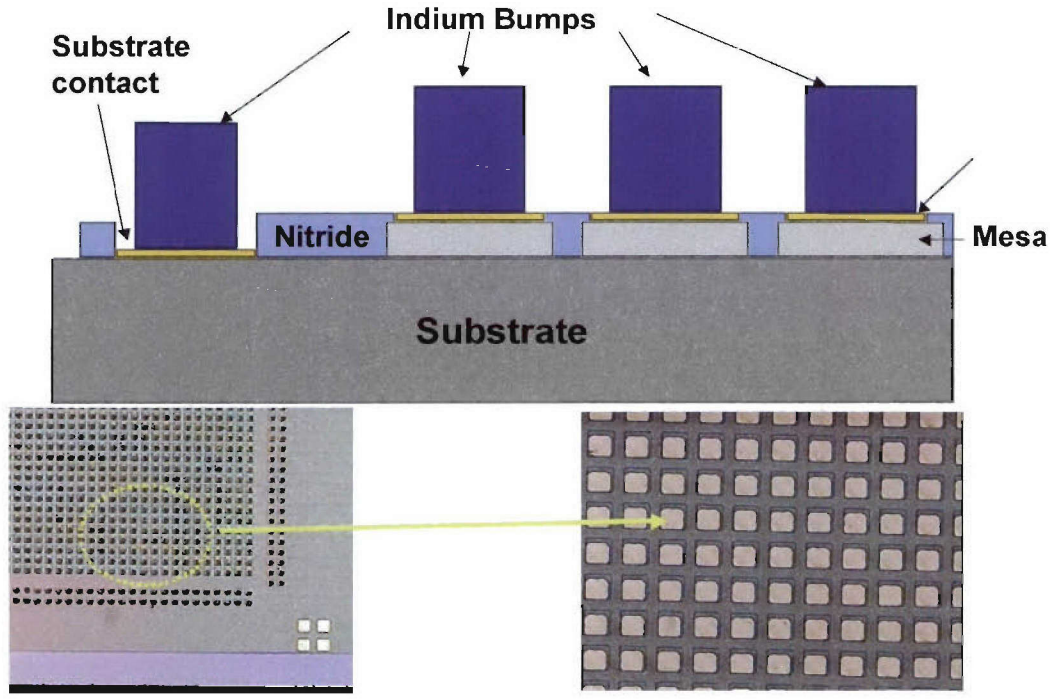


Fig. 1: Process schematic for fabrication of a 320 x 256 focal plane array.

Accomplishments:

Some of the accomplishments of this collaboration in the past year are:

- Demonstration of very long wave infrared (VLWIR) detectors (25 mm) based on intersubband transitions in the quantum dots at 80K. This is the largest operating temperature for any intersubband VLWIR detector
- Demonstrated a three color (4 mm, 8 mm and 25 mm) QD sensor with background limited infrared performance (BLIP) at 91K under f1.7, 300K background. This is the highest reported BLIP temperature in any intersubband LWIR detector
- Demonstration of spectrally adaptive quantum dot detectors that can be used for rock classification
- Demonstration of the first LWIR quantum dot camera using a 320x256 read out integrated circuit

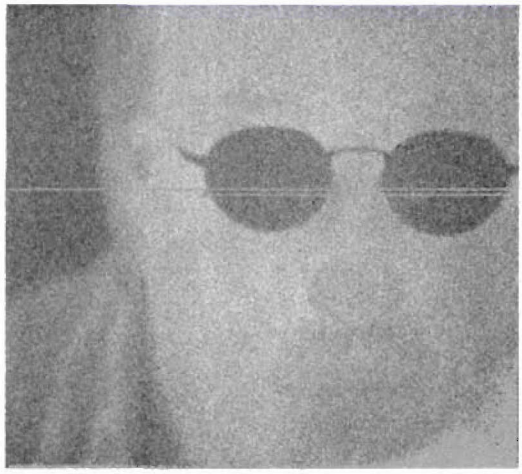


Fig. 2: Image of a 300K object using the first long wave infrared quantum dot camera (Collaboration with Zia Laser Inc and BAE Systems Inc).

Publications and Presentations (relevant to this grant):

- S.Krishna, D. Forman, S. Annamalai, P. Dowd, P. Varangis, T. Tumolillo, A. Gray, J.Zilko, K. Sun, M. Liu, J. Campbell, D. Carothers "Demonstration of a 320 x 256 Two-Color Focal Plane Array Using InAs/InGaAs Quantum Dots in a Well Detectors"Appl. Phys. Lett, **86**, 193501, 2005.
- "Normal Incidence InAs/InGaAs Quantum dots in a Well Detectors Spanning the Long Wave Atmospheric Window", Journal of the Korean Physical Society, Vol.45, S, 875, Dec 2004.
- Zhipeng Wang, Unal Sakoglu, Senthil Annamalai, Nina-Rae Weisse-Bernstein, Philip Dowd, J. Scott Tyo, Majeed M. Hayat, and Sanjay Krishna "Real-time implementation of matched filtering algorithms using adaptive focal-plane array technology" Proc. SPIE Int. Soc. Opt. Eng. 5546, 73 (2004)

1.3 Optical Interactions with Structured Media

PI: S. R. J. Brueck

Work during this period has concentrated on various aspects of optical interactions with structured media, in particular with various waveguide geometries. In particular we have evaluated the distribution of emission of a dipole embedded in an arbitrary plane parallel dielectric stack between bound waveguide modes and free-space radiation out the top/bottom of the slab. This calculation was initiated in the context of vertical cavity lasers, but has added relevance to the issues of efficient light emission from LEDs. Photonic crystals can dramatically impact this emission. To date our explorations have been primarily experimental. In collaboration with Maxion Inc., we have demonstrated the first midwave infrared DFB laser with over 30 db side-mode suppression. We have also begun investigating the improvements in light extraction that can be achieved on GaInN LEDs with the addition of a photonic crystal overlayer. This led to increased understanding of photonic crystal waveguides, and to the first discussion of "generalized transverse Bragg waveguides" wherein the Bragg planes are at an angle to the waveguide direction. This class of waveguide has both new physics – namely the presence of a standing wave component in the guide even for a unidirectional wave – and important applications – to wit the suppression of reflection with application to amplifiers and other unidirectional-gain devices.

Work has also continued on the generation of a second order nonlinearity in poled structures. During this period, we introduced the new concept of a stacked structure including both SiO_2 to control the charge migration that results in the second-order susceptibility and PbO_3 glass to provide a large third order susceptibility. This resulted in the largest reported second order susceptibility. Other work has applied the nanoscale interferometric lithography capability we have developed in a number of promising directions: understanding of the development of stress in heterogeneous materials growth and development of wrap-around gate Si transistor structures with improved mobility and reduced leakage currents. Finally, at the end of the period an invited review article summarizing much of the work in this and related programs was published in the Proceedings of the IEEE.

Optical emission from an arbitrary planar dielectric stack – analytical treatment

An analytical solution for the radiation emitted from a dipole embedded in an arbitrary, planar dielectric film stack was derived. The calculation uses a rigorous Hertz-vector formalism to treat the electromagnetic boundary conditions. The radiation fields are then evaluated in a far-field approximation to get the radiated fields far from the dipole. Both 2D emission into bound modes of the dielectric stack and 3D emission into radiation fields above and below the stack are evaluated. These solutions are explored for two simple cases: a InGaAs slab symmetrically clad with up to four high-contrast (Al_2O_3/GaAs) Bragg mirror pairs and semi-infinite air spaces; and a similar asymmetric structure with a GaAs substrate on one side. The symmetric structure supports both 2D bound and 3D radiation fields. The asymmetric structure only supports 3D radiation fields since there are no strictly bound modes, but "leaky" modes appear that are very similar to the bound modes in the symmetric structure except that the radiated power ultimately is transmitted into the substrate in a very highly directional beam. This calculation is applicable a wide range of solid-state photonic devices including vertical-cavity and edge-emitting lasers, spontaneous light-emitting diodes, and photodetectors.

Some results for parameters appropriate to the thin-film LED devices are shown in Fig. 1. The output radiation is normalized to the radiation from a dipole in an infinite GaN medium. The periodic steps in the power radiated into modes (the unwanted bound mode radiation) is due to the appearance of additional bound modes as the thickness increases. There is a peak in the radiated emission just before the appearance of each mode. As shown in the bottom figure, the

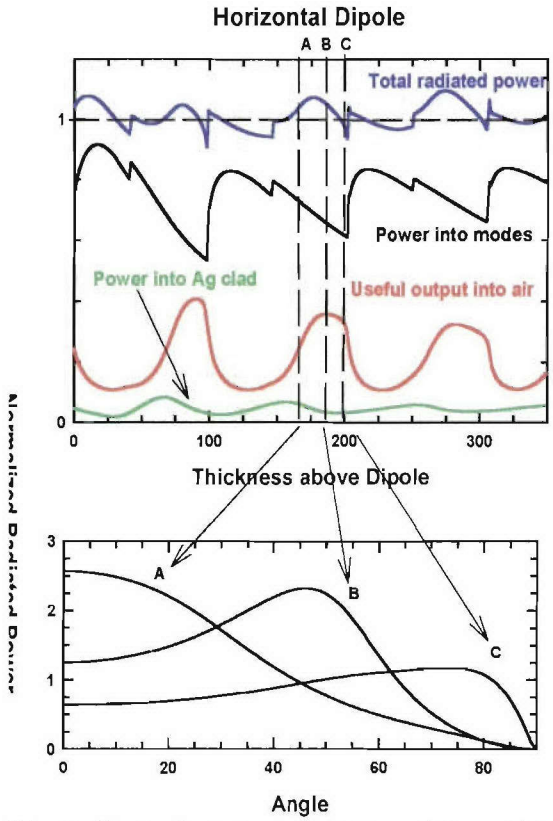


Fig. 1: First principles calculation of the radiation emitted from a dipole in a thin-film GaN LED as a function of the GaN thickness. The bottom figure shows the variation in the radiation pattern as the thickness is varied.

radiation pattern changes markedly for small changes in the film thickness, with the highest output powers corresponding to undesirable emission to the sides and lowered emission in the forward direction (angle = 0).

The next step in the modeling is to add the effects of a photonic crystal, which we expect to include using a rigorous coupled wave approach (RCWA) perturbative approach. This is in contrast to many other calculations that use exact numerical techniques such as finite element and FDTD approachs, that provide accurate calculations but are not amenable to clear physical interpretation.

Mid-IR DFB lasers

A distributed-feedback, type-II interband cascade laser is demonstrated in pulsed mode, emitting near 3.145 mm at temperatures between 50 and 80 K. Feedback is provided by a surface etched grating formed using interferometric lithography. Between 50 and 80 K, the device's single longitudinal mode red-shifts with temperature at ~0:1 nm=K. At 70K and 190mA of pulsed injection current, side-mode suppression exceeds 30 dB. The characteristics of related Fabry–Perot IC lasers are also described and contrasted with those of the distributed feedback device.

Photonic Crystal LEDs

Electrical operation of III-Nitride light emitting diodes (LEDs) with photonic crystal structures is demonstrated. Employing photonic crystal structures in III-Nitride LEDs is a method to increase light extraction efficiency and directionality. The photonic crystal is a triangular lattice formed by dry etching into the III-Nitride LED. A range of lattice constants is considered (a ~ 270 - 340nm). The III-Nitride LED layers include a tunnel junction providing good lateral current spreading without a semi-absorbing metal current spreader as is typically done in conventional III-Nitride LEDs. These photonic crystal III-Nitride LED structures are unique because they allow for carrier recombination and light generation proximal to the photonic crystal (light extraction area) yet displaced from the absorbing metal contact. The photonic crystal Bragg scatters what would have otherwise been guided modes out of the LED, increasing the extraction efficiency. The far-field light radiation patterns are heavily modified compared to the typical III-Nitride LED's Lambertian output. The photonic crystal affects the light propagation out of the LED surface, and the radiation pattern changes with lattice size. LEDs with photonic crystals are compared to similar III-Nitride LEDs without the photonic crystal in terms of extraction, directionality, and emission spectra.

Generalized Transverse Bragg Waveguides

A coupled-mode analysis of 2-D generalized transverse Bragg waveguides (GTBW) with tilted distributed Bragg reflectors is developed. As a result of the absence of inversion symmetry about a plane perpendicular to the guiding stripe, the modes supported by these guides are not separable into the familiar form of transverse standing wave and longitudinal traveling-wave components. This fundamental change in the modal description yields new and potentially useful guided-mode behavior. Expressions for the spatial distribution of the optical field, phase and group velocity, and the dispersion relation as well as applications of GTBW are presented.

Second Harmonic in Poled Waveguide Structures

Thermal poling of silica-lead glass-silica waveguides formed by laser ablation of lead glass and e-beam evaporation is reported. A large nonlinearity localized within the Pb-glass layer was found by scanning the probe laser beam across an angle-polished sample, and a peak $\chi^{(2)}$ as high as 15 pm/V was achieved in the Pb-glass layer. A simple theoretical model based on charge transport in the different materials during poling is proposed and the complex $\chi^{(2)}$ profile is explained. The high third order nonlinearity of lead glass plays a key role in the generation of the large SH signal.

Stress creation during Coalescence in Heterogeneous Materials Growth

Island coalescence during Volmer–Weber thin film growth is generally accepted to be a source of tensile stress. However, the stochastic nature of unpatterned film nucleation and growth prevents meaningful comparison of stress measurements taken during growth to that predicted by theoretical models. We have overcome this by systematically controlling island geometry using selective growth of Ni films on patterned substrates via electrodeposition. It was determined that the measured power-law dependence of mean stress on island size agreed well with theory. However, our data clearly demonstrates that the majority of the tensile stress associated with coalescence actually occurred after the initial contact of neighboring islands as the film planarizes with additional deposition. Sample results are shown in Fig. 2.

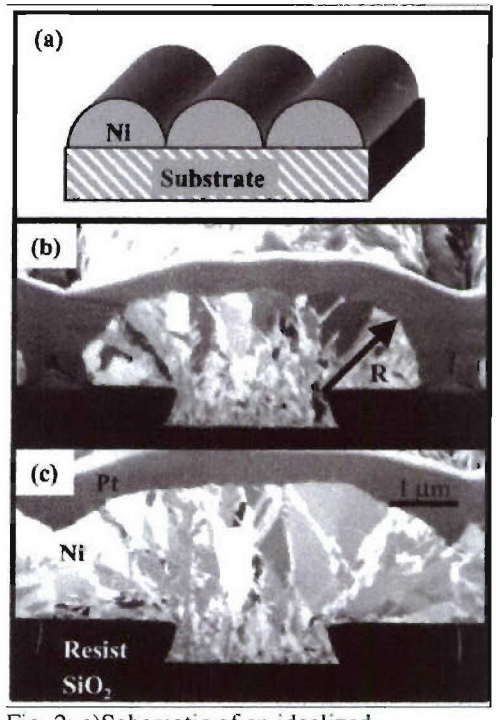


Fig. 2: a)Schematic of an idealized cylindrical structure, b) ion channeling focused ion beam cross-section image of actual structure prior to coalescence, and c) image of the actual structure after coalescence.

Nanochannel MOSFETs

The current conduction process through a nanowire wrap-around-gate, ~50 nm channel diameter, silicon MOSFET has been investigated and compared with a ~2 mm wide slab, ~200 nm thick silicon (SOI) top-only-gate planar MOSFET with otherwise similar doping profiles, gate length and gate oxide thickness. The experimental characteristics of the nanowire and planar MOSFETs were compared with theoretical simulation results based on semi-empirical carrier mobility models. The SOI nanowire MOS devices were fabricated through interferometric lithography in combination with conventional I-line lithography. A significant increase (~3_) in current density was observed in the nanowire devices compared to the planar devices. A number of parameters such as carrier confinement, effects of parallel and transverse

field-dependent mobilities, and carrier scattering due to Coulomb effects, acoustic phonons, impurity doping profile and surface roughness influences the transport process in the channel regions. The electron mobility in the nanochannel increases to ~1200 cm^2/V s compared to ~400cm^2/V s for a wide slab planar device of similar channel length. Experiments also show that the application of the channel potential from three sides in the nanowire structure dramatically improves the subthreshold slope characteristics.

Optical and Interferometric Lithography – Nanotechnology Enablers

Interferometric lithography, the interference of a small number of coherent optical beams, is a powerful technique for the fabrication of a wide array of samples of interest for nanoscience and nanotechnology. The techniques and limits of interferometric lithography are discussed with particular attention to the smallest scales achievable. With immersion techniques, the smallest pattern size for a single exposure is a half pitch of $l/4n$ were l is the optical wavelength and n is the refractive index of the immersion material. Currently with a 193-nm excimer laser source and H_2O immersion, this limiting dimension is ~ 34 nm. With nonlinear spatial frequency multiplication techniques, this limit is extended by factors of 1/2, 1/3, etc. - extending well into the nanoscale regime. Interferometric lithography provides an inexpensive, large-area capability as a result of its parallelism. Multiple exposures, multiple beams, and mix-and-match with other lithographies extend the range of applicability. Imaging interferometric lithography provides an approach to arbitrary structures with comparable resolution. Numerous application areas including: nanoscale epitaxial growth for semiconductor heterostructures; nanofluidics for biological separations; nanomagnetics for increased storage density; nanophotonics including distributed feedback and distributed Bragg reflectors, 2D and 3D photonic crystals, metamaterials and negative refractive index materials for enhanced optical interactions are briefly reviewed.

Publications:

S. R. J. Brueck, V. A. Smagley and P. G. Eliseev, *Radiation from a Dipole Embedded in a Multilayer Dielectric Slab,* Phys. Rev. **E 68**, 036608 (2003)

J. L. Bradshaw, J. D. Bruno, J. T. Pham, D. E. Wortman, S. Zhang and S. R. J. Brueck, *Single-Longitudinal-Mode Emission from Interband Cascade DFB Laser with a Grating Fabricated by Interferometric Lithography,* Proc. IEE-Optoelectronics **150**, 288-292 (2003).

Ying Luo, Abani Biswas, A. Frauenglass and S. R. J. Brueck, *Large Second Harmonic Signal in Thermally Poled Lead Glass-Silica Waveguides,* Appl. Phys. Lett. **84**, 4935-4937 (2004).

A. K. Sharma, S. H. Zaidi, S. Lucero, S. R. J. Brueck and N. E. Islam, *Mobility and Transverse Electric Field Effects in Channel Conduction of Wrap-Around Gate Nanowire MOSFETs,* IEE Proc. Circuits, Devices and Systems **151**, 422–431 (2004).

S. J. Hearne, S. C. Seel, J. A. Florio, C. W. Dyck, W. Fan and S. R. J. Brueck, *Quantitative Determination of Tensile Stress Creation during Island Coalescence using Selective-Area Growth,* Jour. of Appl. Phys. **97**, 083530 (2005).

J. J. Wierer, M. R. Krames, J. E. Epler, N. F. Gardner, J. R. Wendt, M. M, Sigalas, S. R. J. Brueck, D. Li, and M. Shagam, *III-Nitride LEDs with Photonic Crystal Structures,* Proc. SPIE **5739**, 102-107 (2005).

S. R. J. Brueck, *Optical and Interferometric Lithography – Nanotechnology Enablers,* Proc. IEEE **93**, 1704-1721 (2005).

B. D. Burckel and S. R. J. Brueck, *Generalized transverse Bragg waveguides,* Optics Express (to be published)

1.4 Investigations of Surface Plasmon Nanophotonics - Surface plasmon-polariton propagation in the presence of gain

K. J. Malloy and Jing Chen

The propagation length of surface plasmon polariton (SPP) is limited due to energy dissipation in non-ideal metals. The presence of an active medium near the metallic/dielectric surface to compensate the ohmic losses in the metal is a possible route to increasing the propagation length. Ploz *et al.*, [1] analyzed enhanced total internal reflection (TIR) from an amplifying medium with surface plasmon excitation. Sudarkin and Demkovich [2] theoretically studied excitation of surface electromagnetic waves (SEWs) on the boundary of a metal with an amplifying medium. Nezhad *et al.*, [3] expanded these concepts to investigate gain-assisted propagation of SPPs on planar metallic waveguides. Here we present a numerical investigation using rigorous coupled-wave analysis (RCWA) for SPPs supported by metallic gratings in the presence of gain medium.

Diffraction on a periodic structure provides wavevector conservation and coupling to surface polaritons. For a one-dimensional (1D) structure, the coupling condition for normal incident is described by [4]:

where is the light wavevector, is the grating periodicity, and is the real part of complex permittivity of adjacent dielectric medium and metal respectively. Numerical modeling [5] shows that SPPs on an Au/GaAs interface at wavelength 1.3 um can be achieved by the structure shown in Fig. 1 and modeled in Fig. 2. The period of the gold grating is 380 nm, the gold fill factor is 70% and the grating height is 65 nm. The wavelength dependence of transmittance (T) and reflectance (R) for structure in Fig. 1 without gain medium is shown in Fig. 2 for different dielectrics filled between metal stripes. Figure 2 shows the importance of filling the gap between Au stripes with a dielectric as no SPP coupling occurs for an air gap between Au stripes while coupling occurs for n=3.41 at 1.3 um.

Figure 3 shows the effect of introducing gain in the dielectric region below the grating. Reflectance and transmittance of the complete structure are shown for a layer with a real index of 3.41 but with material gain varying between 0 and $2x10^4 cm^{-1}$. In this range, transmission is enhanced, and reflection is first reduced and then increased again (this has a straightforward

Figure 1: Schematic diagram of the metallic grating structure.

origin in the overlap of the field with the gain region). The loss in the metal is compensated by energy fed from the gain medium and re-radiated, resulting the enhancement of reflectance and transmittance.

A finite thickness gain layer in proximity to the metallic grating can compensate for loss in the metal. The function 1-R-T indicates the net gain or loss in structure. The gain value necessary for for different gain layer thickness versus distance between gain layer and grating is plotted in Fig. 4. This gain value is required for lossless SPP propagation on this grating structure. As expected, the necessary gain increases for thinner gain layers or wider separations.

For the conditions considered here, currently available semiconductor-based gain media can provide enough gain for lossless or nearly lossless SPPs propagation. The gain could be a multiple quantum well stack (material gain of 2600 cm^{-1} for a double quantum well [6]) or layers of self assembled quantum dots (material gain of $6.8x10^{4}cm^{-1}$ reported for a layer of self assembled quantum dots [7]).

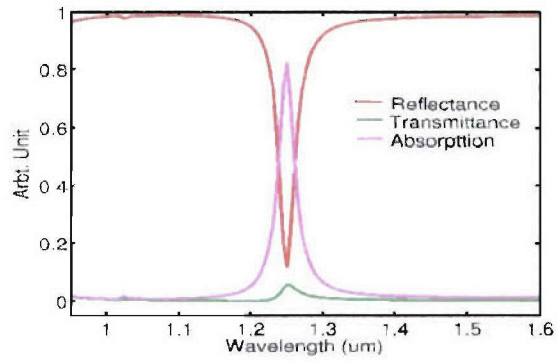


Figure 5 (a) and (b). The two-level metallic grating studied the resulting modeled

The localization of visible electromagnetic fields into nanometer volumes was also investigated through modeling. Figure 5 shows the structure studied and the resultant fields.

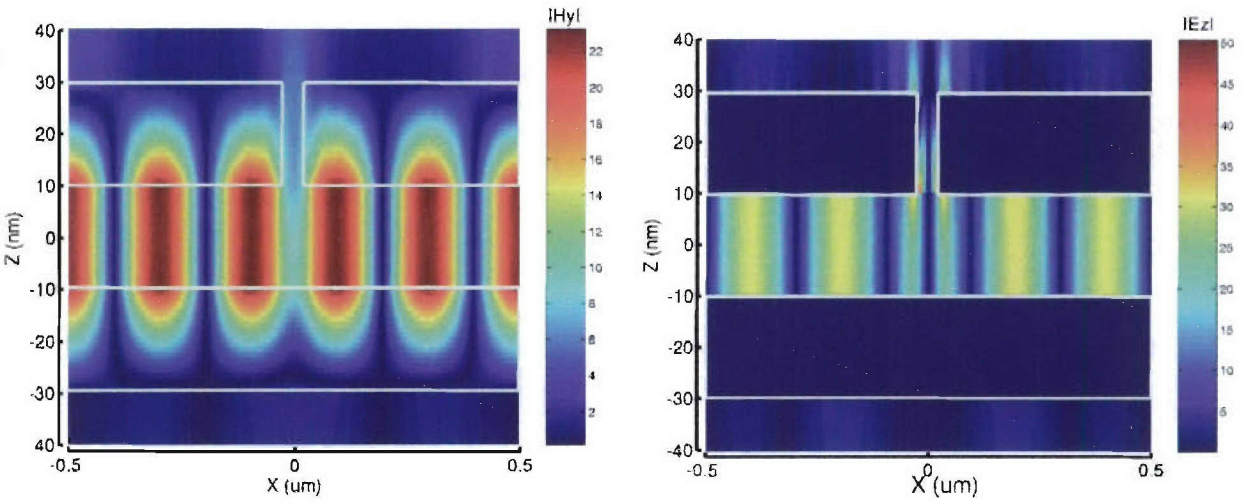


Figure 5 (c) and (d). The calculated magnetic (c) and electric (d) field associated with the grating-coupled plasmon waveguide.

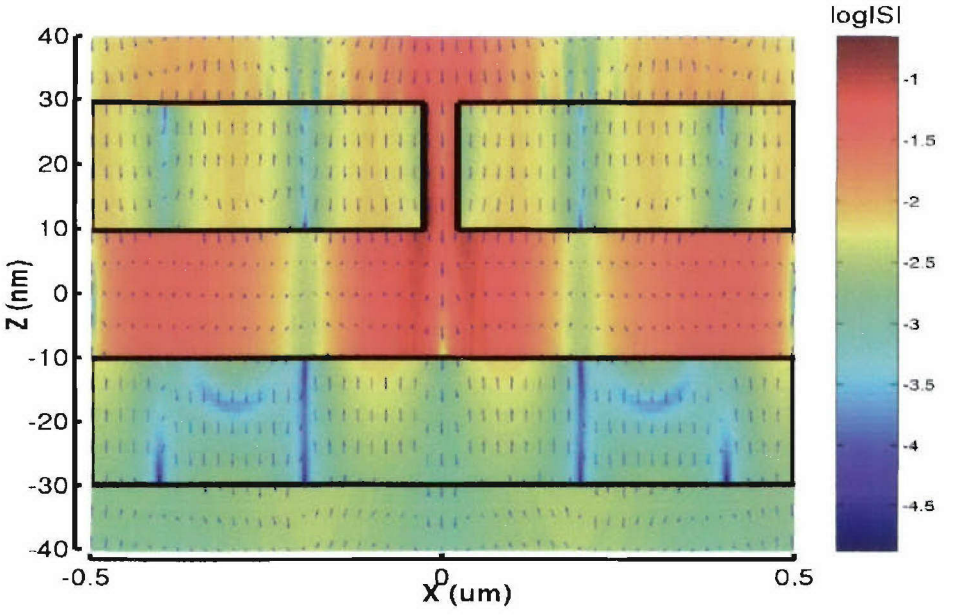


Figure 5 (e). The calculated Poynting vector for the fields present in the grating-coupled plasmon waveguide.

Numerical modeling for the grating-coupled plasmon waveguide illuminated with TM electromagnetic plane wave are depicted in Fig. 5. The details of the waveguide design are as follows: Pitch , fill factor 0.95, metal thickness and core thickness . (In Fig. 5, the field amplitudes and are normalized to the incident field

magnitudes and the log of the Poynting vector, log S, is shown in Fig. 5 (e). The gold dielectric properties parameters taken from [8] and [9] are use here.

Resonance occurs at wavelength 1.25 um. Figure 5(e) clearly shows the collective oscillation on metal surfaces. Inside the core, the energy propagates parallel to the planar plane. Radiation is efficiently coupled into this structure which resonantly absorbs and propagates at wavelengths

more than 50 times its thickness. Field enhancement of 20 and 35 times are obtained for

and , respectively.

REFERENCES

[1] G. A. Plotz, H. J. Simon, J. M. Tucciarone, "Enhanced total reflection with surface plasmons," JOSA 69, 419-421 (1979).
[2] A. N. Sudarkin and P. A. Demkovich, "Excitation of surface electromagnetic waves on the boundary of a metal with an amplifying medium," *Sov. Phys.Tech. Phys.* 34, 764-766 (1989).
[3] Maziar P. Nezhad, Kevin Tetz, Yeshaiahu Fainman, "Gain assisted propagation of surface plasmon polaritons on planar metallic waveguides", *Optics Express*, 12, No. 17,4072-4079 (2004)
[4] Raether H 1988 *Surface Plasmons* (Berlin: Springer)
[5] B.K. Minhas, W. Fan, K. Agi, S.R.J. Brueck, and K.J. Malloy, "Metallic inductive and capacitive girds: theory and experiment", *J. Opt. Soc. Am. A* 19(7), 1352-1359,2002.
[6] S. Y. Hu, D. B. Young, S. W. Corzine, A.C. Gossard, L. A. Coldren, "High-efficiency and low-threshold InGaAs/AlGaAs quantum-well lasers," *J. of Appl. Physics* **76** , 3932-3934 (1994).
[7] N. Kirstaedter, O.G. Schmidt, N.N. Ledentsov, D. Bimberg, V.M. Ustinov, A.Y. Egorov, A.E. Zhukov, M.V. Maximov, P.S. Kopev and Z.I. Alferov, "Gain and differential gain of single layer InAs/GaAs quantum dot injection lasers," *Appl. Phys. Lett.* **69**, 1226-1228 (1996), and Schmidt O G *et al* 1996 *Electron. Lett.* **32** 1302.
[8] M.A. Ordal, L. L. Long, R. J. Bell, S. E. Bell, R. W. Alexander, Jr., and C. A. Ward, "Optical properties of the metals Al, Co, Cu, Au, Fe, Pb, Ni, Pd, Pt, Ag, Ti, and W in the infrared and far infrared," *Appl. Opt.*, **22**, No. 7, 1 April 1983, pp. 1099-1119L.
[9] G. Shulz, "The optical constants of silver, gold, copper and aluminum. 1) the absorption coefficient k and 2) the index of refraction n," *J. Opt. Soc. Am.*, **44**, No. 5, pp. 357-362 and 362-368

Research Area 2 – Novel Optical Systems and Materials

2.1 Nanoheteroepitaxy for the Combination of Lattice-Mismatched Semiconductors – S.D. Hersee

During this 3-year program we have made excellent progress in the development of nanoheteroepitaxy (NHE) for the combination of lattice-mismatched semiconductors. Four new defect reduction mechanisms were identified as being active in the typical NHE sample structure and dramatic improvements in optical and electronic properties were observed in NHE grown materials. In collaboration with Prof Steve Brueck and Prof. Sang Han of the Chemical & Nuclear Eng. Dept the NHE approach has been successfully applied to GaN on various substrates and to the Ge/Si system. Two Ph.D degrees and two MS degrees were awarded to students working in my group. Also, 14 papers and presentations (including 3 invited talks) were given and 4 patents were issued during this project.

Nanoheteroepitaxy (NHE)

The NHE concept[1] is shown schematically in Fig. 1. Two lattice-mismatched semiconductors are connected by an array of nanoscale bridges. The bridges are extremely compliant and are able to accommodate the mismatch strain, allowing the two semiconductors to be connected pseudomorphically (i.e., without defects).

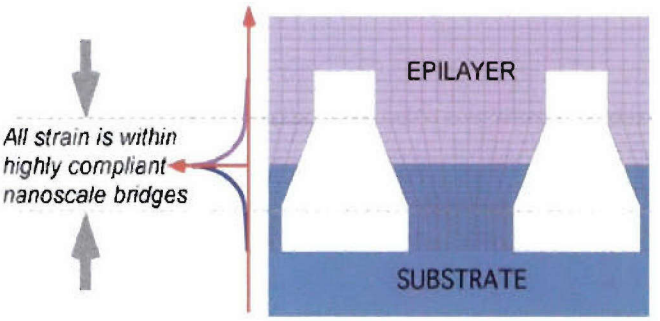


Figure 1: The NHE concept

We showed in the previous phase of this program that the NHE approach reduces the integrated strain energy at the mismatched interface. This will reduce the probability of creating mismatch defects, which is important as these defects can thread vertically

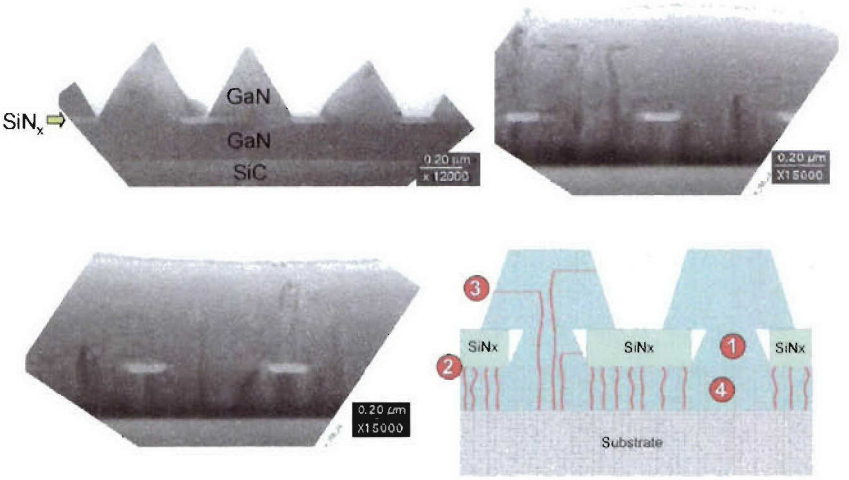


Figure 2: Multiple defect reduction mechanisms are active during NHE growth.

[1] "Nanoheteroepitaxy: The Application of nanostructuring and substrate compliance to the heteroepitaxy of mismatched semiconductor materials," D. Zubia and S. D. Hersee, *J. Appl. Phys.*, **85**, 6492 (1999)

through the heterostructure and degrade its materials and device properties.

During this phase of the program we have applied the NHE approach to several materials systems and we have identified four additional defect reduction mechanisms that are active during the typical NHE process. Referring to figure 2, mechanism 1 represents the main NHE strain energy reduction mechanism, discussed above. Mechanism 2, is the blocking of threading defects by the silicon nitride growth mask. Examples of mechanism 2 can be seen in the top right and lower left micrographs of Fig. 2. Mechanism 3 is the bending of threading dislocations (TDs) towards a sidewall surface. Given the generous availability of such surfaces in the NHE approach (Fig. 1) TDs are generally close enough to a sidewall that they will bend and terminate at a sidewall in order to minimize their length and therefore their free energy.

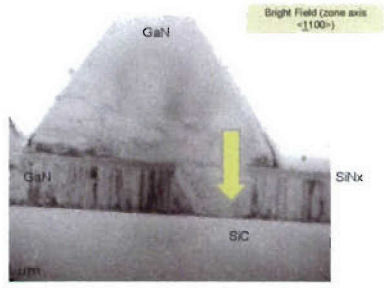


Figure 3: Defect reduction in window region

Mechanism 4 is shown more clearly in Fig. 3 (see arrow) and is the reduction of the TD density within the open window region in the silicon nitride growth mask. This TD reduction is believed to be a result of lateral strain at the growth window in the Si_3N_4/GaN interface.

We have recently identified a further defect reduction mechanism (paper submitted to Appl. Phys. Lett.) that results from the clustering of defects in the NHE sample and the mutual annihilation TDs within the cluster. Fig. 4 shows the clustering of defects (see arrows) that occurs during coalescence in the NHE growth of GaN on GaN/SiC. These dense clusters contain many screw dislocations and perhaps not surprisingly some of these TDs have equal and opposite Burger's vectors, allowing them to mutually annihilate one another. This annihilation has a dramatic effect on the TD density further away from the coalescence region as shown in Fig. 5.

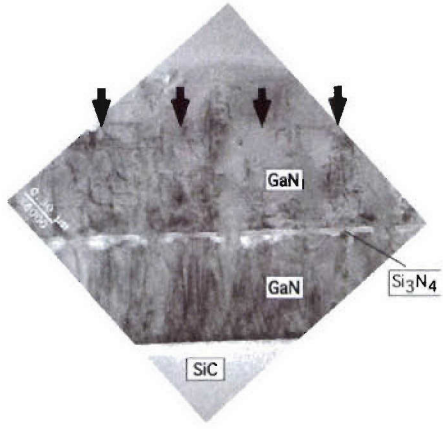


Figure 4: Defect clustering above nitride growth mask

Fig. 5 compares the TD density as revealed by photoelectrochemical (PEC) etching for (left) a planar GaN on GaN/SiC sample and (right) an NHE GaN on GaN/SiC sample, where the TD clustering and mutual annihilation mechanism is active. The whisker features in these images show the location of each dislocation and the TD density in the NHE sample has been reduced by > 10x due to this clustering/annihilation mechanism.

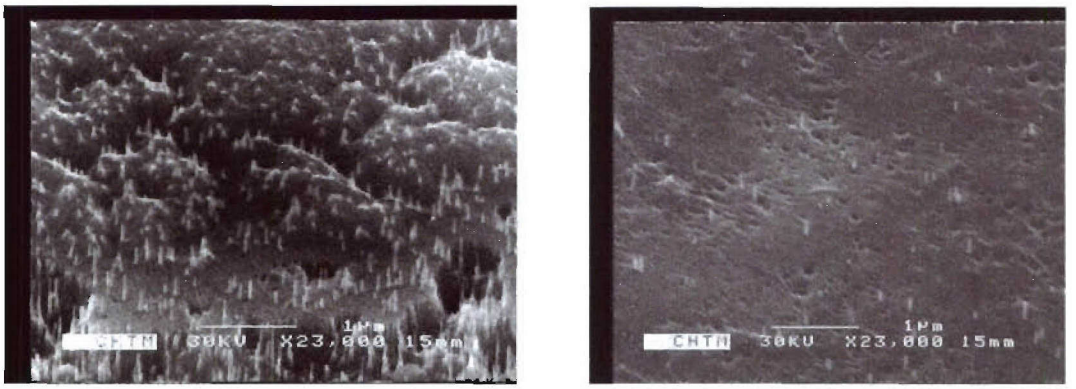


Figure 5: TD density revealed by PEC etching. (Left) planar GaN sample (Right) NHE GaN sample.

In NHE GaN the TD density has been reduced to < 10^8 cm^{-2} and in the case of NHE Ge/Si the TD density[2] has been reduced to < 10^5 cm^{-2}. The optical properties of GaN are demonstrably improved in the NHE samples. For example, Fig. 6 compares the 77°K photoluminescence (PL) spectra of the planar (lower) and NHE (upper) samples that were shown in figure 5. At 77°K the PL intensity is 15x higher in the NHE sample and at 300°K the PL intensity for the NHE sample is 50x higher. The improved radiative recombination efficiency of the NHE material was also reported earlier where the minority carrier lifetime was found to be 12x greater in the NHE sample[3].

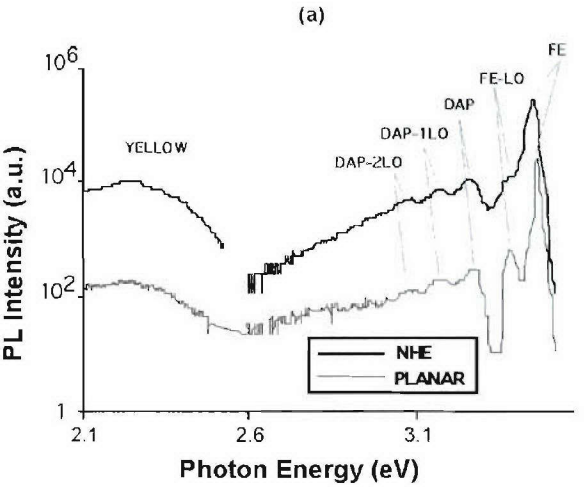


Figure 6: Increased 77K PL intensity in NHE GaN sample compared to planar grown GaN sample

New MOCVD Reactor

Results on this program were leveraged to win an AFOSR sponsored DURIP award for the purchase of a new MOCVD reactor. This state-of-the-art reactor has been installed and is fully functional. It features a high-speed-rotating-disk vertical geometry that is specifically designed for GaN MOCVD growth (Veeco TurboDisk, model P75). The reactor gas-panel

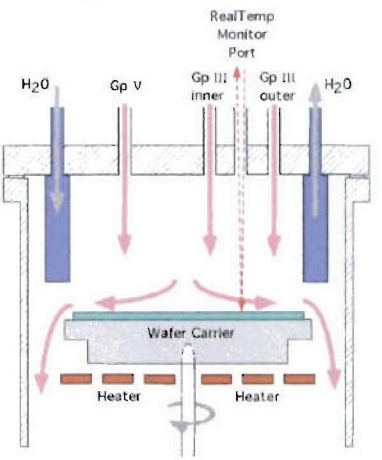


Figure 7: Schematic showing gas flow inside MOCVD growth chamber. Gas mixing occurs at the wafer surface.

---

[2] "Heteroepitaxy of high-quality Ge on Si by nanoscale seed pa Qiming Li, Ying-Bing Jiang, Joshua L. Krauss, Huifang Xu, Stev Sang M. Han, *Proceedings of "Quantum Dots, Nanoparticles and N. #5734-14, Jan 2005, San Jose, CA.*

[3] "Defect Reduction Mechanisms in the Nanoheteroepitaxy of GaN Burckel, A. Frauenglass, M. Fairchild, S.R.J.Brueck, G.A. Garrett, *Phys.*, **95** (2004) 1450 –1454

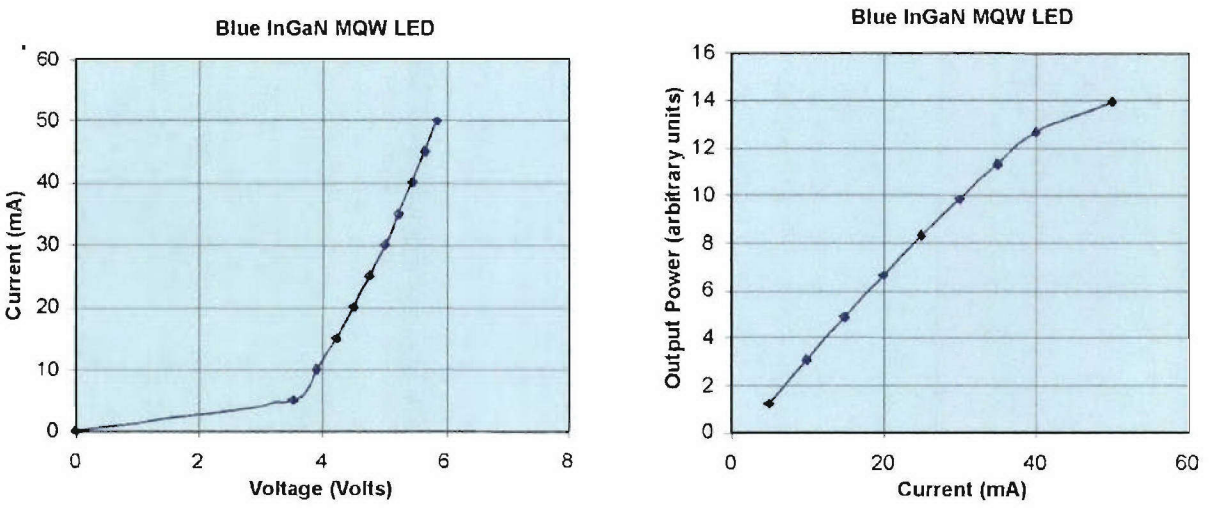


Figure 10: I/V and L/I characteristics of a base-line QTA LED

is all digital allowing unparalleled accuracy in gas switching and metering, the reactor also allows extensive retroactive data-mining. A schematic of the growth chamber geometry is shown in Fig. 7. The reactor is equipped with an *in-situ* RealTemp 2 monitor system. This monitor combines laser reflectance and pyrometry and allows the growth rate and temperature to be accurately monitored. Temperature control is critical for the growth of GaN and related materials, especially during the growth of InGaN/GaN QW regions.

LED process

In parallel with the above work we have developed a quick-turn-around (QTA) LED process that we are now beginning to use to test the materials improvements of the NHE approach. Major steps in the process are shown schematically in Fig. 8 and base-line LED results are summarized in Fig. 9 and 10. This LED structure (or simpler variants of it) will be used extensively during the next phase of this AFOSR program to test the effects of NHE defect reduction and other materials improvements in real devices.

Research output during this program phase

Publications and Presentations

1. Invited: "Nanoheteroepitaxy for the Integration of Highly Mismatched Semiconductor Materials", S.D. Hersee D.Zubia, X. Sun, R. Bommena, M. Fairchild, S. Zhang, D. Burckel, A. Frauenglass, S.R.J.Brueck, *IEEE J. Quantum Electronics*, **38**, 1017 (2002).
2. "Strain Partitioning in Compliant Heterostructures", D. Zubia, S.D. Hersee, T. Khraishi, *Appl. Phys. Lett.*, **80,** 740-420 (2002)
3. "Selective growth of Ge on Si(100) through vias of SiO2 nanotemplate using solid source molecular beam epitaxy", Q. Li and S. M. Han, S. R. J. Brueck, S.D. Hersee, Y.B. Jiang and H. Xu, *Appl. Phys. Lett.*, **83**, 5032 (2003)

4. "Defect Reduction Mechanisms in the Nanoheteroepitaxy of GaN on SiC", X.Y. Sun*, R. Bommena*, D. Burckel, A. Frauenglass, M. Fairchild*, S.R.J.Brueck, G.A. Garrett, M. Wraback and S.D. Hersee, *J. Appl. Phys.*, **95** (2004) 1450 -1454
5. "Spatial phase separation of GaN selectively grown on a nanoscale faceted Si surface", S. C. Lee, X. Sun, S. D. Hersee, H. Xu, and S. R. J. Brueck, *Appl. Phys. Lett.*, **84** (2004) 2079
6. "MBE of High-Quality Ge on Si by "Touchdown" of Nanoscale Ge Seeds," Qiming Li, Darin Leonhardt, Ying-Bing Jiang, Huifang Xu, Steven R. J. Brueck, Stephen Hersee, and Sang M. Han, *2004 AVS International Symposium*, Anaheim, CA (November 16, 2004
7. "MBE of High-Quality Ge on Si by "Touchdown" of Nanoscale Ge Seeds," Qiming Li, Darin Leonhardt, Ying-Bing Jiang, Huifang Xu, Stephen Hersee, and Sang M. Han, *AIChE 2004 Annual Meeting*, Austin, TX (November 11, 2004)
8. "Molecular Beam Epitaxy of High-Quality Ge on Si by Self-directed "Touchdown" of Nanoscale Seed Pads," Qiming Li, Darin Leonhardt, Ying-Bing Jiang, Huifang Xu, Steven R. J. Brueck, Stephen Hersee, and Sang M. Han, *40th. Annual New Mexico American Vacuum Society Symposium*, Albuquerque, NM (May 17, 2004).
9. "MBE of high-quality Ge on Si through vias of SiO2 nanotemplate and by self-directed "touchdown" of nanoscale seed pads," Qiming Li, Darin Leonhardt, Ying-Bing Jiang, Huifang Xu, Steven R. J. Brueck, Stephen Hersee, and Sang M. Han (speaker), *Materials Research Society 2004 Spring Meeting*, San Francisco (April 15, 2004)
10. "Heteroepitaxy of High Quality Ge on Si by nanoscale Ge seeds grown through a thin layer of SiO_2," Q. Li, Y. B. Jiang, H. Xu, S.D. Hersee and S. M. Han, *Appl. Phys. Lett.* **85**, 1928-1930 (2004) and *Virtual Journal of Nanoscale Science & Technology*, October 4 (2004).
11. "Heteroepitaxy of high-quality Ge on Si by nanoscale seed pads grown through a SiO_2 interlayer," Qiming Li, Ying-Bing Jiang, Joshua L. Krauss, Huifang Xu, Steven R. J. Brueck, Stephen Hersee, and Sang M. Han, *Proceedings of "Quantum Dots, Nanoparticles and Nanoclusters" SPIE Volume 5734, paper #5734-14, Jan 2005, San Jose, CA.*
12. "Nanoheteroepitaxial Growth of GaN on Si (111) Nanopillars", S. D. Hersee, X. Y. Sun, X. Wang, M. Fairchild, J. Liang, J. Xu, *J. Appl. Phys.*, **97**, 124308 (2005).
13. Invited: "Nanoheteroepitaxy: The Use of Compliant Nanostructures to Accommodate Large Lattice Mismatch in Semiconductor Heterostructures," Stephen Hersee, Sang M. Han, Xin Yu Sun, Xin Wang, and Qiming Li, *The 11th European Workshop on Metalorganic Vapor Phase Epitaxy*, Lausanne, Switzerland (June 5th-8th, 2005)
14. "Understanding of Surface Phenomena Responsible for the Selective Growth of Ge on Si over SiO2 During Molecular Beam Epitaxy," Qiming Li, Joshua L. Krauss, Stephen Hersee, and Sang M. Han, *Spring MRS Meeting*, San Francisco, CA (March 30, 2005)

Patents Awarded

1. G.M. Peake, S.D. Hersee, "Method of Making Non-Planar Micro-Optical Structures", (2002) Patent No. 6,363,237

2. S.D.Hersee, D.Zubia, S.R.J. Brueck, S. H. Zaidi, "Thin Film Product and Method of Forming". (2003) Patent No. 6,596,377
3. "Nanostructured Devices for Separation and Analysis", G.P. Lopez, S.R.J. Brueck, S.D. Hersee, (2004) Patent No. 6,685,841 B2
4. "Method for Making an Icosahedral Boride Structure", S.D. Hersee, R. Wang, D. Zubia, T. Aselage, D. Emin, (2005) Patent No. 6,841,456 B2

Graduate Student Degrees

MS degree:
Xinyu (Sunny) Sun (2004)
Xin (Allen) Wang (2004)

Ph.D degree:
David Zubia (2003)
Xinyu Sun (2004)

2.2 InNAs – a New Optoelectronic Material

PI: Marek Osinski

Main accomplishments:

- Invention of "*Semiconductor nitride structures*" for nitride-based unipolar optoelectronics devices, including quantum cascade laser and LEDs (United States Patent number 6,593,589, issued on 15 July 2003) (Marek Osinski and Petr G. Eliseev)

- Studies of UV-emitting diodes with quaternary InAlGaN barriers (Marek Osinski, Jinhyun Lee, Petr G. Eliseev, Shiping Guo, Milan Pophristić, Dong-Seung Lee, Boris Peres, Ian T. Ferguson)

  In collaboration with EMCORE Corporation, nitride-based UV heterostructures with InGaN quantum wells and AlInGaN barrier layers have been grown by MOCVD on sapphire substrates. The emission band was at 3.307 eV (375 nm) at room temperature (RT) and its FWHM was ~82 meV. In addition to the UV band, some blue emission admixture was found in a single-quantum-well (SQW) structure, which we attribute to recombination of injected electrons that are not captured into the SQW and enter the *p*-side of the structure. We have demonstrated a significant advantage in utilizing multiple-quantum-well (MQW) structures that provide more effective capture of injected carriers into wells and predominance of UV emission. We have observed temperature-sensitive competition between two emission mechanisms in MQW structures. Below ~170 K, the blue impurity-related emission dominated. In the 170-190 K range, an anomalous temperature-induced "blue jump" by over ~340 meV to UV region occurred, with UV emission dominating above 190 K.

- High-temperature characterization of UV-emitting diodes (Marek Osinski, Jinhyun Lee, Petr G. Eliseev)

  We have characterized optically and electrically InGaN/AlInGaN-based UV LEDs over a wide temperature range up to 600 K At elevated temperatures, we have observed evidence of increasing carrier escape from the quantum wells. The temperature dependence of the optical power at a given injection current can be described by $P \propto \exp(-T/T_0^*)$, where the temperature constant T_0^* is characteristic of the device quality. We found that T_0^* is 110 and 120 K at 30 and 60 mA, respectively. The decrease of the radiation quantum yield is mainly associated with thermally-activated escape of excess carriers from the quantum wells. Ultimately, these carriers are lost due to nonradiative recombination, which probably occurs in the *p*-barrier. The emission from that side has been observed at low temperatures as a blue band, associated with recombination of electrons through the Mg-related centers. The blue tail decreases with increasing temperature, indicating enhanced nonradiative recombination in that region.

- MOCVD growth of InN_xAs_{1-x} on GaAs using dimethylhydrazine, with record-high nitrogen content (Marek Osinski, Abdel-Rahman A. El-Emawy, Hongjun Cao, Noppadon Nuntawong, Edward Zhmayev, Jinhyun Lee)

  InNAs/GaAs multiple-quantum-well samples were grown by MOCVD on (100) n^+-GaAs substrates at 500 °C and 60 Torr using uncracked dimethylhydrazine (DMHy). Quantum well layers were grown using trimethylindium, tertiarybutylarsine, and 95-97.5% of DMHy in the vapor phase, while GaAs buffer, barrier, and cap layers were grown using trimethylgallium and arsine. The crystalline quality and solid phase composition were evaluated using high-

resolution x-ray diffraction analysis. Nitrogen content in InNAs wells was determined to be 18%. Surface morphology was investigated by atomic force microscopy (AFM) and field emission microscopy (FEM). Photoluminescence measurements confirm that the bandgap energy of InNAs is significantly lower than that of InAs. The peak emission wavelength of ~6.5 μm at 10 K is the longest reported so far for dilute nitride semiconductors.

- Analysis of GaAs/AlGaAs oxide-confined vertical-cavity surface-emitting lasers using electrical-thermal-optical simulation (Marek Osinski, Vladimir A. Smagley, Min Lu, Gennady A. Smolyakov, Petr. G. Eliseev)

Our three-dimensional electrical-thermal-optical numerical solver has been applied to model GaAs/AlGaAs-based top-emitting oxide-confined vertical-cavity surface-emitting lasers (VCSELs) with GaAs multiple-quantum-well active region. CW mode of operation has been simulated over a range of voltages, covering sub-threshold spontaneous emission and lasing emission. Effect of self-distribution of electrical current has been demonstrated for the first time in self-consistent electrical-thermal-optical simulation of VCSELs.

- Analysis of lateral mode confinement in VCSELs with ring metal apertures using the effective frequency method (Gennady A. Smolyakov, Marek Osinski)

The role of metal apertures in the mechanism of lateral mode confinement in VCSELs has been clarified by means of a detailed effective-frequency-method analysis of an oxide-confined VCSEL structure with the oxide window larger than the p-contact metal aperture. We have shown that a ring metal contact on top of the VCSEL structure can change the conditions for the lateral waveguiding by significantly modifying the local resonant properties of the VCSEL cavity. Resonant effects have been demonstrated in the longitudinal coupled-cavity system consisting of the designed laser cavity, determined by the two DBRs and the spacer, and a very short cavity formed by the top DBR and semiconductor-metal interface. The conditions for suppression of higher-order lateral modes using metal apertures have been established.

- Studies of operator ordering of a position-dependent effective-mass Hamiltonian in lattice-matched semiconductor superlattices and quantum wells. (Marek Osi_ski, Vladimir A. Smagley, Mohammad Mojahedi)

The position-dependent effective mass Hamiltonian $H = (\eta/2)[m(z)]^{\alpha}\nabla[m(z)]^{\beta}\nabla[m(z)]^{\alpha}+V(z)$ with $2\alpha + \beta = -1$ is applied to the problem of periodic heterostructure with abrupt interfaces and discontinuous mass distribution. In order to determine the most suitable operator ordering, numerical results for interband and intersubband transition energies are compared with experimental data for various GaAs/$Al_xGa_{1-x}As$ superlattices and quantum wells. The ordering-related energy shift as a function of structural parameters (well thickness, barrier thickness and height) is investigated. We find that variation of kinetic energy operator ordering can cause transition energy shift exceeding 40 meV. The model with $\alpha = 0$ and $\beta = -1$ consistently produces the best fit to experimental results.

Bullet list of main accomplishments

- Invention of "*Semiconductor nitride structures*" for nitride-based unipolar optoelectronics devices, including quantum cascade laser and LEDs (United States Patent number 6,593,589, issued on 15 July 2003) (Marek Osinski, Petr G. Eliseev)

- Studies of UV-emitting diodes with quaternary InAlGaN barriers (Marek Osinski, Jinhyun Lee, Petr G. Eliseev, Shiping Guo, Milan Pophristić, Dong-Seung Lee, Boris Peres, Ian T. Ferguson)

- High-temperature characterization of UV-emitting diodes (Marek Osinski, Jinhyun Lee, Petr G. Eliseev)

- MOCVD growth of InN_xAs_{1-x} on GaAs using dimethylhydrazine, with record-high nitrogen content (Marek Osinski, Abdel-Rahman A. El-Emawy, Hongjun Cao, Noppadon Nuntawong, Edward Zhmayev, Jinhyun Lee)

- Analysis of GaAs/AlGaAs oxide-confined vertical-cavity surface-emitting lasers using electrical-thermal-optical simulation (Marek Osinski, Vladimir A. Smagley, Min Lu, Gennady A. Smolyakov, Petr. G. Eliseev)

- Analysis of lateral mode confinement in VCSELs with ring metal apertures using the effective frequency method (Gennady A. Smolyakov, Marek Osinski)

- Studies of operator ordering of a position-dependent effective-mass Hamiltonian in lattice-matched semiconductor superlattices and quantum wells (Marek Osi_ski, Vladimir A. Smagley, Mohammad Mojahedi)

- Calculation of energy levels in cylindrical quantum dots using perturbation theory (Gennady A. Smolyakov, Marek Osinski)

Publications acknowledging AFOSR ORC support published between Oct. 1, 2002 and July 15, 2005:

1. S.-P. Guo, M. Pophristić, D. S. Lee, B. Peres, I. T. Ferguson, J.-H. Lee, and M. Osiński, "*Quaternary InAlGaN based multi-quantum wells for ultraviolet light emitting diode application*", Solid State Lighting II (I. T. Ferguson, N. Narendran, S. P. DenBaars, and Y.-S. Park, Eds.), The International Symp. on Optical Science and Technol., SPIE's 47th Annual Meeting, Salt Lake City, UT, 9-11 July 2002, Proc. of SPIE, Vol. 4776, pp. 18-25.

2. M. Osiński, "*InNAs – a new optoelectronic material for mid-IR applications (Invited Lecture)*", Programme and Abstracts, International Conf. on Solid State Crystals - Materials Science and Applications, Zakopane, Poland, 14-18 Oct. 2002, p. 35.

3. M. Osiński, N. Nuntawong, H.-J. Cao, E. Zhmayev, and A. A. El-Emawy, "*MOCVD growth and characterization of InNAs on GaAs - a new narrow-gap semiconductor (Invited Paper)*", Meeting Abstracts, 202nd Meeting of The Electrochemical Soc., Salt Lake City, UT, 20-24 Oct. 2002, Abstract No. 589.

4. M. Osiński, N. Nuntawong, H.-J. Cao, E. Zhmayev, and A. A. El-Emawy, "*MOCVD growth and characterization of InNAs on GaAs - a new narrow-gap semiconductor (Invited Paper)*", Proc. of the Narrow Bandgap Optoelectronic Materials and Devices Symp. (P. C. Chang, D. N. Buckley, W. K. Chan, and A. G. Baca, Eds.), Salt Lake City, UT, 21 Oct. 2002, ECS Proc. Vol. 2002-14, pp. 60-71.

5. A. A. El-Emawy, H.-J. Cao, N. Nuntawong, C.-Y. Liu, and M. Osiński, "*Effects of MOCVD growth conditions on optical and structural properties of GaInNAs/ GaAs/InGaAs/GaAs quantum wells*", Progress in Semiconductors II - Electronic and Optoelectronic Applications (B. D. Weaver, M. O. Manasreh, C. Jagadish, and S. Zollner, Eds.), Fall Meeting of Materials Research Soc., Boston, MA, 2-6 Dec. 2002, MRS Proc., Vol. 744, pp. 469-474.

6. A. A. El-Emawy, N. Nuntawong, H.-J. Cao, E. Zhmayev, H.-F. Xu, and M. Osiński, "*MOCVD growth and characterization of InNAs/GaAs quantum wells*", Progress in Semiconductors II - Electronic and Optoelectronic Applications (B. D. Weaver, M. O. Manasreh, C. Jagadish, and S. Zollner, Eds.), Fall Meeting of Materials Research Soc., Boston, MA, 2-6 Dec. 2002, MRS Proc., Vol. 744, pp. 507-512.

7. M. Osiński, "*InNAs/GaAs quantum wells for mid-infrared applications (Invited Paper)*", 2002 Conf. on Optoelectronic and Microelectronic Materials and Devices COMMAD 2002, Sydney, Australia, 11-13 Dec. 2002, p. 99.

8. H. Konishi, Y.-B. Jiang, Z.-M. Nie, Y.-F. Wang, J.-H. Lee, M. Osiński, and H.-F. Xu, "*Structure, composition, and optoelectronic property of titanium-oxide based nanotubes*", Programs and Abstracts, NANOSET Workshop, Nano-Structures in Environment & Technol., Albuquerque, NM, 17 Jan. 2003.

9. V. A. Smagley, M. Lu, G. A. Smolyakov, P. G. Eliseev, M. Osiński, B. P. Riely, P. H. Shen, and G. J. Simonis, "*Electrical-thermal-optical simulation of GaAs/ AlGaAs oxide-confined VCSELs*", Physics and Simulation of Optoelectronic Devices XI (M. Osiński, H. Amano, and P. Blood, Eds.), SPIE International Symp. on Integrated Optoelectronic Devices OPTO 2003, San Jose, CA, 27-31 Jan. 2003, Proc. of SPIE, Vol. 4986, pp. 332-342.

10. J.-H. Lee, P. G. Eliseev, M. Osi_ski, D.-S. Lee, D. I. Florescu, S.-P. Guo, and M. Pophristić, "*Properties of InGaN/AlInGaN/AlGaN quantum-well UV-light-emitting diodes*", Physics and Simulation of Optoelectronic Devices XI (M. Osiński, H. Amano, and P. Blood, Eds.), SPIE International Symp. on Integrated Optoelectronic Devices OPTO 2003, San Jose, CA, 27-31 Jan. 2003, Proc. of SPIE, Vol. 4986, pp. 595-607.

11. J.-H. Lee, P. G. Eliseev, M. Osiński, D. S. Lee, D. I. Florescu, S.-P. Guo, and M. Pophristić, "*High-temperature properties of InGaN/AlInGaN-based quantum-well UV LEDs in 300-600 K range*", Techn. Digest CD-ROM, Twenty Third Annual Conf. on Lasers and Electro-Optics CLEO 2003, Baltimore, MD, 2-6 June 2003, Paper CMX4.

12. N. Nuntawong, H.-J. Cao, A. A. El-Emawy, and M. Osiński, "*Effects of MOCVD growth conditions on properties of GaInNAs/GaAs quantum wells*", Techn. Program with Abstracts, 45th 2003 TMS Electronic Materials Conf., Salt Lake City, UT, 25-27 June 2003, Paper HH5, p. 88.

13. A. A. El-Emawy, N. Nuntawong, H.-J. Cao, and M. Osiński, "*Optical and structural properties of GaInNAs/GaAs quantum wells grown by MOCVD*", Abstract Book, 11th Biennial (US) Workshop on Organometallic Vapor Phase Epitaxy, Keystone, CO, 20-24 July 2003, Paper OM6, p. 120.

14. H. Xu, Y.-B. Jiang, Z. Nie, J. Lee, H. Konishi, Y. Wang, and M. Osiński, "*Titanium oxide based nanotubes, nanofibers, nanoflowers, and nanodiscs*", Proc. of Microscopy and Microanalysis 2003 Meeting, San Antonio, Texas, 3-7 Aug., 2003, Paper 184/Poster 62, Microscopy and Microanalysis, **9** (#S2), pp. 354CD-355CD, 2003.

15. J.-H. Lee, P. G. Eliseev, M. Osiński, D.-S. Lee, D. I. Florescu, S.-P. Guo, and M. Pophristić, "*InGaN-based ultra-violet emitting heterostructures with quaternary AlInGaN barriers*", IEEE J. of Selected Topics in Quantum Electron., Semiconductor Lasers Issue, **9** (#5), pp. 1239-1245, Sept./Oct. 2003.

16. G. A. Smolyakov and M. Osiński, "*Perturbation theory approach to calculation of energy levels in cylindrical quantum dots*", Techn. Digest, Nineteenth Lasers Science Conf. LS-XIX, Annual Meeting of the Division of Laser Science of the American Physical Soc., Tucson, AZ, 5-9 Oct. 2003, Paper WMM8.

17. M. Osiński, "*Wide-bandgap group-III-nitride-based diode lasers – overview of present status (Invited Paper)*", Abstracts, XVII School of OptoElectron.: Photovoltaics, Solar Cells and Photodetectors, Kazimierz Dolny, Poland, 13 -16 Oct. 2003, p. 28.

18. M. Osiński, "*InNAs – a new optoelectronic material for mid-infrared applications*", Opto-Electron. Review **11** (#4), pp. 321-326 (2003).

19. G. A. Smolyakov, V. A. Smagley, W.-L. Chen, and M. Osiński, "*Resonant coupled-cavity effects in VCSELs with annular ring contacts*", Physics and Simulation of Optoelectronic Devices XII (M. Osiński, H. Amano, and F. Henneberger, Eds.), SPIE International Symp. on Integrated Optoelectronic Devices OPTO 2004, San Jose, CA, 26-29 Jan. 2004, Proc. of SPIE, Vol. 5349, pp. 385-396.

20. J.-H. Lee, P. G. Eliseev, M. Osiński, D. S. Lee, J. C. Ramer, D. I. Florescu, and E. A. Armour, "*Optical and electrical properties of interdigitated InGaN/GaN green light emitting diodes*", Physics and Simulation of Optoelectronic Devices XII (M. Osiński, H. Amano, and F. Henneberger, Eds.), SPIE International Symp. on Integrated Optoelectronic Devices OPTO 2004, San Jose, CA, 26-29 Jan. 2004, Proc. of SPIE, Vol. 5349, pp. 408-415.

21. W. Nakwaski, M. Wasiak, P. Maćkowiak, W. Bedyk, M. Osiński, A. Passaseo, V. Tasco, M. T. Todaro, M. De Vittorio, R. Joray, J. X. Chen, R. P. Stanley, and A. Fiore, "*Oxidation kinetics of AlAs and (AlGa)As layers in GaAs-based diode laser structures: Comparative analysis of available experimental data*", Semiconductor Science and Technol. **19**, no. 3, pp. 333-341, March 2004.

22. M. Osiński, V. A. Smagley, and M. Mojahedi, "*Operator ordering of effective-mass Hamiltonian in semiconductor superlattices and quantum wells*", Program & Abstracts, International Conf. on Superlattices, Nano-Structures, and Nano-Devices ICSNN 2004, Cancun, Mexico, 19-23 July 2004, Paper 2.7.19, p. 57.

23. P. G. Eliseev, J. Lee, and M. Osiński, "*Electro-optical properties of UV-emitting InGaN heterostructures accounting for injection-induced conductivity*", Kvantovaya Elektronika **34** (#12), pp. 1127-1132, Dec. 2004.

24. G. A. Smolyakov, P. G. Eliseev, and M. Osiński, "*Effects of resonant mode coupling on optical characteristics of InGaN-GaN-AlGaN lasers*", IEEE J. of Quantum Electron. **40**, no. 4, pp. 517-524, April 2005.

25 P. G. Eliseev, J.-H. Lee, and M. Osiński, "*InGaN-based quantum-well LEDs: Explanation of anomalous electro-optical characteristics*", Twenty Fifth Annual Conf. on Lasers and Electro-Optics CLEO 2005, Baltimore, MD, 23-27 May 2005, Paper CMI3.

26. G. A. Smolyakov and M. Osiński, "*Analysis of lateral mode confinement in VCSELs with ring metal apertures*", accepted for publication in J. of Lightwave Technol..

Publications follow.

HTML ABSTRACT + LINKS

Large second-harmonic signal in thermally poled lead glass-silica waveguides

Y. Luo, A. Biswas, A. Frauenglass, and S. R. J. Brueck[a)]
Center for High Technology Materials and Electrical and Computer Engineering Department, University of New Mexico, Albuquerque, New Mexico 87106

(Received 13 January 2004; accepted 21 April 2004; published online 28 May 2004)

Thermal poling of silica-lead glass-silica waveguides formed by laser ablation of lead glass and e-beam evaporation of the silica cladding is reported. A large nonlinearity localized within the Pb-glass layer was found by scanning the probe laser beam across an angle-polished sample, and a peak second-order nonlinear susceptibility $\chi^{(2)}$ as high as 15 pm/V was achieved in the Pb-glass layer. A simple theoretical model based on charge transport in the different materials during poling is proposed to explain complex $\chi^{(2)}$ profile. The large third-order nonlinearity of lead glass plays a key role in the generation of the large second-harmonic signal. © *2004 American Institute of Physics.* [DOI: 10.1063/1.1760213]

Second-order nonlinear materials play an important role in many nonlinear optical processes including integrated switching and routing devices. Thermally poled glasses,[1] silicate optical fibers, and planar waveguides are all of great interest. A large number of investigations have been reported on the physical mechanism and potential applications of the second-order nonlinearities of glasses. In particular, silica glass thin film waveguides have attracted much attention.[2–7]

Thermally poled bulk lead glasses have shown much larger nonlinearities[8,9] than fused silica, most likely associated with the large third-order susceptibilities in these glasses. The third-order susceptibility $\chi^{(3)}$ of lead glass[10,11] is $2-9\times10^{-21}$ m^2/V^2, while the $\chi^{(3)}$ of fused silica[12] is an order of magnitude lower at $\sim2\times10^{-22}$ m^2/V^2. The nonlinearity in fused silica has been attributed to charge separation and the creation of a large permanent electric field that interacts with the third-order susceptibility to create a large second-order effect, as $\chi^{(2)}_{\text{eff}}\sim3E\chi^{(3)}$. In contrast the mechanisms in lead glasses are much less well understood. The impetus behind this series of experiments was to combine the understanding of charge separation in silica with the large third-order susceptibilities in Pb glass to achieve higher nonlinearities and, at the same time, to form a planar waveguide structure suitable for integrated optical applications.

In this letter, we report a large second-harmonic generation (SHG) obtained in PbO-silica thin-film waveguide structures. The depth profile of the induced nonlinearity is probed by monitoring the SHG signal as a pump laser beam is scanned across angle polished samples. A simple theoretical model, based on charge transport in the different materials during poling, is proposed and the complex $\chi^{(2)}$ profile is explained.

Thin films (0.05 to ~0.2 μm) were formed by laser ablation of commercial lead glass targets onto 1-mm-thick fused quartz substrates [GE104 (equivalent to optosil)]. Laser ablation was carried out in a vacuum chamber (10^{-4} Torr) using the fourth-harmonic output of a Q-switched Nd:YAG laser (266 nm). The samples were heated to 250 °C during the deposition, and subsequently annealed at 600 °C for 24 h. Cladding layers of SiO_2 (~0.5 μm) were deposited by dielectric evaporation to complete the structure.

Thermal poling was performed in an enclosed, atmospheric-ambient oven by sandwiching samples between aluminum plate electrodes. Typical poling conditions were 3 kV at 275 °C for 15 min and cooling over about 30 min with the field applied. SHG was measured with a Q-switched Nd:YAG laser (1060 nm), a typical Maker fringe pattern was obtained from the poled lead glass thin film waveguide samples. The SHG increases with the incident angle and reaches maximum at around 60°. However, due to the thinness of the nonlinear region, this Maker fringe analysis is limited by refraction to relatively shallow angles in the higher index materials, and hence to low spatial resolution, so it was not possible to infer the nonlinear coefficient and the thickness of the nonlinear region from these measurements.

Following the thermal poling, a few samples were exposed to UV laser radiation at 244 nm with an output power density of 300 mW/cm^2 for 30 min to check the stability of the induced nonlinearity. SH signal strength measured before and after UV irradiation is given in Table I. It can be seen from the data that fused quartz, lead glass film, and SiO_2 cladding all generated signals after poling, however, as expected, the signals are not simply additive, but show a complex structural dependence. UV radiation is able to erase some part of the SH signal originating from the SiO_2 claddings.

In order to further investigate the origin of the nonlinearity, SHG depth profiles were measured by angle polishing the samples and scanning the probe laser beam across the various layers. Samples were angle-polished at 1° at one end, and the Nd:YAG pump laser beam was focused to a spot with ~5.0 μm diameter, and scanned along the wedge of the samples in a step of 5.0 μm, which resulted in a ~85 nm vertical resolution [85 nm=5 μm×tan(1°)]. As shown in Fig. 1(a), the SH signal increases in the substrate region,

a)Electronic mail: brueck@chtm.unm.edu

 © 2004 American Institute of Physics
Downloaded 28 May 2004 to 64.106.37.66. Redistribution subject to AIP license or copyright, see http://apl.aip.org/apl/copyright.jsp

TABLE I. Typical SH intensity for different samples before and after UV irradiation.

SHG (a.u.) before or after UV	Substrate	Substrate with only lead glass	Substrate with only cladding	Lead glass thin film waveguide
Before	0.5	1.8	1.5	2.0
After	0.5	1.8	0.5	1.8

reaches a maximum, and then decreases and drops almost to zero at the interface between the substrate and lead glass film. The signal increases very sharply throughout the lead glass film until it reaches the interface between the lead glass film and the cladding. It finally reaches a stable value, which is a little lower than that at the peak. An expanded view of the SH depth profile in the region with large nonlinearity is shown in Fig. 1(b). As a result of the finite experimental resolution, the lead glass region in the experimental data is a little bit wider than that in the simulation. For fused quartz substrates with only cladding layers [Fig. 1(c)], the SH signal monotonically increases with increasing thickness of the angle-polished samples, until it reaches a peak value at the cladding layer. Comparing the two graphs, it is clearly seen that the lead glass thin film plays a very critical role in creating the large second-order nonlinearity in the waveguides. These experiments suggest that the nonlinear region is located largely in the Pb glass layer. Since the thickness of this layer is ~0.2 μm, this suggests a much larger nonlinear coefficient than that in the silica, where the thickness of the nonlinear region (the depletion width) is ~5 μm. The sharp decrease in the signal at the substrate:Pb film interface also suggests that the nonlinearity of the Pb glass might have an opposite polarity to that of silica.

To explain the experiment results, a simple model based on the space-charge model of bulk silica[13] is proposed, according to which, during the process of thermal poling, a negative depletion region is formed near the anode area while a positive sheet charge accumulates at the cathode surface. From this model, the poled sample can be divided into five regions as in Fig. 2(a).

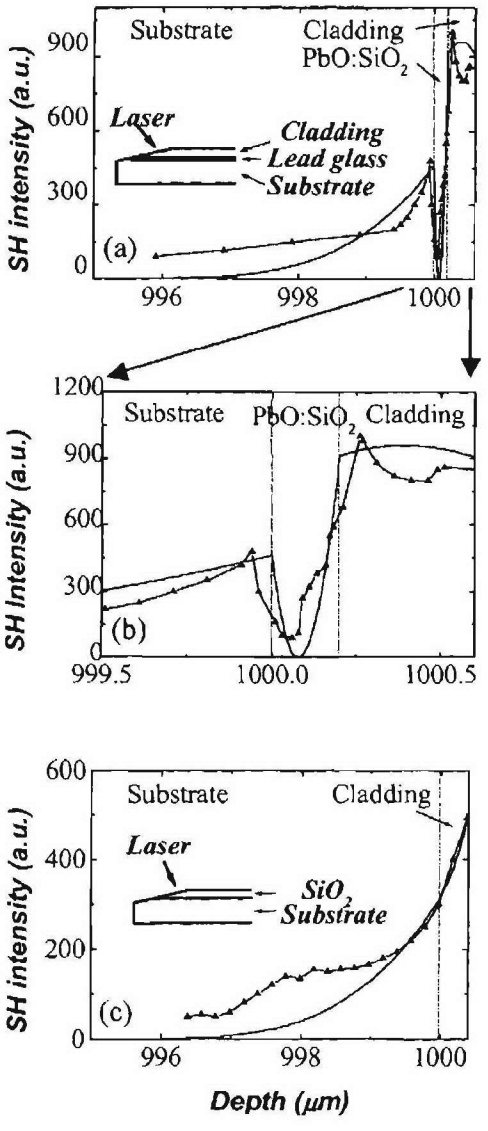


FIG. 1. SH intensity depth profiles for (a) a lead glass thin film waveguide; (b) expanded view of lead glass film region of (a); (c) a fused quartz substrate with only a cladding layer. (Lines with triangles are experimental data, and solid lines are modeling results.)

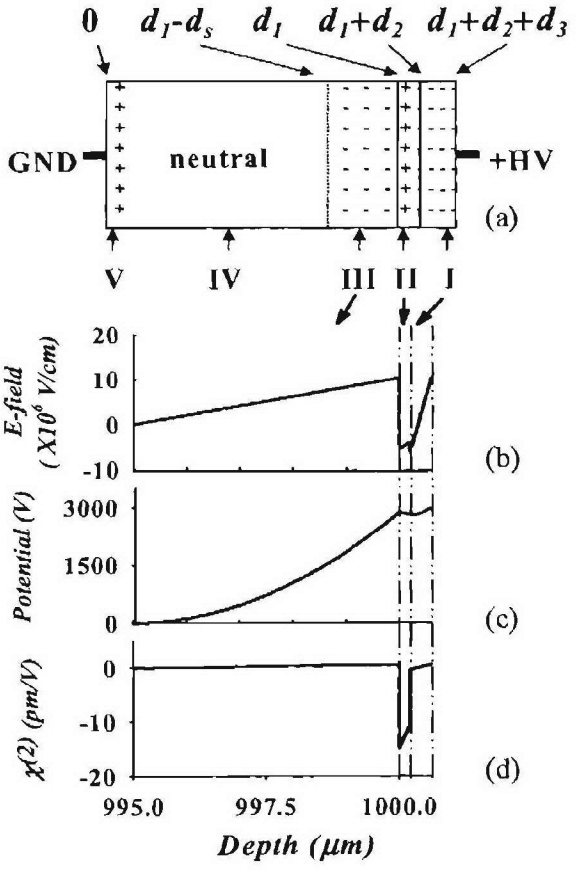


FIG. 2. Theoretical model of the thermally poled Pb-glass waveguide. (a) Charge distribution; (b) electrical field distribution; (c) potential; and (d) $\chi^{(2)}$ distribution.

Downloaded 28 May 2004 to 64.106.37.66. Redistribution subject to AIP license or copyright, see http://apl.aip.org/apl/copyright.jsp

TABLE II. Parameters used in the model.

d_1 (mm)	d_2 (μm)	d_3 (μm)	d_s (μm)	N_s (ppm)	N_f (ppm)	N_c (ppm)	ϵ_{SiO_2}	ϵ_{Pb}	$\chi^{(2)}_{SiO_2}$ (m^2/V^2)	$\chi^{(2)}_{Pb}$ (m^2/V^2)
1	0.2	0.4	5	2	12	30	3.9	6	2×10^{-23}	87×10^{-22}

Region I is the depleted cladding layer, with a net negative charge due to bound charges. Since the cladding layer is only 0.5 μm thick, we assume that the mobile cations are depleted throughout the cladding. Region II is the lead-glass layer, which is also a depletion region. The mobile positive ions from both the cladding layer and lead glass layer are assumed to accumulate at the interface between the lead-glass layer and the substrate. This is because lead glass is soft compared with cladding and substrate, so it is relatively easy for the positive charges to penetrate the lead glass at the elevated poling temperature; while the denser substrate remains relatively impermeable. This assumption leads to the dip in the signal and the sign reversal for the nonlinearity. Region III is the depletion region of the substrate. Region IV, consisting of most of the substrate, is the neutral central region, and region V, close to the cathode, is the sheet charge of the accumulated cations from the substrate. As depicted in Fig. 2(a), the thickness of substrate, lead-glass layer, and cladding layer are taken as d_1, d_2, d_3, respectively, and the depletion region of substrate is taken as d_s.

From Poisson's equation we calculated the electrical field and potential in each region given this postulated charge distribution. Figure 2(b) shows the internal electrical field associated with the different regions of the sample. We find that when the impurity concentrations in the cladding and lead-glass layers are sufficiently large, a negative E-field exists in region II as a result of both the dielectric discontinuity and the presence of the positive charge sheet at this interface. This further results in a negative $\chi^{(2)}_{\text{eff}}$ in region II, generated by a $\chi^{(2)}_{\text{eff}}\sim 3E\chi^{(3)}$ process, where E is the internal electrical field generated by the creation of the depletion regions, $\chi^{(3)}$ is the third-order nonlinearity of the material. Assume that $\chi^{(3)}$ is uniform throughout the material and unchanged by the poling process, then the resulting SHG signal is given by

$$\frac{dE_{2\omega}}{dx} = -\frac{i\omega}{2}\sqrt{\frac{\mu_0}{\epsilon}}\chi^{(2)}(x)E^2_{\omega}(x)e^{i\Delta k(x)x}. \tag{1}$$

Assuming that the depletion of the fundamental wave at ω is negligible and that all of the lengths are short compared to a coherence length, the SHG power is proportional to the square of the integral of $\chi^{(2)}$ along the optical path,

$$I_{2\omega}(x) = E_{2\omega}(x)\cdot E^*_{2\omega}(x) \propto \left|\int \chi^{(2)}(x)dx\right|^2. \tag{2}$$

Integrating $\chi^{(2)}$ across the appropriate subsections of the sample, we get the depth profile of the SHG intensity shown in Fig. 1(a). We find that we can fit the simulation result (solid line) to the experimental data (line with triangles) for a reasonable set of parameters as listed in Table II, where N_s, N_f, and N_c are the impurity charge number density of the substrate, Pb-glass film and cladding, ϵ is the dielectric constant. Figures 2(c) and 2(d) are the potential difference and $\chi^{(2)}$ distribution of the sample, respectively. A maximum $\chi^{(2)}$ as high as $\sim$15 pm/V [Fig. 2(d)], opposite in sign to silica, was achieved in Pb-glass film. Using an equivalent model with the same parameters, the SHG depth profile of the sample with only a silica cladding was also simulated, the result was consistent with our experimental data [Fig. 1(c)].

SHG is a useful probe of the nonlinearity. For switching applications, the waveguide electro-optic nonlinearity is the interesting quantity. We can evaluate this nonlinearity after calculating the mode distribution in the symmetric slab waveguide composed of the high-index Pb glass film ($n_f = 1.65$) and the silica substrate and cladding ($n_s = 1.45$). Although the mode is not very well confined due to the thin guiding layer, we estimate an electro-optic nonlinearity of $\sim$4 pm/V.

To achieve a higher electro-optic nonlinearity, we need better confinement, which can be achieved by increasing the thicknesses of both the guiding film and the cladding layer. We can also decrease the impurity concentration of the cladding layer, to achieve a positive E field in the lead-glass film region, and take better advantage of its large $\chi^{(3)}$.

In summary, a large thermal-poling-induced second-order nonlinearity has been observed in Pb-glass waveguides with a maximum $\chi^{(2)}\sim$15 pm/V, opposite in sign to silica. The nonlinear region was probed by scanning across angle polished samples. A simple model based on space charge is proposed, and the complex $\chi^{(2)}$ profile resulting from charge transport during poling in the different materials was explained. The average electro-optic nonlinearity γ_{eo} for a waveguide mode is about a factor of 4 larger than for silica based waveguides.

Support for this work was provided by the Air Force Office of Scientific Research.

[1] R. A. Myers, N. Mukherjee, and S. R. J. Brueck, Opt. Lett. **16**, 1732 (1991).
[2] A. Okada, K. Ishii, K. Mito, and K. Sasaki, Appl. Phys. Lett. **60**, 2853 (1992).
[3] R. A. Myers, S. R. J. Brueck, and R. P. Tumminelli, Proc. SPIE **2289**, 158 (1994).
[4] S. Horinouchi, H. Imai, G. J. Zhang, K. Mito, and K. Sasaki, Appl. Phys. Lett. **68**, 3552 (1996).
[5] O. Sugihara, M. Nakanishi, H. Fujimura, C. Egami, and N. Okamoto, J. Opt. Soc. Am. B **15**, 421 (1998).
[6] J. Arentoft, K. Pedersen, S. I. Bozhevolnyi, M. Kristensen, P. Yu, and C. B. Nielsen, Appl. Phys. Lett. **76**, 25 (2000).
[7] J. Arentoft, M. Kristensen, K. Pedersen, S. I. Bozhevolnyi, and P. Shi, Electron. Lett. **36**, 1635 (2000).
[8] M. Qiu, F. Pi, and G. Orriols, Appl. Phys. Lett. **73**, 3040 (1998).
[9] M. Qiu, T. Mizunami, H. Koya, F. Pi, and G. Orriols, in *Proceedings of Nonlinear Optics: Materials, Fundamentals, and Applications* (IEEE, Piscataway, NJ, 1998), p. 370.
[10] S. R. Friberg and P. W. Smith, IEEE J. Quantum Electron. **QE-23**, 2089 (1987).
[11] L. L. Chase and E. W. Van Stryland, *CRC Handbook of Laser Science and Technology* (CRC Press, Boca Raton, FL, 1995), Sec. 8.1.
[12] R. Adair, L. L. Chase, and S. A. Payne, J. Opt. Soc. Am. B **4**, 875 (1987).
[13] N. Mukherjee, R. A. Myers, and S. R. J. Bueck, J. Opt. Soc. Am. B **11**, 665 (1994).

Downloaded 28 May 2004 to 64.106.37.66. Redistribution subject to AIP license or copyright, see http://apl.aip.org/apl/copyright.jsp

Generalized Transverse Bragg Waveguides

D. B. Burckel[#] and S. R. J. Brueck[§,*]
Center for High Technology Materials and Department of Electrical and Computer Engineering,
University of New Mexico, Albuquerque, NM 87106

Abstract

A coupled-mode analysis of 2-D generalized transverse Bragg waveguides (GTBW) with tilted distributed Bragg reflectors is presented. As a result of the absence of inversion symmetry about a plane perpendicular to the guiding stripe, the modes supported by these guides are not separable into the familiar form of transverse standing wave and longitudinal traveling-wave components. This fundamental change in the modal description yields new and potentially useful guided-mode behavior. Expressions for the spatial distribution of the optical field, phase and group velocity, and the dispersion relation as well as applications of GTBW are presented.

Familiar waveguides, including metallic, dielectric slab/fiber, transverse Bragg waveguides[1,2] and photonic crystal (holey) fibers[3] are based on reflection with momentum transfer perpendicular to the guide direction at the transverse guide edges. In these cases, the guided mode can be functionally described as $f(\vec{r}_\perp)e^{ik_\parallel z}$ where f is a function only of the transverse spatial coordinates, $\vec{r}_\perp$, while $k_\parallel$ is the wavenumber along z. In 2D and 3D photonic crystal waveguides,[4,5] the functional form becomes $f(\vec{r})e^{ik_\parallel z}$ where f is now a periodic function of all coordinates in accordance with Bloch's theorem, but the propagating plane wave remains a function of only the longitudinal coordinate.

This universality of description has led to the general belief that such a separable functional description is always appropriate for describing guided modes.[6] The purpose of this report is to point out that, despite its dominance in our experience and thinking for almost a century, this is only a special case of guiding and that more general guided modes, which cannot be described by the simple, separated functional form given above, are possible and show interesting properties that may be of technological as well as fundamental interest. One characteristic common to all of the above examples is reflection symmetry about sets of planes perpendicular to the guide. If this symmetry is broken, the separable functional dependence no longer holds, but there can still be guiding and energy transport along the guide. An important consequence of breaking this symmetry is that the mode is no longer symmetric to reflection in such a plane, thus reflection from any planar surface perpendicular to the guide, such as an exit facet, will not be guided.

The simplest example of such a structure is the tilted 2D Bragg waveguide shown in Fig. 1 where the planes of the Bragg structure are at an angle α to the guide direction. The Bragg reflectors extend for a distance L, not shown, both above and below the core. The variation of the dielectric constant along a line perpendicular to the grating (along ζ as shown in Fig. 1) is taken as $\varepsilon - \delta\sin(\zeta/\Lambda)$. In the core region, the field is composed of two unperturbed plane waves propagating with wavevectors $\vec{k}_+$ and $\vec{k}_-$. In the top Bragg reflector, these two waves are coupled such that the $\vec{k}_+$ wave is reflected into the $\vec{k}_-$ wave. At the bottom boundary these roles are reversed. As long as the magnitude of the product of the reflectivities is unity and the total round trip phase accumulation is an integer multiple of 2π, a well-defined mode is obtained.

Present address: Sandia National Laboratories, Albuquerque, NM
§ Also Department of Physics and Astronomy
* Email: brueck@chtm.unm.edu

The momentum transfer on reflection from the tilted Bragg structure is not perpendicular to the guiding direction with the result that the standing wave associated with the reflection is also oriented at an angle to the guide and the simple, separable description is not valid. The requirements for a mode are that the power in the guide direction be invariant with x (assuming lossless materials) and that it be localized in the vicinity of the core (the region of width W between the Bragg reflectors in Fig. 1).

Assuming that the dielectric modulation is not too large, this situation is conveniently modeled with a simple coupled-mode theory.[7-9] For TE polarized waves, the electric fields are:

$$\begin{aligned}
\vec{E}(x,z) &= \begin{cases} A_t(z-W/2,\theta_+)e^{ik_n(x\sin\theta_+ +(z-W/2)\cos\theta_+)} \\ +\,B_t(z-W/2,\theta_+)e^{ik_n(x\sin\theta_- -(z-W/2)\cos\theta_-)} \end{cases} \quad z > W/2 \\
\vec{E}(x,z) &= e^{ik_n(x\sin\theta_+ +(z-W/2)\cos\theta_+)} + R_t(\theta_+)e^{ik_n(x\sin\theta_- -(z-W/2)\cos\theta_-)} \\
&\quad -W/2 < z < W/2 \\
\vec{E}(x,z) &= R_t(\theta_+)e^{ik_n(\cos\theta_+ +\cos\theta_-)W} \times \\
&\quad \begin{cases} B_t(z+W/2,\theta_-)e^{ik_n(x\sin\theta_+ +(z+W/2)\cos\theta_+)} \\ +\,A_t(z+W/2,\theta_+)e^{ik_n(x\sin\theta_- -(z-W/2)\cos\theta_-)} \end{cases} \quad z < -W/2
\end{aligned} \tag{1}$$

with $k_n = 2\pi n/\lambda$. Coupling between the plane waves in the cladding is described by the spatially varying amplitude coefficients $A_{t,b}(z, \theta_\pm)$ and $B_{t,b}(z, \theta_\pm)$. Reflection at the core boundaries is described by the angle-dependent reflection coefficient $R_{t,b}(\theta_\pm)$, expressed as the ratio of incident and reflected plane wave coefficients evaluated at the core boundary. Expressions for $A_t(z, \theta_\pm)$, $B_t(z, \theta_\pm)$, and $R_t(\theta_\pm)$ are:

$$\begin{aligned}
A_t(z-W/2) &= \frac{\begin{cases} -i\Delta\beta\sinh[H(z-W/2-L)] \\ +2H\cosh[H(z-W/2-L)] \end{cases}}{[i\Delta\beta\sinh(HL)+2H\cosh(HL)]} e^{i\frac{\Delta\beta}{2}(z-W/2)} \\
A_t(0) &= 1 \\
B_t(z-W/2) &= \frac{2\kappa^*}{\cos(\theta_-)} \frac{-\sinh[H(z-W/2-L)]}{[i\Delta\beta\sinh(HL)+2H\cosh(HL)]} e^{-i\frac{\Delta\beta}{2}(z-W/2)} \\
R_t &= B_t(0) = \frac{2\kappa^*}{\cos(\theta_-)} \frac{\sinh(HL)}{[i\Delta\beta\sinh(HL)+2H\cosh(HL)]}
\end{aligned} \tag{2}$$

with analogous expressions for A_b, B_b and R_b. Here

$$\begin{aligned}
\Delta\beta &\equiv -[k_n(\cos\theta_+ + \cos\theta_-) - K\cos\alpha] \quad , \quad \kappa \equiv k_n\delta \\
H &\equiv \sqrt{\frac{|\kappa|^2}{\cos\theta_+\cos\theta_-} - \left(\frac{\Delta\beta}{2}\right)^2}
\end{aligned} \tag{3}$$

$\Delta\beta$ is the wavevector detuning from the Bragg resonance, κ is the coupling strength, and H is the inverse coupling length. Note that with the particular geometry we have adopted, κ is a real positive quantity and the reflection phase is zero for $\Delta\beta = 0$.

The self-consistency condition can be found by equating the field expressions in Eq. (1) at $z = -W/2$, yielding:

$$1 - R_t(\theta_+)R_b(\theta_-)e^{ik_n(\cos\theta_+ + \cos\theta_-)W} = 0 \tag{4}$$

For a given set of waveguide physical parameters, n, W, α, and Λ, the roots of Equation (4) yield the allowed bounce angles, θ_+ and θ_- for self-consistent modes inside the waveguide core.

From Fig. 1 and the usual Bragg analysis,

$$\begin{aligned} &\theta_+ = \theta_B + \alpha + \delta\theta \equiv \alpha' + \theta_B, \quad \theta_- = \alpha - \theta_B + \delta\theta \equiv \alpha' - \theta_B \\ &\theta_B = \cos^{-1}(\lambda/2n\Lambda) = \cos^{-1}(\pi c/\omega n\Lambda) \end{aligned} \tag{5}$$

and the self-consistency expression reduces to:

$$1 - R_t(\theta_B + \alpha')R_b(\theta_B - \alpha')e^{i\frac{2\pi W}{\Lambda}\cos(\alpha')} = 0 \tag{6}$$

The phase shift due to the round trip propagation across the guiding region, $2\pi W\cos(\alpha')/\Lambda$ is independent of wavelength. Thus, for any wavelength above the cutoff frequency, the relative position of the resonance within the bandpass is fixed, e.g. $\alpha' = \alpha + \delta\theta$ is independent of λ. It is straightforward to evaluate the phase and group velocities.

$$\begin{aligned} v_{phase} &= \frac{\omega}{k} = \frac{c}{n\sin(\theta_B)\cos(\alpha')}; \\ v_{group} &= \frac{\partial\omega}{\partial k} = \frac{c}{n}\frac{\sin(\theta_B)}{\cos(\alpha')}. \end{aligned} \tag{7}$$

At cutoff, corresponding to counter propagating waves at the grating normal, $\lambda_{cutoff} \sim 2n\Lambda$ $v_p \rightarrow \infty$ and $v_g \rightarrow 0$; at the other extreme, as the wavelength is decreased, $\theta_B \rightarrow \pi/2 - \alpha'$ [and $\sin(\theta_B) \rightarrow \cos(\alpha')$] the group velocity reaches c/n, the velocity of light in the unbounded core medium. At wavelengths below this limit, one of the constituent plane waves is no longer confined to the guiding region and the mode is no longer bound. Thus, there is a short-λ cutoff for $\alpha' \neq 0$ as well as the long-λ cutoff associated with the Bragg condition.

Additional insight into the self-consistency relationship is provided by some simple numerical evaluations. We take $\lambda = 1300$ nm, $\varepsilon = (1.7)^2 = 2.89$ (appropriate to a high-index polymer), $\Lambda = 450$ nm, $\delta = 0.005$, $W = 2000$ nm and $L = 250$ μm and the grating tilt, $\alpha = 45°$ - all readily accessible parameters. The top panel of Figure 2(a) shows the magnitude of the reflectivity from the top Bragg reflector for these parameters with a stop band centered at $\theta_+ \sim 77°$. The maximum field reflectivity is about ~0.5 and varies across the stop band. The reflectivity at the second interface has just the inverse magnitude (e.g. ~2.0) and the product, Fig. 2(b), the round trip reflectivity, is of magnitude unity for incident angles spanning an angular bandwidth of $\pm\Delta$ about the geometrical Bragg angle. Figure 2(c) shows the corresponding 2π phase variation across the stop band. Finally, Fig. 2(d) shows the magnitude of the self-consistency expression of Eq. 6 across this angular range. There is a clearly defined root, and thus a mode with bounce angles $\theta_+ = \theta_B + \alpha + \delta\theta = 76.16°$ and $\theta_- = 13.34°$.

Referring to the k-space diagram in Fig. 3f, the phase in the propagation direction progresses in the forward direction as the θ_+ wave propagates from the bottom to the top interface, and then

regresses in the opposite direction as the θ_- wave propagates from top to bottom. The resulting intensity pattern, Fig. 3, shows standing waves at an angle of 45°, corresponding to the tilt of the grating. The extent of the core region, without the Bragg gratings, is indicated by the horizontal dotted lines. For this modest coupling constant the mode extends well into the cladding regions; tighter confinement is available with higher δ. The two inner line plots are the variation of the intensity, $|E|^2$, along x [Fig. 3b)] and along z [Fig. 3c)]. The outer line plots [Fig 3d) and 3e)] are the components of the Poynting vector in the respective directions. These figures confirm the central result. There is a mode confined to the core-guiding region that propagates along the z-direction without loss of power and with a wavelength-scale variation of the intensity along both the longitudinal and transverse directions.

Evaluation of the self-consistency equation as a function of wavelength yields the dispersion relation. The result of this process for a geometry for Λ = 400 nm and W = 850 nm, is shown in Fig. 4 in normalized frequency versus normalized longitudinal momentum with α as a parameter. The $\alpha = 0$ curve looks very much like a metal waveguide dispersion relation. In the absence of material dispersion, there is no upper frequency cutoff for the mode in a Bragg waveguide with $\alpha = 0$. As α varies, the position of the mode within the Bragg stop band varies in accordance with the self-consistency condition, such that the low frequency cut-off occurs at $\lambda_{cutoff} \sim 2n\Lambda$. For all waveguides with $\alpha > 0$, there is also a high frequency cutoff. In the limiting case 90° tilt, the upper and lower cutoff frequencies are degenerate and the structure exhibits a cavity resonance rather than a waveguide mode.

For realistic applications, an operational definition of acceptable loss must be defined. This acceptable loss impacts both the minimum reflectivity magnitude (controlled by the cladding thickness and index contrast), and the angular bandwidth of the central high reflectance lobe (controlled by index contrast), and subsequently the range of possible values for the phase of reflectivity. In general, for cladding regions of length such that $HL>>1$, the round trip reflectivity is $\sim 1-4e^{-|\kappa|L/\sqrt{\cos\theta_+ \cos\theta_-}} \sim 1$, and the angular width of the high-reflectivity pass band is given by $\Delta \sim 2\tan(\alpha)\left[\sqrt{1+|\kappa|\Lambda\cos(\alpha)/\left[\pi\sin^2(\alpha)\cos(\theta_+)\cos(\theta_-)\right]}-1\right]$, with a nearly 2π swing in the allowed values of ϕ_r. This fact has two consequences. First, waveguides with sufficiently thick grating regions exhibit a continuum of allowable waveguide widths, just as a traditional dielectric waveguide. Second, similar to symmetric dielectric slab waveguides, generalized transverse Bragg waveguides of vanishing width W support guided modes.

In contrast, several recent publications[10,11] have suggested that Bragg guides have low loss modes only for specific W = $\Lambda/2$, $3\Lambda/2$, $5\Lambda/2$,... The difference can be traced to the assumption[10,11] that $\Delta\beta = 0$ so that the phase shift of the Bragg reflections is fixed at the center of the pass band and the only phase shift is given by the propagation term. Since the reflection phase shift can vary over a wide range for $HL >> 1$, it is always possible to find the necessary phase shift for the existence of a mode, independent of W. In contrast to the assertions that there are only specific widths, W that support modes, we find that there are some specific widths that do not support modes, but that these widths become vanishingly narrow as the length of the Bragg regions is increased. This is fully consistent with previous results that showed that bound modes exist in VCSEL structures for any active region width.[12]

These waveguides lack reflection symmetry about a plane perpendicular to the guide. After a reflection operation about the normal to the guide direction, the propagation angles become $\theta'_+ = -$

θ_+ and $\theta'_- = -\theta_-$. These do not correspond to a bound mode in the guide and the energy is lost into the cladding. The very important conclusion is that these modes are effectively unidirectional under inversion symmetry operations. Two potential applications are immediately suggested, optical amplifiers and high power fiber lasers. In both cases, back-scattered light limits the available performance either through increased ASE (semiconductor amplifiers) or SBS (fiber lasers). Even though back-reflected light from an external optical surface may be coupled back into the guide, the coupling is to the opposite polarity mode and is lost at the back surface of the guide.

As is the case for all Bragg guides, these guides lend themselves to single mode behavior for wide (large W) guides.[13] This is a result of the limited angular bandwidth of the Bragg reflector. A second mode is not allowed until both modes can be accommodated within the Bragg resonance, a substantially more demanding requirement than for index guides, where any angle larger than the critical angle is allowed. This permits larger area single-mode waveguides that are desirable for high power applications to ameliorate heating and laser damage limitations.

In conclusion, we have presented an analysis of tilted Bragg reflector waveguides that do not exhibit inversion symmetry about a plane perpendicular to the core. For what we believe is the first time, we demonstrate the possibility of low loss modes with non-separable traveling and standing wave components. These modes were analyzed using a simple coupled-mode theory. These guides have potential application to situations where reflected waves are problematic – for example optical amplifiers where it is necessary to avoid spurious reflections and lasing. Finally, these modes are intimately connected to the modes of photonic crystal waveguides, and their further experimental and theoretical investigation will provide insight into this important new class of waveguides.

Acknowledgement: This work was supported by the ARO/MURI in "Deep Subwavelength Optical Nanolithography."

References

[1] P. Yeh and A. Yariv, Opt. Commun. 19, 427 (1976).

[2] A. Y. Cho. A. Yariv and P. Yeh, Appl. Phys. Lett. **30**, 471 (1977).

[3] P. Russell, Science **299**, 358 (2003).

[4] S.G. Johnson, P.R.Villeneuve, S.Fan, and J.D.Joannopoulos, Phys. Rev. B, **62**, 8212, (2000).

[5] L.C. Andreani and M. Agio, Appl. Phys. Lett. **82**, 2011 (2003).

[6] As just one example: "Modes are fields that maintain the same transverse distribution and polarization at all distances along the waveguide axis." B.E.A. Saleh and M. C. Teich, Fundamentals of Photonics, (John Wiley and Sons, Inc. New York, 1991).

[7] H. Kogelnik, Bell Syst. Tech. J. **48**, 2909-2947 (1969).

[8] L. Solymar and D. J. Cooke, Volume Holography and Volume Gratings (Academic Press, London, 1981).

[9] A. Yariv and P. Yeh, Optical Waves in Crystals (John Wiley & Sons, New York, 1984).

[10] A. Yariv, Y. Xu, and S. Mookherjea, Opt. Lett. **28**, 176 (2003).

[11] J. M. Choi, W. Lang, Y. Xu and A. Yariv, J. Opt. Soc. Am. **A21**, 426 (2004).

[12] S. R. J. Brueck, V. A. Smagley and P. G. Eliseev, Phys. Rev. **E 68**, 036608 (2003).

[13] J.S. Lee and S.Y. Shin, Opt. Lett. **14**, 143 (1989).

Figure Captions:

Fig. 1: a) Geometry of the tilted Bragg grating waveguide defining θ, θ and θ_B. The core of width W is between two Bragg grating regions tilted by an angle α from the guiding direction. b) The wavevector diagram and c) the sinusoidal variation of the index along the direction ζ.

Fig. 2: a) Angular variation of the reflectivity around the Bragg peak for $\Lambda = 450$ nm, $\lambda = 1.3$ μm, $\alpha = 45°$, $\delta = 0.005$ and $L = 250$ μm. The peak reflectivity is a function of angle and the maximum is ~50%; b) and c) Absolute value and phase of the round trip reflectivity. The maximum amplitude is unity and the phase shift varies from 0 to 2π across the bandpass; d) Absolute value of the self-consistency expression showing the presence of a low loss mode.

Fig. 3: a) Mode intensity, $|E|^2$, as a function of position; b) Variation of $|E|^2$ along x; c) Variation of $|E|^2$ along z; d) x-component of the Poynting vector; e) z-component of the Poynting vector; f) wavevector diagram.

Fig. 4: Modal dispersion relation (bottom) and expanded view (top). For $\alpha = 0$, the mode is present at all frequencies above the cutoff (assuming no material dispersion). For $\alpha \neq 0$ there is an upper cutoff as well, corresponding to $\theta_+ = \pi/2 - \alpha$.

Figure 1

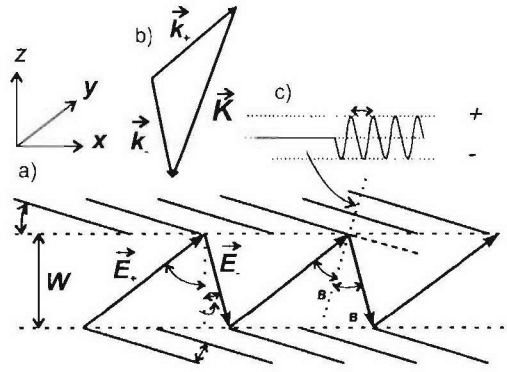


Figure 2:

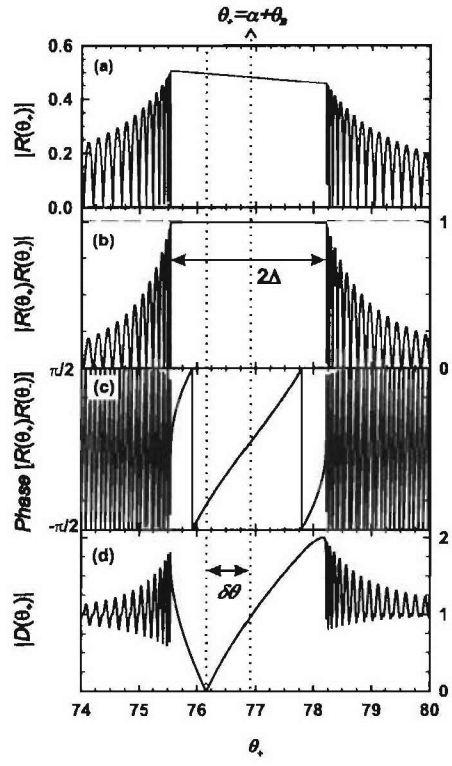

θ*=α+θB
(a)
|R(θ*)|
0.6
0.4
0.2
0.0
(b)
|R(θ*)R(θ*)|
2Δ
1
0
(c)
Phase [R(θ*)R(θ*)]
π/2
-π/2
(d)
|D(θ*)|
δθ
2
1
0
74
75
76
77
78
79
80
θ*

Figure 3:

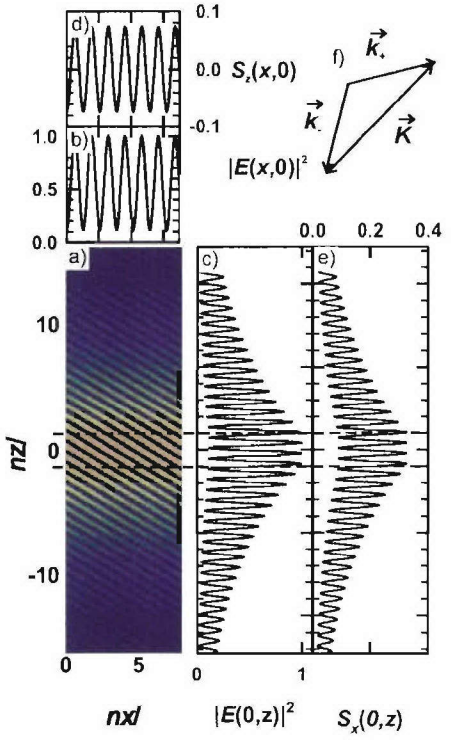
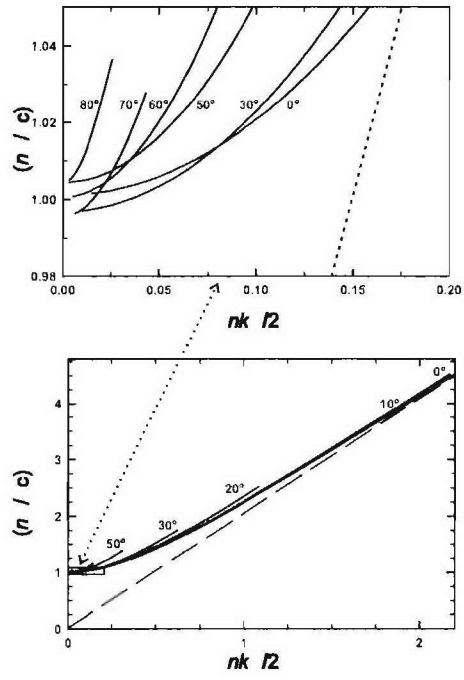

d)
b)
a)
c)
e)
f)
0.1
0.0
-0.1
$S_z(x,0)$
$|E(x,0)|^2$
$\vec{k}_+$
$\vec{k}_-$
$\vec{K}$
1.0
0.5
0.0
10
0
-10
nz/
0
5
nx/
0.0
0.2
0.4
0
1
$|E(0,z)|^2$
$S_x(0,z)$

Figure 4:


1.04
1.02
1.00
0.98
(n / c)
80°
70°
60°
50°
30°
0°
0.00
0.05
0.10
0.15
0.20
nk /2
4
3
2
1
0
(n / c)
0°
10°
20°
30°
50°
0
1
2
nk /2

Mobility and transverse electric field effects in channel conduction of wrap-around-gate nanowire MOSFETs

A.K. Sharma, S.H. Zaidi, S. Lucero, S.R.J. Brueck and N.E. Islam

Abstract: The current conduction process through a nanowire wrap-around-gate, ~50 nm channel diameter, silicon MOSFET has been investigated and compared with a ~2 μm wide slab, ~200 nm thick silicon (SOI) top-only-gate planar MOSFET with otherwise similar doping profiles, gate length and gate oxide thickness. The experimental characteristics of the nanowire and planar MOSFETs were compared with theoretical simulation results based on semi-empirical carrier mobility models. The SOI nanowire MOS devices were fabricated through interferometric lithography in combination with conventional I-line lithography. A significant increase (~3×) in current density was observed in the nanowire devices compared to the planar devices. A number of parameters such as carrier confinement, effects of parallel and transverse field-dependent mobilities, and carrier scattering due to Coulomb effects, acoustic phonons, impurity doping profile and surface roughness influences the transport process in the channel regions. The electron mobility in the nanochannel increases to ~1200 $cm^2/V s$ compared to ~400 $cm^2/V s$ for a wide slab planar device of similar channel length. Experiments also show that the application of the channel potential from three sides in the nanowire structure dramatically improves the subthreshold slope characteristics.

1 Introduction

Scaling of semiconductor devices to the nanoscale regime can lead to device and performance parameter improvements including reduction in operating voltage, increased speed and greater packaging densities. As silicon is the material of choice for a large percentage of semiconductor devices, the fabrication, analysis and testing of scaled down versions of existing Si devices has been an active research subject [1, 2]. The scaling of device parameters of many structures is under consideration and theories for improved effective channel length for a fully depleted, surrounding-gate MOSFET and double-gate SOI MOSFET have been proposed [3, 4]. Dimension reduction for current technologies, however, has its limits set by optical lithography, and scaling of MOSFETs has complexities of short-channel-effects (SCEs). Scaling of double gate and silicon-on-insulator (SOI) Delta MOSFETs to the nanoscale regime shows promise but further scaling has been limited due to fabrication difficulties [5].

For MOS transistors, scaling studies have mainly focused on decreasing channel length to submicron dimensions while the width has remained several microns in size due to the necessity of maintaining the current driving capability (width-to-length ratio) of the transistor True nanoscaling requires the reduction of the overall size of the transistor and not just the gate length. Such studies have recently attracted considerable research interest since the electrical, optical and thermodynamic properties of nanostructures can be significantly different from those of bulk material of the same composition [6]. MOSFETs with a nanowire channel wrap-around-gate (WAG) structure have been shown to have significantly improved carrier transport properties over conventional devices because of reduced scattering and better gate control. Additional study is necessary in order to fully determine the physical processes impacting the transport mechanisms [7].

In this paper we demonstrate that the current density is enhanced in nanowire channel WAG MOSFETs as a result of higher carrier mobilities. We discuss the physical processes contributing to the increased mobility, specifically quasi-1D transport at the channel centre of such devices. Equations for the mobility model and a physical interpretation are provided. For this study, we fabricated ~50 nm diameter nanowire, wrap-around-gate MOSFETs with single and multiple parallel channels and compared their characteristics with ~2 μm wide, 200 nm thick slab, top-only-gate MOSFETs that were identical in all aspects except for dimensionality of the channel region. In order to focus on the effects of scaling the channel width region, the nanowire channel length and the slab gate length were both made intentionally long (~2 μm) for this study so that short channel effects would be minimised. Simulations of carrier mobility for both nanowire WAG and slab gate devices are presented. The device conduction processes are explained in

© IEE, 2004

IEE Proceedings online no. 20040993

doi:10.1049/ip-cds:20040993

Paper first received 10th October 2003 and in revised form 5th April 2004

A.K. Sharma and S. Lucero are with the Air Force Research Laboratory, Space Vehicles Directorate, Kirtland AFB NM 87111, USA

S.H. Zaidi is with Gratings Inc., Albuquerque, NM 87109, USA

S.R.J. Brueck is with the Department of Physics and Astronomy, University of New Mexico, Albuquerque NM 87106, USA

N. E. Islam is with the Department of Electrical and Computer Engineering, University of Missouri, Columbia MO 65211, USA

A.K. Sharma and S.R.J. Brueck are also with the Centre for High Technology Materials, University of New Mexico, Albuquerque NM 87106, USA

terms of changes in the channel mobility, the influence of transverse and parallel components of the channel electric field, and the impurity distribution within the channel as a result of the fabrication process.

2 Nanowire fabrication

Interferometric lithography (IL) is a well-developed technique for inexpensive, large-area nanopatterning and was used in the nanowire fabrication process [8]. In its simplest version, IL is interference between two coherent waves resulting in a 1D periodic pattern with a pitch of $\lambda/2\sin\theta$ where λ is the optical wavelength and 2θ is the included angle between the interfering beams. A typical IL configuration consists of a collimated laser beam incident on a Fresnel mirror (FM) mounted on a rotation stage for period variation [9]. There is no depth dependence to an IL exposure pattern, for which the depth-of-field is limited only by the laser coherence length and beam overlaps. The 1D nanoscale patterns were first formed in photoresist followed by pattern transfer on to the underlying substrate using reactive-ion-etching (RIE) in a parallel plate reactor using CHF_3/O_2 plasma chemistry [10]. Figure 1 shows cross-sectional views of these structures after thermal oxidation. These nanowires form the channel region of a wrapped-around-gate nanochannel MOSFET as described in Section 3.

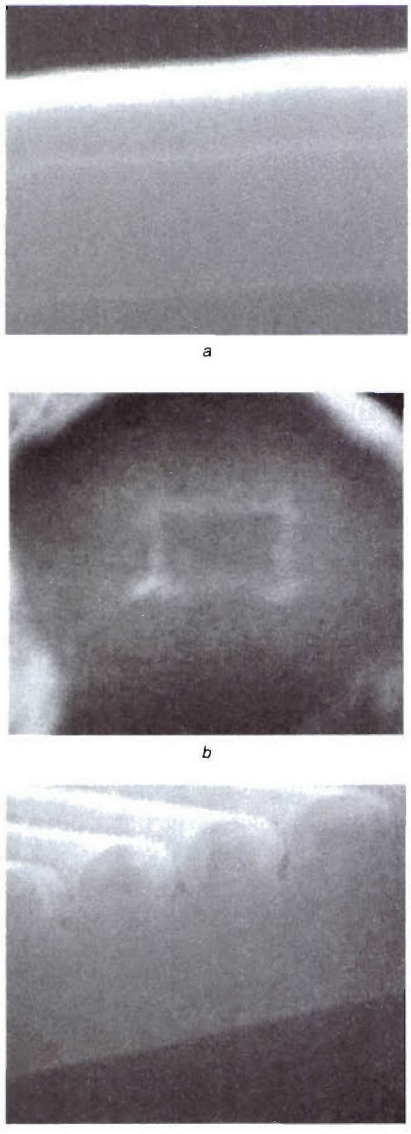


Fig. 1 *SEM micrographs showing results of thermal oxidation*
a SOI slab gate region
b single nanowire surrounded by thermally grown SiO_2
c multiple parallel nanowires surrounded by thermally grown SiO_2

3 Nanowire WAG channel and top-only-gate slab MOSFET fabrication

Nanowires were fabricated using the processes described in Section 2 in localised channel/gate areas of the MOSFET devices using IL, along with conventional I-line contact mask printing [11] for defining the device source and drain regions. For comparison, we also fabricated MOSFET devices with slab top-only-gate regions.

Figure 2 shows a process flow sequence. A 10–22 Ω-per-square bare silicon on insulator (SOI) wafer with a 200 nm thick active Si layer on top of a 400 nm thick buried oxide (BOX) isolation layer was spin coated with photoresist (PR) and exposed to an interference pattern as described above. A 30 nm thick blanket layer of Cr was then deposited by e-beam evaporation and a lift-off step was used to create an array of Cr lines that are an effective RIE etch mask. In order to localise the Cr lines to the regions where the wires would be produced, the wafer was again spin coated with a PR layer and a mask was then used to selectively pattern the PR to protect portions of the Cr lines from a chemical

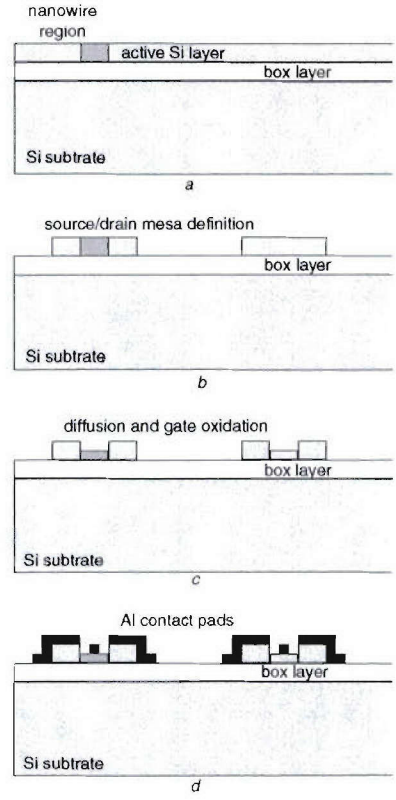


Fig. 2 *Process flow sequence for fabrication of nanowire wrap-around-gate MOSFET (left) and slab-top-only-gate MOSFET device (right)*

Cr-etch solution. Once the Cr was etched from the unwanted regions, the PR was removed. Once again a layer of PR was applied on to the sample to define the source and drain regions. The source and drain definition mask was aligned to the Cr lines (gate pattern). After the exposure and develop processes, the remaining structure had source and drain mesas masked by PR and Cr lines masking the gate region between the source and drain regions. The samples were then etched to the BOX layer by RIE, thus defining the channel and source/drain regions. Figure 3 shows SEM micrographs of a slab gate and nanowire gate structures before thermal oxidation. Basically at this point we have two mesa structures (source and drain regions) connected by a wide slab or by wires, respectively. After the RIE step the PR and the Cr etch mask lines were removed. There is considerable damage left by the RIE step. In order to remove some of this damage, two rapid thermal anneal (RTA) steps were performed. The first RTA was performed at 900°C for 5 min in a nitrogen environment to anneal the damaged surface [12] followed by a second RTA step for 3 min at 450°C in a hydrogen environment to passivate the Si surfaces. Next a thick ~0.5 μm thick silicon nitride layer was deposited on to the samples to be used as a diffusion mask. A layer of PR was spin coated on to the wafer and windows were opened in the nitride layer above the source and drain regions using buffered oxide etch (BOE) solution. PR was removed and a layer of phosphorous spin on glass (PSG) was coated on to the sample for the pre-deposition step that was performed at ~900°C for 5 min. Next the PSG and nitride layers were removed using BOE. The gate oxidation and dopant drive-in were performed in a single thermal step using an oxidation furnace at 1000°C. As a thermal oxide was grown around the wire structures it consumed the Si, thus decreasing the width of the wire. Careful characterisations were performed in order to optimise the thermal process in order to result in a Si nanowire region diameter of ~50 nm. This process grew a gate oxide that was ~60 nm thick around the nanowires. Similarly a ~60 nm gate oxide was grown on the slab gate devices in order to minimise any oxide capacitance (C_{ox}) effects in our final analysis. The time for the oxidation to yield ~50 nm diameter Si wires drove some of the dopant into the channel region. Figure 4*a* shows a process simulation of the predicted phosphorous impurity content in the wires. The resultant doping profile resulted in an $n^+ n\ n^+$ structure as shown in the process simulation (Fig. 4*b*–4*c*), which shows the modelled impurity profiles before and after the oxidation/diffusion process. Next a layer of PR was deposited and patterned for metallisation. A 300 nm thick Al layer was e-beam deposited using multiple shadow evaporations and liftoff in order to achieve conformal gate coverage. The samples were cleaned and annealed at ~430°C in a rapid thermal anneal (RTA) to create ohmic contacts at the source and drain region. Completely fabricated single and multiple nanowire channel WAG MOSFETs and top-only-gate slab MOSFET are shown in Fig. 5.

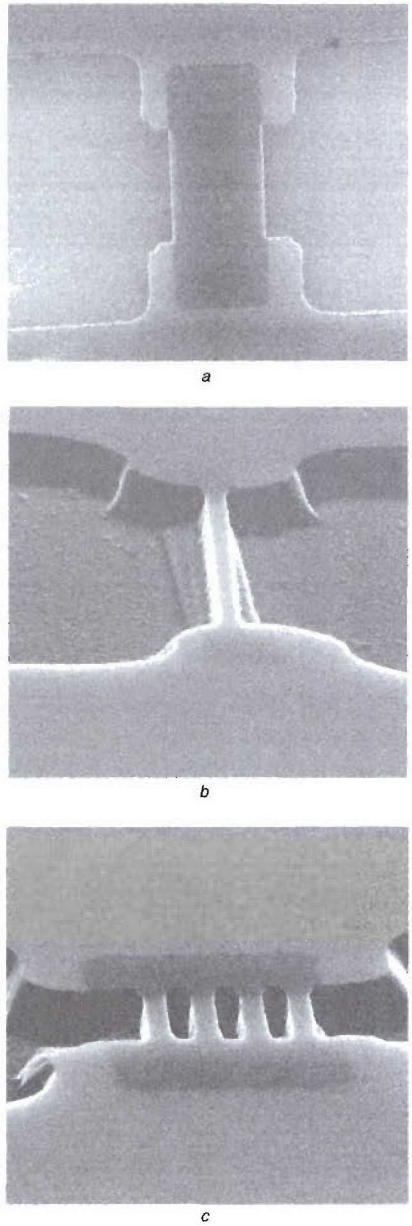


Fig. 3 *SEM micrographs of slab structure and precursors to single and multiple nanowire gate structures*
a Slab structure connecting top source mesa region and bottom drain mesa region
b Precursor to nanowire gate structure connecting source and drain mesa regions
c Precursor to multiple nanowire gate structure connecting source and drain mesa regions

4 Current–voltage measurements, modelling, and analysis

Experimental I-V plots for both the nanowire and slab devices are shown in Fig. 6. The drain current (I_d) as a function of drain-to-source voltage (V_{ds}) for various gate biases was measured using a digital curve tracer. As seen from the plots, for similar doping profiles, gate length and gate oxide thicknesses the current–voltage characteristics of the nanowire and slab MOSFET are considerably different. The drain current in the nanowire is rather flat in the saturation region ($V_{ds} > 1$ V) compared to the significant slope in the slab device. This is due to the geometry of the slab MOSFET, in which the fringing fields at the edges of the slab significantly impact the drain current. As the channel approaches pinch-off, the carrier charge drops at the drain end and the lateral fringing field increases at the edges of the slab. Further increasing V_{ds} causes the high-field region at the drain end to widen the channel enough to accommodate the additional potential drop, thus resulting in a further increase in the drain current. In contrast, when

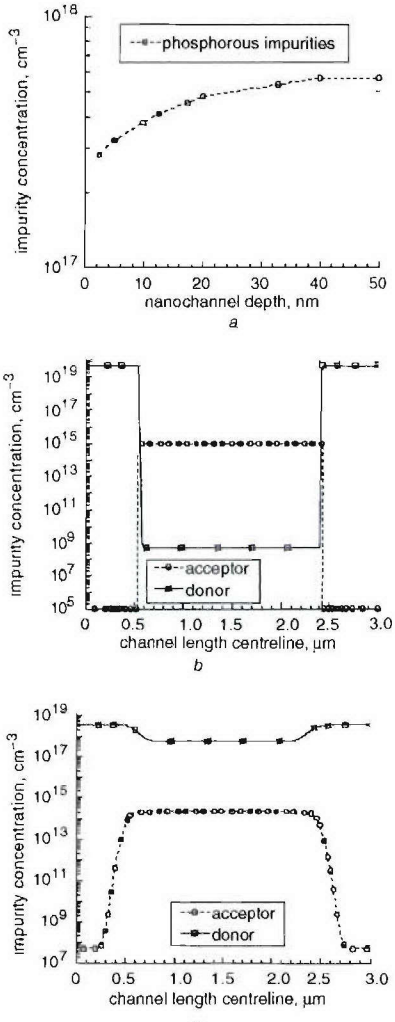


Fig. 4 *Simulation plots of impurity concentrations*
a Impurity concentration through the nanowire diameter width from the base of the nanowire ($x = 0$ nm) to the top surface ($x = 50$ nm)
b Pre-diffusion impurity concentration of acceptors (substrate doping) and donors (phosphorous doping) throughout the source–gate–drain regions
c Post-diffusion impurity concentration of both acceptors and donors throughout the source–gate–drain regions

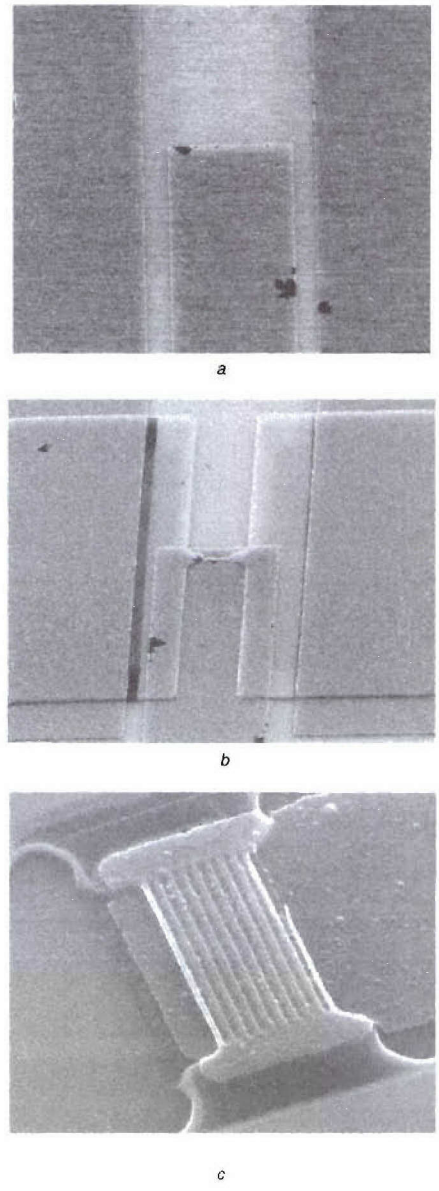


Fig. 5 *SEM micrographs of various MOSFET structures*
a Slab-MOSFET where the centre electrode is the gate surrounded by the source and drain electrodes
b Single nanowire-MOSFET
c Multiple nanowire-MOSFET

the nanowire device is biased in the saturation region, the effective channel length of the nanowire device is essentially unaffected since the depletion region at the drain terminal is physically restricted to ~50 nm. This effect, known as channel length modulation, is a well-known phenomenon in conventional transistor designs [13]. This phenomenon is more dominant in conventional short channel devices. Suppressing such effects in the $\sim 1\,V_{ds}$ nanowire device (as is the case here) is of significant benefit, specifically in the development of low voltage circuit applications.

Figure 6 shows that in the nanowire MOSFET the current is an order of magnitude less than for the slab device. Scaling to the cross-sectional area shows that the nanowire device current density is three times higher than that of the planar slab device. From the experimental data the resultant conductivities for the slab and nanowire devices are $\sigma_{slab} \sim 9 \times 10^3$ A/V cm^2 and $\sigma_{wire} \sim 3 \times 10^4$ A/V cm^2. This means that we can obtain the same amount of total current driving capability in nanowire channel devices that have much smaller cross-sections by configuring several nanowires in parallel. In order to understand and improve the current characteristics of the nanodevice, we also modelled the current voltage characteristics of the transistors. We are not aware of any reported standard nanowire channel wrap-around-gate MOSFET drain current-voltage (I_d–V_{ds}) relations and in order simulate the results we developed a very simple model based on the 2-D sketch of Fig. 7*a*.

Poisson's equation in cylindrical coordinates can be written as

$$\frac{1}{r}\frac{\partial}{\partial r}\left(r\frac{\partial \psi}{\partial r}\right) = -\frac{\rho}{\varepsilon_s} \qquad (1)$$

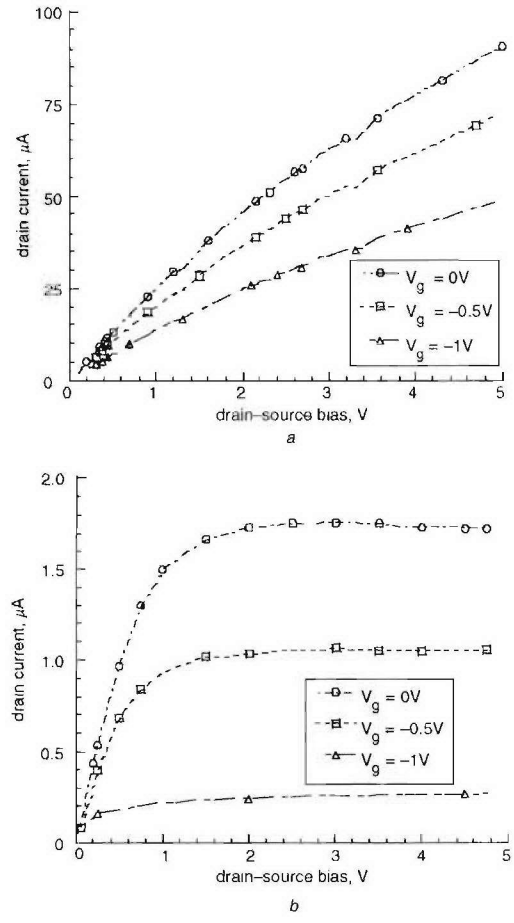


Fig. 6 *Experimental plots of drain current as a function of drain-to-source bias for various gate voltages*
a Slab-MOSFET
b Single nanowire-MOSFET

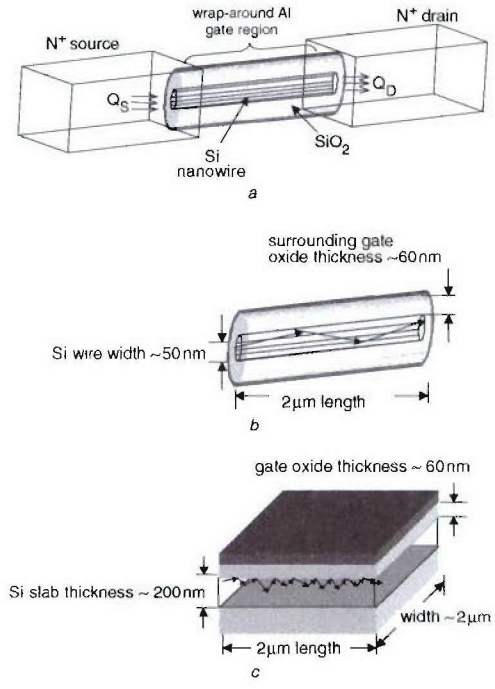


Fig. 7 *Schematic views of nanowire WAG MOSFET and carrier conduction*
a Schematic configuration of a nanowire WAG MOSFET
b Carrier conduction through a nanowire gate
c Carrier conduction through a slab gate

where ψ is the electron potential, r is the radius vector, ρ is the charge density per unit volume, and ε_s is the dielectric constant of silicon.

We assume that the average charge in the cylindrical channel is

$$Q_{\text{average}} \approx (Q_S + Q_D)/2 \tag{2}$$

where Q_S is the charge per unit area in the channel near the source and Q_D near the drain regions. The current density in the channel can be then approximated by

$$J_d \approx -Q_{\text{average}} v_{\text{drift}} \tag{3}$$

where v_{drift} is the channel region carrier drift velocity. The cylindrical nanowire oxide capacitance C_{rox} near the source and drain regions can be written as a function of the regional charge and applied source, drain and gate potentials as follows:

$$\begin{aligned} C_{\text{rox}} &= -(Q_s/V_{\text{gs}} - V_t) \\ &= -Q_D/(V_{\text{gd}} - V_t), \text{ where } V_{\text{gd}} = V_{\text{gs}} - V_{\text{ds}} \end{aligned} \tag{4}$$

where V_{gs} is the gate-to-source potential, V_{dg} is the drain-to-gate potential, and V_t is the threshold voltage.

Substituting Q_S and Q_D into the equation for J_d results in

$$J_d \approx C_{\text{rox}}[(2V_{\text{gs}} - Vt - V_{\text{ds}})/2]v_{\text{drift}} \tag{5}$$

Thus the current density J_d depends on the drift velocity, the drain and gate biases and the channel capacitance. Any variation in these parameters will be reflected in the current density value. Since the channel capacitance per unit area (F/cm^2) is fixed for a given oxide thickness and because the oxide thickness is about the same ($\sim$60 nm) for both the nanowire and the bulk devices, the capacitance per unit area effect may not contribute significantly to the current density. Neglecting contributions from the terminal bias effects, the major contribution comes from the drift velocity component. The drift velocity is a function of carrier mobility while the mobility itself depends on the electric field in the channel. The electric field at any channel region is the vector sum of the parallel ($E_\parallel$) and transverse ($E_\perp$) component, where $E_\parallel$ is in the direction of the current flow. It may be noted that even without significant change in 'actual' mobility, changes in parallel and transverse electric field component can alter the mobility (carrier velocity) components (and hence the drain current) significantly. For example, the magnitude of the E-field at any point can be written as $|\vec{E}| = \sqrt{\vec{E}_\perp^2 + \vec{E}_\parallel^2}$ which can be satisfied by various values for $E_\perp$ and $E_\parallel$. (e.g. $|E| = \sqrt{50}$ kV/m is satisfied for $E_\perp = 5$ kV/m and $E_\parallel = 5$ kV/m, or $E_\perp = 1$ kV/m and $E_\parallel = 7$ kV/m). The increase in $E_\parallel$ (second case), results in an increase in the parallel drift velocity, thus increasing current flow. The hypothesis stated above was tested through incorporating mathematical models for mobility and electric fields in the channel regions of the devices. Most mobility models incorporate saturation at high parallel field of the form as suggested by Thornber [14],

$$\begin{aligned} v_{\text{drift}}(E_\parallel, E_\perp, N_I, T) = \mu(E_\perp, N_I, T).\{1 \\ + [\mu(E_\perp, N_I, T)E_\parallel/v_s(T)^\beta]^{1-\beta}\}.E_\parallel \end{aligned} \tag{6}$$

where N_I is the local impurity concentration, and T is the absolute temperature. The carrier saturation velocity, v_s in the channel region is assumed independent of normal electric field, impurity concentration, and direction of current flow with respect to the crystal orientation. The fitting parameter β has been well characterised with a value of 2 for both electrons and holes [15]. Besides the electric field dependence, other mechanisms such as acoustic phonon scattering, impurity scattering and surface scattering also contribute to the mobility. Thus the mobility can be approximated by the sum of the following terms, [16, 17]:

$$1/\mu = 1/\mu_{ac} + 1/\mu_b + 1/\mu_{sr} + 1/\mu_{Coulomb} \quad (7)$$

where μ_{ac} is the mobility limited by scattering acoustic phonons and is given by [17]

$$\mu_{ac} = qh^3\rho\mu_l/(m^* m_\mu Z_A^2 k_B T) \quad (8)$$

where q is the elementary charge, h is Dirac constant, μ_l is the sound velocity, m^* and m_μ is the effective mass and mobility mass, respectively, Z_A is the deformation potential, k_B is the Boltzmann constant, T is the absolute temperature and ρ is the areal mass density of silicon.

The bulk mobility of silicon μ_b is given by [18]

$$\mu_b(N_I, T) = \mu_0 + (\mu_{max}(T) - \mu_0)/[1 + (N_I/C_r)^\alpha] - \mu_1/[1 + (C_s/N_I)^\beta] \quad (9)$$

where N_I is the local impurity concentration, μ_{max} is the ohmic (pure-lattice) electron mobility, C_r and C_s are fitting parameters and α, β, μ_1 are model parameters for electrons or holes where the values can be found in Masetii *et al.* [16] For example, $\mu_{max} = 1417\,cm^2/Vs$, $\mu_0 = 52.2$ and $44.9\,cm^2/Vs$ for electrons and holes respectively.

μ_{sr} is the mobility limited by surface roughness scattering and is given by [19]

$$\mu_{sr}(E_\perp) = \delta/E_\perp^2 \quad (10)$$

where $E_\perp$ is the transverse electric field and δ is a model parameter and is $5.82 \times 10^{14}\,V/s$ and $2.0546 \times 10^{14}\,V/s$ for electrons and holes respectively [20].

$\mu_{Coulomb}$ is due to the effect of Coulomb scattering, which is mainly due to oxide fixed charge and surface states charge and can be found from [20]

$$\mu_{Coulomb} \propto T/Q_f \quad (11)$$

where Q_f is the fixed oxide charge and T is the absolute temperature.

Details of mobility models and parameters for non-planar structures can be found in Lombardi *et al.* [21] and will not be discussed here. However, it is important to note that μ_{sr} is the main reason for the higher mobility in the nanowire devices, and that the values of μ_{ac}, μ_b, $\mu_{Coulomb}$, are comparable for both devices. The carrier transport is based on changes in the mobility components due to transverse and parallel electric fields, and is also due to the physics described in (8)–(11), which is reflected in the final mobility value and hence the drift velocity component. Any reduction in the transverse field (expected to be minimum near the centre of the nanowires) increases the μ_{sr} component (10) and the overall mobility value in the Mathiesen's summation (7). In the slab device, the transverse field is directed from the top towards the substrate, while in the wrap around gate structure, the transverse field is directed from all around and is minimum at the centre. Thus, due to the electric field configuration affecting the surface interactions the mobility is expected to increase at the centre of the nanowires. Figure 7*b*–7*c* shows an expected schematic model of the carrier transport mechanism for both nanochannel and slab devices. For reasons discussed above, the nanowire is expected to show 'enhanced forward' motion compared to the conventional MOSFET surface scattering model for the slab geometry.

Figures 8 and 9 show a 2D simulation plot of carrier parallel ($\mu_{||}$) and perpendicular ($\mu_\perp$) mobilities for both slab and nanochannel devices. In the slab device (Fig. 8*a*) the mobility is lower at the Si SiO_2 interface due to surface interactions and the large transverse electric field. Further away from the interface in the perpendicular direction these effects decrease and the mobility increases and levels out to the bulk mobility value. The dip in $\mu_\perp$ is due to the location of the edge of the depletion region where the field-

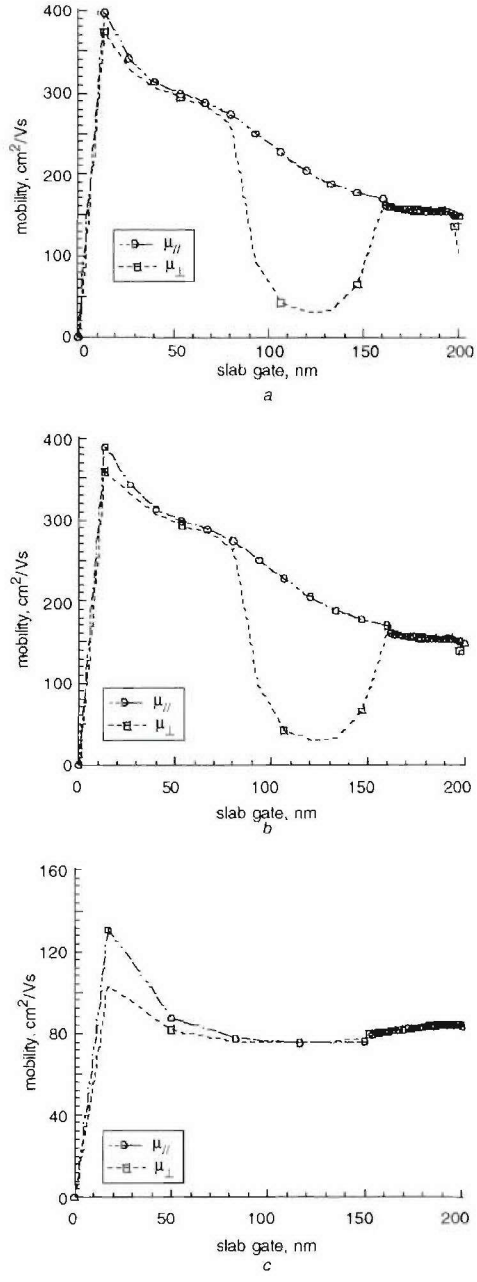


Fig. 8 *Simulation plots for slab channel carrier mobility in the parallel and transverse directions for various gate biases*
a $V_g = 0\,V$
b $V_g = -0.5\,V$
c $V_g = -1.0\,V$

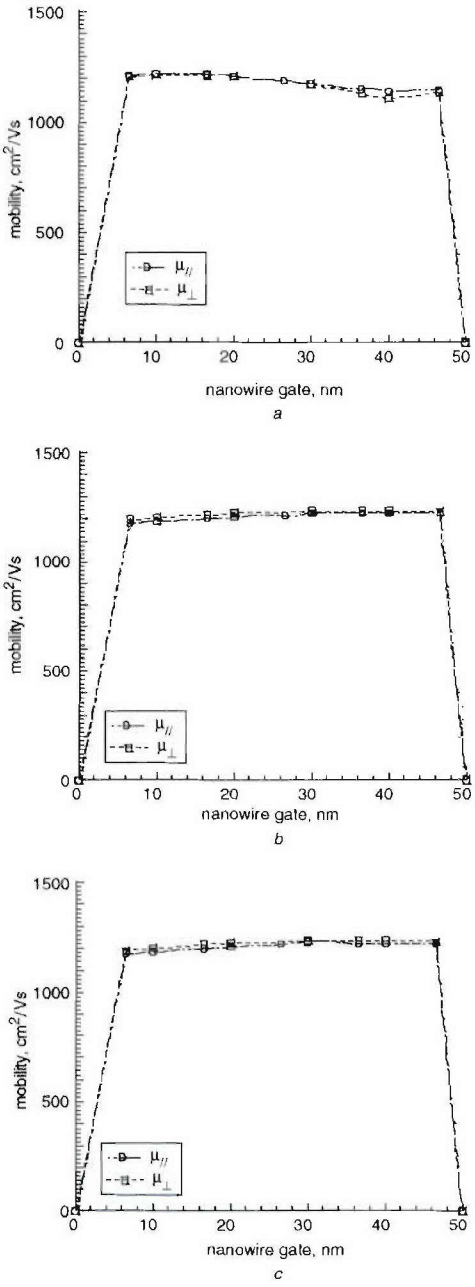


Fig. 9 *Simulation plots for nanowire channel carrier mobility in the parallel and y transverse directions for various gate biases*
a $V_g = 0$ V
b $V_g = -0.5$ V
c $V_g = -1.0$ V

dependent component drops rapidly. The nanowire device (Fig. 9*a*) shows similar trends but the mobility at the channel centre is about three times larger than the slab devices. The enhanced mobility is due to the fact that the transverse field has an equipotential configuration in the channel instead of from the top only as in the slab case. This results in an improved parallel electric field distribution through the centre of the cross-sectional channel region, where the surface scattering and Coulomb effects are also minimal. Figures 8*b*–8*c* and 9*b*–9*c* show plots of the effects of applying gate bias (transverse electric field) on carrier mobility for both wire and slab devices. As can be seen from

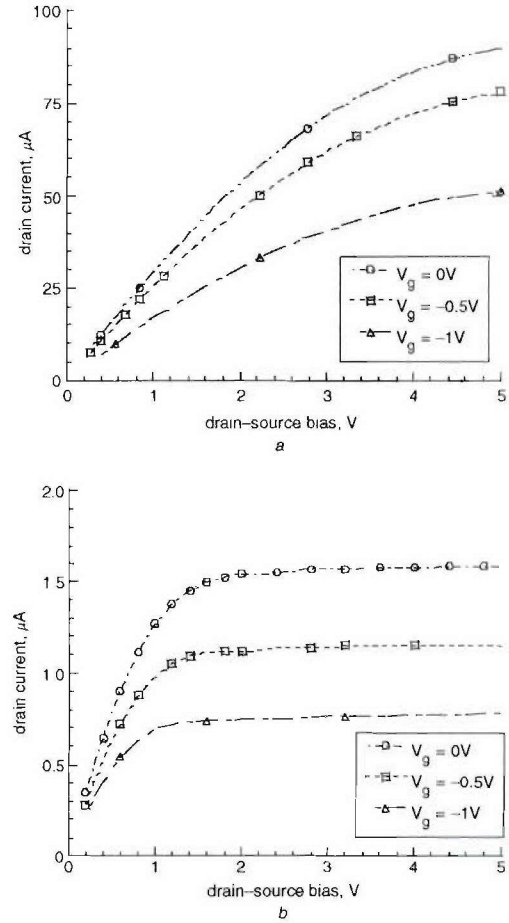


Fig. 10 *Simulation plots of drain current as a function of drain–source bias for various gate biases*
a Slab-MOSFET;
b Single-nanowire MOSFET

the plots the variations in transverse electric field are more pronounced in the slab gate devices compared to the nanowire channel devices. Figure 10 shows simulated I–V characteristics for the ~50 nm channel device at different gate biases. The results are in agreement with the measured I–V for the fabricated single channel device as shown in Fig. 6. The close match between the simulated and measured I–V plots is an indication of the validity of the model and material parameters chosen for the simulation.

The simulation also shows that the nanowire channel device has characteristics that are somewhat similar to a buried channel MOSFET [22]. Our simulations show that the I–V characteristic of the device is very sensitive to the doping profile of the narrow ~50 nm thick channels. The best fit is for the case where an n-type dopant is near the upper surface and decreases monotonically in the y-direction (Fig. 4). This profile is expected since during the fabrication process the source and drain were diffused at 1000°C with an n-type dopant with a peak concentration of 10^{18} cm^{-3}. It is very likely that diffusion into the channel region also took place. The net effect is the creation of a device very similar to a normally-on n-buried channel MOSFET The channel doping profile prior to and following the diffusion process is different as is evident from the process simulation in Fig. 4 [23]. As can be anticipated, during device operation the conducting channel is the n-region rather than an inversion layer at the Si–SiO_2

interface as would normally be the case if the p-type channel were the dominant dopant. Buried n-layer MOSFETs have been analysed and the physics of the device I–V characteristics for the linear and saturation regions are different from that for an inversion layer formed at the Si-SiO_2 interface [24].

5 Subthreshold currents

The subthreshold region performance is particularly important when evaluating the suitability of MOSFETs for low voltage, low power applications, such as when the MOSFET is used in high bit rate switching applications. The subthreshold currents as a function of gate bias are shown in Fig. 11 for a single WAG nanochannel and slab devices. As can be seen from the figure the current drops about three decades for a small ($\Delta V \sim 0.1$ V) variation in the gate bias. In contrast, the subthreshold current in the slab gate device did not drop one decade for a much larger variation in gate bias. Typical nanochannel devices characterised had ~ 50 nm width Si surrounded by ~ 60 nm oxide with an Al wrap-around-gate electrode and the slab devices had ~ 200 nm thick Si that was $\sim 2\,\mu$m wide with a ~ 60 nm thick oxide with top only Al gate. Both nanochannel and slab channels were $\sim 2\,\mu$m long. From Fig. 11 we can calculate the gate voltage swing S using the standard definition given by (12), which results in a subthreshold slope of ~ 100 mV/decade for the nanowire MOSFET.

$$S = \ln 10 |d V_G / d(\ln I_D)| \tag{12}$$

Since the subthreshold current did not drop even one decade we extrapolated the subthreshold slope to be ~ 4 V/decade for the slab gate devices where the current cannot be effectively turned off. This is due to the fact that these devices do not have a typical n-channel MOSFET doping profile but are essentially buried channel devices with an $n^+n^-n^+$ doping profile in which there are sufficient carriers in the channel for conduction even at 0 V gate bias.

Considering we have a similar doping profile for the nanowire channel device that has a gate oxide thickness of ~ 60 nm, the subthreshold performance is truly remarkable. These results also demonstrate that narrow channels provide better control over the channel potential due to the enhanced gate control from all sides in contrast with only the front surface coverage in conventional planar transistors, even for these unconventional device-doping profiles.

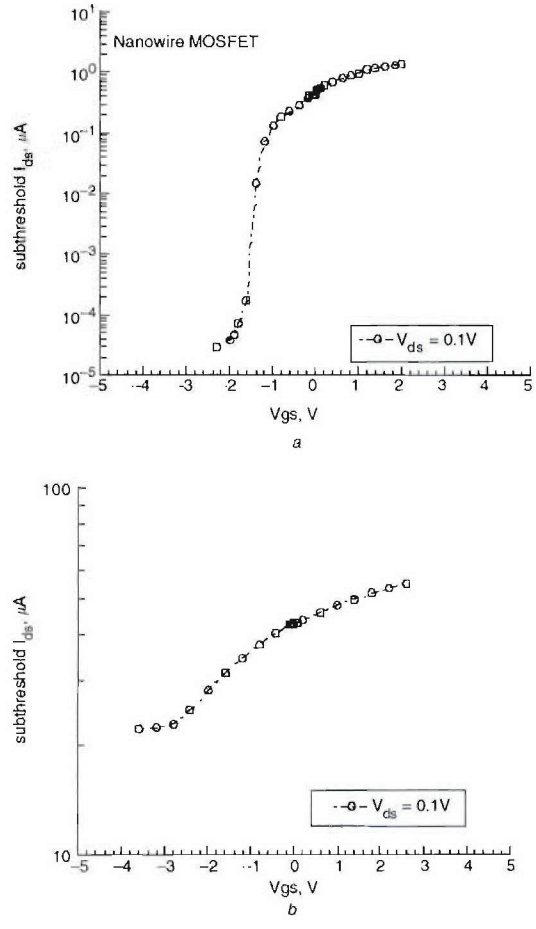


Fig. 11 *Measured subthreshold drain current plots as a function of gate bias*
a Nanowire WAG MOSFET
b Slab top only gate MOSFET

6 Analysis and conclusion

Through experiments and simulation, we have explained the carrier transport properties of Si nanowire channel wrap-around-gate MOSFET. Nanowire WAG MOSFET devices were fabricated along with slab top-only-gate MOSFETs for a comparative study. Interferometric lithography was used to define the nanowire in the channel region and conventional lithography was used to define the source and drain regions. Devices characterised had ~ 50 nm diameter wire channels and ~ 200 nm thick, $\sim 2\,\mu$m wide slab regions that were both $\sim 2\,\mu$m in length. In future studies we plan to investigate shorter devices to understand non-equilibrium effects as a function of lateral and transverse dimensions. A semi-empirical carrier mobility model for non-planar silicon structures was used to model the current–voltage characteristics. Simulation results show good agreement with experiment. Analysis showed that the current density is about ~ 3 time higher in the nanowire channel WAG devices as then in the slab devices. This is primarily due the average higher carrier mobilities in the nanowire channel devices as well as conformal uniform electric flux densities in the wire devices. Study also shows that MOSFET width scaling is possible while maintaining the current driving capability high by integrating multiple nanowires in parallel. The experimental results showed that the current was a linear function of the number of wires.

7 Acknowledgment

The authors would like to thank Mr Richard Marquardt for assisting in the experimental setup for the subthreshold response, Dr P Varangis for assisting in the critical fabrication steps of the devices, and Mr George Jzeremes for setting up the computer simulations.

8 References

1 Wind, S.J., *et al.*: 'Lithography and fabrication processes for sub-100nm scale complementary metal-oxide-semiconductor', *J. Vac. Sci. Technol. B*, 1995, **13**, (6), pp. 2688–2695
2 Fritze, M., Astolfi, D., Liu, H., Chen, C.K., Suntharalingam, V., Preble, P., and Wyatt, D.W.: 'Sub-100 nm KrF lithography for complementary metal-oxide-semiconductor circuits', *J. Vac. Sci. Technol. B*, 1999, **17**, (2), p. 345–349
3 Auth, C.P., and Plummer, J.D.: 'Scaling theory for cylindrical, fully-depleted surrounding-gate MOSFET's', *IEEE Electron Device Lett.*, 1997, **18**, (2), p. 74–76

4 Suzuki, K., Tanaka, T., Tosaka, Y., Horie, H., and Arimoto, Y.: 'Scaling theory for double-gate SOI MOSFETs', *IEEE Trans. Electron Devices*, 1993, **40**, (12), p. 2326
5 Colinge, J.P., Gao, M.H., Rodriguez, A.R., and Claeys, C.: 'Silicon-on-insulator gate-all-around devices', *IEDM Tech. Dig.*, 1990, pp. 595–598
6 Persans, P. D., Lurio, L.B., Pant, J., Lian, G.D., and Hayes, T.M.: 'Zn incorporation in Cds nano particles in glass', *Phys. Rev.*, 2001, **63**, pp. 115320(1)–115320(8)
7 Leobandung, E., Gu Gian, Lingjie, G., and Chao, S.Y.: 'Wire-channel and wrap-around-gate metal-oxide semiconductor field-effect transistors with a significant reduction of short channel effects', *J. Vac. Sci. Technol., B*, 1997, **5**, (6), p. 2791
8 Chen, X., and Brueck, S.R.J.: 'Imaging interferometric lithography: a wavelength division multiplex approach to extending optical lithography', *J. Vac. Sci. Technol.*, 1998, **B16**, pp. 3392–3397
9 Zaidi, S.H., and Brueck, S.R.J.: 'Multiple exposure interferometric lithography', *J. Vac. Sci. Technol.*, 1993, **B11**, p. 653
10 Zaidi, S.H., and Brueck, S.R.J.: 'Si-texturing with sub-wavelength structures', *Proc. 26th IEEE Photovoltaic Specialists Conf. PVSC*, 1997, **26**, pp. 171–174
11 Zaidi, S.H., Brueck, S.R.J., Hill, T., and Shagam, R.N.. 'Mix and match interferometric and optical lithographies for nanoscale structuring', *Proc SPIE*, 1998, **3331**, p. 406–413
12 Wolf, S., and Tauber, R.N.: 'Silicon Processing for the VLSI Era' (Lattice Press, 1986), Vol. **1**, pp. 57–58
13 Gary, P.R., and Meyer, R.G.: 'Analysis and Design of Analog Integrated Circuits' (John Wiley & Sons, Inc., 1993, 3rd edn.), pp. 59–66
14 Thornber, K.K.: 'Relation of drift velocity to low-field mobility and high-field saturation velocity', *J. Appl. Phys.*, 1980, **51**, pp. 2127–2136
15 Masetti, G., Severi, M., and Solmi, S.: 'Modeling of carrier mobility against carrier concentration in arsenic-, phosphorous-, and boron-doped silicon', *IEEE Trans. Electron Devices*, 1983, **ED-30**, pp. 764–769
16 Sah, C.T., Ning, T.H., and Tschopp, L.L.: 'Scattering of electrons by surface oxide charges and by lattice vibrations at the silicon-silicon dioxide interface', *Surf. Sci.*, 1972, **32**, pp. 561–575
17 Deybe, P.P., and Conwell, E.M.: 'Electrical properties of n-type germanium', *Phys. Rev.*, 1954, **93**, pp. 693–706
18 Masetti, G., Severi, M., and Solmi, S.: 'Modeling of carrier mobility against concentration in arsenic-, phosphorous-, and boron-doped silicon', *IEEE Trans. Electron Devices*, 1983, **ED-30**, pp. 764–769
19 Fang, F.F., and Fowler, A.B.: 'Electron scattering in inverted silicon surfaces', *Phys. Rev. B*, 1968, **169**, (3), pp. 619–631
20 Goodnick, S.M., Gann, R.G., Ferry, D.K., Wilmsen, C.W., and Krivanek, O.L.: 'Surface roughness induced scattering and band tailing', *Surf. Sci.*, 1982, **113**, pp. 233–238
21 Lombardi, C., Manzini, S., Saporito, A., and Vanzi, M.: 'A physically based mobility model for numerical simulation of nonplanar devices', *IEEE Trans. Computo-Aided Design*, 1988, **7**, (11)
22 Sze, S.M.: 'Physics of Semiconductor Devices' (John Wiley and Sons, NY, 1981, 2nd edn.), Chap. 8
23 Process simulation software, Athena, Silvaco International Software, Users Manual, 2000
24 Merckel, G.: 'Ion Implanted MOS Transistors-Depletion Mode Devices', *in* Engle, F. and Jespers, W.L. (Eds.) 'Process and Device Modeling for IC Design' (Noordhoff, Leyden, 1977)

Single-longitudinal-mode emission from interband cascade DFB laser with a grating fabricated by interferometric lithography

J.L. Bradshaw, J.D. Bruno, J.T. Pham, D.E. Wortman, S. Zhang and S.R.J. Brueck

Abstract: A distributed-feedback, type-II interband cascade laser is demonstrated in pulsed mode, emitting near 3.145 μm at temperatures between 50 and 80 K. Feedback is provided by a surface-etched grating formed using interferometric lithography. Between 50 and 80 K, the device's single longitudinal mode red-shifts with temperature at ~0.1 nm/K. At 70 K and 190 mA of pulsed injection current, side-mode suppression exceeds 30 dB. The characteristics of related Fabry–Perot IC lasers are also described and contrasted with those of the distributed feedback device.

1 Introduction

In this paper, we report on the first demonstration of a distributed feedback (DFB) interband cascade (IC) laser. Light–current–voltage (L–I–V) and spectral characteristics of the DFB device are reported, along with the L–I–V characteristics of related Fabry–Perot (FP) devices for comparison. Possible improvements to the DFB device structure are also identified.

The results reported below are significant because they represent another step forward in the ongoing development of quantum-cascade-based semiconductor diode lasers (SDLs), which include the type-I intersubband quantum cascade (QC) lasers and the type-II IC lasers. These cascade laser designs partially overcome fundamental limitations of more conventional mid-IR laser designs, and hold the potential of providing single-mode SDLs throughout the mid-IR region that can operate under CW conditions at ambient temperatures (or temperatures accessible with thermoelectric coolers).

The QC laser has recently demonstrated CW operation at 300 K from a FP device, emitting at 9.1 μm [1], and single-mode DFB QC lasers have been demonstrated between 4.5 and 16.5 μm (see [2] for a recent review). FP IC lasers have been demonstrated in the 3 to 5 μm wavelength region, and recently, room temperature, pulsed operation was demonstrated at 3.51 μm [3]. However, single-mode IC lasers have not, to our knowledge, been reported previously.

2 Experimental details

The laser sample used to fabricate the DFB device, referred to below as M2, was grown by molecular beam epitaxy (MBE) on a p-type (001) GaSb substrate. The layer structure and DFB device geometry are shown schematically in Fig. 1. A 2.26-μm-thick n-type InAs/AlSb superlattice region serves as the waveguide's lower cladding and is followed by a 1.34-μm-thick core region. The core consists of 18 identical cascaded active regions separated by n-type injection regions. A 0.3-μm-thick, p-doped GaSb layer was grown above the core region and serves as a separate confinement/top contact layer and host layer for the etched grating of the DFB devices.

The active region of the laser's core consists of InAs and GaInSb quantum well (QW) layers and GaSb and AlSb blocking/barrier layers, and the injection regions consist of digitally graded n-InAs and AlSb layers. A schematic energy band diagram of a single period of a typical IC laser's cascaded active and injection regions is shown in Fig. 2. Electrons injected into the active region's InAs QW relax to the lowest heavy-hole state in the neighbouring GaInSb QW with the emission of a photon. Subsequent transport, facilitated by interband tunnelling, moves the electrons into the adjacent injection region, where they are transported through the region's conduction miniband for injection into the next active region. The active/injection regions of M2 and the MBE procedures used in its growth are the same as those used in the growth of the sample in [3] and have been described elsewhere [4].

After MBE growth, the M2 sample was cleaved to provide laser material for the fabrication of both DFB and FP devices. Prior to wet-etching for mesa definition of DFB devices, a grating was etched into the top of the DFB material as follows. First, an antireflection coating (ARC) and photoresist (PR) layer were deposited onto the top p-GaSb epilayer of the M2 sample. Two beams formed from the third harmonic of a yttrium-aluminium-garnet (YAG) laser at 355 nm were then directed from opposite positions onto the sample, each making angles of ~45° relative to the sample's surface. The angle was chosen so that the beam's interference formed a 465-nm-period standing-wave pattern in the PR above the ARC layer, exposing the PR. The grating period was determined by dividing the expected emission wavelength of the M2 device (3.32 μm at 80 K) by twice the waveguide's modal index n. The latter was estimated at 3.47 by measuring the FP fringe spacing, $\Delta\lambda$,

© IEE, 2003

IEE Proceedings online no. 20030613

doi: 10.1049/ip-opt:20030613

Paper received 9th January 2003

J.L. Bradshaw, J.D. Bruno, J.T. Pham and D.E. Wortman are with Maxion Technologies, Inc., Hyattsville, MD 20782-2003, USA

S. Zhang and S.R.J. Brueck are with the Center for High Technology Materials, University of New Mexico, Albuquerque, NM 87106, USA

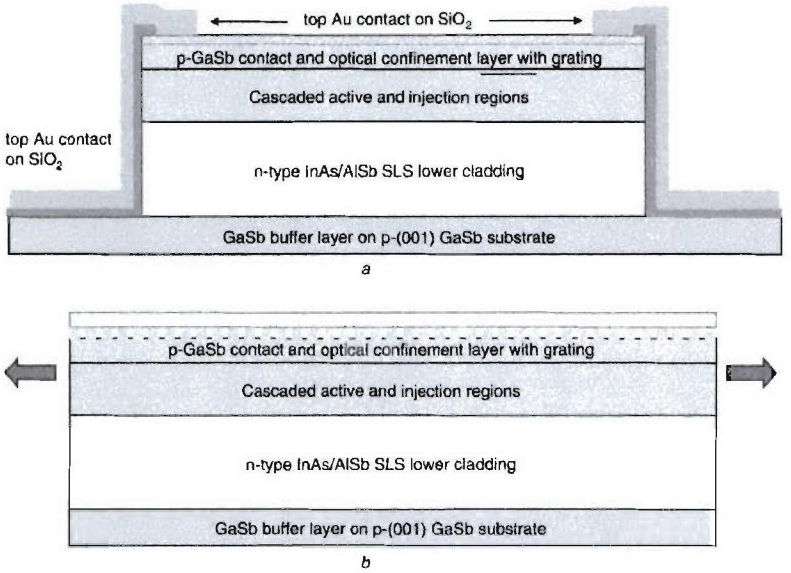


Fig. 1 *Schematic layer structure and device geometry used for DFB devices*

a Cross sectional view showing DFB edge-contacting scheme
b Side view showing top-grating orientation

of a similar device's below-threshold amplified spontaneous emission spectrum and using the relation $n = \lambda^2/(2L\Delta\lambda)$, where $\Delta\lambda$ is the separation between adjacent FP fringes, λ is the expected emission wavelength and L is the device's cavity length.

The exposed PR and underlying ARC layers were then removed, and an ion beam was used to etch a shallow vertical trench into the exposed p-GaSb layer. After cleaning, this process resulted in an ~40-nm-deep, 465-nm-period grating with a duty cycle of approximately 50% on the top p-GaSb layer of the DFB laser material.

The FP and DFB materials were processed into ridge mesa devices, with mesa widths of 65 and 115 μm, defined with optical lithography and wet chemical etching. Insulating layers of SiO_2 were deposited after the mesas were defined, leaving openings on top of the ridges to allow for electrical contacts to the devices (Fig. 1). In the case of DFB devices, only 5-μm-wide windows were opened for metal contact along each top edge of the mesa ridge. This left most of the top of the (wider) DFB mesas without a metal contact over the grating; a step intended to reduce optical losses. Metal contacts were then deposited onto the tops of the mesas, as appropriate, and onto the bottom substrate for electrical contact. Some DFB devices were intentionally fabricated with metal contacts covering their gratings for the purpose of performance comparisons. Laser bars were cleaved into cavities approximately 1-mm long, and both facets were left uncoated.

The fabricated lasers were indium-soldered onto a copper heatsink and mounted onto the temperature-controlled cold finger of an optical cryostat. L–I–V and spectral characterisations were carried out using a liquid-nitrogen-cooled InSb detector and a grating monochromator with lock-in electronic detection.

3 Performance of Fabry–Perot lasers

Figure 3 shows the L–I–V characteristics of a 115-μm-wide by 0.96-mm-long cavity length M2 FP device. This device had the entire top of the mesa contacted with a 0.3-μm-thick Au contact layer. The threshold currents at

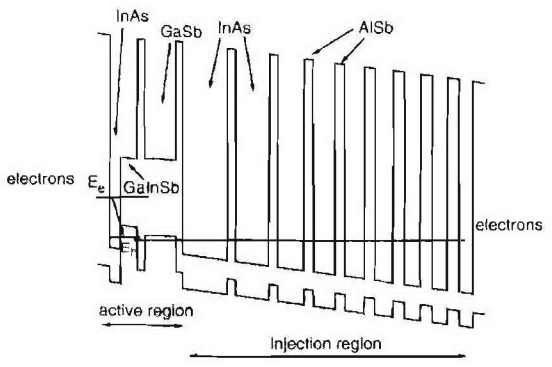


Fig. 2 *Energy band diagram showing single stage of a typical IC laser structure at operating bias*

Active region (left) shows interband optical transition and interband tunnelling transition; injection region (right) transports electrons to next stage of device

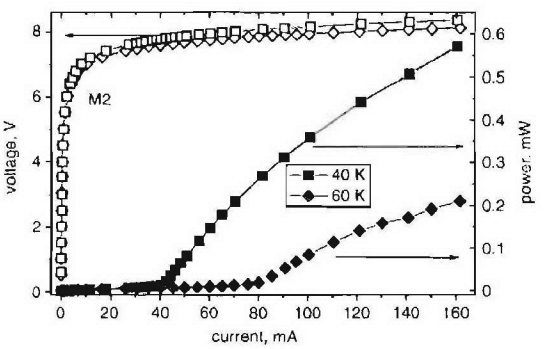


Fig. 3 *CW L–I–V characteristics of a 115-μm × 0.96-μm M2 FP device at heatsink temperatures of 40 and 60 K*

Device does not have a grating structure, and the top mesa is covered with a thick Au contact

heatsink temperatures of 40 and 60 K are 40 and 80 mA, respectively (corresponding to current densities of 36.2 A/cm^2 and 72.4 A/cm^2, respectively). The output power is very low: at 100 mA of CW injection current at 60 K, the measured power from a single facet is below 0.1 mW. The device slope efficiencies at 40 and 60 K are also low.

For comparison purposes, Fig. 4 shows the L–I–V characteristics of a 65-μm-wide by 0.98-mm-long cavity length FP IC laser, fabricated from a laser structure that included an upper cladding region. The Fig. 4 device is the one described in [3] (referred to below as M1) and has active and injection regions that are nominally identical to those of the M2 FP device. The differences lie above the active/injection regions: in the M1 device, an upper cladding region separates the laser core from the top metal contact, whereas in the M2 device the optical mode is confined between the lower cladding and the metal contact and/or air, depending on how the mesa top is contacted. The M1 characteristics show a threshold current density of 13.2 A/cm^2 and an initial slope efficiency of 0.65 W/A at a heatsink temperature of 80 K. The initial slope efficiency corresponds to a differential external quantum efficiency of ~350% (approximately 19% differential efficiency per stage) when the output from both facets is assumed to be equal. At 100 mA of CW current, the output power measured from a single facet was 57 mW. The I–V characteristics of M1 exhibit a high resistance below threshold and an abrupt decrease in differential resistance at threshold, with the decrease occurring at 6.95 V. Based on the observed 80 K laser emission at 3.315 μm (373.9 meV) and the presence of 18 cascaded stages, this corresponds to a voltage efficiency of 96%. By comparison, the output power and slope efficiencies of the M2 FP device are greatly reduced. It is clear that this reduction in M2's performance relative to M1 is not due to the active/injection region designs, but is instead related to the waveguide structure and/or to the quality of the electrical contacts made to the core region. In the M2 FP design, the optical mode is larger at the top metal contact than in the M1 device. Consequently, optical losses were expected to be larger in the M2 FP and DFB devices. Because of this, the p-GaSb separate-confinement/contact layer was doped with Be at a relatively low level of 5-6 × 10^{17} cm^{-3}. This doping level was chosen as a compromise between the simultaneous requirements of high electrical conductivity in the layer and low free-carrier losses. Despite the generally inferior characteristics of the M2 device relative to the M1 device, the M2 device still has a reasonably good diode characteristic, showing a high initial resistance to current flow and a rapid drop in resistance above approximately 7 V.

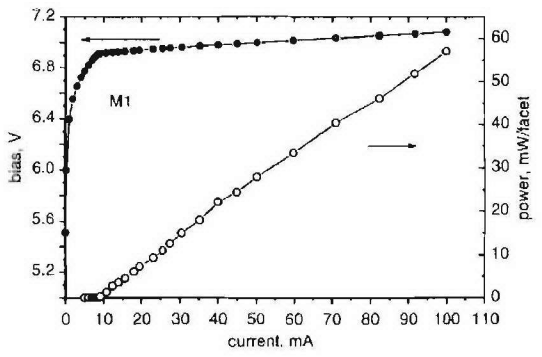


Fig. 4 *CW L–I–V characteristics of the 65-μm × 0.98-μm FP device of [3] at a heatsink temperature of 80 K*

4 Performance of DFB lasers

L–I–V characteristics of the DFB laser structure processed with the M2 grating material and with metal contacts along only the top edges of the mesa are shown in Fig. 5. The laser exhibited a threshold current of ~165 mA in the pulsed mode at 60 K. Note that the I–V characteristics do not show the high resistance at low current that was observed for the M2 FP device (Fig. 3) whose mesa was covered with a thick Au contact. To determine whether this might be related to the relatively low doping in the Be-doped contact layer, another DFB device was fabricated from the same M2 DFB material, but a 100-Å-thick Au contact was deposited over the entire top of the grating structure (electrically connecting the thicker Au edge contacts). The L–I–V characteristics of this device are shown in Fig. 6, and the data shows significantly improved I–V characteristics with a high initial resistance and improved forward bias diode characteristics. Additionally, the device exhibited a lower threshold current of ~10 mA at 80 K, corresponding to a threshold current density of ~27 A/cm^2. This threshold current density compares favourably with the threshold current density of 72 A/cm^2 at 60 K of the device shown in Fig. 5, presumably due to the thinner gold contact layer resulting in a lower optical loss and reduced spreading resistance in the top GaSb layer. Note, however, that this same device did not emit in a single longitudinal mode but exhibited FP emission characteristics.

Lasing spectra acquired under pulsed conditions are shown in Fig. 7 for the DFB laser device shown in Fig. 5. The lasing spectrum exhibits a single longitudinal mode near 3.142 μm at 60 K. When the device is processed with the grating-free laser material in a FP geometry, it exhibits a FP lasing spectra centred near a wavelength of 3.30 μm (multimode spectra at right-hand side of Fig. 7). The separation between these lasing energies is nearly 19 meV; an energy comparable to the width of the device's spontaneous-emission spectrum. This difference could be explained if our estimate of the modal index in the DFB material were ~5% larger than its actual value. This would also be consistent with the high threshold current density seen in Fig. 5. Note also that the cavity length for the DFB laser is half that of the FP device. Thus, the longitudinal mode spacing in the DFB device would be twice the spacing

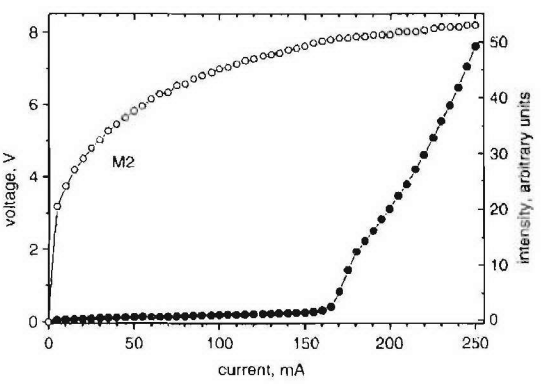


Fig. 5 *L–I–V characteristics of an edge-contacted, 115-μm-wide by 0.54-mm-long mesa DFB laser*

Data were acquired under pulsed conditions using a 1-μs pulse width and a 10 kHz repetition rate at a heatsink temperature of 60 K

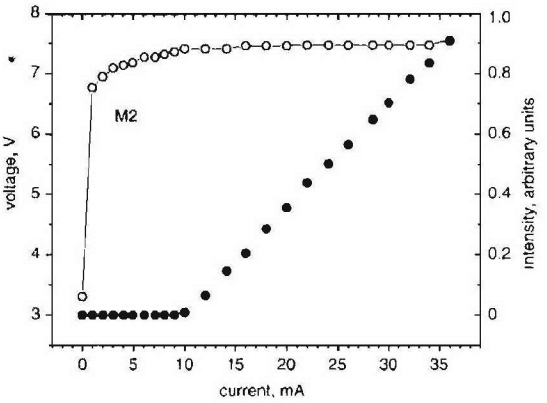


Fig. 6 *L–I–V characteristics of an edge-contacted, 35-μm-wide by 1.04-mm-long mesa DFB laser acquired under pulsed conditions using a 1-μs pulse width and a 10 kHz repetition rate at a heatsink temperature of 80 K*

Top of grating is covered with an 80-Å-thick Au contact

of the cavity modes shown in Fig. 7 for the FP device. Consequently, the DFB lasing spectra clearly consists of a single longitudinal mode. However, because the processed mesa widths are rather broad (>65 μm), all the lasers investigated here probably emitted several lateral modes.

Higher resolution lasing spectra are shown in Fig. 8. At a temperature of 70 K and a pulsed injection current of 190 mA, the DFB laser exhibits a side-mode suppression ratio in excess of 30 dB. At 200 mA injection current, the emergence of another mode can be seen near 3.122 μm. Note that the vertical axis is logarithmic. Figure 9*a* shows spectra acquired under pulsed conditions at temperatures ranging from 50 to 80 K. The DFB lasing wavelength is plotted as a function of temperature in Fig. 9*b*. The laser exhibits a temperature tuning rate of 0.1 nm/K, which is consistent with expectations based on the variation of the refractive index of III–V materials with temperature.

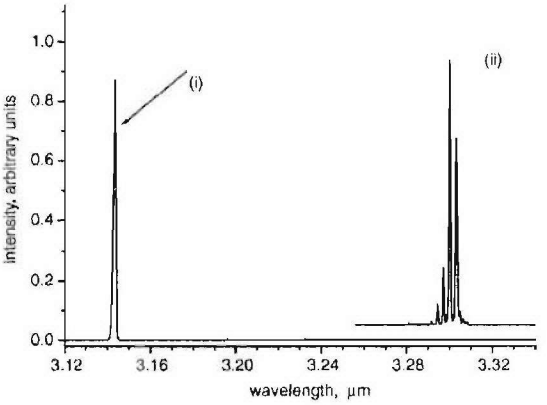


Fig. 7 *Emission spectra of the DFB Single longitudinal mode emission at 60 K (left) from edge-contacted DFB laser device described in Fig. 5 and multimode emission is observed from FP device fabricated from the same M2 laser material (right) at 80 K. Both spectra were acquired using a 1-μs pulse width and a 10 kHz repetition rate*

(i) Single-longitudinal-mode DFB operation, 115 μm × 0.54 mm mesa, $T = 60$ K, $I = 175$ mA
(ii) 65 μm × 1.01 mesa, Fabry–Perot laser, $T = 80$ K, $I = 60$ mA

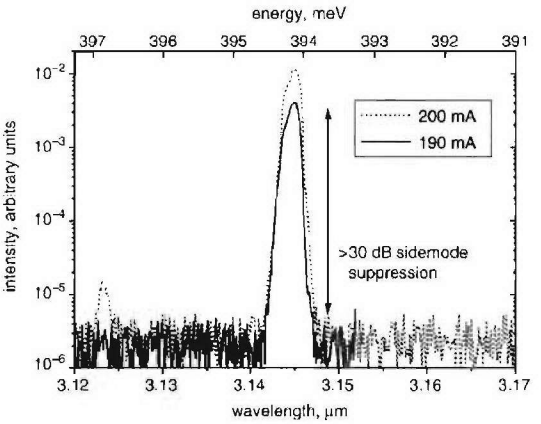


Fig. 8 *High-resolution emission spectrum of the DFB device described in Fig. 5 under pulsed conditions at 70 K*

Vertical scale is logarithmic showing side-mode suppression exceeding 30 dB at 190 mA injection current. The spectra were acquired using 1-μs pulses at a 10 kHz repetition rate

At higher pulsed-current levels, the DFB laser exhibits linewidth broadening. Several lasing spectra at high pulsed-current levels are shown in Fig. 10. Note the significant broadening of the laser linewidth at higher current levels. The broadening is attributed to heating during the current pulse as well as the influence of the higher order lateral modes at higher injection-current levels.

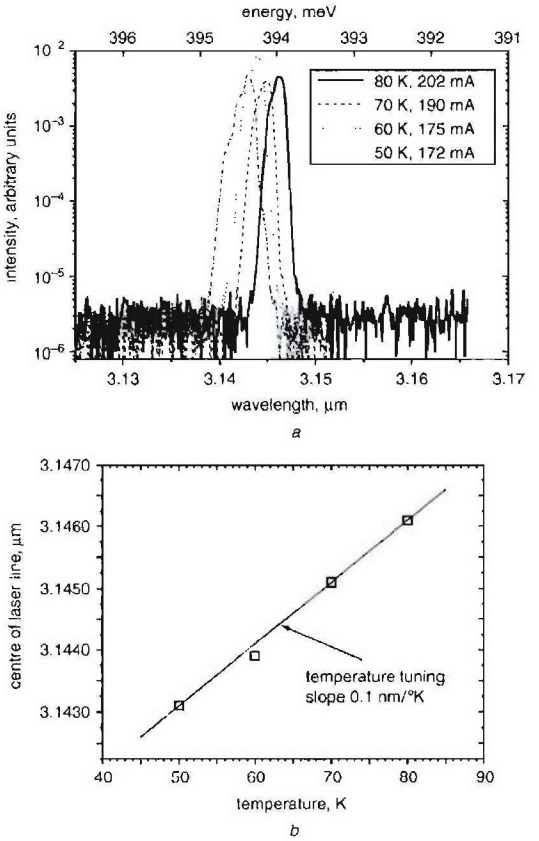


Fig. 9 *Emission characteristics of DFB device described in Fig. 5*

a High-resolution emission spectrum under pulsed conditions between 50 K and 80 K
b Emission wavelength against heatsink temperature between 50 K and 80 K

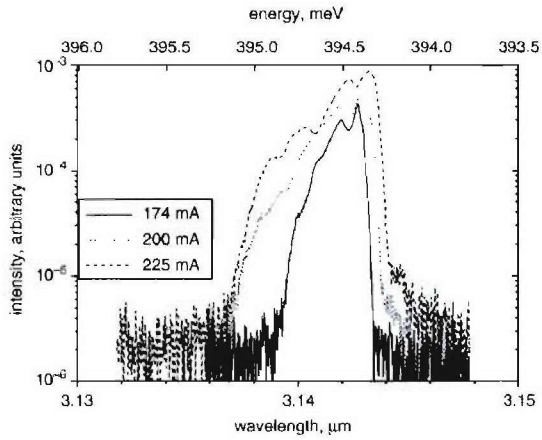


Fig. 10 *High-resolution emission spectra of the DFB device described in Fig. 5 under pulsed conditions at 50 K and injection currents of 174, 200 and 225 mA*

Effects of heating during the pulse and multiple lateral modes are evident

5 Summary and conclusions

We have described the fabrication and performance characteristics of the first DFB IC laser. The laser exhibits single-longitudinal mode operation in pulsed mode between 50 and 80 K, emitting near 3.144 μm at 60 K. Results show that improved performance can be expected from designs with a slightly larger (~+5%) grating period and a more heavily p-doped GaSb contact layer. The larger period will provide feedback closer to the M2 material's gain peak, and the improved top GaSb layer conductivity will allow for a reduced spreading resistance and eliminate the need for covering the grating with Au to achieve improved I–V characteristics. This should significantly reduce optical losses, and improve device output power, slope efficiency and temperature performance.

6 Acknowledgments

This work was supported in part by the Army Research Laboratory through a Cooperative Research and Development Agreement (CRDA# 0105-A-C980) and by a Phase I SBIR Contract funded by the Missile Defense Agency and managed by Dr R. Soref of the Air Force Research Laboratory, Hanscom, MA (Contract F19628-01-C-0035). The authors also wish to thank Dr R.Q. Yang for his contributions and Dr J.R. Meyer and I. Vurgaftman of the Naval Research Laboratory for helpful discussions.

7 References

1 Beck, M., Hofstetter, D., Aellen, T., Faist, J., Oesterle, U., Ilegems, M., Gini, E., and Melchoir, H.: 'Continuous wave operation of a mid-infrared semiconductor laser at room temperature', *Science*, 2002, **295**, p. 301

2 Gmachl, C., Straub, A., Colombelli, R., Capasso, F., Sivco, D.L., Sergent, A.M., and Cho, A.Y.: 'Single-mode, tunable distributed-feedback and multiple-wavelength quantum cascade lasers', *IEEE J. Quantum Electron.*, 2002, **38**, p. 569

3 Yang, R.Q., Bradshaw, J.L., Bruno, J.D., Pham, J.T., Wortman, D.E., and Tober, R.L.: 'Room temperature type-II interband cascade laser', *Appl. Phys. Lett.*, 2002, **81**, p. 397

4 Yang, R.Q., Bradshaw, J.L., Bruno, J.D., Pham, J.T., and Wortman, D.E.: 'Mid-infrared type-II interband cascade lasers', *IEEE J. Quantum Electron.*, 2002, **38**, p. 559

HTML ABSTRACT + LINKS

JOURNAL OF APPLIED PHYSICS 97, 083530 (2005)

Quantitative determination of tensile stress creation during island coalescence using selective-area growth

S. J. Hearne, S. C. Seel, J. A. Floro, and C. W. Dyck
Sandia National Laboratories, Albuquerque, New Mexico 87185-1415

W. Fan and S. R. J. Brueck
Center for High Technology Materials, University of New Mexico, Albuquerque, New Mexico 87106

(Received 15 October 2004; accepted 21 January 2005; published online 7 April 2005)

Island coalescence during Volmer–Weber thin film growth is generally accepted to be a source of tensile stress. However, the stochastic nature of unpatterned film nucleation and growth prevents meaningful comparison of stress measurements taken during growth to that predicted by theoretical models. We have overcome this by systematically controlling island geometry using selective growth of Ni films on patterned substrates via electrodeposition. It was determined that the measured power-law dependence of mean stress on island size agreed well with theory. However, our data clearly demonstrates that the majority of the tensile stress associated with coalescence actually occurred after the initial contact of neighboring islands as the film planarizes with additional deposition. © *2005 American Institute of Physics*. [DOI: 10.1063/1.1870109]

I. INTRODUCTION

The effective mechanical properties of a material are highly dependent upon the residual stress state introduced during fabrication. This is particularly true for thin films where the residual stress can be a significant portion of the yield strength. Unfortunately, the evolution of intrinsic stress during deposition of Volmer–Weber thin films is quite complex and still highly debated.[1–3] The only region where there is a consensus as to the mechanism is during island coalescence, where tensile stresses have been observed to exceed one gigapascal.[4] Conceptually, tensile stress is generated when adjacent islands initially touch one another, and then elastically deform to contact over a finite area in order to reduce the overall surface energy. Existing theoretical models for coalescence stress all determine the mean tensile stress in mechanical equilibrium, as a function of island size and geometry at the moment of coalescence.[1,4–8] However, computational necessity requires use of highly simplified island geometries with uniform sizes and simultaneous coalescence. In real films, coalescence events are stochastically distributed in time and occur among islands with a broad range of sizes and shapes. Furthermore, multiple mechanisms for stress generation can be operating at the same time. As a result, it is not possible to quantitatively equate theoretical predictions for the tensile coalescence stress with existing measurements in stochastically nucleated films and a meaningful comparison is only obtainable when island geometries are systematically controlled.

We obtain both the functional dependence of mean tensile stress on island radius, and the absolute magnitude of the stress, by measuring stress changes during electrodeposition of Ni islands where the coalescence process was constrained via lithographically-defined island nucleation sites and selective-area growth (Fig. 1). We demonstrate that the experimentally measured coalescence stress is in good agreement with the predictions from the Hertzian contact model of Freund and Chason[7] and with two-dimensional finite element (FE) analysis. We have also determined that the initial coalescence stress was the minority component of the total stress created during the coalescence and planarization of the film. This determination lays the groundwork for future analysis of the postcontact stress generation process, which is considerably more complex (and beyond the scope of this paper).

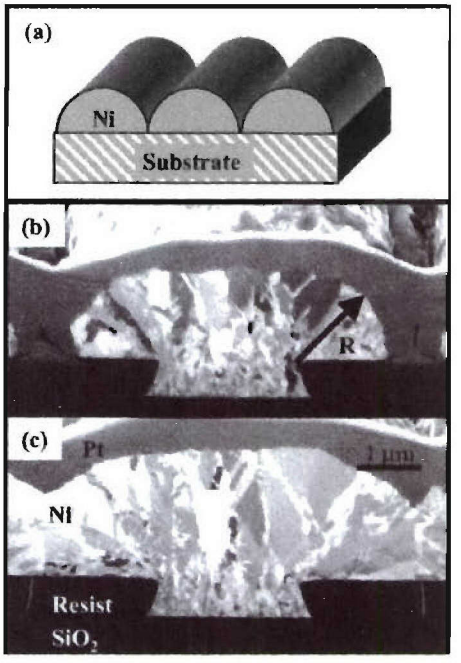


FIG. 1. (a) Schematic of an idealized cylindrical structure, (b) ion channeling focused ion beam (ICFIB) cross-section image of actual structure prior to coalescence, and (c) ICFIB image of the actual structure after coalescence. Note, the islands were coated after electrodeposition with Pt for processing in the FIB.

 © 2005 American Institute of Physics

Downloaded 18 Apr 2005 to 134.253.26.12. Redistribution subject to AIP license or copyright, see http://jap.aip.org/jap/copyright.jsp

II. EXPERIMENTAL TECHNIQUES

Motivated by recent models for coalescence stress by Freund and Chason[7] and by Nix and Clemens,[6] we chose to experimentally evaluate the "two-dimensional" coalescence geometry, where the islands were idealized as an array of parallel half-cylinders, as shown in Fig. 1(a). In order to accomplish this, periodic trench arrays were patterned into a photoresist layer to expose a 1500 Å thick Au nucleation layer. This Au film was grown on a Ti adhesion layer on a thermally oxidized Si (001) substrate. Island size was controlled by varying the spacing of the trenches, while keeping the nominal trench pitch-to-width ratio $(d_{\text{pitch}}/d_{\text{trench}})=2.65$. The effective cylinder radii, R, ranged from 0.3 μm to 26 μm. Ni films were potentiostatically electroplated from an additive-free Ni–sulfamate bath at 40 °C. Prior to electrodeposition of the coalescence samples, the bath was conditioned at 10 mA/cm^2 for 4 h to remove trace ionic contaminants such as Fe and Co. Additionally, ultrahigh purity N_2 was bubbled through the bath for a minimum of 24 h, which increased run-to-run reproducibility. The plating efficiency was determined by comparing the Faradic current to thicknesses measured using Rutherford backscattering spectrometry. During deposition, the substrate curvature induced by thin-film stress was measured using laser deflectometry,[3] with the wafer clamped in a cantilever configuration. Because film thicknesses were often an appreciable fraction of the substrate thickness, the usual Stoney's equation did not hold, and the following relation for curvature (κ) was used:[9]

$$\kappa=\frac{6h_f\sigma}{h_s^2}\left[\frac{1+H}{1+HY(4+6H+4H^2)+H^4Y^2}\right], \tag{1}$$

where H is the ratio of the film thickness (h_f), to the substrate thickness (h_s), σ is the mean film stress, and Y is the ratio of the film modulus to the substrate modulus. Young's modulus was used rather than the biaxial modulus due to the uniaxial loading geometry used here.

III. RESULTS

Figures 1(b) and 1(c) demonstrate the selective lateral growth that can be obtained using electrodeposition. At coalescence, the islands were not true half-cylinders, as shown in Figs. 1(b) and 1(c), and we will account for this in our analysis. Figure 2 shows the measured evolution of "stress-thickness," σh_f, calculated from curvature using Eq. (1). In the figure, Ni was electrodeposited into an array of trenches that yielded nominally 4.2 μm radius cylinders [with the radius as defined in Fig. 1(b)]. The first rise in the tensile stress was the result of random Ni nucleation and coalescence within the trenches themselves to form the Ni lines. The second tensile rise was due to the coalescence of adjacent cylindrical islands, and was the stress change that we analyzed. In order to do this, we found it necessary to differentiate between the stress created during the initial coalescence event and the subsequent stress created as the film evolved from cylinders towards a planar surface.

During potentiostatic deposition plating current is linearly proportional to the surface area. Therefore, since the surface roughness of a film is maximum at the moment of coalescence there must be a corresponding maximum in the plating current at the same moment. To quantify this we developed a geometric model that predicts the evolution of the surface area and in turn, the deposition current of a cylindrical geometry as shown in Fig. 3. Prior to coalescence, the surface is given by the sum of two quarter cylinders and the trench that grow radially outwards due to the growth direction being normal to the growth surface during electrodeposition [Fig. 3(a)]. This results in the total current (I_{tot}) of the wafer prior to coalescence being

$$I_{\text{tot}}=(\pi r+w_{\text{tr}})\frac{dr}{dt}\frac{dq}{dV}n_{\text{tr}}w_s, \tag{2}$$

where, r is the island radius, n_{tr} is the number of trench across the samples, w_s width of the sample, w_{tr} width of the trench, dr/dt is the deposition rate, and dq/dV is the plating efficiency measured to be 3.7×10^7 mC/cm^3 from RBS

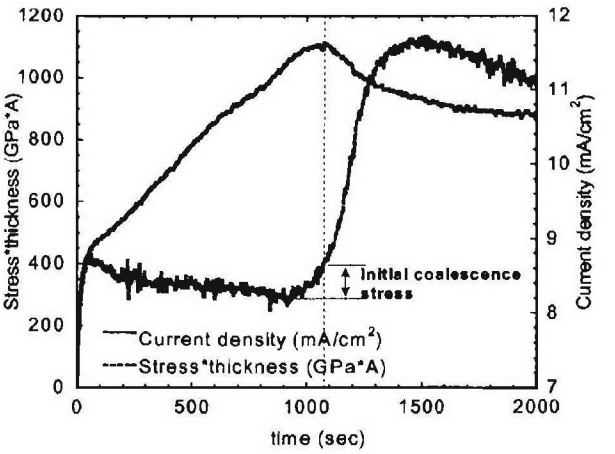


FIG. 2. Stress-thickness vs time plot for a 4.2 μm radius coalescence sample showing a measured change in stress*thickness during coalescence of 96 GPa Å.

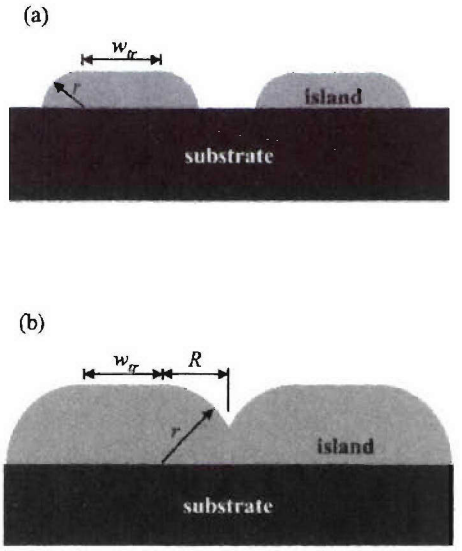


FIG. 3. Idealized cross-sectional geometry used in current evolution model, (a) prior to coalescence, (b) postcoalescence.

Downloaded 18 Apr 2005 to 134.253.26.12. Redistribution subject to AIP license or copyright, see http://jap.aip.org/jap/copyright.jsp

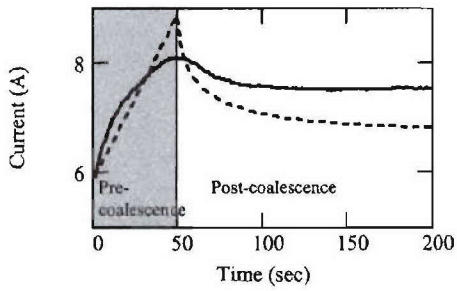


FIG. 4. Overlay of current predicted from geometric model (dashed line) with the current measured during deposition (solid line).

thickness measurement of unpatterned films. After contact, the islands asymptotically approached a planar surface due to the overlapping of the cylinder [Fig. 3(b)] with the total current being equal to

$$I_{\text{tot}} = \left[2r \cdot \arcsin\left(\frac{R}{r}\right) + w_{\text{tr}} \right] \frac{dr}{dt}\frac{dq}{dV} n_{\text{tr}} w_s, \tag{3}$$

where R is the radius of the islands when they coalesced.

Figure 4 is an overlay of the predicted (dashed line) and measured (solid line) currents for a single representative experiment. The only fitting parameter was the position of the maximum current, which was required because the plating rate is larger than the steady-state value during the formation of the diffusion zone. This initial increase in the deposition rate causes the peak to occur earlier than was predicted by a constant deposition rate. In comparing, the modeled and measured current two main features are apparent, rounding of the measured peak current and a higher asymptotic current. Rounding of the peak in the measured current was likely the results of variation in the thickness of the photoresist, variation in the trench width across the samples, and surface roughness, where as the difference between the measured and predicted asymptotic currents is likely the result of the increased surface area due to surface roughness. For the sample used in Fig. 4 the difference between the asymptotic currents was ~12%, where as AFM measurements of the surface indicated the surface area was ~6% larger than a planar film, which is reasonable considering the reduction in the measured surface roughness due to the finite radius of curvature of the AFM tip.

IV. DISCUSSION

Figure 4 demonstrates that the moment of initial coalescence corresponds to the maximum surface area of the film. Therefore, the change in stress-thickness due to the initial coalescence of the islands was determined as the deviation in stress-thickness from the background level to the point of maximum current, as shown in Fig. 2. The remainder of the tensile rise was the result of continual coalescence of the islands during subsequent deposition and planarization. Our data demonstrates that the majority of the tensile stress was actually the result of postcontact coalescence processes. Similar behavior has been observed during chemical vapor deposition of unpatterned diamond films and was attributed to the continual coalescence of faceted grains.[10] Our results

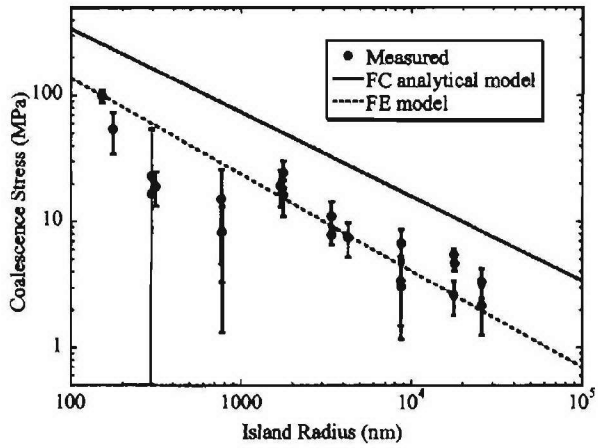


FIG. 5. RMS roughness surface roughness of planar films measured using *ex situ* AFM. The % RMS roughness decreased significantly and stabilized at ~1 micron of thickness.

support the generality of that observation. The detailed understanding of continual coalescence requires significant additional experimentation and analysis, which will be reported in future work.

Figure 5 summarizes our results for the measured stress associated with initial coalescence as a function of the island contact radius. This volume-average stress was obtained by dividing the total change in stress-thickness due to coalescence, as defined above and in Fig. 2, by the mean thickness determined from the plating current.[8,11] On a log–log plot the data exhibits a roughly linear increase in mean stress with decreasing island radius. There is some negative deviation from linear behavior at smaller radii, which was typically associated with depositions where the very poor signal-to-noise ratio created unacceptably large error in the measured stress. Additionally, AFM measurements indicate that the *relative* roughness on surfaces of the half-cylinders was significantly larger for cylinder radii below 1 μm (Fig. 6). Surface roughness decreases the contact area between islands, which reduces the measured stress. Therefore, in the follow-

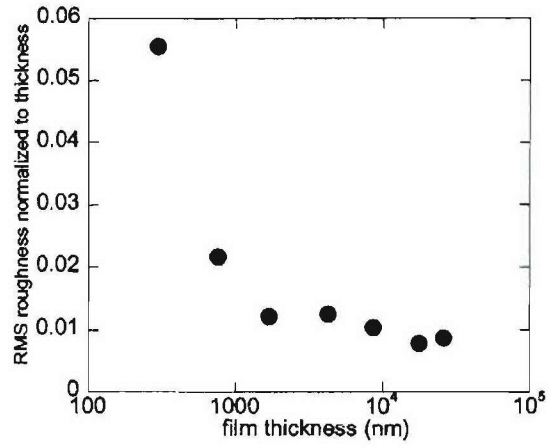


FIG. 6. Plot of measured, FC, and FE calculated island coalescence stress as a function of radius. Both models assume perfect cylinders coalescing and therefore should overestimate the coalescence stress.

Downloaded 18 Apr 2005 to 134.253.26.12. Redistribution subject to AIP license or copyright, see http://jap.aip.org/jap/copyright.jsp

ing analysis we shall only consider samples with radii larger than 1 μm for quantitative comparison with the analytical and FE models.

The Freund and Chason model (FC) (Ref. 7) uses Hertzian contact theory to determine the volume average stress (σ_{avg}) created within the islands as a function of the initial coalescence geometry of the island, e.g., blocks, cylinders, or hemispheres. Our experiments used cylinders with their axes parallel to the substrate, whereas FC used cylinders with their axis of symmetry normal to the substrate. This required a slight modification to the FC model as follows.

According to FC the total contact force per unit length (P) for the general case for cylinder contacting under plane strain along their axis of symmetry is given by

$$P = p(\pi R\bar{E})(\zeta/R)^{2/3}, \tag{4}$$

where p the normalized contact force for cylinders and was determined by FC to equal 0.3, $\bar{E}$ is the plane strain modulus, $\zeta = 2\gamma/\pi\bar{E}$, and γ is the difference between the surface energy and half the grain boundary energy, i.e., the energy of the interface between the coalesced islands. The volume average stress is found by dividing the contact force per unit area by the mean film height for the modified geometry, which for a half cylinder is given by $\pi R/4$. Therefore, the volume average stress for a cylinder with its axis parallel to the substrate is

$$\sigma_{avg} = 1.2\bar{E}\left(\frac{2\gamma}{\pi\bar{E}R}\right)^{2/3} = 0.888\bar{E}^{1/3}\left(\frac{\gamma}{R}\right)^{2/3}. \tag{5}$$

This volume average stress, for half cylinders coalescing with their axis of symmetry parallel to the substrate, is twice that of cylinders with their axis perpendicular to the substrate. However, the power-law dependence of the predicted stress with island radius is the same for both geometries and equal to $-2/3$.

As shown in Fig. 1, the true geometry of the coalescing islands used in these experiments was more complex than the idealized analytical model due to the additional block of material in and above the trench. This had two effects on the volume average stress: First, it decreased the number of boundaries formed per unit area causing an overall decrease in the magnitude of the volume average stress. Second, the material above the trench acted as a "shear-lag zone" that transmitted the stress to the substrate, which acted to increase the volume average stress. 2D FE modeling was used to quantify the effect of the material in and above the trench on the functional dependence of the volume average stress on island radius. The details of using FE to model island coalescence have been presented elsewhere.[12] Two geometries were compared using FE modeling: ideal half cylinders [Fig. 1(a)] and the actual island structure (Fig. 7). We found no significant variation in the functional dependence of stress on island radius (slope of -0.76 to -0.74) as a result of the different geometries and only a slight decrease in the magnitude of the stress with the addition of the trench and photoresist. This result supports the use of a simplified geometry (pure cylinders) in the FC model. In calculating the theoretical stress shown in Fig. 5 no fitting parameters were used

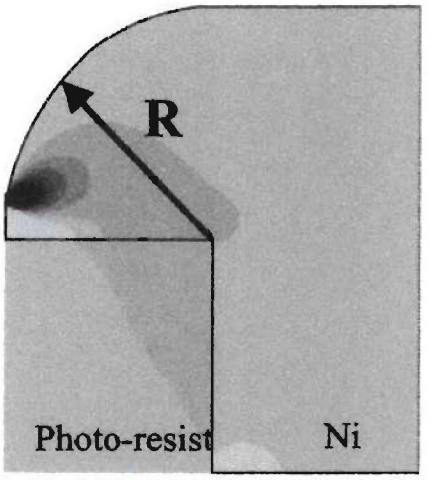


FIG. 7. In-plane stress (σ_{yy}) fields in the full structure as calculated from FE model. Darker color indicates stronger tensile stress.

and both the FE and FC models were calculated assuming $\gamma = 1.85$ J/m^2,[13] and $\bar{E} = 200$ GPa (measured in our films using nanoindentation). It should be noted that both the FE and the analytical models predict the maximum possible stress created during initial coalescence and any error in γ or $\bar{E}$ would result in a shift in the magnitude of both curves and cannot be used to explain the difference between the results. Mechanisms such as incomplete coalescence due to surface roughness or localized yielding will always act to reduce the observed stress. Additionally, the slight difference in the exponents between the FE ($-3/4$) and the Hertzian models ($-2/3$) was likely the result of the lack of an exact solution for the force distribution in contacting cylinders used in the Hertzian model.[7,14]

Figure 5 compares the calculated coalescence stress for the FE (dashed line) and the FC (solid line) models with the experimentally measured initial coalescence stress. In comparing theory vs data, we consider the power-law behavior and the absolute stress magnitudes independently, because the magnitude depends on materials properties whereas the power-law behavior is solely a function of geometry. The observation that the stress magnitudes of the measured data and FE results are similar might appear fortuitous, because there is considerable uncertainty in the surface and grain-boundary energies used in the models and because of potential surface roughness effects. However, since the observed stress was of a similar magnitude to the predicted stress, which is an upper bound, it is reasonable to conclude that any reduction in the initial coalescence area by surface roughness was minimal. More definitively, Fig. 5 shows that the power-law behavior predicted by both the FE and the FC models is within the experimental variation of the measured coalescence stress versus island radius for samples larger than

1 μm (-0.70 ± 0.25). Furthermore, the data lie outside the predicted behavior for both slope and magnitude for the 1D and 3D coalescence geometries in the FC model. *Therefore, the analytical models capture the dominant physical mecha-*

Downloaded 18 Apr 2005 to 134.253.26.12. Redistribution subject to AIP license or copyright, see http://jap.aip.org/jap/copyright.jsp

nisms underlying the generation of tensile stress during island coalescence.

V. CONCLUSION

In conclusion, using lithographically defined nucleation and selective area growth via electrodeposition, we have obtained the first meaningful comparison of experimentally measured stresses due to island coalescence with the stresses predicted by theory. These experiments yielded two main results: First, the measured initial coalescence stress had a functional behavior similar to that of the FC and FE models for coalescence stress. From this we conclude that both models correctly account for all of the dominant physical mechanisms active during the initial coalescence of islands. Second, the majority of the stress associated with island coalescence occurred during planarization of the films, not during the initial contact of the islands. This striking result had not been previously recognized in unpatterned metal films due to the inability to differentiate the stress created at the initial contact from that created during planarization.

ACKNOWLEDGMENTS

The authors would like to acknowledge fruitful discussions with Ben Freund, Thomas Buchheit, Brian Sheldon, Eric Chason, and Harley Johnson. This work was supported by the DOE office of Basic Energy Science and by the ARO/MURI in Deep Subwavelength Optical Nanolithography at the University of New Mexico. Sandia is a multiprogram laboratory operated by Sandia Corporation, a Lockheed Martin Company, for the United States Department of Energy's National Nuclear Security Administration under Contract No. DE-AC04-94AL85000.

[1] R. Koch, J. Phys.. Condens. Matter **6**, 9519 (1994).
[2] J. A. Floro, S. J. Hearne, J. A. Hunter, P. Kotula, E. Chason, S. C. Seel, and C. V. Thompson, J. Appl. Phys. **89**, 4886 (2001).
[3] J. A. Floro, E. Chason, and S. R. Lee, Mater. Res. Soc. Symp. Proc. **405**, (1996) (381).
[4] R. Abermann and P. Martinz, Thin Solid Films **115**, 185 (1984).
[5] R. W. Hoffman, Thin Solid Films **34**, 185 (1976).
[6] W. D. Nix and B. M. Clemens, J. Mater. Res. **14**, 3467 (1999).
[7] L. B. Freund and E. Chason, J. Appl. Phys. **89**, 4866 (2001).
[8] Allison Suh, Ning Yu, Ki Myung Lee, Andreas A. Polycarpou, and H. T. Johnson, J. Appl. Phys. **96**, 1 (2004).
[9] L. B. Freund, J. A. Floro, and E. Chason, Appl. Phys. Lett. **74**, 1987 (1999).
[10] B. W. Sheldon, K. H. A. Lau, and A. Rajamani, J. Appl. Phys. **90**, 5097 (2001).
[11] L. B. Freund and S. Suresh, *Thin Film Materials* (Cambridge University Press, Cambridge, 2003), Vol. 1, p. 206.
[12] S. C. Seel, C. V. C. V. Thompson, S. J. Hearne, and J. A. Floro, J. Appl. Phys. **88**, 7079 (2000).
[13] J. P. Hirth and J. Lothe, *Theory of Dislocations*, 2nd ed. (Wiley, New York, 1975), p. 839.
[14] K. L. Johnson, *Contact Mechanics*, 1st ed. (Cambridge University Press, Cambridge, 1985), Chap. 4.2, p. 99.

Downloaded 18 Apr 2005 to 134.253.26.12. Redistribution subject to AIP license or copyright, see http://jap.aip.org/jap/copyright.jsp

Radiation from a dipole embedded in a multilayer slab

S. R. J. Brueck,*,† V. A. Smagley,† and P. G. Eliseev
Center for High Technology Materials, University of New Mexico, Albuquerque, New Mexico 87106, USA
(Received 21 March 2003; published 12 September 2003)

An analytical solution for the radiation emitted from a dipole embedded in an arbitrary, planar dielectric film stack is presented. The calculation uses a rigorous Hertz-vector formalism to treat the electromagnetic boundary conditions. The radiation fields are then evaluated in a far-field approximation to get the radiated fields far from the dipole. Both two-dimensional (2D) emission into bound modes of the dielectric stack and three-dimensional (3D) emission into radiation fields above and below the stack are evaluated. These solutions are explored for two simple cases: a InGaAs slab symmetrically clad with up to four high-contrast (Al_2O_3/GaAs) Bragg mirror pairs and semi-infinite air spaces, and a similar asymmetric structure with a GaAs substrate on one side. The symmetric structure supports both 2D bound and 3D radiation fields. The asymmetric structure only supports 3D radiation fields since there are no strictly bound modes, but "leaky" modes appear that are very similar to the bound modes in the symmetric structure except that the radiated power ultimately is transmitted into the substrate in a very highly directional beam. This calculation is applicable to a wide range of solid-state photonic devices, including vertical-cavity and edge-emitting lasers, spontaneous light-emitting diodes, and photodetectors.

DOI: 10.1103/PhysRevE.68.036608 PACS number(s): 41.20.−q, 42.25.−p, 42.55.−f, 42.82.−m

I. INTRODUCTION

The coupling of an electric dipole with electromagnetic fields in solids is fundamental to solid-state light emitting and detecting devices (LEDs, lasers, displays, photodetectors, etc.). In a uniform infinite medium the dipole radiation fields are very well known. The study of these radiation fields in the presence of metallic and dielectric interfaces has been a recurring topic in electromagnetism. Sommerfeld [1,2] made seminal contributions to the solution that provide the basis of the work presented here. He was concerned with issues of long-wavelength radio wave propagation over the surface of the earth and addressed the single interface problem of a dipole above a lossy dielectric. As is very well known [3,4], the addition of a second interface, e.g., a dipole embedded within a dielectric slab, adds significant complexity to the problem, since the radiation is now distributed between three-dimensional (3D) radiation out the sides of the slab and the two-dimensional (2D) bound modes supported by the slab. With the development of multilayer structures with very high, and precisely tailorable, reflectivities, such as vertical-cavity lasers, resonant cavity LEDs, and photodetectors, there is a need for a more detailed understanding of the distribution of the radiation between these components and the corresponding angular and thickness/wavelength dependencies. Both approximate analytic treatments [5,6] and numerical solutions [7] have appeared in the literature. Recently, two equivalent detailed analytical treatments for the simple slab case have been reported [4,8]. Both of these treatments presented fully analytic results for the radiation into both the 2D bound modes and the 3D radiation modes and investigated in detail the dependence on dielectric contrast and slab thickness.

The purpose of this paper is to extend these results [4] to arbitrary multilayer dielectric structures and to investigate in particular the impact of high-reflectivity Bragg mirrors on the dipole radiation. The analysis is extended to asymmetric cases, including mode-free cases that support "leaky" modes that are not bound in the strict sense, but rather build up significant intensity within the multilayer structure and ultimately radiate their power into 3D radiation within the substrate.

Section II presents the Hertz vector formulation and introduces a significant algebraic simplification by introducing both electric and magnetic Hertz vectors. Section III presents the closed form analytic results for arbitrary multilayer structures. Detailed investigation of the results for a symmetric structure with high-reflectivity Bragg reflectors is presented in Sec. IV A. A related asymmetric structure with a high-index substrate is analyzed in Sec. IV B. Finally, conclusions are presented in Sec. V.

II. HERTZ VECTOR FORMULATION

A. Geometry of the problem

The geometry of the problem is shown in Fig. 1. A dipole is embedded in an arbitrary film stack taken as infinite in the (x,y) directions. The z direction is perpendicular to the films. The dipole is oriented at an angle θ_d from the z direction in the (x,z) plane. The layer stacks above and below the dipole have arbitrary numbers of layers with arbitrary relative dielectric constants ($\kappa_i = n_i^2$) and thicknesses (L_i). The total physical thicknesses of the top and bottom cladding layers from the position of the dipole to the edge of the outermost layer are $L_{t\text{-}tot}$ and $L_{b\text{-}tot}$. For the sample calculations presented below, the inner cladding layers (shaded)

*Also at Department of Electrical and Computer Engineering, University of New Mexico, Albuquerque, New Mexico 87131, USA. Email address: brueck@chtm.unm.edu
†Also at Department of Physics and Astronomy, University of New Mexico, Albuquerque, New Mexico 87131, USA.

 ©2003 The American Physical Society

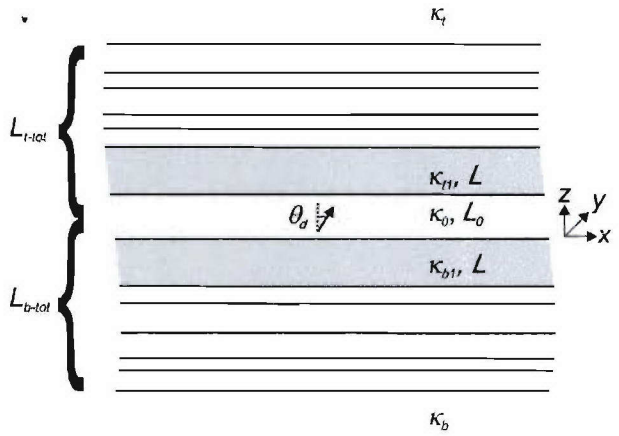


FIG. 1. Geometry of the problem. A radiating dipole oriented at an angle θ_d in the (x,z) plane is embedded in the center of a infinite slab of material of relative dielectric constant κ_0 and thickness L_0. The slab is bound with arbitrary film stacks ending in top and bottom semi-infinite media of relative dielectric constant κ_t and κ_b. For the example calculations, the shaded inner cladding thicknesses L are identical and variable. The total physical thicknesses of the upper and lower claddings from the position of the dipole to the edge of the semi-infinite media are indicated by $L_{t\text{-tot}}$ and $L_{b\text{-tot}}$.

have identical dielectric constants, $\kappa_{t1}=\kappa_{b1}=\kappa=n^2$, and an equal thickness, $L_{t1}=L_{b1}=L$ that is varied in the calculation. The thickness of the layer containing the dipole is denoted as L_0.

B. Hertz vector formalism

In our previous paper [4] we used the Hertz vector formalism introduced by Sommerfeld [1] to evaluate the radiation from a simple dielectric slab structure. Lukosz [9,10] has developed an alternate formulation of the Hertz vector source terms that has the significant advantage that the boundary conditions are uncoupled for the TE and TM radiation from a horizontal dipole. This dramatically simplifies the algebra of the calculation; the final results are identical. Lukosz's formulation is briefly described here and is followed in the evaluations of the radiated power.

Lukosz [9,10] has shown that the electromagnetic field for any orientation of the dipole can be represented by two scalar functions, $\phi(\vec{x})$ and $\psi(\vec{x})$, which are the z components (perpendicular to the layers) of an electric and a magnetic Hertz vector, respectively,

$$\vec{\Pi}^{(E)}(\vec{x})=(0,0,\phi(\vec{x})),$$

$$\vec{\Pi}^{(H)}(\vec{x})=(0,0,\psi(\vec{x})). \tag{1}$$

Both scalar functions satisfy the homogeneous Hemholtz equation in source-free regions, viz.,

$$(\nabla^2-\kappa_i\varepsilon_0k_0^2)\phi(\vec{x})=(\nabla^2-\kappa_i\varepsilon_0k_0^2)\psi(\vec{x})=0, \tag{2}$$

where ε_0 is the free-space permittivity, $\kappa_i=n_i^2$ is the relative dielectric permittivity of the medium, and $k_0=\omega/c$ is the magnitude of the free-space photon wave vector. The fields are given by

$$\vec{E}(\vec{x})=i\omega\vec{\nabla}\times\vec{\Pi}^{(H)}(\vec{x})+(\kappa\varepsilon_0)^{-1}\vec{\nabla}\times\vec{\nabla}\times\vec{\Pi}^{(E)}(\vec{x}),$$

$$\vec{H}(\vec{x})=-i\omega\vec{\nabla}\times\vec{\Pi}^{(E)}(\vec{x})+(\mu_0)^{-1}\vec{\nabla}\times\vec{\nabla}\times\vec{\Pi}^{(H)}(\vec{x}). \tag{3}$$

where ε_0 and μ_0 are the free-space values of the electric and magnetic permeabilities, respectively.

From Eqs. (1) and (3) it is straightforward to show that $\phi(\vec{x})$ corresponds to a TM wave and $\psi(\vec{x})$ describes a TE wave; since these are orthogonal there is no coupling between them. In the Sommerfeld basis [1], there is only an electric Hertz vector with components both in the z direction and in the x direction; the boundary conditions at interfaces are coupled which algebraically complicates the general solution for an arbitrary film stack.

C. Expansion of the dipole field into TE and TM plane waves

To begin the calculation, it is necessary to express the field of a dipole, located at the origin in an infinite medium, in a superposition of TE and TM plane waves. Then the boundary value problem for each independent plane wave can be directly solved by standard thin-film electromagnetic methods; finally the results are transformed back to real space using the techniques developed by Sommerfeld [1,2,11].

The infinite-medium real-space electric-Hertz vector corresponding to a dipole is simply

$$\vec{\pi}(\vec{x})=p_o\frac{e^{in_ik_0r}}{4\pi\varepsilon_0\kappa_ir}(\sin\theta_d\hat{e}_x+\cos\theta_d\hat{e}_z), \tag{4}$$

where p_o is the dipole moment, $(\hat{e}_x,\hat{e}_y)$ are unit vectors in the corresponding directions. The total radiated power for this dipole in an infinite medium is given by the well-known result [12]

$$P_{\inf}=\frac{k_o^4\,\mathrm{Re}(n_i)|p_o|^2}{12\pi\eta_0\varepsilon_0^2}, \tag{5}$$

where $\eta_0=\sqrt{\mu_0/\varepsilon_0}$. In the following, radiated powers are shown normalized to this value. The corresponding Fourier transform of the infinite-medium Hertz vector is

$$\vec{\Pi}_\infty^{(E)}(\vec{K})=\frac{p_o}{\varepsilon_0\kappa_ik_0^2}\frac{1}{K^2-\kappa_i}(\sin\theta_d\hat{e}_x+\cos\theta_d\hat{e}_z)$$
$$\equiv\Phi(K)(\sin\theta_d\hat{e}_x+\cos\theta_d\hat{e}_z), \tag{6}$$

where k_0K is the transform coordinate. This expression can be put in a more suitable form for the planar geometry of the problem by carrying out the inverse transform in the z direction and expressing the remaining integrals in cylindrical coordinates,

$$\Phi(\rho,z)=\frac{p_o}{\kappa_i}\int_0^\infty \frac{k_0}{\gamma_i}e^{-\gamma_i|\tilde{z}|}J_0(\lambda\tilde{\rho})\lambda d\lambda$$

$$=\frac{p_o}{2\kappa_i}\int_{-\infty}^{\infty}\frac{k_0}{\gamma_i}e^{-\gamma_i|\tilde{z}|}H_0^1(\lambda\tilde{\rho})\lambda d\lambda, \qquad (7)$$

where $k_0\lambda$ is the radial transform coordinate [$\lambda^2=\xi^2+\eta^2$ with $k_0\xi$ ($k_0\eta$) the $x(y)$-directed transform coordinate], $\tilde{\rho}=k_0\rho$ and $\tilde{z}=k_0z$ are the dimensionless radial and vertical spatial coordinates, and

$$\gamma_i=\sqrt{\lambda^2-\kappa_i}\xrightarrow[\lambda\to 0]{}-in_i, \qquad (8)$$

where the sign of the square root is chosen to ensure $\mathrm{Re}(\gamma_i)>0$ for convergence of Eq. (7). J_0 is the zeroth-order Bessel function and H_0^1 is the Hankel function of the first kind of zeroth order. The second form of this expression will be useful for evaluation of the complex integrations since the integration extends along the entire λ axis.

The scalars ϕ and ψ for the unbounded medium are found in terms of Φ by equality of the z components of the electric and magnetic fields from Eqs. (3) and (6), giving

$$\phi(\xi,\eta;z)=\Phi(\lambda;z)\left(\cos\theta_d\mp i\frac{\xi\gamma_i}{\lambda^2}\sin\theta_d\right) \qquad (9a)$$

and

$$\psi(\xi,\eta;z)=\Phi(\lambda;z)\left(\eta_0\frac{\eta}{\lambda^2}\sin\theta_d\right), \qquad (9b)$$

where the $(-)$ sign in Eq. (9a) is appropriate in the upper half plane ($z>0$) and the $(+)$ sign in the lower half plane ($z<0$). For a vertical dipole ($\sin\theta_d=0$) there are only TM waves (*only a single* scalar function $\phi(\xi,\eta;z)$ is required); for a horizontal dipole ($\sin\theta_d=1$) there are both TM and TE waves [*both* scalar functions $\phi(\xi,\eta;z)$ and $\psi(\xi,\eta;z)$ are required]. The source terms for a horizontal dipole ($\sin\theta_d=1$) depend on the transverse transform coordinates (ξ,η) which results in a dependence of the radiated fields on the polar angle φ where $\varphi=0$ is the radial direction parallel to the dipole.

III. EVALUATIONS OF THE RADIATED FIELDS AND POWER

A. Boundary value problem and evaluation of the Hertz potential; vertical dipole ($\cos\theta_d=1$)

The boundary conditions for ϕ at an interface between media 1 and 2 are [9]

$$\phi_1=\phi_2,$$

$$\frac{1}{\kappa_1}\frac{\partial\phi_1}{\partial z}=\frac{1}{\kappa_2}\frac{\partial\phi_2}{\partial z}. \qquad (10)$$

It is a standard multiple-interface thin-film matrix-analysis problem to solve for the Hertz potential everywhere. The result is

$$\phi_0^V=\frac{p_o}{2\kappa_1}\int_{-\infty}^{\infty}\frac{k_0}{\gamma_0}H_0^1(\lambda\tilde{\rho})\lambda d\lambda$$
$$\times\left[\frac{e^{-\gamma_0\tilde{L}_0}R_b^p(1+e^{-\gamma_0\tilde{L}_0}R_t^p)}{1-e^{-2\gamma_0\tilde{L}_0}R_b^pR_t^p}e^{\gamma_0\tilde{z}}\right.$$
$$\left.+\frac{e^{-\gamma_0\tilde{L}_0}R_t^p(1+e^{-\gamma_0\tilde{L}_0}R_b^p)}{1-e^{-2\gamma_0\tilde{L}_0}R_b^pR_t^p}e^{\gamma_0\tilde{z}}+e^{-\gamma_0|\tilde{z}|}\right] \qquad (11)$$

for the slab region (subscript 0), and

$$\phi_t^V=\frac{p_o}{2\kappa_t}\int_{-\infty}^{\infty}\frac{k_0}{\gamma_t}H_0^1(\lambda\tilde{\rho})\lambda d\lambda$$
$$\times\left[\frac{T_t^pe^{-\gamma_0\tilde{L}_0/2}(1+e^{-\gamma_0\tilde{L}_0}R_b^p)}{1-e^{-2\gamma_0\tilde{L}_0}R_b^pR_t^p}\right]e^{-\gamma_t(\tilde{z}-\tilde{L}_{t-tot})},$$

$$\phi_b^V=\frac{p_o}{2\kappa_b}\int_{-\infty}^{\infty}\frac{k_0}{\gamma_b}H_0^1(\lambda\tilde{\rho})\lambda d\lambda$$
$$\times\left[\frac{T_b^pe^{-\gamma_0\tilde{L}_0/2}(1+e^{-\gamma_0\tilde{L}_0}R_t^p)}{1-e^{-2\gamma_0\tilde{L}_0}R_b^pR_t^p}\right]e^{+\gamma_b(\tilde{z}+\tilde{L}_{b-tot})} \qquad (12)$$

for the top [above the slab and top film stack (subscript t)] and bottom [below the slab and bottom film stack (subscript b)] semi-infinite outer cladding regions. In these expressions, $k_0^{-1}\tilde{L}_{t-tot}$ and $k_0^{-1}\tilde{L}_{b-tot}$ are the total physical thicknesses of the top and bottom cladding layers from the position of the dipole to the edge of the outer cladding regions as shown in Fig. 1. The Hertz potential within the film stacks is readily evaluated from these results. Here the R's and T's refer to the magnetic field reflectivity looking from inside the slab from the multilayer top (bottom) stacks for a TM wave propagating upwards (downwards) in the slab $R_t^p(R_b^p)$ and the T's are the corresponding transmissions through the entire film stacks. In the limit of a single dielectric interface at the top of the slab these reduce to the familiar results for a TM-wave incident from the slab towards the top dielectric (and similar expressions for the bottom interface)

$$R_t^p=\frac{\kappa_t\gamma_0-\kappa_0\gamma_t}{\kappa_t\gamma_0+\kappa_0\gamma_t},$$

$$T_t^p=\frac{\kappa_t}{\kappa_0}(1-R_t^p)=\frac{2\kappa_t\gamma_t}{\kappa_t\gamma_0+\kappa_0\gamma_t}. \qquad (13)$$

Comparing this result with Eq. (10) of Ref. [1] for a simple dielectric slab, the only changes are (1) the substitution of the multilayer refection/transmission coefficients for their single interface values; (2) the separate identification of top and bottom reflection and transmission coefficients re-

quired for this generalized asymmetric calculation; and (3) setting the dipole position to the center of the slab ($a=0$ from Ref. [1]) since any shift of the dipole position can be accommodated by adding additional films (with the same dielectric constant). The bracketed terms have simple physical interpretations. There are two contributions to the fields in the top region, one direct transmission from the upward directed plane waves of the dipole and a second reflected from the bottom slab interface. The resonant denominator accounts for the multiple reflections within the slab. The zeros of this denominator correspond to poles of the integrand and, thus, the radiation into 2D bound waveguide modes. There are branch cuts in the λ plane as a result of the multivalued γ_i's. Integration around these branch cuts gives the 3D free-space radiation. The inverse transform will be discussed following the presentation of the boundary value solutions for the horizontal dipole in the next section.

B. Boundary value problem and evaluation of the Hertz potential; horizontal dipole ($\cos\theta_d=0$)

For a horizontal dipole, both ϕ and ψ must be evaluated. Since the boundary conditions are uncoupled, the solution proceeds straightforwardly using the source terms in Eq. (9) for $\theta_d=\pi/2$. The boundary conditions are [9]

$$\phi_1=\phi_2, \quad \psi_1=\psi_2,$$
$$\frac{1}{\kappa_1}\frac{\partial\phi_1}{\partial z}=\frac{1}{\kappa_2}\frac{\partial\phi_2}{\partial z}, \quad \frac{\partial\psi_1}{\partial z}=\frac{\partial\psi_2}{\partial z}. \tag{14}$$

This decoupling of the boundary conditions for the two scalar functions is a major algebraic advantage of the Hertz vector representation introduced by Lukosz [9]. The solutions again are obtained by straightforward thin-film analysis based on the boundary conditions Eq. (14) and the source terms Eq. (9),

$$\psi_0^H=\frac{p_0}{2}\eta_0\int_{-\infty}^{\infty}\frac{1}{\gamma_0}\sin\varphi H_0^1(\lambda\tilde{\rho})d\lambda \times\left[\frac{e^{-\gamma_0\tilde{L}_0}R_b^s(1+e^{-\gamma_0\tilde{L}_0}R_t^s)}{1-e^{-2\gamma_0\tilde{L}_0}R_b^sR_t^s}e^{-\gamma_0\tilde{z}} + \frac{e^{-\gamma_0\tilde{L}_0}R_t^s(1+e^{-\gamma_0\tilde{L}_0}R_b^s)}{1-e^{-2\gamma_0\tilde{L}_0}R_b^sR_t^s}e^{\gamma_0\tilde{z}}+e^{-\gamma_0|\tilde{z}|}\right],$$

$$\phi_0^H=\frac{ip_0}{2\kappa_0}\int_{-\infty}^{\infty}k_0\cos\varphi H_0^1(\lambda\tilde{\rho})d\lambda \times\left[\frac{e^{-\gamma_0\tilde{L}_0}R_b^p(1-e^{-\gamma_0\tilde{L}_0}R_t^p)}{1-e^{-2\gamma_0\tilde{L}_0}R_b^pR_t^p}e^{\gamma_0\tilde{z}} - \frac{e^{\gamma_0\tilde{L}_0}R_t^p(1-e^{-\gamma_0\tilde{L}_0}R_b^p)}{1-e^{2\gamma_0\tilde{L}_0}R_b^pR_t^p}e^{\gamma_0\tilde{z}(\mp)}e^{-\gamma_0|\tilde{z}|}\right] \tag{15}$$

for the slab, and

$$\psi_t^H=\frac{p_0}{2}\eta_0\int_{-\infty}^{\infty}\frac{1}{\gamma_t}\sin\varphi H_0^1(\lambda\tilde{\rho})d\lambda \times\frac{T_t^se^{-\gamma_0\tilde{L}_0/2}(1+e^{-\gamma_0\tilde{L}_0}R_b^s)}{1-e^{-2\gamma_0\tilde{L}_0}R_b^sR_t^s}e^{-\gamma_t(\tilde{z}-\tilde{L}_{t-tot})},$$

$$\phi_t^H=\frac{-ip_0}{2\kappa_t}\int_{-\infty}^{\infty}k_0\cos\varphi H_0^1(\lambda\tilde{\rho})d\lambda \times\frac{T_t^pe^{-\gamma_0\tilde{L}_0/2}(1-e^{-\gamma_0\tilde{L}_0}R_b^p)}{1-e^{-2\gamma_0\tilde{L}_0}R_b^pR_t^p}e^{-\gamma_t(\tilde{z}-\tilde{L}_{t-tot})}, \tag{16a}$$

$$\psi_b^H=\frac{p_0}{2}\eta_0\int_{-\infty}^{\infty}\frac{k_0}{\gamma_b}\sin\varphi H_0^1(\lambda\tilde{\rho})d\lambda \times\frac{T_b^se^{-\gamma_0\tilde{L}_0/2}(1+e^{-\gamma_0\tilde{L}_0}R_t^s)}{1-e^{-2\gamma_0\tilde{L}_0}R_b^sR_t^s}e^{+\gamma_b(\tilde{z}+\tilde{L}_{b-tot})},$$

$$\phi_b^H=\frac{ip_0}{2\kappa_b}\int_{-\infty}^{\infty}k_0\cos\varphi H_0^1(\lambda\tilde{\rho})d\lambda \times\frac{T_b^pe^{-\gamma_0\tilde{L}_0/2}(1-e^{-\gamma_0\tilde{L}_0}R_t^p)}{1-e^{-2\gamma_0\tilde{L}_0}R_b^pR_t^p}e^{+\gamma_b(\tilde{z}+\tilde{L}_{b-tot})} \tag{16b}$$

for the top and bottom semi-infinite outer cladding regions. In these expressions, $R_{t,b}^s, T_{t,b}^s$ are the electric field reflectivities for TE polarized waves incident from the slab on the respective interfaces. In the limit of a simple dielectric interface these reduce for the top interface to

$$R_t^s=\frac{\gamma_0-\gamma_t}{\gamma_0+\gamma_t}, \quad T_t^s=1-R_t^s=\frac{2\gamma_t}{\gamma_0+\gamma_t}. \tag{17}$$

In Eq. (15), the minus sign in the parentheses is appropriate for $\tilde{z}>0$ and the plus sign for $\tilde{z}<0$. As mentioned above, the polar angle φ, defined relative to the orientation of the dipole in the slab, arises from the presence of the transverse transform coordinates (ξ,η) in the source terms for the horizontal dipole.

The physical interpretation of these equations is similar to that for the vertical dipole. Now the coupling is to both TE and TM radiation and bound modes. The zeros of the denominators correspond to the bound modes (TM for $1-e^{-2\gamma_0\tilde{L}_0}R_b^pR_t^p=0$; TE for $1-e^{-2\gamma_0\tilde{L}_0}R_b^sR_t^s=0$). In each numerator there is a term that corresponds to the radiation directly incident from the dipole and a second term from the radiation reflected from the opposite interface. For the potential within the slab there are upward and downward reflected

waves and the source terms. For the potential in the half-spaces the numerators correspond to transmission from the source at the center of the slab. The denominators account for the multiple reflections, and include all near field terms; no approximations to the full electromagnetic calculation have been made to this point. These approximations will be made in the branch cut integrals, which are evaluated by the method of steepest descents that is only valid far (many wavelengths) from the source point, and in the evaluation of the contributions from the poles using the asymptotic limits of the Hankel function, again valid many wavelengths from the source point. There are branch cuts corresponding to each of the thin film layers. In the half-spaces above and below the structure, only the integral around the branch cut corresponding to that specific medium contributes to the radiation fields; the other branch cuts contribute only to the near fields and thus are excluded from the subsequent analysis.

C. Evaluation of the inverse transform

The apparatus of a complex analysis can now be applied to the remaining integrals. As noted above, there are contributions due to integration around the branch cuts (corresponding to 3D radiation into the semi-infinite half-spaces above and below the structure) and due to poles of the denominators (2D bound modes). The manipulations have been presented for a single interface in great detail in Ref. [11] for a single interface and in Ref. [4] for the simple slab case. Only the final results will be presented here.

1. Vertical dipole

2D bound modes. For the vertical dipole, the Hertz potential within the slab is evaluated using the asymptotic limit of the Hankel function $[H_0^1(z)\rightarrow -ie^{iz}\sqrt{2/\pi z}]$ and taking the residues at the zeros of the denominator,

$$\phi_0^{2D}=p_0k_0\sum_l \sqrt{\frac{8\pi}{k_l^p\tilde{\rho}}}e^{ik_l^p\tilde{\rho}}\frac{k_l^p}{\kappa_0\gamma_{0,l}^p\delta D_l^p} \times[(1+R_{sym}^p e^{-\gamma_{0,l}^p\tilde{L}_0})\cosh(\gamma_{0,l}^p\tilde{z}) + R_{asym}^p e^{-\gamma_{0,l}^p\tilde{L}_0}\sinh(\gamma_{0,l}^p\tilde{z})], \tag{18}$$

where the denominator is expanded around the roots (k_l^p, where the subscript is the mode index) of the TM (p superscript) modal dispersion relation, viz.,

$$D_l^p=1-e^{-2\gamma_1\tilde{L}_0}R_b^pR_t^p\approx(\lambda-k_l^p)\left.\frac{\partial D_p}{\partial k}\right|_{k_l^p}\equiv(\lambda-k_l^p)\delta D_l^p \tag{19}$$

and

$$R_{sym}^p\equiv\frac{R_t^p+R_b^p}{2},\quad R_{asym}^p\equiv\frac{R_t^p-R_b^p}{2}. \tag{20}$$

The superscript on the γ's takes note of the fact that they are evaluated at the roots of the TM dispersion relation and the subscripts on the γ's refer to the layer index (j) and the mode index (l) $[\gamma_{j,l}^p\equiv\gamma_j(\lambda)|_{\lambda=k_l^p}]$. The corresponding indices on the reflection coefficients are suppressed for convenience.

From this result, the next step is to evaluate the fields and to integrate across the mode profile to get the radiated power with the result for the central slab containing the dipole,

$$\hat{P}_{V,TM}^{2D}=\frac{3\pi k_0}{\mathrm{Re}(\kappa_1)\sqrt{\varepsilon_0}}\sum_l\frac{|k_l^{p\prime}|^4}{|\delta D_l^p|^2} \times\left[\begin{array}{l}[|c_{0,l}|^2+|d_{0,l}|^2]\dfrac{\sinh(\gamma_{0,l}^{p\prime}\tilde{L}_0/2)}{\gamma_{0,l}^{p\prime}} \\ +[c_{0,l}d_{0,l}^*+c_{0,l}^*d_{0,l}]\dfrac{\sin(\gamma_{0,l}^{p\prime\prime}\tilde{L}_0/2)}{\gamma_{0,l}^{p\prime\prime}}\end{array}\right], \tag{21}$$

where the summation is over all modes (l), $\gamma_{0,l}^p=\gamma_{0,l}^{p\prime}+i\gamma_{0,l}^{p\prime\prime}$, and the coefficients $c_{0,l}$ and $d_{0,l}$ are the complex amplitudes of the upward and downward directed fields in each layer at the center of the slab. From Eq. (18)

$$\begin{aligned}c_{0,l}&=\frac{1}{2}(1+R_{sym}^p e^{-\gamma_{0,l}\tilde{L}_0}+R_{asym}^p e^{-\gamma_{0,l}\tilde{L}_0})\\&=\frac{1}{2}(1+R_t^p e^{-\gamma_{0,l}^p\tilde{L}_0}),\\ d_{0,l}&=\frac{1}{2}(1+R_{sym}^p e^{-\gamma_{0,l}\tilde{L}_0}-R_{asym}^p e^{-\gamma_{0,l}\tilde{L}_0})\\&=\frac{1}{2}(1+R_b^p e^{-\gamma_{0,l}^p\tilde{L}_0}).\end{aligned} \tag{22}$$

Similar expressions need to be evaluated over the entire film stack, including the top and bottom semi-infinite regions, and summed to get the total 2D radiated power.

3D radiated energy. The calculation proceeds by substituting the integral expression for the Hankel function

$$H_0^1(z)=\frac{4}{\pi}e^{iz}\int_0^\infty(4iz-y^2)^{-1/2}e^{-y^2/2}dy\approx e^{iz}\sqrt{\frac{2}{i\pi z}}, \tag{23}$$

where the last approximation is valid in the radiation zone, many wavelengths from the dipole. Then the Hertz potential in the semi-infinite cladding regions can be evaluated by integrating around the branch cut by the method of steepest descents with the result for the top half-space:

$$\phi_t=\frac{p_0k_0e^{in_t\tilde{R}}}{\tilde{R}}\frac{1-R_t^p}{\kappa_0}\frac{[1+e^{in_0\tilde{L}_0\cos(\vartheta)}R_b^p(\theta)]}{1-e^{2in_0\tilde{L}_0\cos(\vartheta)}R_t^p(\theta)R_b^p(\theta)} \times e^{i(n_0\cos\vartheta-n_t\cos\theta)\tilde{L}_0/2}, \tag{24}$$

where $\tilde{R}$ is the dimensionless radial distance coordinate, ϑ is the propagation angle inside the slab for an external angle of θ $[\cos^2\vartheta\equiv 1-(\kappa_t/\kappa_1)\sin^2\theta]$ and the reflection coefficients are evaluated at the external angle θ.

For the radiated power, normalized to the power radiated by the dipole in an infinite medium, the final result is

$$\hat{P}_{TM}^{V}=\frac{3}{4}\left|\frac{\kappa_l}{\kappa_0}\right|^{5/2}\int_0^{\pi/2}\left|\frac{[1-R_t^p(\theta)][1+e^{in_0\tilde{L}_0\cos\vartheta}R_b^p(\theta)]e^{i(n_0\cos\vartheta\ \ n_t\cos\theta)\tilde{L}_0/2}}{1-e^{2in_0\tilde{L}_0\cos\vartheta}R_t^p(\theta)R_b^p(\theta)}\right|^2\sin^3\theta d\theta \tag{25}$$

with a similar expression for the power radiated into the bottom half-space with the obvious interchange ($t\Leftrightarrow b$). As expected, this result is identical to that for the simple slab [4] with the substitution of the film-stack reflectivities for those of the simple dielectric interface and the generalization to an asymmetric cladding structure.

2. Horizontal dipole

A horizontal dipole couples to both TE and TM radiation. The calculations are very similar to those presented above and only the results are given here.

2D bound modes. For TE coupling

$$\psi_0^{2D,H}=\sin\varphi p_0\eta_0\sum_l\sqrt{\frac{8\pi}{k_l^s\tilde{\rho}}}e^{ik_l^s\tilde{\rho}}\frac{1}{\delta D_l^s}\times[(1+R_{sym}^s e^{-\gamma_{0,l}^s\tilde{L}_0})\cosh(\gamma_{0,l}^s\tilde{z})+R_{asym}^s e^{-\gamma_{0,l}^s\tilde{L}_0}\sinh(\gamma_{0,l}^s\tilde{z})], \tag{26}$$

$$\hat{P}_{TE}^{2D,H}=\frac{3\pi}{4\,\mathrm{Re}(n_0)}\sum_l\left|\frac{k_l^s}{\delta D_l^s}\right|^2\times\left[\begin{array}{l}[|c_{0,l}|^2+|d_{0,l}|^2]\dfrac{\sinh(\gamma_{0,l}^{s\prime}\tilde{L}_0/2)}{\gamma_{0,l}^{p\prime}}\\ +[c_{0,l}d_{j,l}^*+c_{0,l}^*d_{j,l}]\dfrac{\sin(\gamma_{0,l}^{sn}\tilde{L}_0/2)}{\gamma_{0,l}^{p\prime\prime}}\end{array}\right],$$

$$c_{0,l}=\frac{1}{2}(1+R_t^s e^{-\gamma_{0,j}^s\tilde{L}_0}),$$

$$d_{0,j}=\frac{1}{2}(1+R_b^s e^{-\gamma_{0,j}^s\tilde{L}_0}). \tag{27}$$

For TM coupling

$$\phi_0^{2D,H}=\cos\varphi p_0k_0\sum_l\sqrt{\frac{8\pi}{k_l^p\tilde{\rho}}}e^{ik_l^p\tilde{\rho}}\frac{1}{\delta D_l^p}\times[(1-R_{sym}^p e^{\ \gamma_{0,l}^p\tilde{L}_0})\sinh(\gamma_{0,l}^p\tilde{z})-R_{asym}^p e^{\ \gamma_{0,l}^p\tilde{L}_0}\cosh(\gamma_{0,l}^p\tilde{z})] \tag{28}$$

$$\hat{P}_{TM}^{2D,H}=\frac{3\pi}{4\,\mathrm{Re}(\kappa_0^{3/2})}\sum_l\left|\frac{k_l^p}{\delta D_l^s}\right|^2\times\left[\begin{array}{l}[|c_{0,l}|^2+|d_{0,l}|^2]\dfrac{\sinh(\gamma_{0,l}^{p\prime}\tilde{L}_0/2)}{\gamma_{0,l}^{p\prime}}\\ +[c_{0,l}d_{j,l}^*+c_{0,l}^*d_{j,l}]\dfrac{\sin(\gamma_{0,l}^{p\prime\prime}\tilde{L}_0/2)}{\gamma_{0,l}^{p\prime\prime}}\end{array}\right],$$

$$c_{0,j}=\frac{1}{2}(1-R_t^p e^{\ \gamma_{0,l}^p\tilde{L}_0}),$$

$$d_{0,j}=-\frac{1}{2}(1-R_b^p e^{\ \gamma_{0,j}^p\tilde{L}_0}). \tag{29}$$

3D radiation into top half-space. For TE coupling

$$\psi_t^H=p_0k_0\eta_0\frac{\sin\varphi}{\sin\theta}\left(\frac{e^{ik_t\tilde{R}}}{n_t\tilde{R}}\right)T_t^s\frac{1+R_b^s e^{in_0\tilde{L}_0\cos\vartheta}}{1-R_t^sR_b^s e^{2in_0\tilde{L}_0\cos\vartheta}}\times e^{i(n_0\cos\vartheta-n_t\cos\theta)\tilde{L}_0/2}, \tag{30}$$

$$\hat{P}_{TE,t}^{3D,H}=\frac{3}{8}\mathrm{Re}\left(\frac{n_t}{n_0}\right)\int_0^{\pi/2}\times\left|T_t^s\frac{1+R_b^s e^{in_0\tilde{L}_0\cos\vartheta}}{1-R_t^sR_b^s e^{2in_0\tilde{L}_0\cos\vartheta}}e^{i(n_0\cos\vartheta-n_t\cos\theta)\tilde{L}_0/2}\right|^2\times\sin(\theta)d\theta. \tag{31}$$

For TM coupling

$$\phi_t^H=p_0k_0\frac{\cos\theta\cos\varphi}{\sin\theta}\left(\frac{e^{in_t\tilde{R}}}{n_t\tilde{R}}\right)T_t^p\frac{-1+R_b^p e^{in_0\tilde{L}_0\cos\vartheta}}{1-R_t^pR_b^p e^{2in_0\tilde{L}_0\cos\vartheta}}\times e^{i(n_0\cos\vartheta-n_t\cos\theta)\tilde{L}_0/2}, \tag{32}$$

$$\hat{P}_{TM,t}^{3D,H}=\frac{3}{8}\mathrm{Re}\left(\frac{n_t}{n_0}\right)\int_0^{\pi/2}\times\left|n_tT_t^p\frac{-1+R_b^p e^{in_0\tilde{L}_0\cos\vartheta}}{1-R_t^pR_b^p e^{2in_0\tilde{L}_0\cos\vartheta}}e^{i(n_0\cos\vartheta-n_t\cos\theta)\tilde{L}_0/2}\right|^2\times\cos^2(\theta)\sin(\theta)d\theta. \tag{33}$$

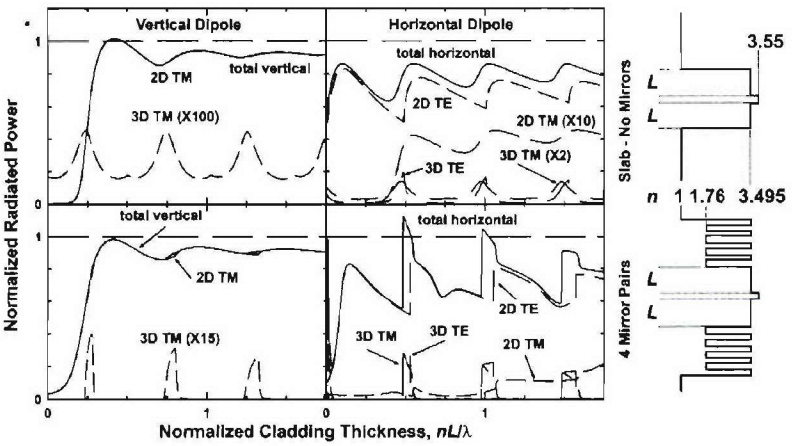


FIG. 2. Radiated power from a dipole embedded in a slab (top) and in the same slab with four mirror stacks (bottom). The results for a vertical dipole are shown in the left panels and for a horizontal dipole in the right panels. In each case the dipole is embedded in a thin (10-nm-wide) InGaAs ($n=3.55$) section clad top and bottom with GaAs ($n=3.495$) spacers of thickness L. For the slab, the semi-infinite outer claddings are air ($n=1$); for the mirror stacks are $\lambda/4$ pairs of Al_2O_3 ($n=1.76$) and GaAs, again with semi-infinite air outer claddings. See text for detailed discussion.

with equivalent expressions for the radiation into the bottom half space.

Again, it is instructive to compare these expressions for a horizontal dipole with the equivalent expressions derived for the symmetrically clad slab with Sommerfeld's Hertz vector approach [4]. For the TE coupling the results are again very similar with the straightforward substitutions of the multilayer reflectivities, the more careful tracking of reflection coefficients necessary for nonequivalent surfaces, and the automatic placement of the dipole in the center of the slab. The TM results are significantly simpler in this formulation, particularly for the Hertz potential and the 3D radiation contributions. In the previous treatment, based on the Sommerfeld formulation, the possible algebraic simplification was only recognized for the bound mode contributions.

IV. RESULTS

In the following two sections, results using these expressions are presented for two related vertical-cavity structures. First, we consider a slab bound by two symmetric quarter wavelength mirror stacks with air on both sides. The power is radiated into both bound modes and 3D radiation. In the second case, the same structures are atop a GaAs substrate, again with air cladding the top surface. Now there are no bound modes, but there are "leaky" modes with field distributions very similar to the bound modes, but whose energy leaks into radiation modes in the substrate. Absorption has been set to zero (all indices taken as pure real quantities), interface roughness has been neglected, and the structure is taken as infinite within the plane. Additionally, the dipole radiation has been assumed to be at a continuous single frequency ω, without any dephasing (T_2) or decay (T_1) events. The impact of all of these assumptions is to allow the coherent addition of fields over many transits of the multilayer structure, e.g., to investigate very high finesse resonances. This allows beautiful examples of resonance effects; however, due consideration of these limiting effects must be taken in applying this analysis to the interpretation of experimental results.

A. Slab with DBR mirrors—bound modes and radiation

The slab structure consists of a thin (10 nm) InGaAs quantum well ($n=3.55$) with the dipole in the center of the well, symmetric GaAs inner cladding layers ($n=3.495$) whose thicknesses are equal and are varied in the calculation, symmetric $\lambda/4$ Al_2O_3/GaAs ($n=1.76/3.495$) mirror pairs (results for zero to four mirror pairs are presented), and air ($n=1$) upper and lower outer cladding half-spaces. The spatial index profile is shown as an inset in Fig. 2. These index values are appropriate to a wavelength of 980 nm; results are shown normalized to the wavelength in the GaAs layers.

The calculated radiated power, normalized to the radiated power in an unbounded InGaAs medium as a function of the GaAs inner cladding thickness for a simple slab (top, no mirror stacks) and for a slab bound on each side by four mirror stacks (bottom) is shown in Fig. 2 for both a vertical dipole source (left) and a horizontal dipole source (right). For the vertical dipole source, all of the radiation is into TM bound and radiation modes. For the air-clad slab, the 3D radiation shows strong Fabry-Perót resonances for slab thicknesses near $2n_1\tilde{L}\sim(2j+1)\lambda/2$, $j=0,1,\ldots$, and much weaker resonances for even numbers of half-wave resonances. This alternation arises from the factoring of the resonant denominator for this symmetric case and the cancellation of one set of resonances by the numerator in Eq. (25). The horizontal dipole has a similar set of resonances but now at even numbers of half-waves and the cancellation for odd numbers of half-waves, for both the TE and TM radiation components. These resonance conditions are a direct consequence of the boundary conditions in Eqs. (10) and (14). The TM radiation boundary conditions for a vertical dipole require that the Hertz potential be zero at the edges of the inner cladding as the magnitude of the reflectivity approaches unity, whereas the TE and TM boundary conditions for a horizontal dipole force the derivative of the potential to zero at the same locations. The high symmetry of a dipole located in the precise center of the slab results in these alternating resonance selection rules; more complex behavior is found for a dipole displaced from the center of the slab. For the 2D bound modes, the vertical dipole exhibits a strong suppression of the radiation for very thin slabs ($L\ll\lambda/n$) while the radiation is more pronounced for the horizontal dipole at these thicknesses. In both cases, the total radiated power rises approximately to that for the dipole in an infinite medium as the inner cladding thickness is increased; the slightly lower value (<1) than in an infinite InGaAs medium is be-

cause the normalization is to the dipole in the higher index InGaAs, but the majority of the bound mode radiation is confined to the GaAs layers. Each of the contributions to the total radiated power has been multiplied by various factors to make them visible in the figure. As is well known, for the vertical dipole, only very weak radiation into the air spaces is observed (3D×100). More interesting is the result for the horizontal dipole, where most of the radiation is into the TE mode; the 2D TM radiation is multiplied by 10, while the 3D TM radiation contribution to the total power is multiplied by 2.

The impact of the mirror pairs on the distribution of power between the individual radiation components is significant, whereas the total radiated power is only modestly impacted. For a vertical dipole, there is a noticeable increase in the radiated power into the 2D TM mode for very thin slabs. This is a result of the increased mode volume due to the mirrors (see the left side of Fig. 2). For the air-clad slab, only the lowest-order mode is propagating for $2n_1L \leq \lambda$ while for the four-mirror-clad slabs, there are six propagating modes even for $\tilde{L}=0$. For both dipole orientations, the 3D radiation is significantly increased at the alternating half-wave resonances, and suppressed away from these resonances. For a horizontal dipole at the first two resonances, the total radiated power is slightly larger ($\sim 15\%$) than that for a dipole in an infinite medium corresponding to a decrease in the radiative lifetime. The 3D radiation is strongly peaked at the even integral resonances for both the TE and TM components. Away from these resonances, essentially all of the radiated power is in the 2D bound modes. As the number of mirror pairs is increased, more of the energy is shifted into the TM radiation, although it remains a significantly smaller fraction of the total power than that radiated into the TE mode. There is a more equal balance of radiated power between TE and TM for the 3D radiation.

The evolution of the total radiated power as the number of mirror pairs is shown more clearly in Fig. 3. Results are shown for both vertical (top) and horizontal (bottom) dipoles for the slab case and for one through four mirror pairs. The curves are offset for clarity. In each case, the radiation from a dipole in an infinite medium is shown as the associated dotted line.

For a vertical-cavity laser, the radiated power for a horizontal dipole in the normal direction, perpendicular to the layers, is of particular interest. The maximum intensity into the normal direction occurs when the TE and TM powers are equal, just at the leading edge of the resonances of Fig. 2 (see also Fig. 5B). Figure 4 (top) shows the normalized forward direction emission for a horizontal dipole as a function of the slab thickness for the five cases of a slab and one through four mirror pairs. The angular variation at the peak is also shown in Fig. 4 (bottom). The variation with slab thickness shows the expected Lorentzian line shape from the expansion of the resonant denominator at an increasing cavity finesse F as the reflectivity increases with the number of mirror pairs. (The calculated normal emission power reflectivities and corresponding F's are $|R|^2=0.31$, $F\sim 2.5$, slab; $|R|^2=0.75$, $F\sim 11$, one mirror pair; $|R|^2=0.93$, $F\sim 43$, two mirror pairs; $|R|^2=0.982$, $F\sim 173$, three mirror pairs; and $|R|^2=0.995$, $F=628$, four mirror pairs.) The slight shift of the resonance away from $2nL/\lambda=1$ is due to the optical thickness of the InGaAs quantum well. As ex-

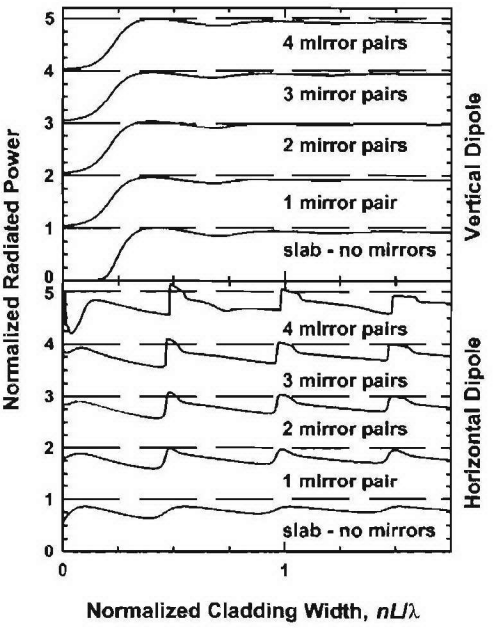


FIG. 3. Evolution of the total radiated power for a symmetric structure as the number of mirror pairs is varied. The curves are offset for clarity; in each case the dashed line represents the power radiated by the dipole into an infinite InGaAs medium.

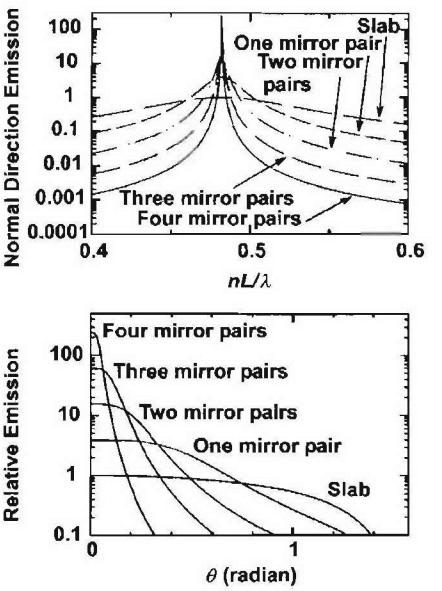


FIG. 4. Vertical emission (normal to the layer structure) into 3D radiation modes for a horizontal dipole embedded in a symmetrically clad slab as a function of the inner cladding thickness (top) and the angular variation for the peak vertical emission (bottom), both with the number of mirror pairs as a parameter. As expected, the increasing finesse of the resonance with increasing numbers of mirror pairs is reflected in both plots.

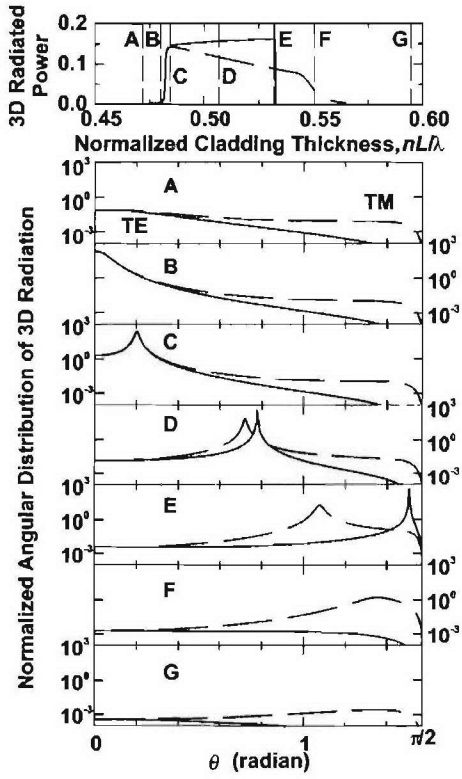


FIG. 5. Angular variation of the 3D radiation from a horizontal dipole in a symmetrically clad slab with four mirror pairs as the inner cladding thickness is varied. The top panel shows an expanded view of the integrated TE and TM 3D radiation in the vicinity of the first-resonance inner cladding thickness. The angular traces (A though G) show the evolution of the angular dependence of the emission as the inner cladding thickness is varied in this region.

pected, the angular variation of the emission at the peak of each of these resonances narrows significantly as F increases.

As the inner cladding thickness L increases beyond this resonance, the peak of the 3D emission shifts to steeper angles for both TE and TM radiation, and the total 3D radiated power increases dramatically. The top panel of Fig. 5 shows an expanded view of the total integrated 3D radiated power emitted from both surfaces around the first peak region ($nL/\lambda \sim 0.5$) for the four-mirror-pair case for a horizontal dipole. From the symmetry of this geometry, the same power is emitted from both surfaces. The angular dependence of the radiated power is shown for various values of L (A through G) as indicated in the top panel. Case A is before the resonance; the radiated power is quite small and does not show a pronounced angular dependence. Case B is the maximum of the normal-direction emitted power shown previously in Fig. 4. Notice that this peak normal emission corresponds to a very small fraction of the power radiated from the dipole. Case C is just past the sharp increase in the 3D emitted power for both TE and TM radiation. There is a peak in the angular dependence, for both TE and TM radiation, at a small angle away from normal. This peak can be traced to the round-trip resonance condition in the denominators [Eqs. (31) and (33)] that must move away from normal as the thickness is increased. The explicit dependence in Eqs. (31) and (33) is on the thickness of the central slab medium containing the dipole, which is fixed in this calculation. The dependence on the thickness of the cladding is contained in the phase of the reflection coefficients. This lowest order round trip resonance condition is simply, $4n_{GaAs}\cos\vartheta_{GaAs}L + 2n_{InGaAs}\cos\vartheta L_{InGaAs} + 2\phi(\theta) = \lambda/2\pi$, which clearly exhibits the dependence of ϑ_{GaAs}, the angle of propagation in the inner cladding, on L. The final phase term $\phi(\theta)$ represents the phase shift in the reflector stack beyond the inner cladding. The external angle θ is related to ϑ_{GaAs} by the Fresnel condition $n_{GaAs}\sin\vartheta_{GaAs} = \sin\theta$ for the present case of a semi-infinite air ($n_t = 1$) outer cladding. The change in the external angle for a given change in L is amplified by the GaAs refractive index. For case D, corresponding roughly to the middle of the thickness region with substantial radiation, the peaks for TE and TM radiation occur at different angles and the TE peak is significantly sharper. This is because of the lower TM reflectivity related to Brewster's angle for TM radiation incident on a single interface. The splitting is due to phase shifts as the angle is increased. This trend is continued for case E, just before the cutoff of the TE radiation. The angular peak in the TE emission is close to $\pi/2$. For a further increase in the inner cladding thickness, the peak shifts beyond the angle for total internal reflection and the emitted power shifts from 3D radiation out the sides of the structure to 2D modes propagating within the structure. This same transition is more gradual for the TM radiation (case F) consistent with the more gradual onset of the 2D TM emission with inner cladding thickness seen in Fig. 2. Finally, case G is for a thickness beyond the significant 3D emission region where the total 3D power is weak and again does not show any strong angular dependence.

B. Active region and mirrors on substrate—No bound modes

We now make a change in the structure, replacing the bottom semi-infinite air cladding with a semi-infinite GaAs cladding. This simple change greatly modifies the calculation, but of course the results should not be dramatically different since, at least as the number of mirrors is increased, the dipole should not "see" the substrate refractive index. The major change in the calculation is that there are no bound modes in this structure, in the sense that the zeros of the dispersion relation all correspond to "modal" indices that are lower than the GaAs substrate refractive index for the entire thickness region L investigated. Thus the radiated power is either emitted out the top surface, or "leaks" from the film stack into the GaAs substrate. As before, some of the power is radiated into the upper air space. Mathematically, having the substrate index higher than the solution to the dispersion relation puts the poles on a different sheet of the Riemann surface of the inverse transform integrand (e.g., the negative sign must be taken for the square root corresponding to the substrate propagation constant whereas a positive sign was taken in the true bond mode case) so that the poles do not contribute to the inverse transform integration.

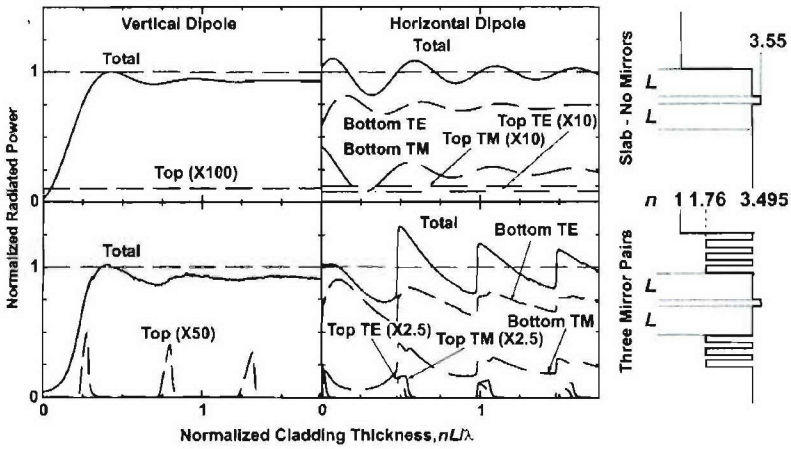


FIG. 6. Radiated power from a dipole embedded in an asymmetric film structure with air upper and GaAs lower outer claddings. The top panels are for a simple InGaAs/GaAs structure, the bottom panels include three Al_2O_3/GaAs $\lambda/4$ mirror pairs. In each case the dipole is embedded at the center of a thin InGaAs region. The left panels are for a vertically oriented dipole; the right for a horizontal dipole. The only emission is into 3D radiation for these cases. There are no strictly bound modes, however, for the three mirror-pair case; there are "leaky" modes largely confined to the film stack but with radiation that leaks into the substrate.

Figure 6 shows the total radiated power for a simple slab case (top), with just a buried InGaAs layer, and for three mirror pairs (bottom). Results are shown for both a vertical dipole (left) and a horizontal dipole (right). As there are no bound modes, there are no 2D contributions; the calculation proceeds only from Eqs. (31) and (33) and their bottom surface counterparts. For a vertical dipole, the results are very similar to those for the symmetrically clad slab with air on both sides. There are somewhat larger differences for a horizontal dipole. The roughly factor of two decrease compared with the equivalent figure for the symmetrically clad geometry is due to the counting of the radiated power out of both top and bottom surfaces in Figs. 2 and 5, whereas the top and bottom surface radiated powers are shown individually in this figure. There are differences in the details of the emission dependence on inner cladding thickness that will be discussed in conjunction with Figs. 8 and 9. The total horizontal dipole emission does not exhibit the sharp transitions between 2D and 3D emission that characterized the symmetric air-clad slab, but the overall dependence of the emission on the inner cladding thickness is similar. The total emission at the peak around $nL/\lambda \sim 0.5$ is larger than for the similar symmetric air-clad three-mirror-pair case. There is also a significant change in the distribution of energy between TE and TM emission, the TM emission being more pronounced in this substrate geometry.

Figure 7 shows the progression of the total emitted power as a function of the inner cladding thickness with the number of mirror pairs as a parameter. The curves have been offset for clarity. The radiated power for a dipole in an infinite medium is shown as the dashed line associated with each curve.

An expanded view of the first top surface emission region for a horizontal dipole, in the vicinity of $nL/\lambda \sim 0.5$, is shown in the top panel of Fig. 8. This should be compared with the comparable panel in Fig. 5 for the symmetrically air-clad slab. Again, the overall results are similar, but there are some noticeable differences. The overall shapes are inverted, in Fig. 5 the TE power increases slightly as the inner cladding thickness increases up to a very sharp cutoff while the TM power decreases and shows a much more gradual cutoff. In Fig. 8 the TM power increases while the TE power decreases as the inner cladding thickness increases. The limits of the emission with inner cladding thickness are more gradual and less well defined for this case. The TM emission is larger than the TE, the opposite of the symmetrically clad slab case.

The angular dependencies of the emission out the top (air-clad) surface are shown in panels A through G. Panel A is for inner cladding thicknesses smaller than those that correspond to the peak emission. The emission is relatively weak and featureless. Panel B corresponds to the peak of the normal emission. Notice that this peak occurs for a thickness further up the knee of the emission than was the case for the symmetrically air-clad slab (Fig. 5B). Nonetheless, the emission is weaker in the present asymmetric case. In comparable units, the emission at normal for the air-clad case with three mirror pairs was 60, both top and bottom; in this case it is 11

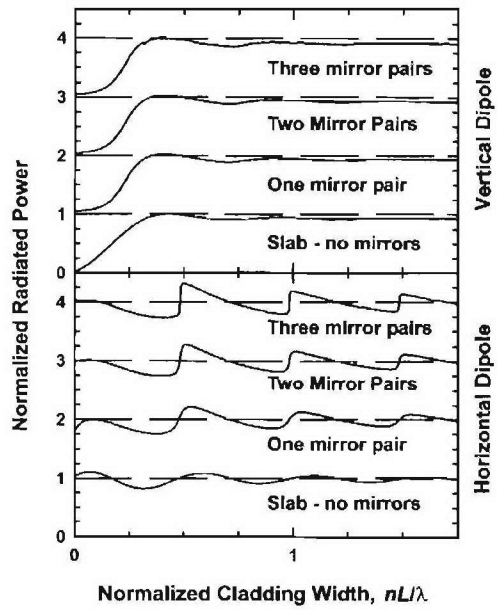


FIG. 7. Evolution of the total radiated power for an asymmetrically clad slab with an air upper and a GaAs substrate lower cladding. The curves have been offset for clarity; in each case the dashed line represents the power radiated by the dipole into an infinite InGaAs medium.

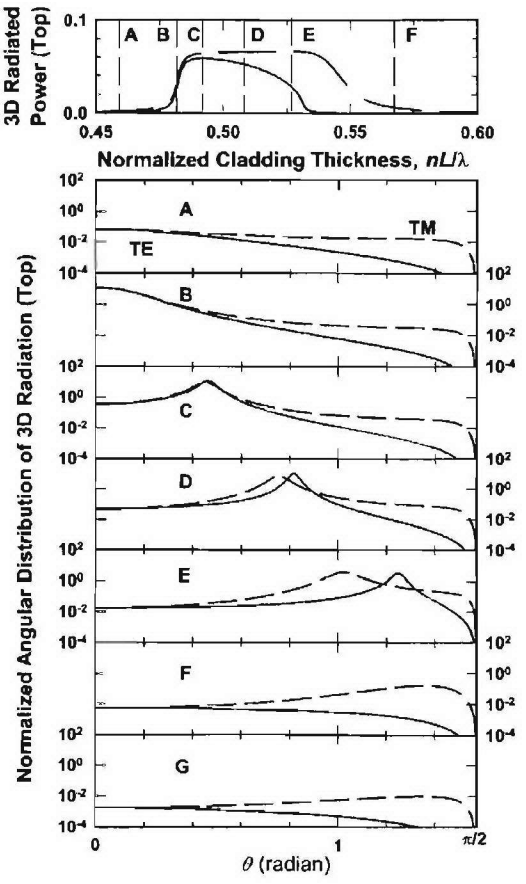


FIG. 8. Angular variation of the 3D radiation (horizontal dipole) from the top (air) surface of an asymmetrically clad slab (air upper and GaAs lower outer claddings) with three mirror pairs as the inner cladding thickness is varied. The top panel shows an expanded view of the integrated TE and TM 3D radiation in the vicinity of the first-resonance inner cladding thickness. The angular traces (A though G) show the evolution of the angular dependence of the emission as the inner cladding thickness is varied in this region. Curve G is for a normalized inner cladding thickness $nL/\lambda \sim 0.65$, beyond the thicknesses plotted in the top curve.

top and 134 bottom. Overall the normal emission is comparable, but much is lost to substrate emission in this asymmetric case. Panel C is for an inner cladding thickness near the peak TE emission. Both TE and TM emissions show comparable peak emission angles as was the case for Fig. 5. Panel D is for an inner cladding thickness near the mid point of the significant top-surface emission. As was the case for the symmetrically clad structure, at these higher angles a splitting is observed between the TE and TM peak emission angles as a result of different phase contributions from the TE and TM reflectivities. Panel E is for a thickness near the upper edge of the TE emission. The peak of the TE emission is close to $\pi/2$ as expected. Panels F and G are at the upper edge of the TM emission and beyond both TE and TM emission regions. Panel G is for a nL/λ of 0.65, outside the range of the top panel, which was plotted on the same horizontal scale as Fig. 5 for comparison. Since these curves are for emission out the top surface, the same amplification of the external angle relative to the internal angle as was found for the previous symmetrically clad structure is also found in these cases.

In contrast to the relatively orderly behavior of the top surface emission shown in Fig. 8, the bottom surface emission shows a much more pronounced angular dependence as shown in Fig. 9 for five different values of the normalized inner cladding thickness, again for a horizontal dipole. Note the much larger vertical axis scale from 10^{10} to 10^{-5}. The TE and TM emission angular dependencies are shown side by side for clarity in this figure. The top pair of panels is for the same inner cladding thickness as panel B of Fig. 8, just at the peak of the normal emission. In addition to the angular peak at $\phi=0$, both the TE (left) and TM (right) emission show additional structure. There are sharp dips, which are relatively independent of inner cladding thickness and are related to changes in reflectivity. A notable feature is the very strong peak in the TE emission at $\phi \sim 1.25$ (labeled TE1) and the comparable, but significantly smaller peak in the TM emission at $\phi \sim 0.66$ (TM1). These correspond to energy transmitted into the substrate from the lowest order "leaky" mode. That is from a field distribution in the upper cladding layers that looks very similar to the zero-order bound mode for the symmetrically air-clad structure. Compared to the peak normal emission of ~ 134 into the substrate, the value of this emission is 5×10^7! The resonance linewidth is correspondingly narrow, so the normalized integrated radiated power is ~ 0.5 as shown in Fig. 6. As the inner cladding thickness is increased, both TE1 and TM1 peaks shift to steeper angles. Since the refractive index of the substrate (3.495) is very similar to that of the InGaAs slab (3.55), the amplification of the angle by refraction is small. As the inner cladding thickness is further increased, both of these peaks saturate at angles close to $\pi/2$. The last pair of panels in Fig. 9 is for an inner cladding thickness such that there are two propagating leaky modes and consequently two pairs of sharp peaks, TE1 and TE2 and TM1 and TM2. These very sharp angular dependences posed some numerical integration challenges. It was easy to miss the peak in the overall integrals [the bottom surface equivalents of Eqs. (31) and (33)]. Care had to be taken to track the peaks as a function of inner cladding thickness and integrate carefully over the peak with a very fine step size to get accurate results. This is also the reason that only the three-mirror-pair rather than the four-mirror-pair case was evaluated for the asymmetric structure; the resonances became too narrow and too peaked to deal with within the 16-bit precision of the present computer program. Adding losses to the dielectric constant limits the peak value, but also results in energy loss to absorption within the dielectric stack that must be accounted for in evaluating the total radiated energy.

V. SUMMARY AND CONCLUSIONS

A fully analytic treatment of the radiation from a dipole embedded in an arbitrary dielectric stack has been presented. The treatment starts from a Hertz-vector formalism introduced by Sommerfeld [1] and extended by Lucosz [9]. The analysis proceeds by finding the Fourier transform of the

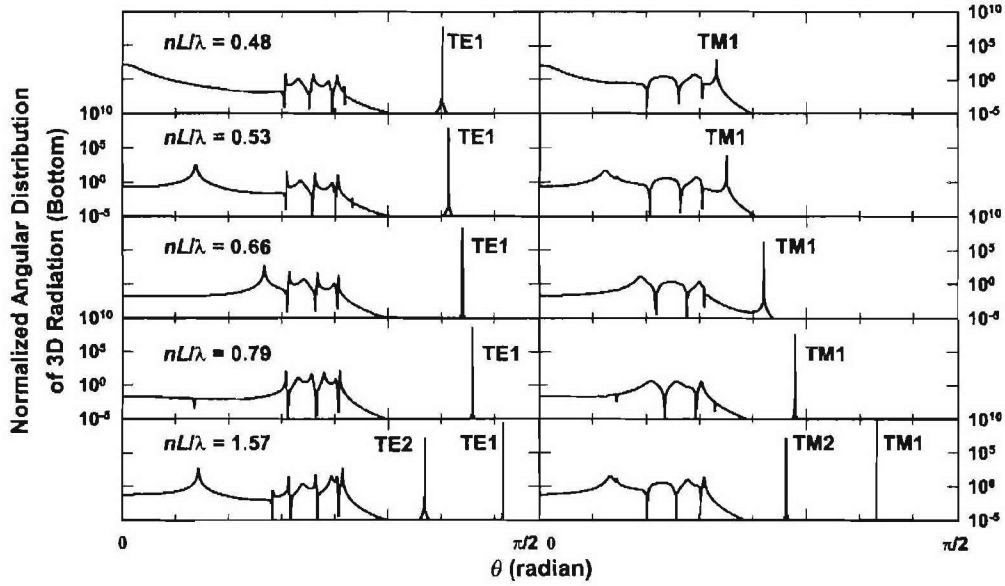


FIG. 9. Angular variation of the 3D radiation from the bottom (GaAs substrate) of an asymmetrically clad slab (air upper and GaAs lower) with three mirror pairs as the inner cladding thickness is varied for a horizontal dipole. The various values of nL/λ are given in the figure. The top panels, $nL/\lambda = 0.48$, correspond to position B, the peak normal emission, in Fig. 8 (top). The second set of panels, $nL/\lambda = 0.53$, corresponds to position E, the edge of the TE emission peak, in Fig. 8 (top). The third row of panels, $nL/\lambda = 0.79$, corresponds to a cladding thickness just before the emergence of the second top-surface emission peak (Fig. 6). The final row of panels, $nL/\lambda = 1.57$, corresponds roughly to the middle of the third top-surface emission peak in Fig. 6.

dipole fields for an unbounded medium, solving the independent boundary conditions across the multilayer stack for each Fourier component, and transforming back to real space. This procedure provides a rigorous solution to the multilayer boundary conditions. Two different classes of singularities are present in the integrand for the inverse transform: poles that correspond to bound 2D waveguide modes confined within the multilayer stack, and branch cuts that correspond to 3D radiation emitted from the sides of the stack into the upper and lower outer cladding half-spaces. While the boundary conditions are strictly valid, approximations are made in order to evaluate the radiated fields that are accurate only many wavelengths from the position of the dipole, e.g., in the radiation zone away from the near fields. The results are directly related to previous work [4] that investigated a simple dielectric slab geometry with the straightforward replacement of single layer reflectivities with their multilayer counterparts.

This formalism was applied to two closely related structures, both of which are germane to the design of semiconductor vertical-cavity lasers. Both structures contain a thin active region containing the dipole with symmetric inner claddings and an equal numbers of Bragg reflector mirror pairs on both sides. In the first case, the structure is fully symmetric with an air cladding both above and below the stack. In the second case, the lower cladding is replaced with a substrate with the same refractive index as the inner cladding. These two cases illustrate some interesting points. For the symmetrically air-clad structure, the dipole couples to both the bound modes of the slab and the radiation fields in the air spaces. For the asymmetric structure, on the other hand, there are no bound modes because of the high-index outer cladding and only the 3D radiation calculation is operative. However, for high reflectivities, e.g., a sufficient number of Bragg reflector pairs, the results should be essentially equivalent since the dipole can not "see" the substrate because of the high reflectivity. Instead of true bound modes, there are leaky modes that look very much like the bound modes of the air-clad structure, but whose power is transmitted into the substrate after many round trips within the film stack. Because of the very high reflectivities in these structures, especially at steep angles, very sharp angular dependences are found for this radiated power, corresponding to the bound modes in the symmetric air-clad case. In both cases, the 3D radiation into the upper low-index (air) half-space is a sharp function of the thickness of the inner cladding with TM and TE resonances at alternating half-wave inner cladding thicknesses. The asymmetric case is very close to that of some LEDs on solid substrates. For example, visible-emission, nitride-based quantum-well LEDs [13] are examples of mode-free structures [14]. Modes similar to guided modes but losing power due to leakage into the substrate are observed in such structures.

Finally, we present the following conclusions.

(1) Analytic solutions are presented using a rigorous Hertz-vector formalism for dipole emission within a multilayer dielectric structure. These solutions are suitable for application to edge-emitting and vertical-cavity surface-emitting lasers (VCSELs), resonant light-emitting diodes and photodetectors, and other multilayer optoelectronic devices. Expressions are presented as functions of a normalized optical thicknesses of the various layers and can be used to ana-

lyze either thickness or wavelength variations.

(2) Enhancement/suppression of the dipole radiation relative to that in an infinite medium is obtained. The results are very dependent on the structure; however, even with a very high finesse planar cavity, the maximum enhancement is limited to $\sim 31\%$ for a horizontal dipole at the first resonance peak, e.g., for a total inner cladding thickness of $\sim n\lambda$. The inner cladding thickness for peak emission is close to, but slightly longer than, the peak normal emission thickness.

(3) A larger fractional suppression of the dipole emission is found for a vertical dipole for very short inner-cladding thicknesses lengths $\ll n\lambda/2$. This is due to destructive interference between the radiated and reflected fields at the position of the dipole.

(4) The distribution of the radiated power between 3D radiation into the outer claddings and 2D radiation into the waveguide modes shows a larger variation with structure than does the total radiated power. For a free-standing symmetric structure, the addition of high-reflectivity Bragg mirrors modifies significantly the fraction of power emitted into the air space and its inner cladding thickness and angular variations. As expected, the angular width and inner cladding thickness tolerance of the normal-emission resonance decreases with increasing mirror reflectivities.

(5) In the asymmetric case, with a high-index substrate, the bound modes of the structure evolve into leaky modes whose energy is radiated into the substrate. The top-surface emission for this case is similar to that for the symmetric case. The bottom (substrate) 3D emission is characterized by a complex dependence at small angles corresponding to the reflectivity coefficient for this multilayer structure, and by very intense and narrow resonance peaks at higher angles corresponding to the leaky modes.

[1] A. Sommerfeld, Ann. Phys. (Leipzig) **28**, 665 (1909).
[2] A. Sommerfeld, *Partial Differential Equations in Physics* (Academic Press, New York, 1949).
[3] D. Marcuse, *Theory of Dielectric Optical Waveguides* (Academic Press, San Diego, 1991).
[4] S. R. J. Brueck, IEEE J. Sel. Top. Quantum Electron. **JSTQE-6**, 899 (2000).
[5] G. Björk, S. Machida, Y. Yamamoto, and K. Igeta, Phys. Rev. A **44**, 669 (1991).
[6] H. Rigneault and S. Monneret, Phys. Rev. A **54**, 2356 (1996).
[7] Y. Xu, R. K. Lee, and A. Yariv, Phys. Rev. A **61**, 033807 (2000).
[8] S.-T. Ho, Y. Chu, J.-P. Zhang, S. Wu, and M.-K. Chin, in *Optical Processes in Microcavities*, edited by R. K. Chang and A. J. Campillo (World Scientific, Singapore, 1996), pp. 339–387.
[9] W. Lukosz and R. E. Kunz, J. Opt. Soc. Am. **67**, 1607 (1977).
[10] W. Lukosz, Phys. Rev. B **22**, 3030 (1980).
[11] A. Baños, *Dipole Radiation in the Presence of a Conducting Half-Space* (Pergamon Press, Oxford, 1966).
[12] J. A. Stratton, *Electromagnetic Theory*, 1st ed. (McGraw-Hill, New York, 1941), pp. 573–575.
[13] S. Nakamura, M. Senoh, N. Iwasa, and S. Nagahame, Jpn. J. Appl. Phys., Part 2 **34**, L797 (1995).
[14] I. V. Akimova, P. G. Eliseev, M. A. Osinski, and P. Perlin, Quantum Electron. **26**, 1039 (1996).

Optical and Interferometric Lithography—Nanotechnology Enablers

S. R. J. BRUECK, FELLOW, IEEE

Invited Paper

Interferometric lithography (IL), the interference of a small number of coherent optical beams, is a powerful technique for the fabrication of a wide array of samples of interest for nanoscience and nanotechnology. The techniques and limits of IL are discussed with particular attention to the smallest scales achievable. With immersion techniques, the smallest pattern size for a single exposure is a half-pitch of $\lambda/4n$ where λ is the optical wavelength and n is the refractive index of the immersion material. Currently with a 193-nm excimer laser source and H_2O immersion, this limiting dimension is ~34 nm. With nonlinear spatial frequency multiplication techniques, this limit is extended by factors of 1/2, 1/3, etc.—extending well into the nanoscale regime. IL provides an inexpensive, large-area capability as a result of its parallelism. Multiple exposures, multiple beams, and mix-and-match with other lithographies extend the range of applicability. Imaging IL provides an approach to arbitrary structures with comparable resolution. Numerous application areas, including nanoscale epitaxial growth for semiconductor heterostructures; nanofluidics for biological separations; nanomagnetics for increased storage density; nanophotonics including distributed feedback and distributed Bragg reflectors, two- and three-dimensional photonic crystals, metamaterials, and negative refractive index materials for enhanced optical interactions are briefly reviewed.

***Keywords*—Epitaxy, interference, lithography, metamaterials, nanofluidics, nanomagnetics, nanophotonics, nanoscience, nanotechnology, negative-index materials.**

I. INTRODUCTION

Nanoscience and nanotechnology are increasingly important research directions because of the exciting new physics and chemistry that become accessible at the nanoscale and because of the accompanying potential for new products and processes that will have a major impact on the world's technological future. The new science involves both the increased importance of surfaces (e.g., increased surface/volume ratio) and of the chemical/steric effects that are the basis of much of molecular biology, as well as the quantum phenomena that become dominant as the material scale becomes comparable to the wavefunctions of elementary excitations: electrons, holes, photons, spin waves, magnetic excitations, and others.

Optical lithography is well established as the manufacturing technology of choice for the semiconductor IC industry which is today well into the nanoscale with ~65-nm gate lengths in large-volume manufacturing production. With recent developments such as immersion lithography, it now appears that the hegemony of optical lithography has a significant duration yet to run, despite the continuing refrain that the end of optical lithography as we know it is neigh upon us. In this context, it is worth noting that predictions of the end of optical lithography have held steady at "two generations out" for roughly the past 30 years. The dual purposes of this paper are to discuss the limits to optical lithography on very general grounds and to point out the opportunities for exciting nanoscience research that are made possible by its capabilities.

Any discussion of tools for nanoscience research necessarily involves consideration of the associated costs—in resources and in time. The research community never has resources for everything and must make choices based on affordability and productivity. Thus, for example, e-beam lithography can produce structures at scales smaller than optical lithography and with an almost complete pattern flexibility (within the limits imposed by proximity effects) and is a staple of nanoscience research. Nonetheless, there are many applications that require large areas (many square centimeters of nanopatterned material) where e-beam lithography is not a viable approach as a result of its serial

Manuscript received May 11, 2005; revised May 18, 2005. This work was supported in part by the Army Research Office Multidisciplinary University Research Initiative in Deep Subwavelength Optical Nanolithography, in part by the Defense Advanced Research Projects Agency, in part by the Air Force Office of Scientific Research, in part by the Air Force Research Laboratory, in part by the Department of Energy and in part by International SEMATECH.

The author is with the University of New Mexico, Albuquerque, NM 87106 USA (e-mail: brueck@chtm.unm.edu).

Digital Object Identifier 10.1109/JPROC.2005.853538

0018-9219/$20.00 © 2005 IEEE

point-by-point writing modality and the consequent long times involved in addressing the large number of pixels in a large-area nanoscale image. A linear pixel resolution of 20 nm corresponds to a density of 2.5×10^{11} cm^{-2}! This issue only gets worse as the patterning gets deeper into the nanoscale. As an aside, this is a powerful argument applying to any technique, such as the various approaches to maskless lithography, that requires storage and transfer of information on an individual pixel basis; the data transfer demands are very difficult, even with today's advanced computing and communication technologies.

Optical lithography, in contrast, is a parallel writing technique. Traditional optical lithography uses a mask-based approach along with optical reduction to ameliorate the demands on both the mask fabrication and on the optical system. Once the mask is fabricated, all of the information on the mask is transferred onto the wafer in the lithography step. The economics of the IC industry has put a premium on throughput performance. Current lithography tools expose ~85 wafers per hour. Each 300-mm diameter wafer contains ~125 die with an area of 22×36 mm^2 $= 8.2$ cm^2. This corresponds to a sustained information data rate onto the wafer of ~1 THz!

Nonetheless, the cost of optical lithography remains an issue for nanotechnology both at the research and the early-stage commercialization phases. The impressive and very capable lithography tools used by the IC industry are very expensive both in initial (~$20 million) and in operating costs (typical mask set costs for a modern microprocessor exceed $1 million). Clearly these numbers only make sense in a high-volume, high-product-value manufacturing context and are out of reach for a typical research venue.

Fortunately, many applications require only a periodic or quasi-periodic pattern; and a much simpler laboratory-scale technology, interferometric lithography (IL), based on the interference of a small number (most often two) coherent laser beams, can produce useful patterns over large areas, and volumes, with considerable, but not total, pattern flexibility, and with dimensions that today are approaching 20-nm scales. Combining multiple interferometric exposures and mix-and-match with lower resolution, laboratory-scale optical lithography and with limited use of higher resolution e-beam lithography dramatically expands the available range of patterns.

Nonlinearities at all stages of the patterning process can be used to further extend the spatial scales. In simple terms, the aerial intensity image in IL is a simple $[1 + \cos(2kx\sin\theta)]$ functional dependence, where $k = 2\pi n/\lambda$ is the optical wavevector in the medium above the resist and θ is the angle of incidence in the same medium. After development of the photoresist, a square wave lineshape is typically achieved, described by the functional dependence $\sum_l [(\sin(2lka\sin\theta)/2lka\sin\theta)]\cos(2lkx\sin\theta)$ where a is the critical dimension or CD (width of the line). This expression clearly contains spatial frequencies well above those in the aerial image and provides justification for the claim that *there is no fundamental limit to optical lithography* [1]. These nonlinear concepts, discussed in more detail in Section II-D, are likely to extend the reach of optical lithography by another factor of at least two, to scales of ~10 nm with a 193-nm source. Further similar extensions by integral factors, 3, 4, . . ., are possible but will be increasingly difficult as a result of alignment, process, uniformity, and edge roughness issues. Another direction is the use of directed self-assembly—using molecular moieties as rulers to proceed further into the nanoscale while retaining the capabilities of optical lithography to hierarchically span the range of dimensions from centimeters down to ~10 nm.

The concepts of IL and examples of results are presented in Section II starting from the simplest case of two-beam interference. Particular emphasis is placed on the recent reemergence of an old idea—immersion IL. This section concludes with a discussion of the limits of IL. In Section III, a very brief discussion of the extension of these ideas to a full imaging solution is presented. This is already the topic of many more extensive treatments and cannot be fully developed in the available space. The remainder of the paper contains a survey of active research areas for the application of these technologies. Examples are drawn from nanoscale epitaxial crystal growth, nanofluidics/nanobiological applications, nanomagnetics, and nanophotonics. This is a rich assemblage of topics, each of which could easily be presented to a depth of detail that would overwhelm the space limitations of this paper. The treatment presented here is necessarily very high level. Nonetheless, the juxtaposition of this wide range of application areas serves to make the major point—optical and especially IL are enabling technologies that allow research into, and even manufacturing of, a wide variety of exciting nanoscience and nanotechnology—at an affordable cost that is broadly accessible.

II. IL

IL is the use of a small number of coherent optical beams incident from different directions on a two-dimensional (2-D) (thin photoresist film $\ll \lambda$) or three-dimensional (3-D) (thick photosensitive layer $\gg \lambda$) to produce an interference pattern whose intensity distribution is recorded in the photosensitive layer and is later transferred (developed) by thermal and chemical processes. In the literature, this concept has been variously referred to as holographic lithography, interference lithography, and IL.

IL is a well-established concept that has largely tracked the application of lasers to lithography [2]–[6]. Early work was based on continuous-wave (cw) single-mode lasers such as the Ar^+ line at 488 nm and the Cd^+ line at 442 nm. With the commercial development of i-line lithography (365 nm), attention shifted to the cw Ar^{++} lines at 364 and 352 nm and to the 355-nm third-harmonic of a YAG laser to take advantage of commercial resist developments. As leading-edge commercial lithography shifted to KrF (248 nm) wavelengths, the intracavity doubled Ar-ion line at 244 nm was used. Today, the IC industry is dominantly using ArF excimer lasers (193 nm), and work has been reported both with fifth-harmonic YAG (213 nm) and with line-narrowed ArF lasers at 193

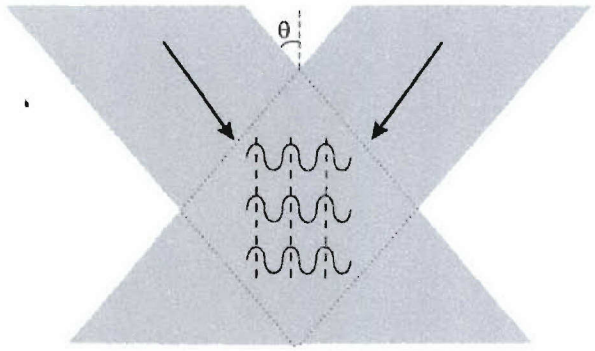


Fig. 1. Schematic representation of two-beam interference. Coherent laser beams are symmetrically incident from the left and the right. The period of the interference pattern is $\lambda/[2n \sin\theta] = \lambda/2\text{NA}$. The standing wave pattern exists throughout the overlap between the beams as long as this overlap distance is shorter than the longitudinal coherence length of the laser beams and the wafer can be placed anywhere inside this coherence volume.

nm. The very small bandwidth tolerance of the high-resolution lenses used in modern lithography has forced the development of line-narrowed excimer lasers with subpicometer bandwidth. These lasers have longitudinal coherence lengths of several centimeters and are more than adequate for interferometric application.

A. Two-Beam IL

The basic concept of two-beam interference is shown schematically in Fig. 1. Two coherent optical plane waves with the same polarization are symmetrically incident on a photosensitive layer coated onto a substrate at angles of $\pm\theta$. The intensity pattern in space is simply given by

$$\begin{aligned} I(x,z) &= |E|^2 |\hat{e}_1 e^{ikx\sin\theta} + \hat{e}_2 e^{-ikx\sin\theta}|^2 \\ &= |E|^2 \left[2 + \left(\hat{e}_1 \cdot \hat{e}_2^* e^{i2kx\sin\theta} + \hat{e}_1^* \cdot \hat{e}_2 e^{-i2kx\sin\theta}\right)\right] \\ &= 2|E|^2 \left[1 + \sigma_{pol}\cos(2kx\sin\theta)\right] \end{aligned} \quad (1)$$

where $k = 2\pi n/\lambda$ with n the refractive index of the medium (one for air) and λ the optical wavelength and $\hat{e}_i$ is the unit polarization vector for each wave. The period of the interference pattern along the x direction is $\lambda/2n\sin\theta$ and $\sigma_{pol} = [1, \cos(2\theta)]$ for (TE, TM) polarization. By Snell's law, this period is invariant across any $\theta = \pi/2$ layer boundaries such as the lithography stack; this is not true for the contrast. TE polarization always gives the maximum contrast, while the contrast is reduced for TM polarization as a result of the π-phase shift between the $\hat{e}_x$ and $\hat{e}_z$ contributions to the interference intensity. For evaluating the polarization dependence, it is important to use the propagation angles inside the photosensitive layer. The contrast reduction for TM polarization becomes significant for steep angles in the resist and will be discussed in detail in the immersion discussion below. For now take $n = 1$; it is relatively easy experimentally to reach $\sin\theta \sim 1$ (for example, at a 75° angle of incidence, $\sin\theta = 0.97$, so the limiting period of IL is $\gtrsim \lambda/2$ and extends below 100 nm at a wavelength of 193 nm.

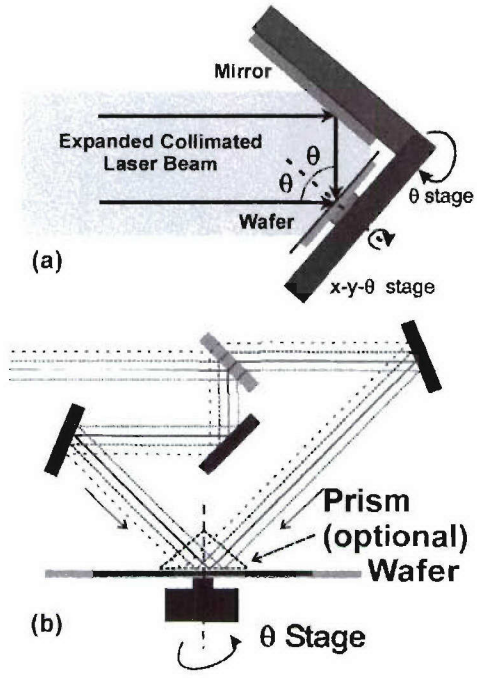


Fig. 2. Experimental arrangements for IL.

Two experimental arrangements for IL are shown in Fig. 2. The top setup [Fig. 2(a)] is a simple corner cube arrangement (Fresnel mirror) where the right and left halves of the beam are folded onto each other using a 90° geometry. This arrangement has been used quite successfully with laser sources with a high transverse coherence such as single-mode TEM_{00} Ar-ion laser beams. Expanding the beam allows quite large areas—especially at periods corresponding to incidence angles θ of $\sim$ 45° where the sizes of the beams incident on the sample and the mirror are equal. At extremely large or small periods, the available area becomes limited by the required size of the folding mirror and alternative experimental configurations are preferable.

Excimer lasers exhibit a large number of transverse modes and consequently a very low transverse coherence. The experimental arrangement in Fig. 2(a) is not suitable in this case, since the two halves of the beam are not, in general, mutually coherent. The interferometer arrangement shown in Fig. 2(b) resolves this problem by splitting the input beam in half and folding it onto itself as indicated by the various line styles in the figure; to maintain contrast, any offset has to be within the transverse coherence length. There remains the requirement of a significant longitudinal coherence (narrow spectral width) since the distances from the beamsplitter to the image plane vary for the two beams across the field. Fortunately, today's very narrow linewidth lithography-optimized excimer lasers have linewidths $\ll$ 1 pm (longitudinal coherence length $\sim \lambda^2/\Delta\lambda \gtrsim$ 4 cm, making large-area (at least several square centimeters) IL straightforward.

Diffractive beam splitters offer an achromatic interferometric solution that has been used with larger linewidth lasers, for example, free-running excimer lasers without line narrowing, to provide large-area patterns [7], [8]. The

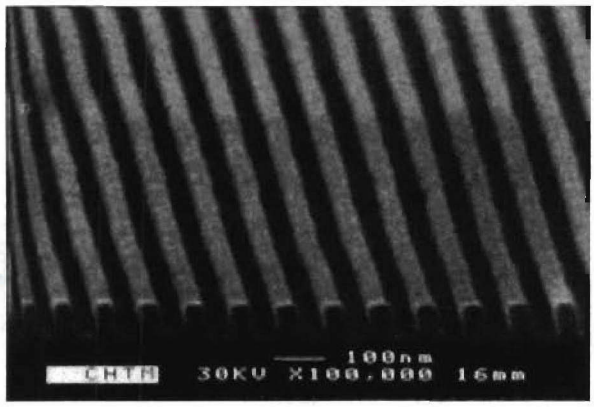


Fig. 3. 45-nm half-pitch pattern in photoresist (resist supplied by AZ Electronic Materials).

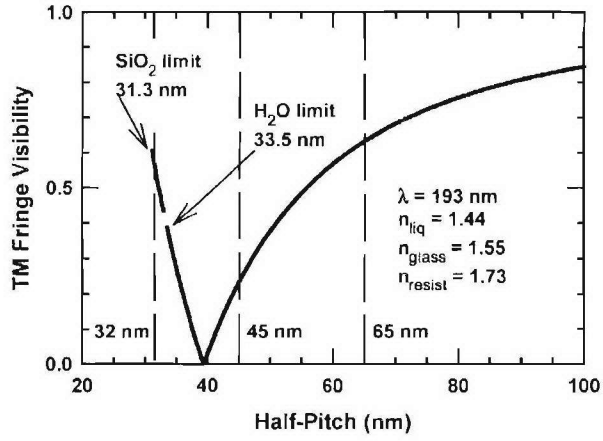


Fig. 4. Aerial image contrast in photoresist as a function of half-pitch.

basic idea is to maintain both the angular relationship of the two beams that gives the interferometric pattern and also equal path lengths for the two beams across the pattern area to provide the necessary self-coherence. A grating beam splitter provides the necessary capability to meet both of these requirements. Generally a phase grating is used optimized to result in maximum coupling into the ± 1 diffraction orders. These two orders are then recombined either with a second grating or with a pair of mirrors to provide the final aerial image pattern.

B. *Immersion IL*

Recently, there has been resurgence of interest in immersion lithography, the use of a suitable fluid between the imaging lens and the wafer [9]–[12]. This allows an improvement in the optical resolution by a factor of the refractive index of the immersion fluid, provided that the lens is suitably modified. At 193 nm, water is a very attractive immersion fluid with a refractive index of 1.44 at 193 nm [13]. The simple addition of a prism to the interferometric arrangement of Fig. 2(b) allows investigation of immersion IL. In the simplest configuration, a drop of water is placed on the wafer and the wafer and water are raised till the water contacts the uncoated prism and forms a high quality optical component. More elaborate automatic fill and dry systems will be used in manufacturing applications.

An example of a 45-nm half-pitch immersion IL pattern is shown in Fig. 3. After the immersion exposure the sample was baked to activate the chemically amplified resist and developed in a standard basic solution. More details are provided elsewhere [14], [15].

Polarization is a very important parameter at the steep angles in the resist enabled by immersion [16]. For TE polarization, as indicated by (1), the fringe visibility $[(I_{\max} - I_{\min})/(I_{\max} + I_{\min})]$ is unity independent of the half-pitch. However, for TM polarization, the fringe visibility decreases as the half-pitch is decreased as a result of competition between the out-of-phase E_x^2 and E_z^2 contributions to the intensity. At an interference angle of 45° in the resist, these two terms are equal and opposite in phase and the visibility goes to zero. For larger interference angles, the line-space pattern is inverted. Fig. 4 shows the simple calculation of the fringe visibility for the parameters indicated. The cusp at ~40 nm corresponds to the inversion of the pattern—the interchange of lines and spaces. The minimum half-pitch available with a 193-nm source and water as the immersion liquid is 33.5 nm; if a higher index liquid becomes available, the glass of the lens sets the limit at 31.3 nm. With a higher index glass as the final lens element, smaller half-pitch patterns are available. Clearly, the reduction in the fringe contrast and the line : space inversion will require some form of polarization control for imaging these small half-pitch patterns.

C. *Multiple-Exposure Interference—Complex 2-D Patterns*

Simple two-beam interference produces an array of uniformly spaced parallel lines covering the exposure area, e.g., a simple grating. By combining multiple such gratings, structures of significant complexity can be constructed [17]. Fourier analysis tells us that any pattern consists of a summation of periodic patterns. A seemingly small, but important, difference between IL and a Fourier expansion is the dc level that accompanies each exposure, cf. (1), since the exposure intensity must be positive for all positions. The consequence is that the dc level increases with the number of exposures and for a large number of exposures, the result is a perfect aerial image of the desired pattern riding atop a large, uniform exposure level. This loss of contrast in the image is an inevitable consequence of summing incoherently related images and is the same reason that the contrast is lower in incoherent imaging than it is in coherent imaging [18]. Today's photoresists are quite nonlinear, giving an approximately sigmoidal response such that every location above (below) a certain threshold is removed (retained) on development. To a point, this nonlinear response can ameliorate this uniform exposure issue and restore the pattern. However, eventually the uniform exposure becomes too large relative to the image information, and pattern details are lost.

Notwithstanding this complexity limitation, there are many useful structures readily available with multiple exposure techniques. The simplest, and perhaps the most useful,

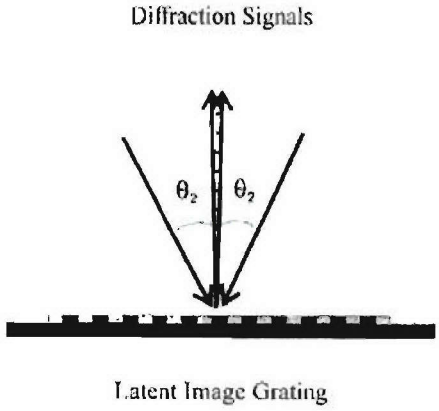


Fig. 5. Experimental configuration for projection moiré alignment. The two beams are incident on the photoresist image produced in the first exposure, or on a predefined grating pattern. The angles are adjusted so that there is only a single fringe across the illuminated area (sets the period), and the sample translation is adjusted so that the fringe is at maximum brightness (sets the phase).

is the square array 2-D pattern obtained by carrying out one IL exposure, rotating the sample by 90°, and performing a second exposure. For low exposure doses in a positive photoresist, such that neither exposure alone is sufficient to clear the resist during developing, the result is a 2-D array of holes; at higher exposure doses where each exposure clears, the result is a 2-D array of posts. For a negative-tone resist, the occurrence of holes and posts are reversed. Details of the pattern, such as the sidewall angle, are sensitive to the exposure dose and need to be optimized in any application [19].

Another simple, but important, application of multiple exposures is to reduce the density of a pattern while retaining the small size capability that is inherent in small-pitch patterns. Again, the idea is quite simple, expose a first pattern at a period $p_1 = p$ with, for example, equal line : space dimensions and a critical dimension (CD) or pattern size of $p/2$, then expose the same area again at a period of $p_2 = p/2$. For a positive photoresist, the result is a pattern with a period of p and a CD of $p/4$. Two constraints that have to be achieved for this approach to be successful are matching of the periods and adjusting the alignment between the two patterns. The linear dimension of the final pattern L, perpendicular to the lines over which the patterns are in phase, depends critically on the deviation of the two periods $\delta = 2p_2 - p_1$ and is given by $L \sim p_1 p_2/\delta$. Fortunately, by using diffraction from the latent image of the first exposure (or from a predefined grating pattern alignment mark) it is possible to derive a feedback signal to allow setting both the frequency and the phase of the second exposure with the necessary precision to cover a large area, as illustrated in Fig. 5 [20]. The basic concept is to monitor the interference between two diffracted beams, one from each input beam over across the exposure area. This can either be done at low intensity over the entire area, or at higher intensity with the sacrifice of a small portion of the final pattern using large-area masks. The goal is to set the input angles on the second exposure so that a single fringe of the interference pattern extends over the entire exposure area (this sets the period, e. g. $\delta \to 0$) and then to adjust the phase of that pattern (light or dark—this sets the relative phase of the two patterns). As a result of the moiré spatial amplification of the pitch differential (small pitch mismatches translate into large, easily measured, distances) this alignment technique has general applicability across nanoscale fabrication.

D. Multiple-Beam Interference—2-D and 3-D Patterns

Adding more input beams to an IL exposure is another direction toward increasing the flexibility of the technique and the complexity of the patterns that can be achieved. The simplest example is to use four beams, two oriented at $\pm\theta$ in the x direction and two at $\pm\theta$ in the y direction. If orthogonal polarizations are used for the two directions, this is identically equivalent to the process for defining a square array in the previous section, with higher throughput, since the two exposures are simultaneous rather than sequential and without the need for a rotation of the wafer.

If all of the interfering beams are inclined at the same angle to the surface normal, the resulting aerial image is again independent of the position of the wafer; however, if the beams are at different angles, the aerial image is no longer invariant along the z direction and the placement of the wafer becomes important. For a small number of beams, the pattern is periodic along z, as the number of beams increases to a continuum, the periodicity along z tends toward infinity and the familiar result of a single focal plane for an imaging system results. A simple, but useful, example is the addition of a normal incidence beam along with the two offset beams of two-beam interference. Assuming TE polarization, the straightforward generalization of (1) is

$$\begin{aligned} I(x,z) &= |E|^2 \left| e^{-ikz} + (e^{ikx\sin\theta} + e^{-ikx\sin\theta}) e^{-ikz\cos\theta} \right|^2 \\ &= |E|^2 \left[3 + 4\cos(kx\sin\theta)\cos\left[kz(1-\cos\theta)\right] \right. \\ &\qquad \left. + 2\cos(2kx\sin\theta) \right]. \end{aligned} \tag{2}$$

For z positions where the second term vanishes, the aerial image is very similar to that of two-beam interference with an additional dc bias. However, at z positions, such as $z = 0$, where the second term is at a maximum, only alternate lines survive. The result is a set of lines for a one-dimensional (1-D) exposure with a linewidth comparable to the dense pattern, but with a twice the separation, e.g., a sparse array. For some applications, for example for field-emitter tips for displays, there are important advantages to the sparse pattern [19]. Fig. 6 shows the aerial images for: (a) a two-beam interference at a period of $2p$ from (1); (b) the three-beam interference for $z = 0$ (spaced at $2p$ but with a linewidth comparable to $p/2$); and (c) the three-beam interference where the second term vanishes (period of p). The smaller pattern feature size for the three beam exposure is evident.

The variation in the z direction also offers the possibility of patterning a full 3-D pattern in a single exposure or set of

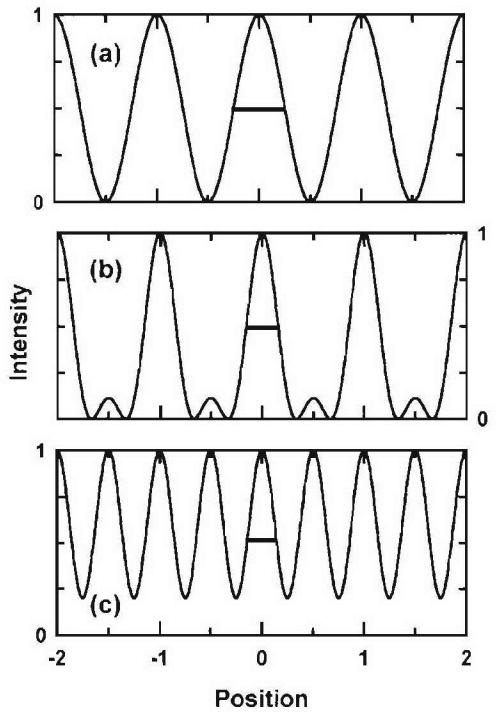


Fig. 6. Aerial image intensity: (a) for a two-beam exposure at twice the period and (b)–(c) at two positions in z for a three-beam exposure. The 50% linewidths are indicated. The three beam exposure offers a smaller linewidth with the same period as the two-beam exposure.

exposures. This possibility will be discussed in more detail in Section IV-D1 as part of the discussion of photonic crystals.

E. Mix-and-Match Approach to Complex Structures

Another straightforward strategy is to use IL to provide large-area periodic patterns and then to use another lithographic technique to add either a small area customization (for example, a defect in a photonic crystal) or large-area aperiodic structures (for example, contact pads and integration with standard microfabrication). In a preliminary investigation of this approach, narrow lines (~200 nm) produced by IL were placed atop a sparse array of much larger lines (2 μm) produced by conventional lithography for electrical test structures [21]. Fig. 7 shows the result. Fig. 7(a) shows a scanning electron micrograph (SEM) of the final structure: the narrow line produced by IL is shown atop the wider pad defined by optical lithography; the next line over misses the pad and has no effect on the measurement. Fig. 7(b) shows the variation of the alignment across the 1-cm-wide die. There is a period mismatch along with random errors. The period mismatch, which corresponds to a $\Delta p/p \sim 6 \times 10^{-5}$, could be eliminated with an adjustment of the IL pitch, the random errors, with a 3σ of only ~140 nm, likely arise from placement errors in the optical lithography mask.

Fig. 8 shows another mix-and-match combination of optical and interferometric lithographies. This was an alternative approach to address the sparse pattern issue discussed above in the context of field-emitter displays [19]. For this integration process, a two lithography-step sequence was

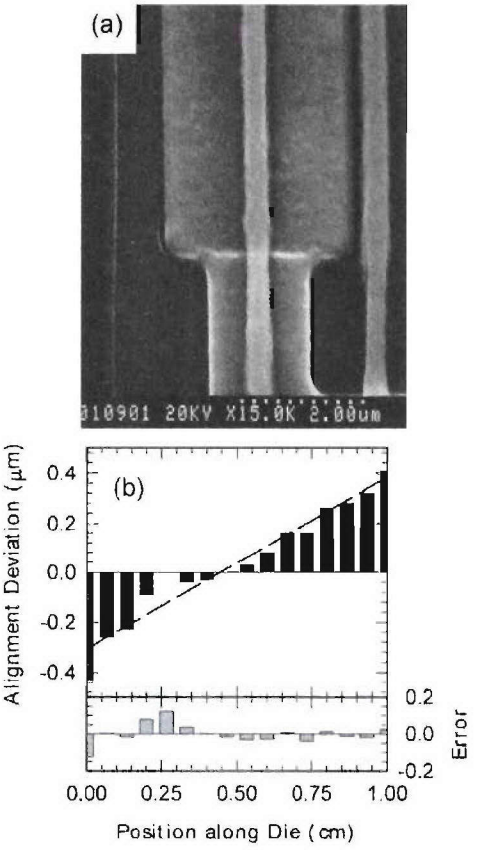


Fig. 7. Demonstration of the integration of OL and IL for an electrical test structure pattern. (a) SEM of the placement of a narrow line defined by IL (200 nm on a 2-μm pitch) atop a wider electrical test structure pattern defined in a separate OL step. (b) Variation of the placement across a 1-cm-wide die. The variation consists of a slight misadjustment of the period ($\sim 6 \times 10^{-5}$, dashed line in the figure) and a random error shown in the bottom part of the figure with a 3σ of 140 nm.

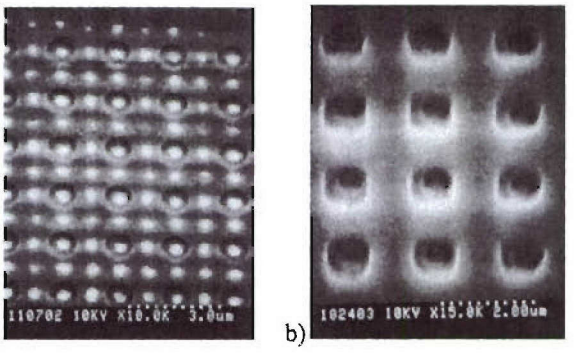


Fig. 8. Sparse array of holes produced by a combination of optical and interferometric lithographies. (a) OL first, IL second. (b) IL first, OL second. In both cases, the first pattern was etched into an oxide film and the second pattern was defined in a separate lithography step.

developed using a sacrificial silicon dioxide layer. A first lithography step, either optical, OL, as in (a) or interferometric, IL, as in (b), was carried out and the results were etched into the sacrificial layer. Then, a second lithography step, using the other lithography technique was carried out to isolate every other hole in the pattern. Alignment was carried out with a grating surrounding the pattern. In (a), a period and phase adjustment very similar to that described

above was carried out. In (b), the alignment was performed using standard, preprinted alignment marks.

F. Nonlinear Process in Lithography and Spatial Frequency Multiplication

As noted in the introduction, the spatial frequencies of the developed pattern can extend well beyond the $2n/\lambda$ bandpass limits of optics as a result of nonlinear processes in the exposure, development and processing—e.g., resulting in transforming a sinusoidal aerial image to a square wave developed resist pattern. Modern resists are engineered to be highly nonlinear—that is to exhibit a sharp threshold between exposed and unexposed regions. Indeed, this is an all-important characteristic that has allowed the development of many of the resolution enhancement techniques such as optical proximity correction and phase shift masks that are routinely employed by the IC industry.

These nonlinear concepts are likely to extend the reach of optical lithography by another factor of at least two, or to scales of ~20- to 10-nm with a 193-nm source. Further similar extensions by integral factors, 3, 4, . . ., are possible but will be increasingly difficult as a result of process, uniformity and edge roughness issues.

In the previous section, we showed that the optical system bandpass limits the 1-D pattern density in a single exposure to $\sim \lambda/\mathrm{NA}$, while the nonlinearities in the processing result in higher harmonics extending in spatial frequency well beyond the diffraction limits of (1). These nonlinearities can be used to extend the available pattern density [22], leading to the claim that "there is no fundamental limit to optical lithography—there are only process control, uniformity and surface roughness issues" [1]. The key is to apply the nonlinearities *between* exposure steps and combine images in such as way as to reduce or eliminate the lower frequency components, leaving the higher density of structures. This is variously know as spatial period division or spatial frequency multiplication depending on whether the focus is on real space (division) or frequency space (multiplication).

A 1-D example of a spatial period division is shown in Fig. 9 to illustrate the general concept. The top panel (a) shows a photoresist pattern atop a sacrificial layer on a substrate. The period of the pattern is limited by the optics to $\lambda/2\mathrm{NA}$; the CD, in contrast, is not limited by the optics and is chosen to be less than $\lambda/8\mathrm{NA}$. This does not violate any optical limits and is, indeed, common practice in IC manufacturing where the transistor gate length is less than 1/2 the pattern period (e.g., 50-nm gates for a 180-nm period in today's microprocessors). In (b), the photoresist pattern has been transferred into the sacrificial layer. In (c), a second photoresist layer has been spun, exposed and developed. The period and CD is the same as in the first case, but the pattern has been shifted by $\lambda/4\mathrm{NA}$ to interpolate the second pattern with the first. Finally this pattern is also transferred into the sacrificial layer [Fig. 9(d)], that layer is then used as a mask to transfer the total pattern into the substrate layers, and finally the sacrificial layer is removed leaving a final pattern

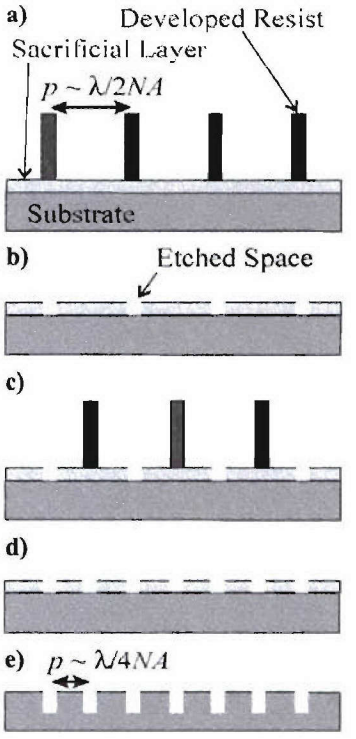


Fig. 9. Illustration of process flow for spatial period division. (a) Expose a develop a line : space pattern with the linewidth $< p/4$ with p the pitch. (b) Transfer this pattern into a sacrificial layer. (c) Expose and develop a second photoresist layer with the same pattern, but shifted by $p/2$. (d) Transfer this pattern into the sacrificial layer. (e) Transfer the composite pattern into the wafer, resulting in a spatial frequency doubled pattern at $p/2$.

at a period of $\lambda/4\mathrm{NA}$, twice as dense as the single exposure optical limit.

The mathematics follows simply

$$\begin{aligned} T(x) &= N[I_1(x)] \otimes N[I_2(x)] \\ &= \frac{a}{2}\left\{\sum_l \frac{\sin\left(\frac{2\pi l \mathrm{NA}a}{\lambda}\right)}{\frac{2\pi l \mathrm{NA}a}{\lambda}}\left[1+(-1)^l\right]\right\} e^{i\frac{4\pi l \mathrm{NA}}{\lambda}x} \\ &= a\sum_l \frac{\sin\left(\frac{4\pi l \mathrm{NA}a}{\lambda}\right)}{\frac{4\pi l \mathrm{NA}a}{\lambda}} e^{i\frac{8\pi l \mathrm{NA}}{\lambda}x}. \end{aligned} \tag{3}$$

The result is the combination of two exposures with the nonlinearities applied to each exposure independently. The symbol used to represent the combination is left ambiguous; in this case, the combination is simple addition. In another case—for example, the use of two resist layers sensitive at different wavelengths—it might be multiplication. The $p/4$ phase shift of the second exposure results in a factor of $(-1)^l$ in the Fourier coefficients, with the net result that all of the odd terms cancel leaving a $\sin(x)/x$ pattern at twice the original pitch or half the period.

This spatial frequency multiplication concept applies equally to arbitrary patterns as to the periodic grating pattern discussed here. The parsing of the pattern into two masks

Table 1
ITRS Requirements and (Imaging) IL Capabilities

Year of Vol. Manufac.	Half-Pitch (nm)	IL Approach	IL Limit (nm) (periodic)	IIL Limit (nm) (arbitrary)
2007	65	Air immersion	48	64
2010	45	H_2O immersion	34	45
2013	32	HI* immersion	27	36
		Air immersion& Freq. Doubling	24	32
2016	22	H_2O immersion & Freq. Doubling	17	23
2019	16	HI* immersion & Freq. Doubling	12	16
		H_2O immersion & Freq. Tripling	12	16

Gray squares are ITRS roadmap requirements.
* HI – High Index immersion (assuming both an immersion liquid index and a glass index of 1.8 @ 193 nm).

becomes a simple coloring problem, with the design rule that no two features on a mask can be closer than twice the final pitch (adjusted for the system magnification). An important difference between the arbitrary and periodic pattern cases is that for a periodic pattern the aerial image contrast is uniform across the pattern, and all that is necessary to ensure a uniform final pattern is to arrange for a uniform illumination; in contrast, for an arbitrary image the aerial image contrast inherently varies across the pattern and additional measures, such as optical proximity correction, to create a more uniform image contrast to maintain the uniformity of the nonlinear processes are necessary.

In principle, this process can be repeated multiple times, for integer spatial frequency multiplications—3, 4, ... The alignment requirements, the image uniformity requirements, and the difficulties of minimizing edge roughness of the resulting patterns will ultimately provide a practical limit [23].

This discussion has so far omitted the important issue of alignment between these multiple exposures. For the periodic pattern case, the image being printed is a large grating, as is well known, the angular resolution of a grating scales as the number of lines in the grating so that alignment schemes based on moiré interference, as discussed above, offer an approach to alignment [24]. Optical aberrations and other contributions to wavefront distortion will introduce positional errors and limit the ability to interpolate patterns. These issues need to be investigated before the ultimate feasibility of these spatial frequency multiplication schemes can be assessed.

G. *Limits of IL*

The semiconductor industry maintains a 15-year plan, the International Technology Roadmap for Semiconductors (ITRS) [25], that projects forward and tries to match industry manufacturing requirements (scaled with a Moore's law 0.7 linear dimension shrink every three years) with available and projected technologies. Table 1 compares the industry requirements as defined in the ITRS with the scales available from IL and from imaging IL (IIL) (discussed below).

For periodic patterns, as used in development of many Si manufacturing processes, the 65-nm hp (half-pitch) requirements are met with IL without the need for immersion techniques. For the 45-nm hp node, water immersion is suitable as demonstrated in Section II-B above. Two alternatives are indicated for reaching the 32-nm hp node: use of a higher index matching fluid (and a higher index final glass element as well), here assumed as an index of 1.8, or a frequency-doubling step from the 65-nm node. Of course, frequency doubling from the 45-nm H_2O immersion result is possible as well. Spatial frequency doubling from the 45-nm hp node will access the 22-nm node. Finally, the 16-nm half-pitch node can be accessed either by frequency doubling from the high index version of the 32-nm node, or by frequency tripling from the 45-nm hp H_2O immersion node. This table gives the very simply derived optical limits. As discussed above, issues of line-edge roughness, alignment, and wavefront distortion are significant and must be carefully investigated to determine ultimate feasibility. Nonetheless, this simple analysis is sufficient to justify the claim that *there are no fundamental limits to optical lithography*! Imaging issues (the right most column in Table 1) will be briefly discussed in Section III.

H. *Directed Self-Assembly*

While the above statement about the optical limits of lithography is correct, the issues associated with line-edge roughness, photoresist mechanical properties, alignment, and wavefront flatness will get continuously more difficult. Self-assembly is a very attractive alternative for extending the spatial scales to subnanometer dimensions. Directed self-assembly using the properties of nanoscale particles and of molecular moieties is an attractive alternative as the lithographic scale decreases below ~20 to 10 nm that both addresses the need for smaller features (extending to the nanometer regime and below) and retains the exquisitely wide scale—from centimeters to nanometers of existing optical lithography [26].

One example of a directed self-assembly process is shown in Fig. 10 which shows ~50-nm silica particles assembled into trenches etched into a Si substrate [27], [28]. This is a very flexible process that can be used to produce nanochannels with controlled porosity and even multilevel structures as shown in Fig. 11.

III. IIL

Optical lithography is the only technology that has been used for volume manufacturing throughout the history of the IC. The parallel nature of lithography in which an entire image is transferred in a single exposure is the primary reason for this dominance. It now seems apparent that optical

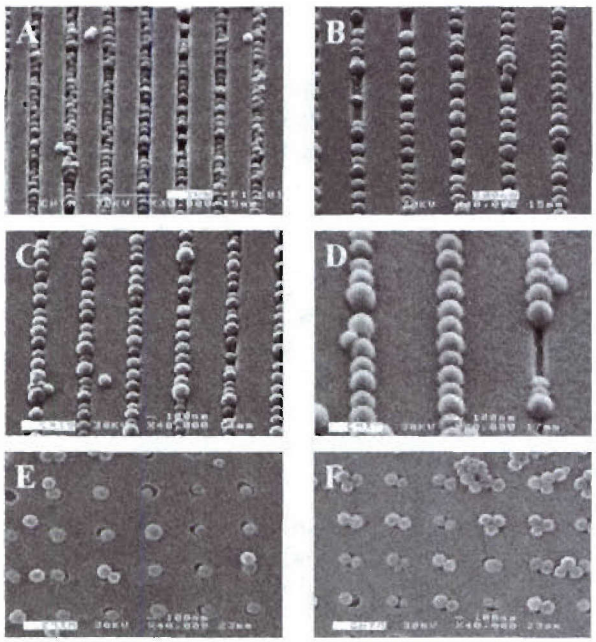


Fig. 10. Examples of directed self-assembly of ~50-nm diameter silica particles into patterns defined in an SiO_2 layer. The particles are deposited by spin coating a colloidal suspension of particles onto an IL patterned wafer. Both 1-D and 2-D patterns are shown. The perfection of the deposition is impacted by the particle size distribution.

lithography—with the extension of water immersion—will continue as the primary manufacturing technology at least through the 45-nm half-pitch node.

Arbitrary images, in principle containing as many spatial frequencies as there are pixels in the image, are significantly more difficult to produce than the simple, single spatial frequency periodic images of IL. The scale of features produced is smaller than the resolution limits of traditional imaging, and many very sophisticated techniques have been introduced to extend the range of feature sizes that can be produced. Optical proximity correction, adding additional subresolution features to the mask to impact the diffraction limited image, off-axis illumination, and phase shift masks have been extensively discussed in the literature and are not covered here [29]–[31].

IIL [32]–[34] is an approach to resolution enhancement that includes both extreme off-axis illumination (tilt of a coherent illumination source to the edge of the image pupil plane) with spatial filters to assure uniform coverage of frequency space. This ensures that the maximum spatial frequency available to the optical system is accessed (corresponding to the interference between coherent beams originating across the diameter of the pupil). In order to print these frequencies in both the x and y spatial directions of the image, both the offset direction and the pupil filter have to be rotated by 90°. Finally, to restore a telecentricity to the image so that deviations from precise focus can be tolerated, additional exposures with illumination from the opposite sides of the pupil are required. This can all be automated within the tool so that exposure times are not impacted by these multiple exposures. An important advantage of IIL for hyper-NA immersion exposures is that the polarization

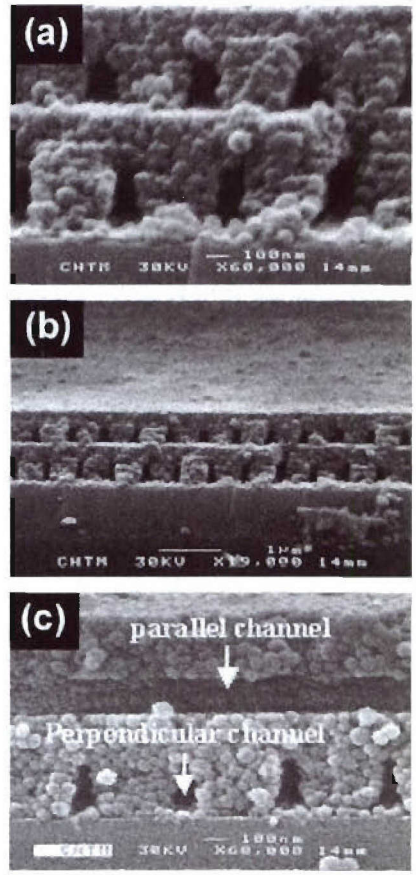


Fig. 11. Multilevel directed self-assembly of silica nanoparticles to form multilevel nanofluidic channels.

of the source can be adjusted at each exposure to ensure that the optimal (TE) polarization is used for both the x and y offsets. This is more difficult to accommodate with phase-shift mask approaches to accessing the limits of image frequency space.

Both OPC and PSM techniques significantly complicate the mask and increase mask costs that are becoming comparable to or even larger than tool costs in a cost-of-ownership calculation. IIL uses simpler binary masks and minimizes the need for OPC; this can be an important cost savings—particularly for small lots as in ASIC production or during initial product development cycles with frequent mask replacements.

The resolution limits for arbitrary patterns are not as small as for periodic patterns as a result of the need to capture the pattern information in the sidebands around the fundamental half-pitch frequency [35]. This reduction in resolution is pattern dependent, a factor of 13% reduction was assumed for the final column of Table 1. Fig. 12 shows simulations for some of the nodes in Table 1. For the 65- and 45-nm hp node, the fidelity of the image is quite good [36]. For the nodes involving spatial frequency multiplication, the variation of the contrast across the image causes more distortion of the pattern. This could be addressed with additional OPC features; some relatively minor OPC has already been applied for the

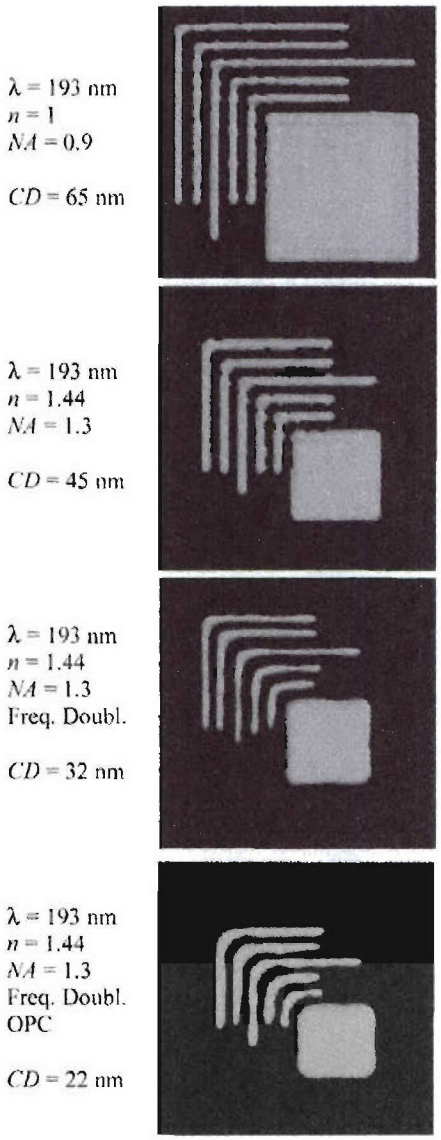


Fig. 12. Simulation of the upcoming ITRS nodes with 193-nm based optical lithography.

modeling of the 22-nm hp node in Fig. 12 [37]. The important result is that there is a path for extending 193-nm based optical lithography all the way to the 16-nm node with relatively small changes to current optical lithography. Investigations are currently underway toward a number of less evolutionary alternatives: EUV; maskless; and nanoimprint lithographies. Ultimately, the manufacturing decision will be based on economics—the most cost-effective solution—including all factors such as throughput and yield—will be adopted by the industry.

IV. Applications of IL

Periodic patterns are suitable—and even desirable—for many experimental nanoscience investigations. The obvious example is a photonic crystal for which periodicity is the primary attribute. In many cases, an important requirement is on the overall sample area. For example, for the study of nanoscale epitaxial crystal growth, it is critical to have large-area samples for detailed characterization, since many semiconductor material probes require large-area samples.

IL provides a unique capability for the inexpensive fabrication of large-area samples with nanoscale features for a wide variety of nanoscience investigations. Because IL is maskless, it is a simple matter to change periodicities, pattern symmetries, line : space ratios, and other pattern details. These periodic patterns find extensive applicability in nanoscale epitaxial growth, in investigations of nanofluidics and of interaction of biomolecular species at the nanoscale, in nanomagnetics, and in nanophotonics, among others. Space does not permit a full recitation of each of these areas. A brief overview of each of these areas is presented to illustrate the broad range of investigations enabled by IL.

A. *Nanoscale Epitaxial Growth*

Epitaxial growth of semiconductors continues to have an enormous impact on the development of information technology. The traditional paradigm of epitaxial crystal growth begins with a nearly perfect crystalline template (the substrate) upon which new materials are deposited in atomic registry with exquisite atomic-level control in the growth direction and with no control whatsoever in the transverse dimensions. When materials with a lattice mismatch of more than ~0.1% are combined, a large strain energy builds up and a prohibitively high defect density results. The situation is entirely different if the links between the two materials are in the form of an array of "bridges" of nanoscale dimensions [38], [39]. In this case, 3-D strain mechanisms are enabled that are forbidden in traditional, large-area epitaxy and the lattice mismatch strain can be localized to the growth interface. Furthermore, during nanoscale growth there are significant modifications to fundamental kinetics and energetics of the crystal growth that lead to new growth modalities that are not available in large-area growth and to the nucleation and propagation of defects that allow defects to be localized at the growth interface. The dimensionless parameters that operate in nanoscale growth are the ratio of the linear pattern dimension to an adatom diffusion length and to the critical thickness for the generation of defects in heterostructure growth.

Patterning can involve masking of the growth surface with a second usually amorphous material such as SiO_2 or the exposing of different crystal faces on the substrate with selectivity coming from preferential growth on one class of facets. An example of growth through a SiO_2 mask is shown in Fig. 13, which shows a sequence of results for the growth of InGaAs on GaAs [40]. Fig. 13(a) shows the starting substrate and 45-nm-thick SiO_2 growth mask patterned at a pitch of 355 nm. Fig. 13(b) is an SEM surface after growth of a 50-nm GaAs buffer layer and a 200-nm $In_{0.06}Ga_{0.94}As$ layer. Except for the incompletely filled hole, which was a rare occurrence across the 2-cm^2 sample, the surface is remarkably smooth and featureless, showing good coalescence between the isolated growth areas. Fig. 13(c) shows a low-resolution cross-section TEM. The SiO_2 mask, the GaAs buffer layer growth, and the InGaAs growth are clearly seen. There are

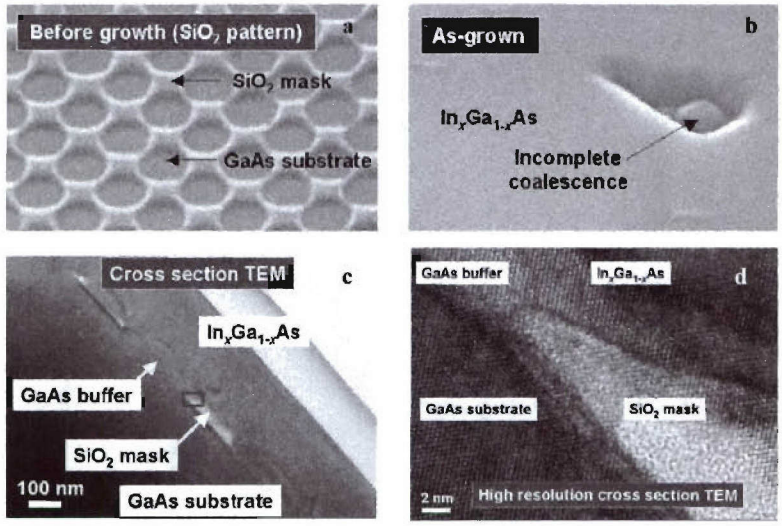


Fig. 13. Nanoscale epitaxial growth of InGaAs on GaAs over a thin SiO_2 mask. The top two panels are SEM pictures showing: (a) the intial SiO_2 mask and (b) the smooth featureless overgrowth. (c) Low-resolution TEM showing the overgrown mask and the GaAs buffer and InGaAs overgrowth. (d) High-resolution TEM showing the coherent interface between the growths and the absence of any long range defects. This InGaAs layer is three times the critical thickness for blanket epitaxy.

no evident long-range defects such as threading dislocations that would be expected for blanket growth, even though the InGaAs layer thickness is three times the critical thickness for this lattice mismatch. Finally, Fig. 13(d) is a high-resolution TEM of the area within the small square in the center of Fig. 13(c). The various films are clearly identified and no extended defect is evident. Both x-ray diffraction and photoluminescence measurements indicate that the InGaAs film is almost fully relaxed. This confirms the initial premise that nanoscale 3-D growth provides strain-relief mechanisms that are not available for traditional blanket-film growth.

An example of selective growth using crystal facets is shown in Fig. 14, which shows the growth of GaN on a nanoscale textured v-groove Si substrate that exhibits both (100) and {111} faces [41], [42]. Fig. 14(a) shows the starting substrate with a pitch of 355 nm. Within a period, two (100) faces and two equivalent {111} faces are exposed. Fig. 14(b) shows the result of ~75 nm of GaN growth. The GaN has nucleated in the hexagonal phase on the two {111} faces, as shown by the opposing white arrows in the figure. There are voids where no material grows at the centers of both (100) faces, clearly evincing the selective nucleation on the {111} surfaces. There is a large density of stacking faults (fluctuations between hexagonal and cubic phases) that provide strain relief of the large lattice mismatch between Si and GaN. After the growth proceeds some small amount, defect-free hexagonal GaN is obtained in two separated nanocrystals located on each Si {111} face. As the growth proceeds, these nanocrystals coalesce, cutting off the material flow to the bottom facet and leaving the void. Symmetry dictates that the GaN crystal cannot maintain the two opposed c-axes, and as a result a cubic symmetry region is established, initially again with a significant density of localized stacking faults. Fig. 14(c) shows a mapping of these regions. Fig. 14(d) is a high-resolution TEM in the central region clearly showing the stacking fault and cubic GaN regions. This spatial phase separation is a demonstration of the radically new and unanticipated growth modalities available with nanoscale growth.

B. Nanofluidics

Microfluidics has become an important research area, particularly for biological separations and other investigations. Very complex systems are being investigated [43]. Nanofluidic systems offer an exciting new domain. This results because the Debye screening length in biologically relevant fluids is ~5 to 50 nm; thus, in a nanofluidic system, the screening from the walls impacts the entire fluid volume. In contrast to the situation in microfluidic systems, where the bulk of the fluid volume is neutral, in nanofluidic channels the entire fluid is charged. This makes it possible to vary the fluid conditions locally along the channel and also strongly modifies electrokinetic transport, since the electroosmotic component extends fully across the channel. In this condition, the fluid flow is modified from the usual plug flow conditions and new phenomena are observed [44], [45].

Fig. 15(a) shows an integrated nanofluidic flow system [46]. Integrated refers to the multiple hierarchical length scales from mm for the pipette interfaces to ~ 100 μm for the microchannels that run between the pipette ports and the ~100-nm-wide nanochannels which are ~1 cm long. Thus the fabrication scales for this chip extend over a range of 10^5! The nanochannels were defined with IL, etched into a Si wafer using and then oxidized to isolate the fluid from the Si and to further narrow the nanochannel dimensions (SiO_2 has a ~40% larger volume than the Si it replaces). The remainder of the structure was fabricated with traditional optical lithography since there are no small features nor is there a critical alignment between the two phases of the

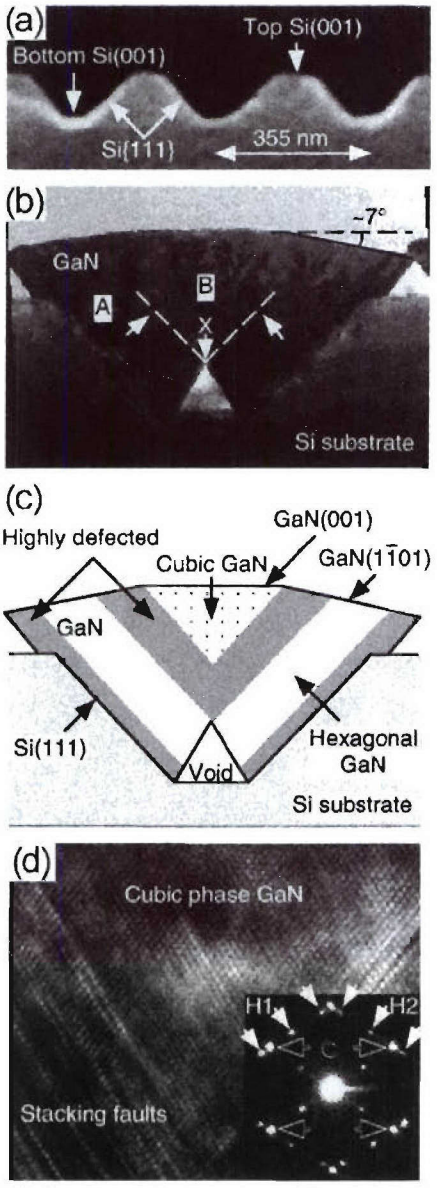


Fig. 14. GaN growth (MOCVD) on a nanoscale patterned {111}-(100) textured Si surface. (a) Patterned substrate with two opposing {111} faces and two (100) faces in each 355-nm period. (b) Result of a growth of ~75 nm of GaN. The GaN nucleates in the hexagonal phase on the two {111} faces with c-axes directed perpendicular to the Si face. (c) Map showing the material evolution. As the two GaN nanocrystals come together, symmetry dictates that a cubic region is formed. There are regions of stacking faults both at the Si : GaN interfaces and again at the hexagonal:cubic interfaces. (d) High-resolution TEM of the cubic region.

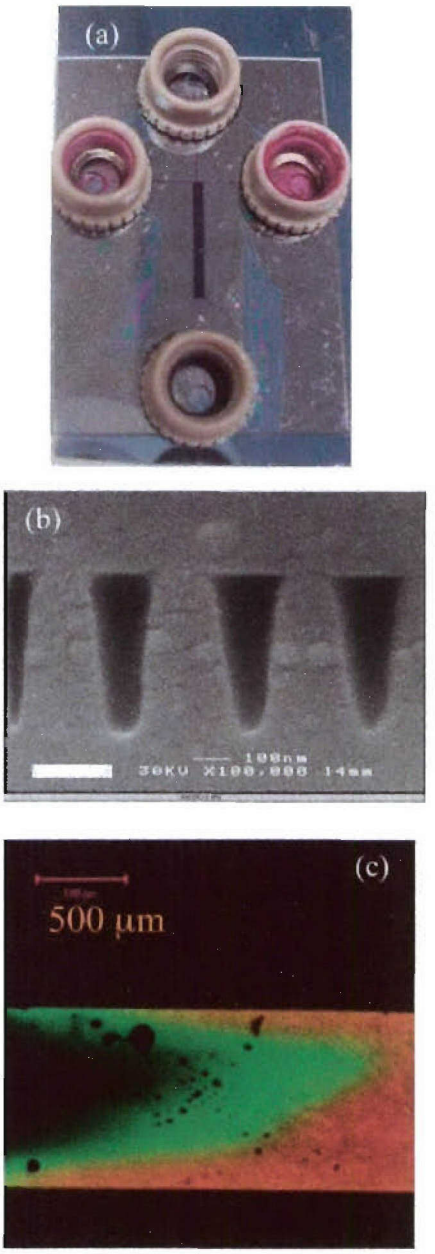


Fig. 15. (a) Optical micrograph of an integrated nanofluidic chip consisting of pipette ports, microchannels in a T configuration, and ~2000 parallel nanochannels (~1 cm long running from top to bottom in the figure). (b) SEM micrograph of a cross section of the nanochannel array. The channels are etched ~ 1 μm deep into Si, oxidized to provide SiO_2 isolation for the fluid, and capped with a pyrex cover slip using anodic bonding. (c) Optical micrograph showing electrokinetic separation of two dyes with different charge states.

fabrication. This is a good example of the mix-and-match fabrication discussed above.

C. *Nanoscale Magnetic Effects*

There has been substantial interest in the magnetic properties of individual single-domain nanomagnetic structures as a result of their potential for increased storage density as compared with traditional multidomain microstructures [47], [48]. IL is a natural technology for the definition of large areas of these patterned magnetic materials [49]–[52]. Interest in this area has been stimulated by the development of lithographically patterned multilayer elements including magnetic tunnel junction (MTJ) [53] and pseudo-spin-valve (PSV) [54], [55] elements that are key components in high-density magnetic RAM (MRAM) architectures.

Superconducting films also show interesting phenomena in the presence of a periodic perturbation such as an array of holes. The holes act as pinning sites for the quantized magnetic flux lines associated with a superconducting film. At low magnetic fields, the flux lines are all associated with these pinning sites and the magnetization shows distinctive

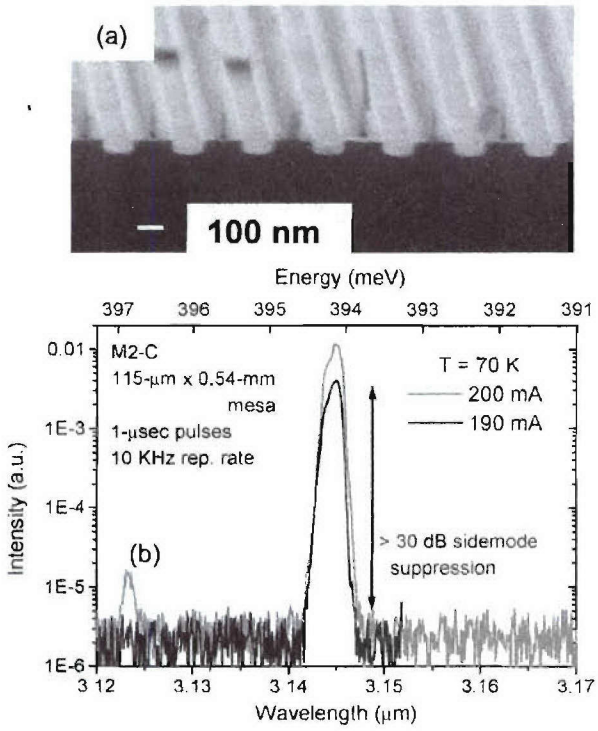


Fig. 16. (a) 465-nm period distributed feedback grating etched into a interband cascade InAs/GaSb laser structure. (b) High resolution output spectrum showing 30 dB side-mode suppression.

structure when the flux density is commensurate with the density of the hole array or is an integral multiple of the hole density so that the flux lattice forms a superstructure locked to the hole array [56]. For a large-area sample, mismatches of the crystal structure between grains nucleated in different regions of the sample, quite analogous to grain boundaries in crystal growth, are observed [57].

D. Nanooptics and Nanophotonics

Nanophotonics is an obvious application area for IL. Often the requirement is for large areas of periodic or quasi-periodic structures. Several immediately evident areas include 1-D, 2-D, and 3-D photonic crystals as well as more complex periodic structures for metamaterial applications such as enhanced transmission and field concentration in arrays of nanoscale metallic structures (holes and toroids) and negative index metamaterials.

1) Distributed Feedback (DFB)/Distributed Bragg Reflector (DBR)/Photonic Crystals: DFB and DBR lasers require simple 1-D gratings. The typical periodicity requirement for a first-order grating is $\lambda/2n$ where λ is the laser wavelength and n is the modal index. For a GaAs laser, $\lambda \sim 860$ nm and $n \sim 3.5$, so $p \sim 125$ nm. As demonstrated earlier in this paper, immersion IL at 193 nm can extend to as small as $p \sim 67$ nm, covering the full range of periods of interest. Fig. 16 shows a typical result for a mid-IR DFB laser [58]. Over 30 dB of side-mode suppression was achieved in this initial, unoptimized experiment.

Two-dimensional photonic crystals in slab geometries have many applications from waveguiding [59] and photonic crystal lasers [60] to photonic crystal light extraction [61]. The required pitch for each of these structures is similar to that for the DFB lasers discussed above, since the same wavelengths and materials are of interest. For photonic crystal LED light extraction, the wavelengths are shorter (~460 nm for blue LEDs) and the refractive index is somewhat lower (~2.5) so the required pitch is as small as 92 nm; again well within the capabilities of immersion IL.

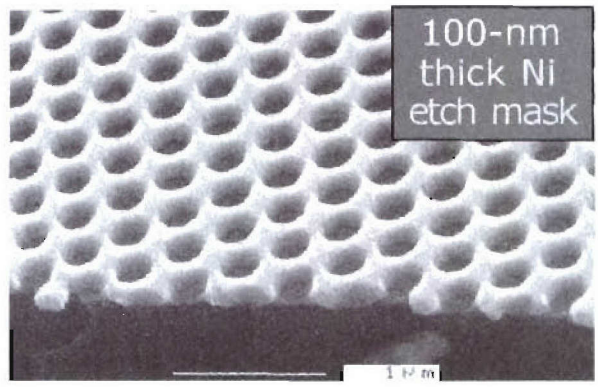


Fig. 17. 2-D patterned Ni etch mask at a hexagonal lattice constant of 405 nm.

There are several approaches to the fabrication of 2-D structures using IL, perhaps the easiest is to use multiple two-beam exposures with appropriate rotation of the wafer between exposures as discussed above in Section II-C. Fig. 17 shows an example of a 2-D hexagonal pattern mask defined in a Ni etch mask deposited onto a GaN wafer with a hexagonal lattice parameter of 405 nm. Pattern transfer becomes a significant issue as the scale of the pattern is reduced. Typically, the thickness of the photoresist layer has to be reduced along with the pattern size to avoid photoresist collapse issues on developing that result from surface tension forces as the resist layer dries. Ultimately, this may force the adoption of a dry developing scheme or a new class of resist with more structural rigidity (higher Young's modulus). Various multilevel resist schemes incorporating a hard mask layer are also possible approaches to this issue.

There are at least two approaches to 3-D structures. Structures can be built up in a layer-by-layer fashion, very analogous to traditional semiconductor manufacturing. In particular, there has been quite a bit of attention devoted to a woodpile structure, with alternating layers of long bars oriented in the x and y directions with each sequential layer in the same direction offset by 1/2 the pitch [62]. Most often the fabrication has used standard semiconductor processing technologies [63], [64]. Alternatively, using multiple-beam, noncoplanar IL the entire 3-D photonic crystal pattern can be produced in a single series of exposures in a thick photosensitive material [65]–[67]. All 14 Bravais lattices and many other space groups are accessible with adjusting the number, intensity and polarizations of the various beams [68], [69]. This interferometric technique has been extended to the fabrication of compound (inter penetrating) lattices such as the woodpile structure and the diamond lattice [66], [70].

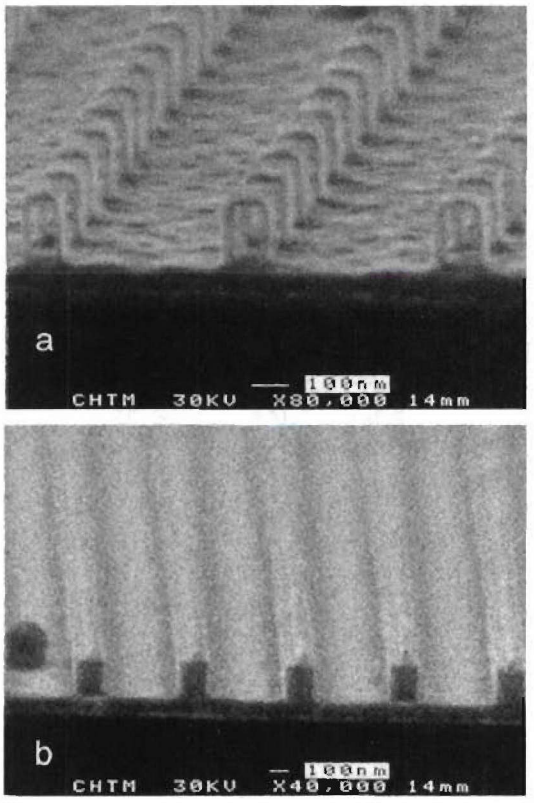


Fig. 18. SEM pictures of the arrays of: (a) 2-D and (b) 1-D staple-shaped nanostructures. The 1-D samples are different from the 2-D sample in that the gold "staples" are continuous in the y direction and the loops are filled with Si_3N_4.

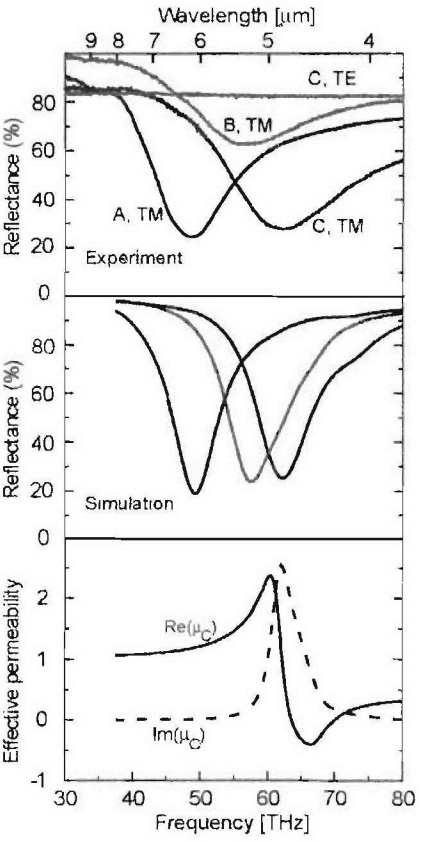


Fig. 19. Experimental (top) and simulation (middle) results for the reflectivity as a function of frequency for three different structures. The resonance frequency is a function of the nanostructure parameters and is independent of array period, which is the same for all three structures. The resonance is observed only for TM polarization, i.e., incident magnetic field coupled into the inductive structure. Only one TE polarization result is shown. The bottom panel shows the effective permeability extracted from the model for the highest frequency resonance.

2) Metamaterials and Negative Refractive Index: Metals naturally provide a negative permittivity at frequencies below the plasma frequency ω_p as a consequence of the free electron response function given by

$$\varepsilon_{\text{plasma}} = 1 - \frac{\omega_p^2}{\omega(\omega + i\gamma)} \tag{4}$$

where γ is the electronic scattering frequency. There is no comparable naturally occurring negative magnetic susceptibility. However, LC resonant (tank) circuits provide a region of negative permeability around their resonance frequency. If an ensemble of such resonant structures with dimensions much less than the wavelength is aggregated into a material with inter structure distances of much less than a wavelength, then an effective medium results with a negative permeability over a limited frequency range. The permeability in this case is dependent upon the properties of the individual resonances and is independent of the details, such as periodicity, of their arrangement into a material. Such a material is classified as a metamaterial. Its permittivity (ε) and permeability (μ) result from the fabricated resonant structures.

Fig. 18 shows an example of magnetic metamaterial structures fabricated using IL [71]. The major feature is a loop formed by shadow evaporation over a 1-D patterned Si_3N_4 sacrificial layer with a 600-nm pitch. In the top panel, this has been segmented into an array of "staples" and the nitride has been selectively removed. The bottom panel shows a 1-D array with the nitride still in place. Fig. 19 shows the measured (top) and simulated (middle) responses for a number of structures with different structural dimensions, but with the same pitch. The response is clearly dependent on the individual structural parameters satisfying the definition of a metamaterial. Finally, the bottom panel shows the permeability derived from the model for the highest frequency resonance. A region of negative $\text{Re}(\mu)$ is clearly established. Other reports of negative permeability at IR frequencies [72] have relied on e-beam lithography to define the smallest feature and, consequently, have been restricted to small samples. In contrast, this process relies on deposition (of a dielectric spacer and of the gold film) to define the smallest features and samples are several square centimeters in size, limited by convenience of handling rather than by cost and time of pattern definition. This illustrates one of the major advantages of a parallel optical lithography approach to nanophotonic structures.

There is great interest in the fabrication of negative index materials [73]—combining a negative permeability,

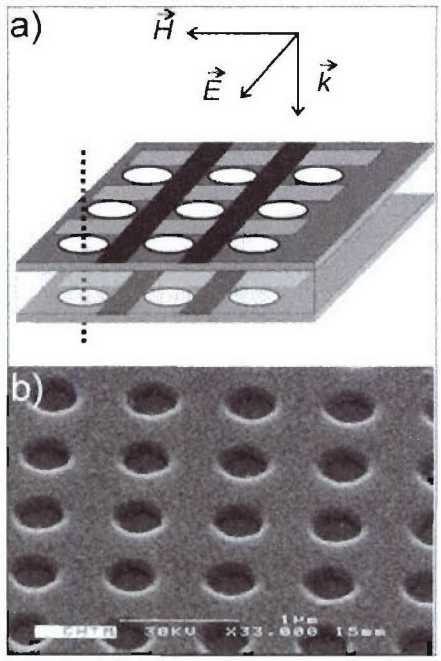


Fig. 20. (a) Negative index material at 2 μm consisting of a Au/Al2O3/Au film stack on a glass substrate perforated with a 2-D array of holes at a pitch of 0.8 μm. The green shaded regions contribute to the permeability while the blue shaded regions are responsible for the negative permittivity. (b) SEM micrograph of the structure.

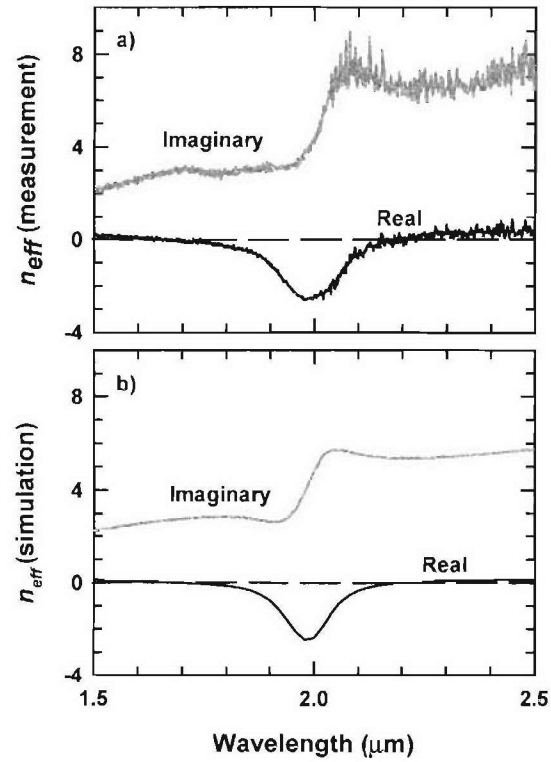


Fig. 21. (a) Measured and (b) simulated real and imaginary parts of the refractive index for the structure of Fig. 15. There is a region of negative index around 2 μm. The maximal real part of the negative index is around -2 while the imaginary part is 3 to 4, indicating a significant loss.

as shown above, with a negative permittivity usually from electron plasma response of a metal film. The interest in this topic has increased dramatically as a result of the prediction of important new effects, including diffractionless imaging, in such a material [74]. A particularly simple realization of such a material, shown in Fig. 20, is a metal/dielectric/metal/substrate multilayer stack perforated by a 2-D hole array [75]. For the incident polarization indicated in the cartoon, the magnetic response—very similar to that discussed above—results from the distributed inductance/capacitance associated with the two separated metal films. Fig. 21 shows the measurement and modeling of the refractive index, clearly showing a negative index over a limited wavelength range. Importantly, in this experiment, the refractive index was obtained uniquely from measurements of both the amplitude and the phase of both the film reflectance and transmission. For the simulation the only adjustable parameter was the electronic scattering frequency in the metal that was taken as approximately 3× the literature value for bulk Au based on fitting the transmission measurements. There is remarkably good agreement between the measurement and the modeling. There remains significant loss in this material with the $\mathrm{Im}(n) > |\mathrm{Re}(n)|$ across the resonance. Detailed investigation shows that for this structure while the permeability shows a resonance response, its real part does not become negative and the negative index is a consequence of the combination of negative real part of the permittivity and a positive imaginary part of the permeability at the resonance. More optimal structures have been designed that promise a significant improvement in the quality of the negative index material ($|\mathrm{Re}(n)/\mathrm{Im}(n)|$) [76].

IL is especially attractive for the fabrication of this class of negative index materials. As has been amply demonstrated earlier, IL is ideally suited to the fabrication of large arrays of 2-D structures such as the pattern of holes. The fabrication in this case was simply to create a 2-D post array, etch through the underlying ARC layer, and then deposit the three films sequentially and dissolve away the photoresist to leave the final structure. Sample dimensions were $\sim 2 \times 2$ cm^2. This simplicity of fabrication of large areas of materials offers promise both for the detailed study and optimization of these effects and also for manufacturing of large areas of nanoscale structures for practical applications.

V. Conclusion

Nanoscale fabrication is a critical aspect of any nanotechnology. Optical lithography is the only large-scale manufacturing technique that the IC industry has ever used for pattern definition. Despite continuing predictions of its demise, optical lithography continues to be extended, most recently with immersion techniques that gain by the refractive index of the material between the lens and the photoresist—initially H_2O with an index of 1.44 at 193 nm. It now appears likely that a hyper-NA (NA > 1) optical lithography will address the industry needs for the 45-nm half-pitch node. Further extensions are possible and are being actively investigated for even finer lithographic patterns.

While this is good news for the semiconductor industry, the cost of these optical lithography tools, ~$20 million to

$30 million, makes them inaccessible to a typical research environment. Much of this cost is associated with the need of the industry to produce fully arbitrary patterns at very high throughputs. Current steppers also require quite expensive masks (~$1 million to $2 million for a microprocessor mask set) to define the patterns and are capable of a throughput of ~85 wafers per hour, each with ~125 dies (22×33 mm^2) across a 300-mm-diameter wafer; this corresponds to an average sustained data throughput rate of $\sim 10^{12}$ b/s.

Fortunately, nanoscience research often requires less flexibility—for example, periodic patterns—and always requires less throughput. The needs of much of nanoscience research can be met at a substantially lower cost. IL, the interference of a small number of coherent laser beams, readily produces large-area patterns (several square centimeters) at the same, and even smaller scales than are available from commercial steppers. With an ArF laser source at 193 nm and H_2O immersion, the smallest half-pitch (equal line : space) pattern accessible extends to 34 nm. Spatial frequency multiplication, taking advantage of nonlinearities in the processing, allows extensions by a factor of two or more, extending this capability ultimately to below 10 nm. Importantly, IL is a maskless approach to lithography that greatly extends flexibility without requiring expensive masks.

Several different techniques were discussed that extend the flexibility of IL. Multiple IL exposures, multiple-beam IL, and mix-and-match with both high resolution (e-beam) and with lower resolution (proximity optical lithography) all offer complimentary capabilities. Taken together, these techniques provide a facile suite of techniques applicable to a broad range of nanoscience applications, with a resolution capability that rivals standard nanofabrication techniques such as electron-beam lithography, but with a large-area capability that often allows additional diagnostic techniques that are not available for very small samples—and of course can sustain volume manufacturing.

Directed self-assembly, the combination of self-assembly to define features extending to molecular dimensions while retaining the organization across multiple length scales from nanometers to centimeters offered by optical lithography, is a promising future direction. Ultimately, this provides a pathway to a subnanometer patterning regime.

IL provides the limiting resolution of optical lithography, but the periodicity poses a problem for some applications, especially for the IC industry. IIL was introduced as an extension of IL to arbitrary patterns. Essentially, IIL is a combination of extreme off-axis illumination, to reach the highest spatial frequencies permitted by a given optical system, along with imaging pupil plane filters, to avoid multiple counting of low frequency information and thereby to balance the image frequency response. With the addition of the concept of spatial frequency multiplication, IIL offers a route for optical lithography to the 16-nm half-pitch limit of the current industry manufacturing roadmap extending to 2019.

Numerous application areas for nanoscale patterns were discussed. Nanoscale heteroepitaxy provides a new paradigm for heterostructure crystal growth. The use of nanoscale seeds for nucleation of many small crystals provides new capabilities for the relief of lattice-mismatch strain. The important dimensionless parameters are: 1) the ratio of the pattern linear dimension to the adatom mean-free path so that an adsorbed atom can sample the entire growing crystal for a preferred, low-energy incorporation site and 2) the ratio of the pattern linear dimension to the critical thickness before the generation of defects in large-area heterostructure growth. These techniques are applicable to both MBE and MOVPE, the dominant growth techniques for advanced heterostructure devices. In the case of MBE, selective area growth, faceting, and lateral overgrowth and coalescence—all of which are rarely, if ever, observed for large-area ($\gtrsim 1$-μm scale) patterning—were clearly observed, illustrating the fundamental difference afforded by nanoscale patterning. Two examples were given: 1) growth of a relaxed InGaAs layer on a GaAs substrate using a 2-D SiO_2 masking layer and 2) spatial phase separation of the cubic and hexagonal phases of GaN grown on a (100)/{111} patterned Si wafer.

Nanofluidic transport and separation, particularly of biomolecules, is another exciting application for nanoscale patterning. Here the important dimensionless parameter is the ratio of the linear pattern dimension to the Debye screening length in the ionic fluids important for biology. A double layer of opposite charges forms at the wall of a nanochannel filled with an ionic fluid. Electrokinetic (electroosmosis and electrophoresis) transport is impacted by the extent of this double layer. This Debye length is of the order of 10 to 100 nm for most situations relevant to biology, which sets the scale differentiating nanochannels from the much more widely studied microchannels where the screening length is a small fraction of the Debye length. An integrated chip was demonstrated that combines features ranging from 50 nm to 1 cm—a five order of magnitude range! Initial flow measurements were presented demonstrating the separation of two dyes with different charge states.

Magnetic storage has long been migrating toward smaller features and higher densities and is now entering an era of single-domain, nanoscale, multilayer structures. Again, IL is a powerful fabrication technique for the production of large areas and for ultimate manufacturing of devices and circuits such as MRAMs.

Nanooptics and nanophotonics are natural applications for IL. Distributed feedback and distributed Bragg reflector lasers, requiring nanoscale 1-D patterning have long been a mainstay for the spectroscopic control of diode lasers. Recently, there has been extended interest in the use of 2-D patterning for photonic crystals to control optical properties. This extends from photonic crystal waveguides with missing or modified rows of holes (posts) to guide optical beams to the use of photonic crystals for light extraction from high-index, semiconductor-based LEDs. Three-dimensional photonic crystals can be fabricated both with layer-by-layer techniques and by using multiple IL beams with varying azimuthal angles. Metamaterials and plasmonics are another area of great current interest. Using simple IL procedures, large areas of resonant magnetically coupled resonators (tank circuits) with resonances throughout the mid-IR spec-

tral region were demonstrated. Very recently, a large-area negative index material at 2 μm was demonstrated using a relatively simple IL implementation.

By now the message should be clear. IL provides a readily available, inexpensive, large-area route to nanoscale patterning of great importance to many areas in nanotechnology. Combining IL with self-assembly techniques in "directed self-assembly" extends the reach of patterning capabilities truly to molecular scales. There is a vast range of possibilities across many different fields and much to be learned from the application and extension of the techniques presented here.

ACKNOWLEDGMENT

The author would like to thank the many students, postdocs, and colleagues who have contributed to the development of the concepts presented in this manuscript. These include A. Biswas, A. Devine, W. Fan, A. Frauenglass, S. Han, Y. Kuznetsova, S. C. Lee, D. Li, G. P. Lopez, S. Naqvi, K. J. Malloy, J. R. McNeil, A. Neumann, M. O'Brien, E. Rabinovitch, A. Raub, S. Smolev, D. Xia, S. Zaidi, J.-L. Zhang, and S. Zhang.

REFERENCES

[1] S. R. J. Brueck, "There are no fundamental limits to optical lithography," in *International Trends in Applied Optics. International Commission on Optics*. Bellingham, WA: SPIE Press, 2002, pp. 85–110.

[2] M. J. Beesley and J. G. Castledine, "The use of photoresist as a holographic recording medium," *Appl. Opt.*, vol. 9, p. 2720, 1970.

[3] R. A. Bartolini, "Characteristics of relief phase holograms recorded in photoresists," *Appl. Opt.*, vol. 13, pp. 129–139, 1974.

[4] L. F. Johnson, G. W. Kammlott, and K. A. Ingersoll, "Generation of periodic surface corrugations," *Appl. Opt.*, vol. 17, p. 1165, 1978.

[5] S. H. Zaidi and S. R. J. Brueck, "High aspect-ratio holographic photoresist gratings," *Appl. Opt.*, vol. 27, pp. 2999–3002, 1988.

[6] M. L. Schattenberg, E. H. Anderson, and H. I. Smith, "X-ray/VUV transmission gratings for astrophysical and laboratory applications," *Phys. Scr.*, vol. 41, pp. 13–20, 1990.

[7] A. Yen, E. H. Anderson, R. A. Ghanbari, M. L. Schattenburg, and H. I. Smith, "Achromatic holographic configuration for 100-nm-period lithography," *Appl. Opt.*, vol. 31, pp. 4540–4545, 1992.

[8] B. W. Smith, A. Bourov, H. Kang, F. Cropanese, Y. Fan, N. V. Lafferty, and L. V. Zavyalova, "Water immersion lithography at 193 nm," *J. Microlith. Microfab. Microsys.*, vol. 3, pp. 44–51, 2004.

[9] C. V Shank and R. V Schmidt, "Optical technique for producing 0.1-μm periodic surface structures," *Appl. Phys. Lett.*, vol. 23, pp. 154–156, 1973.

[10] W. T. Tsang and S. Wang, "Simultaneous exposure and development technique for making gratings in positive photoresist," *Appl. Phys. Lett.*, vol. 23, pp. 196–198, 1974.

[11] J. A. Hoffnagle, W. D. Hinsberg, M. Sanchez, and F. A. Houle, "Liquid immersion deep-ultraviolet interferometric lithography," *J. Vac. Sci. Technol.*, vol. B17, pp. 3306–3309, 1999.

[12] M. Switkes and M. Rothschild, "Immersion lithography at 157 nm," *J. Vac. Sci. Technol.*, vol. B19, pp. 2353–2356, 2001

[13] J. H. Burnett and S. G. Kaplan, "Measurement of the refractive index and thermo-optic coefficient of water near 193 nm," *J. Microlith. Microfab. Microsys.*, vol. 3, pp. 68–72, 2004.

[14] A. K. Raub and S. R. J. Brueck, "Deep UV immersion interferometric lithography," *Proc. SPIE*, vol. 5040, pp. 667–678, 2003.

[15] A. K. Raub, A. Frauenglass, S. R. J. Brueck, W. Conley, R. Dammel, A. Romano, M. Sato, and W. Hinsberg, "Imaging capabilities of resist in deep-UV liquid immersion interferometric lithography," *J. Vac. Sci. Technol.*, vol. 22, pp. 3459–3464, 2004.

[16] A. Biswas and S. R. J. Brueck, "Simulation of the 45-nm half-pitch node with 193-nm immersion lithography," *J. Microlith. Microfab. Microsys.*, vol. 3, pp. 35–43, 2004.

[17] S. H. Zaidi and S. R. J. Brueck, "Multiple-exposure interferometric lithography," *J. Vac. Sci. Technol.*, vol. B11, pp. 658–666, 1993.

[18] J. W. Goodman, *Introduction to Fourier Optics* 2nd ed. New York: McGraw-Hill, 1996.

[19] X. Chen, S. H. Zaidi, S. R. J. Brueck, and D. J. Devine, "Interferometric lithography of sub-micrometer sparse hole arrays for field-emission display applications," *J. Vac. Sci. Technol.*, vol. B14, pp. 3339–3349, 1996.

[20] S. H. Zaidi, A. Frauenglass, and S. R. J. Brueck, "Moiré interferometric alignment and overlay techniques," *Proc. SPIE*, vol. 2196, pp. 371–382, 1994.

[21] S. H. Zaidi, S. R. J. Brueck, T. Hill, and R. N. Shagam, "Mix-and-match interferometric and optical lithographies for nanoscale structures," *Proc. SPIE*, vol. 3331, pp. 406–413, 1998.

[22] S. H. Zaidi and S. R. J. Brueck, "Nonlinear processes to extend interferometric lithography," *Proc. SPIE*, vol. 3676, pp. 371–378, 1999.

[23] J. A. Hoffnagle, W. D. Hinsberg, F. A. Houle, and M. I. Sanchez, "Use of interferometric lithography to characterize the spatial resolution of a photoresist film," *J. Photopolym. Sci. Technol.*, vol. 16, pp. 373–379, 2003.

[24] S. S. H. Naqvi, S. H. Zaidi, S. R. J. Brueck, and J. R. McNeil, "Diffractive techniques for lithographic process monitoring and control," *J. Vac. Sci. Technol.*, vol. B12, pp. 3600–3606, 1994.

[25] "International Technology Roadmap for Semiconductors," [Online]. Available: http://public.itrs.net

[26] A. Hatzor and P. S. Weiss, "Molecular rulers for scaling down nanostructures," *Science*, vol. 291, pp. 1019–1020, 2001.

[27] D. Xia, D. Li, A. Biswas, and S. R. J. Brueck, "Directed self-assembly of silica nanoparticles on nanoscale patterned surfaces by spin-coating," *Adv. Mater.*, vol. 16, pp. 1427–1432, 2004.

[28] D. Xia and S. R. J. Brueck, "Lithographically directed deposition of silica nanoparticles using spin coating," *J. Vac. Sci. Technol.*, vol. 22, pp. 3415–3420, 2004.

[29] A. K.-K. Wong, *Resolution Enhancement Techniques in Optical Lithography*. Bellingham, WA: SPIE Press, 2001.

[30] H. J. Levinson, *Principles of Lithography* 2nd ed. Bellingham, WA: SPIE Press, 2005.

[31] For a compilation of much of the original literature, see, Selected Papers on Resolution Enhancement Techniques in Optical Lithography F. M. Schellenberg Ed., ser. SPIE Milestone Series 178, Bellingham, WA, SPIE Press, 2004.

[32] X. Chen and S. R. J. Brueck, "Imaging interferometric lithography—approaching the resolution limits of optics," *Opt. Lett.*, vol. 24, pp. 124–126, 1999.

[33] ——, "Experimental comparison of off-axis illumination and imaging interferometric lithography," *J. Vac. Sci. Technol.*, vol. B17, pp. 921–929, 1999.

[34] A. Frauenglass, S. Smolev, A. Biswas, and S. R. J. Brueck, "244-nm imaging interferometric lithography," *J. Vac. Sci. Technol.*, vol. 22, pp. 3465–3469, 2004.

[35] S. R. J. Brueck and X. Chen, "Spatial frequency analysis of optical lithography resolution enhancement techniques," *J. Vac. Sci. Technol.*, vol. B17, pp. 908–921, 1999.

[36] A. Biswas and S. R. J. Brueck, "Simulation of the 45-nm half-pitch node with 193-nm immersion lithography," *J. Microlith. Microfab. Microsys.*, vol. 3, pp. 35–43, 2004.

[37] S. R. J. Brueck and A. M. Biswas, "Extension of 193-nm immersion optical lithography to the 22-nm half-pitch node," *Proc. SPIE*, vol. 5377, pp. 1315–1322, 2004.

[38] S. Luri and E. Suhir, "New approach to the high quality epitaxial growth of lattice-mismatched materials," *Appl. Phys. Lett.*, vol. 49, pp. 140–142, 1986.

[39] D. Zubia, S. H. Zaidi, S. R. J. Brueck, and S. D. Hersee, "Nanoheteroepitaxial growth of GaN on Si by organometallic vapor phase epitaxy," *Appl. Phys. Lett.*, vol. 76, pp. 858–860, 2000.

[40] S. C. Lee, L. R. Dawson, B. Pattada, S. R. J. Brueck, Y.-B. Jiang, and H. F. Xu, "A strain-relieved, dislocation-free InxGa1-xAs (100) heterostructure by nanoscale patterned growth," *Appl. Phys. Lett.*, vol. 85, pp. 4181–4183, 2004.

[41] S. C. Lee, X. Y Sun, S. D. Hersee, F. Xu, and S. R. J. Brueck, "Spatial phase separation of GaN selectively grown on a nanoscale faceted Si surface," *Appl. Phys. Lett.*, vol. 84, pp. 2079–2082, 2004.

[42] S. C. Lee, B. Pattada, X. Y Sun, S. D. Hersee, Y.-B. Jiang, H. Xu, and S. R. J. Brueck, "Nanoscale spatial phase modulation of GaN on a 355-nm period array of V-grooves fabricated in a Si(001) substrate," *IEEE J. Quantum Electron.*, vol. 41, no. 4, pp. 596–605, Apr. 2005.
[43] D. J. Harrison, K. Fluri, K. Seiler, Z. Fan, C. S. Effenhauser, and A. Manz, "Micromachining a miniaturized capillary electrophoresis-based chemical analysis system on a chip," *Science*, vol. 261, pp. 895–897, 1993.
[44] H. Daiguji, P. Yang, and A. Majumdar, "Ion transport in nanofluidic channels," *Nano Lett.*, vol. 4, pp. 137–142, 2004.
[45] D. Stein, M. Kruithof, and C. Dekker, "Surface-charge-governed ion transport in nanofluidic channels," *Phys. Rev. Lett.*, vol. 93, p. 035901, 2004.
[46] M. J. O'Brien, P. Bisong, L. K. Ista, E. M. Rabinovitch, A. L. Garcia, S. S. Sibbett, G. P. Lopez, and S. R. J. Brueck, "Fabrication of an integrated nanofluidic chip using interferometric lithography," *J. Vac. Sci. Technol.*, vol. 21, pp. 2941–2945, 2003.
[47] S. Y Chou, M. S. Wei, P. R. Krauss, and P. B. Fischer, "Single-domain magnetic pillar array of 35 nm diameter and 65 Gbits/in2 density for ultrahigh density quantum magnetic storage," *J. Appl. Phys.*, vol. 76, pp. 6673–6675, 1994.
[48] S. Y. Chou, "Patterned magnetic nanostructures and quantized magnetic disks," *Proc. IEEE*, vol. 85, no. 4, pp. 652–671, Apr. 1997.
[49] G. Meier, M. Kleiber, D. Grundler, D. Heitmann, and R. Wiesendanger, "Vertical polarization of quantum magnets in high density arrays of nickel dots with small height-to-diameter ratio," *Appl. Phys. Lett.*, vol. 72, pp. 2168–2170, 1998.
[50] M. A. M. Haast, J. R. Schuurbuis, L. Abelmann, J. C. Lodder, and T L. Popma, "Reversal mechanism of submicron patterned CoNi/Pt multilayers," *IEEE Trans. Magn.*, vol. 34, no. 4, pp. 1006–1008, Jul. 1998.
[51] M. Theilen, S. Kirsch, H. Weinforth, A. Carl, and E. F. Wassermann, "Magnetization reversal in nanostructured Co/Pt multilayer dots and films," *IEEE Trans. Magn.*, vol. 34, no. 4, pp. 1009–1011, Jul. 1998.
[52] C. A. Ross, S. Haratani, F. J. Castaño, Y Hao, M. Hwang, M. Shima, J. Y Cheng, B. Vögeli, M. Farhoud, M. Walsh, and H. I. Smith, "Magnetic behavior of lithographically patterned particle arrays," *J. Appl. Phys.*, vol. 91, pp. 6848–6853, 2002.
[53] S. S. P. Parkin, K. P. Roche, M. G. Samant, P. M. Rice, R. B. Beyers, R. E. Scheuerlin, E. J. O'Sullivn, S. L. Brown, J. Bucchigano, D. W. Abraham, Y Lu, M. Rooks, P. L. Trouilloud, R. A. Wanner, and W. J. Gallagher, "Exchange-biased magnetic tunnel junctions and application to nonvolatile magnetic random access memory," *J. Appl. Phys.*, vol. 85, pp. 5828–5833, 1999.
[54] B. A. Everitt, A. V. Pohm, R. S. Beech, A. Fink, and J. M. Daughton, "Pseudo spin valve MRAM cells with sub-micrometer critical dimension," *IEEE Trans. Magn.*, vol. 34, no. 4, pp. 1060–1062, Jul. 1999.
[55] X. Zhu, P. Grütter, Y. Hao, F. J. Castaño, S. Haranti, C. A. Ross, B. Vögeli, and H. I. Smith, "Magnetization switching in 70-nm-wide pseudo-spin-valve nanoelements," *J. Appl. Phys.*, vol. 93, pp. 1132–1136, 2003.
[56] V. Metlushko, U. Welp, G. W. Crabtree, R. Osgood, S. D. Bader, L. E. DeLong, Z. Zhang, S. R. J. Brueck, B. Ilic, K. Chung, and P. J. Hesketh, "Interstitial flux phases in a superconducting niobium film with a square lattice of artificial pinning centers," *Phys. Rev.*, vol. B60, p. 12585, 1999.
[57] S. B. Field, S. S. James, J. Barentine, V. Metlushko, G. Crabtree, H. Shtrikman, B. Ilic, and S. R. J. Brueck, "Vortex configurations, matching, and domain structure in large arrays of artificial pinning centers," *Phys. Rev. Lett.*, vol. 88, p. 067003, 2002.
[58] J. L. Bradshaw, J. D. Bruno, J. T Pham, D. E. Wortman, S. Zhang, and S. R. J. Brueck, "Single-longitudinal-mode emission from interband cascade DFB laser with a grating fabricated by interferometric lithography," *Proc. Inst. Electr. Eng.—Optoelectron.*, vol. 150, pp. 288–292, 2003.
[59] A. Yariv, Y Xu, and S. Mookherjea, "Transverse Bragg resonance laser amplifier," *Opt. Lett.*, vol. 28, pp. 176–178, 2003.
[60] O. Painter, R. K. Lee, A. Scherer, A. Yariv, J. D. O'Brien, P. D. Dapkus, and I. Kim, "Two-dimensional photonic band-gap defect mode laser," *Science*, vol. 284, pp. 819–1821, 1999.
[61] J. J. Wierer, M. R. Krames, J. E. Epler, N. F. Gardner, J. R. Wendt, M. M. Sigalas, S. R. J. Brueck, D. Li, and M. Shagam, "III-Nitride LED's with photonic crystal structures," *Proc. SPIE*, vol. 5739, pp. 102–107, 2005.
[62] K. M. Ho, C. T Chan, C. M. Soukoulis, R. Biswas, and M. Sigalas, "Photonic band-gaps in 3-dimensions—new layer-by-layer periodic structures," *Solid State Commun.*, vol. 89, pp. 413–416, 1994.
[63] N. Yamamoto, S. Noda, and A. Sasaki, "New realization method for three-dimensional photonic crystal in the optical wavelength region: experimental consideration," *Jpn. J. Appl. Phys.*, vol. 36, pp. 1907–1911, 1997.
[64] S. Y Lin, J. G. Fleming, D. L. Heatherington, B. K. Smith, R. Biswas, M. M. Sigalas, W. Zubrzycki, S. R. Kurtz, and J. Bur, "A three dimensional photonic crystal operating at infrared wavelengths," *Nature (London)*, vol. 394, pp. 251–253, 1998.
[65] M. Campbell, D. N. Sharp, M. T Harrison, R. G. Denning, and A. J. Turberfield, "Fabrication of photonic crystals for the visible spectrum by holographic lithography," *Nature (London)*, vol. 404, pp. 53–56, 2000.
[66] S. Shoji, H. B. Sun, and S. Kawata, "Photofabrication of woodpile three-dimensional photonic crystals using four-beam laser interference," *Appl. Phys. Lett.*, vol. 83, pp. 608–610, 2003.
[67] X. Wang, J. F. Xu, H. M. Shu, Z. H. Zeng, Y. L. Chen, H. Z. Wang, Y. K. Pang, and W Y. Tam, "Three-dimensional photonic crystals fabricated by visible light holographic lithography," *Appl. Phys. Lett.*, vol. 82, pp. 2212–2214, 2003.
[68] L. Z. Cai, X. L. Yang, and Y. R. Wang, "Formation of three-dimensional periodic microstructures by interference of four noncoplanar beams," *J. Opt. Soc. Amer.*, vol. A19, pp. 2238–2244, 2002.
[69] C. K. Ullal, M. Maldovan, M. Wohlgomuth, and E. L. Thomas, "Triply periodic bicontinuous structures through interference lithography: a level set approach," *J. Opt. Soc. Amer.*, vol. A20, pp. 948–954, 2003.
[70] Y.-C. Zhong, S.-A. Zhu, and H.-Z. Wang, "Fabrication of compound lattice by holographic lithography," *Chin. Phys. Lett.*, vol. 22, pp. 369–373, 2005.
[71] S. Zhang, W. Fan, A. Frauenglass, B. Minhas, K. J. Malloy, and S. R. J. Brueck, "Demonstration of mid-infrared resonant magnetic nanostructures exhibiting a negative permeability," *Phys. Rev. Lett.*, vol. 94, p. 037402, 2005.
[72] T. J. Yen, W. J. Padilla, N. Fang, D. C. Vier, D. R. Smith, J. B. Pendry, D. N. Basov, and X. Zhang, "Terahertz magnetic response from artificial materials," *Science*, vol. 303, pp. 1494–1496, 2004.
[73] V. G. Veselago, "The electrodynamics of substances with simultaneously negative values of ε and μ," *Sov. Phys. Usp.*, vol. 10, pp. 509–514, 1968.
[74] J. B. Pendry, "Negative refraction makes a perfect lens," *Phys. Rev. Lett.*, vol. 85, pp. 3966–3969, 2000.
[75] S. Zhang, W. Fan, N. C. Panoiu, K. J. Malloy, R. M. Osgood, and S. R. J. Brueck, "Demonstration of an infrared negative-index material," presented at the Nanophotonics for Information Systems OSA Topical Meeting, San Diego, CA, 2005.
[76] S. Zhang, W. Fan, K. J Malloy, S. R. J. Brueck, N. C. Panoiu, and R. M. Osgood, "Near-infrared double negative metamaterials," *Opt. Express*, vol. 13, pp. 4922–4931, 2005.



S. R. J. Brueck (Fellow, IEEE) was born in New York in 1944. He received the B.S. degree in electrical engineering from Columbia University, New York, in 1965 and the S.M. and Ph.D. degrees in electrical engineering from the Massachusetts Institute of Technology (MIT), Cambridge, in 1967 and 1971, respectively.

From 1971 to 1985, he was a staff member at MIT Lincoln Laboratory. In 1985, he moved to the University of New Mexico, Albuquerque, where he is currently a Professor in the Department of Electrical and Computer Engineering and Physics and Astronomy Departments and Director of the Center for High Technology Materials. His current research interests include nanoscale lithography, the physics of nanostructures, the nonlinear optics of poled glasses, and semiconductor laser physics.

III-Nitride LEDs with photonic crystal structures

J. J. Wierer*[a], M. R. Krames[a], J. E. Epler[a], N. F. Gardner[a], J. R. Wendt[b], M. M. Sigalas[c], S. R. J. Brueck[d], D. Li[d], and M. Shagam[c]
[a]Lumileds Lighting, Advanced Laboratories, 370 W. Trimble Rd., San Jose, CA 95131;
[b]Sandia National Laboratories, P. O. Box 5800, Albuquerque, NM 87185;
[c]Agilent Technologies, Agilent Laboratories, 3500 Deer Creek Rd., Palo Alto, CA 94304;
[d]University of New Mexico, Center for High Technology Materials, 1313 Goddard SE, Albuquerque NM 87106;
[e]Boston University, Boston, MA 02215, formerly Univ. of New Mexico

ABSTRACT

Electrical operation of III-Nitride light emitting diodes (LEDs) with photonic crystal structures is demonstrated. Employing photonic crystal structures in III-Nitride LEDs is a method to increase light extraction efficiency and directionality. The photonic crystal is a triangular lattice formed by dry etching into the III-Nitride LED. A range of lattice constants is considered (a ~ 270 - 340nm). The III-Nitride LED layers include a tunnel junction providing good lateral current spreading without a semi-absorbing metal current spreader as is typically done in conventional III-Nitride LEDs. These photonic crystal III-Nitride LED structures are unique because they allow for carrier recombination and light generation proximal to the photonic crystal (light extraction area) yet displaced from the absorbing metal contact. The photonic crystal Bragg scatters what would have otherwise been guided modes out of the LED, increasing the extraction efficiency. The far-field light radiation patterns are heavily modified compared to the typical III-Nitride LED's Lambertian output. The photonic crystal affects the light propagation out of the LED surface, and the radiation pattern changes with lattice size. LEDs with photonic crystals are compared to similar III-Nitride LEDs without the photonic crystal in terms of extraction, directionality, and emission spectra.

Keywords: III-Nitride, AlInGaN, light-emitting diode, LED, photonic crystal

1. INTRODUCTION

III-Nitride light emitting diodes (LEDs) have a high optical refractive index (n~2.4) compared to the exit medium (air, n=1). The index difference causes guided (trapped) optical modes in the semiconductor slab, and hence low extraction efficiencies. A standard III-Nitride[1] is shown in Figure 1. The III-Nitride material is grown on sapphire or SiC substrates (not shown). If a sapphire substrate is used, all the metal contacts are on the top surface. Current spreading is provided by using a thin Ni/Au spreader/contact because of the low conductivity of p-GaN. This Ni/Au layer is thin for light extraction, but optical losses in the metal are still present. The light that is not in the exit cone is trapped in the GaN by total internal reflection and is either lost by multiple reflections off the Ni/Au spreading layer, absorption in the epitaxial structure, or exits out of the sides of the chip. Flip-chip[2,3] and thin-film designs[4] aid in light extraction. Flip chip and thin-film LEDs have high extraction efficiencies (>70%, encapsulated) but they are not perfect, and also they

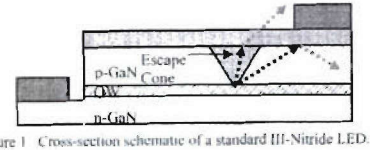


Figure 1 Cross-section schematic of a standard III-Nitride LED.

* E-mail: jonathan.wierer@lumileds.com

Light-Emitting Diodes: Research, Manufacturing, and Applications IX, edited by Steve A. Stockman, H. Walter Yao, E. Fred Schubert, Proc. of SPIE Vol. 5739 (SPIE, Bellingham, WA, 2005) · 0277-786X/05/$15 · doi: 10.1117/12.591718

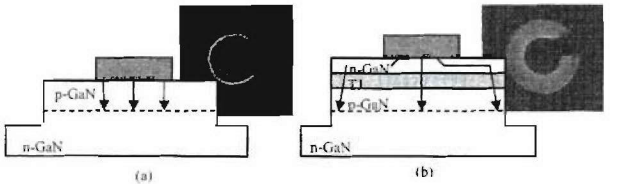


Figure 2 Cross-section schematics and top lit view of a standard (a) and tunnel junction (b) III-Nitride LED.

have Lambertian far-field radiation patterns making them less efficient in étendue limited applications.

Incorporating photonic crystals into III-Nitride LEDs holds the promise of near perfect extraction, and a method of controlling the radiation pattern. Modeling has shown that extraction efficiencies of a photonic crystal LEDs can be as great as 90% (into air)[5]. Various groups have reported electrically injected photonic crystal LEDs in the III-As[6] and in III-Nitride LEDs.[7,8] Using photonic crystals in III-Nitride LEDs is also a means for controlling the radiation pattern.[9]

2. EFFICIENT CURRENT SPEADING WITH TUNNEL JUNCTIONS

Standard III-Nitride LED structures have top p-GaN layers. Although a photonic crystal could be formed into this material by etching into the p-GaN there are some problems. One needs to deposit the spreading metal contact on this structure. If done after etching, deposition in the holes (absorption) needs to be avoided. If done before photonic crystal formation, then a more complicated etch process through the spreading metal layer needs to be performed. The optical loss remains in the LED structure regardless. If one could avoid using the metal spreading layer this would simplify the process of incorporating a photonic crystal into the III-Nitride LED, and avoid metal optical loss.

Using tunnel junctions in III-V semiconductor light-emitting devices has been shown as an effective means for lateral current spreading.[9] This idea has also been incorporated into III-Nitride LEDs.[10] The tunnel junction LED structure is similar to the standard p-up structure and includes a tunnel junction and a top n-GaN layer. A schematic cross-section of both the standard and tunnel junction III-Nitride LED structures is shown in Figure 2. Also shown is a top lit view of the two types of LEDs with circular top contacts. The standard LED only lights up under the contact (no p-GaN current spreading) while the tunnel junction device is able to spread current laterally up to the mesa edge, lighting up the area outside the top contact. Using the tunnel junction structure the photonic crystal can be formed in an area outside the top contact, avoiding the absorbing metal spreading layer.

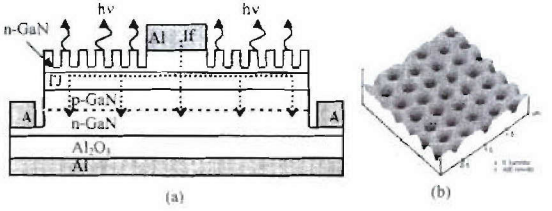
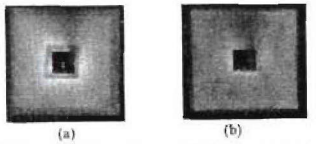


Figure 3 Cross-section of the photonic crystal LED (a) and AFM of the lattice (b).

	a (nm)	d (nm)
PX1	270	200
PX2	295	220
PX3	315	235
PX4	340	250

Table 1



(a) (b)

Figure 4 Top lit view of the photonic crystal LED (a) and the planar LED (b).

3. III-NITRIDE PHOTONIC CRYSTAL – TUNNEL JUNCTION LEDS

In this work III-Nitride epitaxial material with a tunnel junction is employed. Photonic crystal (PX) structures are etched into the top n-GaN layer as shown in cross-sectional schematic in Fig 3a. The photonic crystal is formed by electron-beam lithography and dry etching. The dimensions of the lattices are given in Table 1 where a is the lattice constant and d is the hole diameter. Etch lattice is labeled PX1-4 for the following discussion. The depths of the holes are ~100 nm. A three-dimensional AFM image of one of the lattices is shown in Fig 3b. The photonic crystal area is 150 μm x 150 μm with a non-patterned 50 μm x 50 μm area in the center for the top contact. The total device area is 170 μm x 170 μm. Both contacts are made to n-type material and consisted of Al. Al is also used for a bottom reflector under the sapphire substrate. Located on the same wafer are LEDs without the photonic crystal (planar LED) for comparison. All LED measurements were made without and encapsulent (into air).

Current flows from the top contact and spreads in the top ~1500 nm thick n-GaN layer. This allows for the photonic crystal to be proximal to the active region. The bottom of the holes is ~250 nm above the active region. Lit photographs of the LEDs are shown in Figure 4 with a photonic crystal (a) and without the photonic crystal, or planar (b). Both of the LEDs light up uniformly indicating that the photonic crystal does not affect the current spreading. The outer frame and center area of the photonic crystal LED (Fig 4a) does not contain the photonic crystal and is dimmer, demonstrating the improved extraction of the photonic crystal. No attempt was taken to prevent the current flowing under the contact resulting in light generation under the contact. A portion of this light is lost to absorption in the top contact, and scattering from this center area can be viewed around the top contact.

Figure 5 shows the efficiency and forward voltage (Vf) versus current for both types of LEDs. The current versus voltage characteristics for both LEDs are the same (planer LED Vf not visible because it lies on the PX2 LED Vf curve) another indication that the photonic crystal is not degrading the current spreading. The forward voltages for both LEDs are ~1 V higher (at ~ 30 A/cm^2) than standard LEDs (no tunnel junction) indicating that the tunnel junction is contributing to the larger operating forward voltage. The efficiency of the PX2 LED is greater than the planar LED due to increased light extraction. Gains of 1.5 times over the total emission area and 1.75 times in a ± 30° cone angle

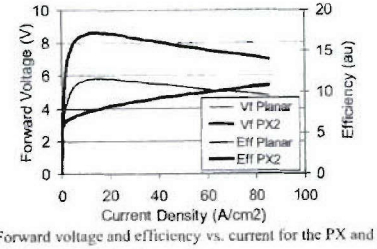
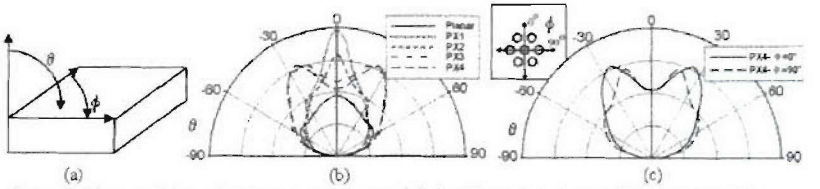


Figure 5 Forward voltage and efficiency vs. current for the PX and planer LED



(a) (b) (c)

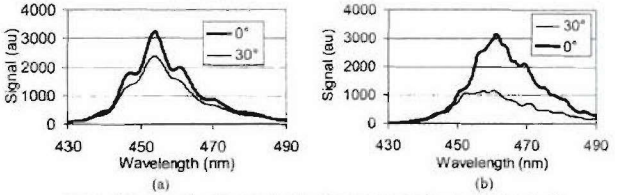
Figure 6 Diagram of the angles (a), radiation patterns of all the LEDs at ϕ=0° (b), and PX4 at ϕ=0° and 90°.

(normal to the LED surface) is achieved with the photonic crystal LED compared to the planar LED.

Measurements of the radiation patterns were made and are shown in Fig. 6. The measurement is performed by scanning a fiber in an arc above the LED, measuring the spectra at various angles. Figure 6 (a) shows the θ direction is out of the LED plane and ϕ is in the LED plane. The measurement was performed in two orthogonal directions (denoted ϕ=0° and 90°) with respect to the lattice orientation, and is diagramed in the inset of Fig. 6 (c). The radiation pattern for the planar LED is near Lambertian with lobes at higher angles due to side light. The radiation patterns for the photonic crystal LEDs are drastically different from the planar LED and from each other; clearly modified by the photonic crystal structure. The radiation patterns of PX4 LED is shown at ϕ=0° and 90° in Fig. 6(c). The patterns are different and two dimensional far-field images show that the patterns are three-fold symmetric as expected by using a the triangular lattice.

Figure 7 shows the spectra of planer (a) and PX2 (b) LEDs at two different angles (θ). The NOPX LED shows the typical Fabry-Perot fringes for a ~ 4 μm thick GaN film on sapphire. These fringes shift slightly with angle because the effective cavity length is longer. The PX2 LED does not show these Fabry-Perot fringes. Instead it displays sharper peaks that are spaced closer together. The spectra also changes more drastically with θ. The photonic crystal is modifying the spectra.

The radiation pattern measurements can also be plotted at a specific wavelength. This is shown for the planar (a) and the PX2 (b) LED for two wavelengths in Fig. 8. The planar LED displays four Fabry-Perot fringes (lobes) that escape the GaN through the exit cone. These lobes shift with wavelength. The PX2 LED also displays wide lobes, but superimposed are sharp, closely spaced peaks. These sharp peaks are optical modes that would have otherwise been wave-guided in a planar LED, scattering out by the photonic crystal. This shows that the photonic crystal structure is acting as a Bragg scatter modifying the light output, and increasing the extraction efficiency of the LED.



(a) (b)

Figure 7 Spectra of the planar (a) and photonic crystal LED (b) at two angles (θ).

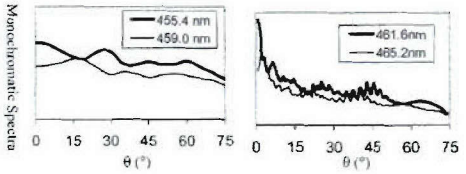


Figure 8 Monochromatic Spectra of the planar (a) and photonic crystal LED (b) at two wavelengths.

4. LITHOGRAPHY TECHNIQUES FOR PHOTONIC CRYSTALS

The photonic crystal LEDs in this work were patterned using electron-beam lithography.[11] This method is extremely flexible in writing different patterns, and is therefore used extensively in research of photonic crystals. The limitation is that for large areas, such as 2" or greater diameter wafers, the write times become long (days). For the high throughput that is necessary for production of LEDs this method is not practical. There are various other faster methods for forming nano-scale features.

One method is to use interfering coherent laser beams called interferometric lithography (IL).[12] The interference pattern periodicity is determined by the laser wavelength (λ), the angle between the two beams (θ), and the ambient index (n) using the equation:

$$\text{Period}=\lambda/(2n\sin\theta) \qquad (1)$$

The shorter the laser wavelength and the larger the ambient index, the smaller the period. With 193nm ArF lasers and immersion techniques the period can easily be sub-100nm, small enough for creating GaN photonic crystals that are in the band-gap for blue-green light. Exposure of full wafers is possible with this method, resulting in high through-put process. Also, it is a mask-less process so changing period and feature sizes is rapid and inexpensive. A demonstration of an IL defined photonic crystal is shown in Figure 9.

Another method is imprint lithography. There are two types of imprint lithography. In both methods a stamp is created with nano-scale features typically with electron-beam lithography. Then an imprint resist is placed on the wafer. In the first method the stamp is brought in contact with the coated wafer and heat and pressure is applied. The underlying resist layer conforms to the stamp; forming the inverse pattern in the resist.[13] In the second method a viscous resist that is sensitive to ultraviolet light is used. The stamp is brought into contact at low pressures and ultraviolet light is used to harden the resist.[14] The only limitation is the feature sizes on the stamp and sub-100nm features are also achievable with imprint lithography.

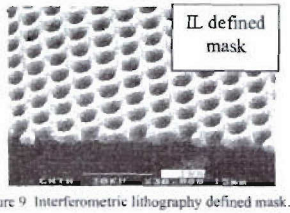


Figure 9 Interferometric lithography defined mask.

5. CONCLUSION

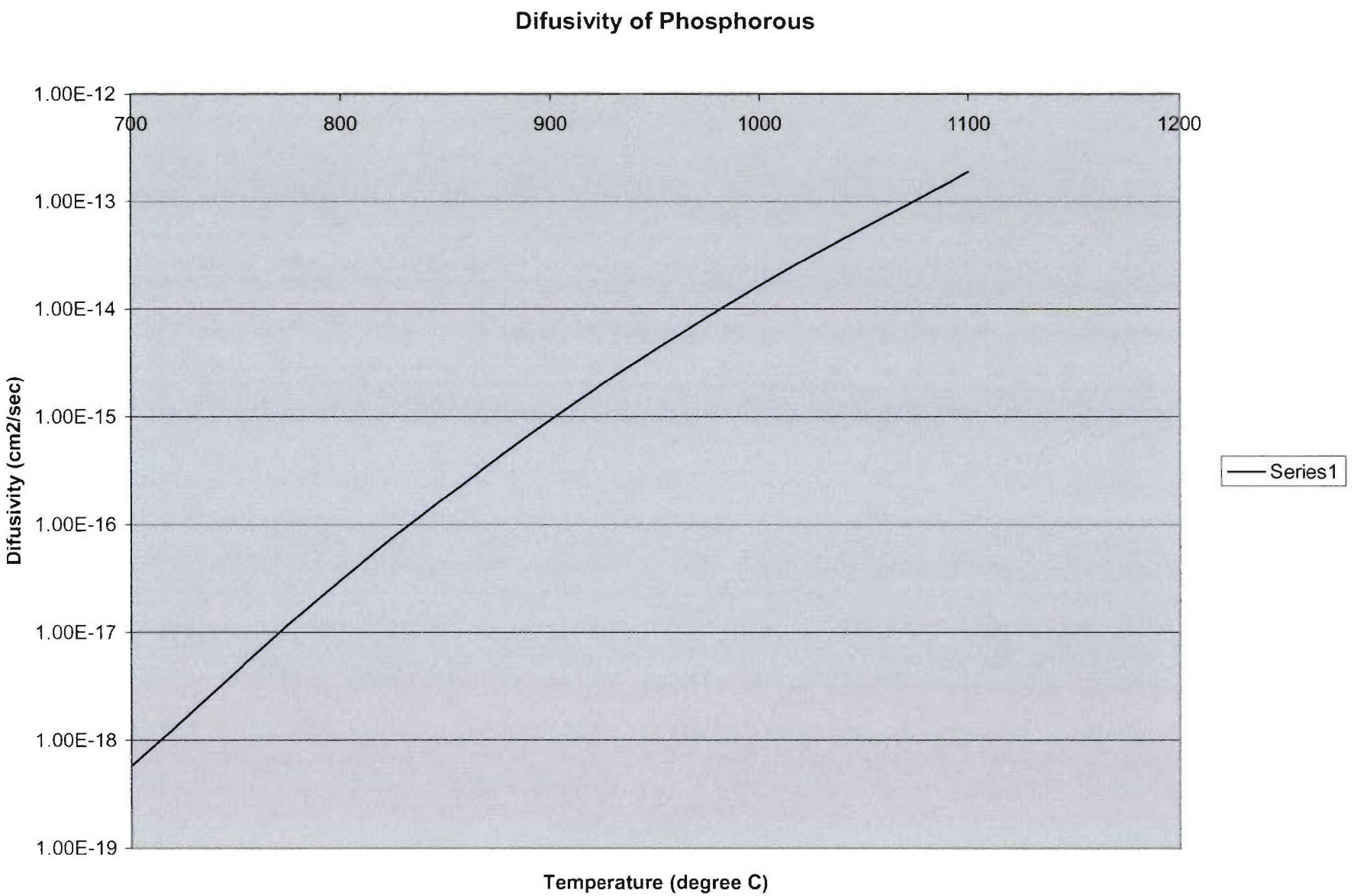
We demonstrated electrically operated III-Nitride LEDs with photonic crystal structures. A tunnel junction is used in the epitaxial structure allowing for efficient current spreading. This also enabled a device where the photonic crystal is proximal to the active light emitting region. The photonic crystal increases the extraction of the device with maximum brightness gains of 1.75 times compared to planar LEDs. The photonic crystal is Bragg scattering what would have otherwise been waveguide modes out of the structure increasing the extraction; clearly shown in the radiation patterns of the photonic crystal LEDs.

ACKNOWLEDGEMENTS

The authors would like to acknowledge several people who have contributed to this work including K. Than, T. Nguyen, and R. Laxamana. Sandia is a multiprogram laboratory operated by Sandia Corporation, a Lockheed Martin Company, for the United States Department of Energy under Contract DE-AC04-94AL85000.

REFERENCES

1. S. Nakamura and G. Fasol: The Blue Laser Diode (Springer-Verlag, Heidelberg, 1997) 1st ed.
2. J. J. Wierer, D. A. Steigerwald, M. R. Krames, J. J. O'Shea, M. J. Ludowise, G. Christenson, Y.-C. Shen, C. Lowery, P. S. Martin, S. Subramanya, W. Götz, N. F. Gardner, R. S. Kern, and S. A. Stockman, "High-power AlGaInN flip-chip light-emitting diodes," Appl. Phys. Lett. **78**, 3379 (2001).
3. D. A. Steigerwald, J. C. Bhat, D. Collins, R. M. Fletcher, M. O. Holcomb, M. J. Ludowise, P. S. Martin, and S. Rudaz, "Illumination with solid state lighting technology, Illumination with solid state lighting technology," IEEE J. Sel. Top. Quantum Electron. **8**, 310 (2002).
4. W. S. Wong, T. Sands, N. W. Cheung, M. Kneissl, D. P. Bour, P. Mei, L. T. Romano, and N. M. Johnson, "Fabrication of thin-film InGaN light-emitting diode membranes by laser lift-off," Appl. Phys. Lett. 75, 1360 (1999).
5. S. Fan, P. R. Villeneuve, J. D. Joannopoulos, and E. F. Schubert, "High extraction efficiency of spontaneous emission from slabs of photonic crystals," Phys. Rev. Lett. **78**, 3294 (1997).
6. H. Ichikawa, and T. Baba, "Efficiency enhancement in a light-emitting diode with a two-dimensional surface grating photonic crystal," Appl. Phys. Lett. **84**, 457 (2004).
7. T. N. Oder, K. H. Kim, J. Y. Lin, and H. X. Jiang, "III-nitride blue and ultraviolet photonic crystal light emitting diodes," Appl. Phys. Lett. **84**, 466 (2004).
8. J. J. Wierer , M. R. Krames, J. E. Epler, N. F. Gardner, M. G. Craford, J. R. Wendt, J. A. Simmons, and M. M. Sigalas, "InGaN/GaN quantum well heterostructure light-emitting diodes employing photonic crystal structures," Appl. Phys. Lett., **84**, 3885 (2004).
9. J. J. Wierer, P. W. Evans, N. Holonyak, Jr., " Buried tunnel contact junction AlGaAs-GaAs-InGaA quantum well heterostructure lasers with oxide-defined lateral currents," Appl. Phys. Lett. **71**, 2286 (1997).
10. T. Takeuchi, G. Hasnain, S. Corzine, M. Hueschen, R. P. Schneider, Jr., M. Blomqvist, Y.-L. Chang, D. Lefforge, M. R. Krames, L. W. Cook, and S. A. Stockmann, "GaN-based light emitting diodes with tunnel junctions," Jpn. J. Appl. Phys., Part 2 **40**, L861 (2001).
11. J. R. Wendt, G. A. Vawter, P. L. Gourley, T. M. Brennan, and B. E.Hammons, "Nanofabrication of photonic lattice structures in GaAs/AlGaAs," J. Vac. Sci. Technol. B **11**, 2637 (1993).
12. S. H. Zaidi and S. R. J. Brueck, "Multiple-exposure interferometric lithography," J. Vac. Sci. Technol. B **11**, 658 (1993).
13. S. Y. Chou, P. R. Krauss, and P. J. Renstrom, "Imprint of sub-25nm vias and trenches in polymers," Appl. Phys. Lett., **67**, 3114 (1995).
14. P. Ruchhoeft, M. Colburn, B. Choi, H. Nounu, S. Johnson, T. Bailey, S. Damle, M. Stewart, J. Ekerdt, J. C. Wolfe, and C. G. Wilson, "Patterning curved surfaces: Template generation by ion beam proximity lithography and relief transfer by step and flash imprint lighography," J. Vac. Sci. Technol. B **17**, 2965 (1999).


Difusivity of Phosphorous
1.00E-12
1.00E-13
1.00E-14
1.00E-15
1.00E-16
1.00E-17
1.00E-18
1.00E-19
Difusivity (cm2/sec)
700
800
900
1000
1100
1200
Temperature (degree C)
Series1